KfK 4313
September 1988

# Interaction between Aluminium Oxide Pellets and Zircaloy Tubes in Steam Atmosphere at Temperatures above 1200° C

## Posttest Results from the CORA Tests B and C

S. Hagen, P. Hofmann, G. Schanz, L. Sepold
Hauptabteilung Ingenieurtechnik
Institut für Material- und Festkörperforschung
Projektgruppe LWR-Sicherheit

Kernforschungszentrum Karlsruhe

Kernforschungszentrum Karlsruhe

Hauptabteilung Ingenieurtechnik
Institut für Material- und Festkörperforschung
Projektgruppe LWR-Sicherheit

KfK 4313

# Interaction between Aluminum Oxide Pellets and Zircaloy Tubes in Steam Atmosphere at Temperatures above 1200 °C (Posttest Results from the CORA Tests B and C)

S. Hagen, P. Hofmann, G. Schanz, L. Sepold

Kernforschungszentrum Karlsruhe GmbH, Karlsruhe

Kernforschungszentrum Karlsruhe GmbH
Postfach 3640, 7500 Karlsruhe 1

ISSN 0303-4003

**Abstract**

The interaction between alumina ($Al_2O_3$) pellets and zircaloy cladding was studied in two high-temperature experiments performed in the CORA facility at the Kernforschungszentrum Karlsruhe (KfK). CORA is an out-of-pile facility designed for Severe Fuel Damage experiments. In these experiments fuel elements are subjected to temperature transients with heatup rates in the order of 1 K/s and peak temperatures of about 2200 °C. In the CORA tests 16 electrically heated fuel rod simulators arranged together with 9 unheated rods in a 25-rod bundle were used. In the first tests the fuel was simulated by alumina pellets. However, using $Al_2O_3$ instead of $UO_2$ as pellets, the high-temperature behavior of "burnable poison rods" could be studied. The burnable poison rods in Light Water Reactors (LWR) consist of $Al_2O_3/B_4C$ pellets surrounded by Zircaloy-4 cladding tubes. In the $Al_2O_3/B_4C$ pellets of a LWR rod alumina is the main constituent (98.6 wt.-%) whereas boron carbide acts as neutron absorber.

Failure of the $Al_2O_3$/zircaloy test rods started at 1350 °C when first droplets of molten material were observed running down the test bundle forming bundle blockages upon solidification. Post test examinations revealed that the process of liquefaction was initiated by a reduction of alumina by zircaloy resulting in a (Zr, Al, O) melt which decomposed on cooldown into two metallic phases, a (Zr, Al) alloy and oxygen-stabilized α-Zr(O).

The components of an extremely porous ceramic melt were also Zr, Al, and oxygen but with a higher oxygen content compared to the metallic melt. The ceramic melt decomposes on cooldown into an $Al_2O_3/ZrO_2$ eutectic with various amounts of primary constituents.

Other types of relocated material were due to melting of essentially unreacted zircaloy cladding and to debris formation by fracturing of oxidized cladding and $Al_2O_3$ pellets stack residues.

The interactions between $Al_2O_3$ and zircaloy occurring in a burnable poison rod are furthermore important for the behavior of the entire LWR core because the generated melts are able to attack the $UO_2$ chemically and dissolve or liquefy the fuel even below the melting point of zircaloy (1760 °C). As a result, fuel elements which contain burnable poison rods are expected to fail under severe accident conditions at about 1500 °C.

**Wechselwirkung zwischen Aluminiumoxid-Tabletten und Zirkaloy-Hüllrohren in Dampfatmosphäre bei Temperaturen oberhalb 1200 °C (Nachuntersuchungsergebnisse der Experimente CORA B und C)**

## Zusammenfassung

In zwei Hochtemperaturexperimenten, die in der CORA-Anlage des Kernforschungszentrums Karlsruhe (KfK) durchgeführt wurden, sollten die chemischen Wechselwirkungen zwischen $Al_2O_3$-Tabletten und Zirkaloy-Hüllrohr untersucht werden. Die CORA-Anlage ist eine Out-of-pile-Versuchsapparatur, in der Experimente zu sogenannten schweren Kernschäden durchgeführt werden. Dabei werden Brennstabbündel Temperaturtransienten mit Aufheizraten von etwa 1 K/s und Maximaltemperaturen von ca. 2200 °C ausgesetzt. Die CORA-Versuchsbündel bestehen aus 25 Brennstabsimulatoren, von denen 16 elektrisch beheizt werden. In den ersten beiden Versuchen war der "Brennstoff" $UO_2$ durch Aluminiumoxid ($Al_2O_3$) ersetzt worden. Durch diese Anordnung war es möglich, das Verhalten von Kernreaktorstäben mit abbrennbaren Giften (engl.: burnable poison rods) bei hohen Temperaturen zu untersuchen. Diese Art von Stäben, die in einigen Leichtwasserreaktoren (LWR) eingesetzt sind, bestehen vorwiegend aus $Al_2O_3$ (98,6 Gew.-%) und aus Borkarbid ($B_4C$) in Tablettenform. Dabei wirkt das Borkarbid als Neutronenabsorber. Die $Al_2O_3/B_4C$-Pellets sind in Hüllrohre aus Zirkaloy-4 eingefüllt.

Das Versagen der $Al_2O_3$/Zirkaloy-Stäbe begann bei ca. 1350 °C, wie erste herabfallende Schmelztropfen anhand von Videoaufnahmen während der Versuche erkennen ließen.Wie die Nachuntersuchungen der beiden Versuchsbündel zeigten, wurde die Entstehung von schmelzflüssigen Phasen durch die Reduktion des $Al_2O_3$ zu Al mittels Zirkonium ausgelöst. Dadurch entstand eine Schmelze aus (Zr, Al, O), die bei der Abkühlung in zwei metallische Phasen, eine (Zr, Al)-Legierung und eine sauerstoffstabilisierten α-Zr(0)-Phase zerfiel.

Die Komponenten einer extrem porösen keramischen Schmelze waren ebenfalls Zr, Al und O, während diese bei der eutektischen Erstarrung in $ZrO_2$, $Al_2O_3$ und unterschiedliche Anteile von Primärkristallen zerfiel.

Weitere Materialverlagerungen ergaben sich aus dem Abschmelzen von im wesentlichen unverändertem Hüllrohrmaterial und der Bildung eines Schüttbetts aus Resten oxidierter Hüllrohre und $Al_2O_3$-Bruchstücke.

Die Wechselwirkungen zwischen $Al_2O_3$ und Zirkaloy, die bei erhöhten Temperaturen in den Stäben mit abbrennbaren Giften ablaufen, sind für das Materialverhalten des gesamten Reaktorkerns von Bedeutung. Die aus der Wechselwirkung entstehenden flüssigen Phasen können den Reaktorbrennstoff $UO_2$ bereits unterhalb des Zirkaloy-Schmelzpunkts von 1760 °C chemisch angreifen und auflösen. Als Folge davon ist ein frühes Versagen (ab etwa 1500 °C) für diejenigen Brennelemente möglich, die sogenannte Burnable-Poison-Stäbe enthalten.

Contents: Page

## 1. Introduction

Two high-temperature experiments with fuel rod simulators using alumina ($Al_2O_3$) as pellet instead of $UO_2$ were performed at the Kernforschungszentrum Karlsruhe (KfK) to study the materials behavior of burnable poison rods at elevated temperatures. The pellet columns were surrounded by zircaloy tubes identical to those used in commercial light-water reactors (LWR).

Alumina was chosen as pellet material for two reasons. First, it was advisable to conduct the scoping tests of an experimental program with alumina as fuel simulator rather than urania as is used in the main test series. Secondly, aluminum oxide is of interest with respect to interactions with zircaloy. $Al_2O_3$ is the main constituent of burnable poison rods. In these rods pellets consisting of 98.6 wt-% $Al_2O_3$ and 1.4 wt-% $B_4C$ (the latter material acts as neutron absorber) are encapsuled in tubes of zircaloy. Chemical interactions between $Al_2O_3$ and zircaloy had to be expected at elevated temperatures because $Al_2O_3$ is thermodynamically unstable with respect to zirconium. Post-accident investigations of the damaged TMI-2 core had provided evidence of pronounced destruction in the upper part of the core, i.e. in the vicinity of burnable poison rods.

The experiments with alumina pellets were conducted in the CORA facility, an out-of pile facility designed to investigate fuel rod behavior under simulated small break LOCA (loss of coolant accident) conditions. Fig. 1 is a photograph and Fig. 2 is a schematic of the test facility.

The CORA test program is part of the overall Severe Fuel Damage (SFD) research program of the Federal Republic of Germany. The facility allows the operation with fuel rod simulator bundles of different configuration and under various system atmospheres /1,2/.

The two tests with aluminum oxide as pellet material were designated CORA B and CORA C. The experiments were conducted on September 3, 1986 and on February 2, 1987, respectively.

## 2. Test Conditions

The CORA test B and C bundle consisted of 25 fuel rod simulators with 16 heated and 9 unheated rods. For heating of the rods solid tungsten pins were inserted in the center of the simulators to work as electric resistance heaters. The arrangement of heated and unheated rods is given in Fig. 3 . Also in Fig. 3 is shown a schematic of the test section with shroud insulation and high-temperature shield with insulation.

Along the heated length of 1.00 m, the bundle was surrounded by a zircaloy shroud. The shroud was insulated by a $ZrO_2$ fiber material in test C but was uninsulated in test B. The insulation significantly reduced the heat loss in test C and provided a flat radial temperature distribution in bundle C compared to test B. Both rod bundles were held in place by three grid spacers of zircaloy. They were mounted below the heated region, in the middle of the heated zone, and above the heated section. The axial locations can be taken from Table 1 in which the design characteristics of the fuel rod simulator bundle are listed.

In both experiments the test section was instrumented with W/Re and NiCr/Ni type thermocouples and two-color pyrometers to measure steam temperature, rod cladding temperature, shroud temperature, and insulation temperature. In test CORA-B eight thermocouples were installed in the test section and 26 at different elevations of the high-temperature insulation. In test CORA-C 34 and 32 thermocouples were used in the bundle and high-temperature insulation, respectively. In addition, one videoscope in test B and ten videoscopes in test C were used to observe the high-temperature materials behavior and the relocation of material during transient testing.

The operational data, e.g. voltage, current, electric power, pressure, and temperatures, and the temperatures of the test section were recorded by a data acquisition system.

The hydrogen production was measured by a quadrupole mass spectrometer (type Leybold PQ 100).

Each test was started from steady state by raising the electric rod power leading to the transient part of the test. The test bundles B and C were exposed to heatup rates of 0.5 and 1.0 K/s, respectively, with maximum temperatures of about 2000 °C in both experiments. Cooldown was accomplished by a reduction in electric power. For an illustration of the test conduct, traces of rod power and

temperature of an unheated rod are given in Fig. 4 . The lower power rate for the case of insulated shroud (test C) is evident in this figure.

Further details of the experimental conduct are available in References /3/ and /4/.

Differences in the conduct of the two experiments were as follows:

1. No steam but stagnant argon was used in test B; argon flow and additional steam flow was used in test C. There was, however, a limited steam supply during the high-temperature phase of test B when approx. 3 liters of water evaporated from the quench unit below the heated bundle. Test C was started with a flow of preheated argon (approx. 5 g/s at 400 °C). From 300 s in transient test the argon flow was changed to 3 g/s and an additional steam flow of 4.5 g/s was turned on. The steam inlet temperature was in the order of 700 °C.

2. The radial temperature profile across the bundle was pronounced in test B and rather flat in test C due to the shroud insulation and additional insulation of the channel between shroud and high-temperature shield (see Fig. 3). The latter measure excluded heat transfer to the outside by convection.

3. A maximum power of 85 kW was input during test B whereas only 30 kW were sufficient to reach the target temperature of about 2000 °C of test C.

**Table 1:** Design characteristics of the fuel rod simulators used in CORA tests B and C

| | | | |
|---|---|---|---|
| Rod outside diameter: | | | 10.75 mm |
| Cladding material: | | | Zircaloy-4 |
| Cladding thickness: | | | 0.725 mm |
| Rod length: | | | 2175 mm |
| Heated length: | | | 1000 mm |
| Bundle size: | | | 25 rods |
| Number of heated rods: | | | 16 |
| Fuel simulator | heated rods: | | $Al_2O_3$ pellets |
| | unheated rods: | | $Al_2O_3$ pellets |
| Heater material: | | | Tungsten |
| Heater diameter: | | | 6 mm |
| Pitch: | | | 14.3 mm |
| Grid spacer | - Material: | | Zircaloy-4 |
| | - Length: | | 42 mm |
| | - Axial location Test B | lower: | - 75 mm [(a)] |
| | | center: | + 525 mm |
| | | top: | + 1125 mm |
| | - Axial location Test C | lower: | - 50 mm |
| | | center: | + 460 mm |
| | | top: | + 900 mm |
| Shroud | - Material: | | Zircaloy-4 |
| | - Wall thickness: | | 1 mm |
| | - Outside dimensions: | | 86 x 86 mm |
| | - Elevation: | CORA B | 36 - 1060 mm |
| | | CORA C | 36 - 1240 mm |
| Shroud insulation (Test CORA C only) | | | |
| | - Material | | $ZrO_2$ fiber |
| | - Thickness | | 20 mm |

(a) Elevations are meant for the bottom of the grid spacer and are referred to the bottom of the heated zone (0 mm = EL 5121).

### 3. Posttest Appearance of the Bundle

The appearance of the test bundles B and C are given as an overview at different orientations in Figs. 5 and 6 . Severe destructions are apparent at both bundles. Differences in the posttest appearance of both bundles are mainly due to the differences in shroud insulation. Test bundle B was not insulated around the shroud. So, there was a significant radial temperature gradient inhibiting interactions between the test rods and the relatively cold shroud. After the test the shroud could easily be removed from the bundle as a whole.

In test C the shroud was thermally insulated by $ZrO_2$ fiber material so that rods and shroud were basically at the same temperature during the test. The shroud was largely deformed in test C, particularly in the lower half of the bundle. Shroud and rods were stuck together indicating interactions between these structures. Remnants of the $ZrO_2$ insulation can be observed at the outside of the shroud (white spots). The shroud became very brittle in test C so that it was difficult to remove the shroud in large pieces after the test. As can be seen in Figs. 6 and 7 , wires were used to hold the shroud of bundle C in place.

The shroud insulation had also an effect on the solidification of the molten material. Keeping most parts of the bundle at high temperature, the holes in the shroud (viewports) worked as heat sinks allowing the melt to solidify locally there (Fig. 7 ).

In the lower parts of both bundles a white ceramic solidified material was found. Besides this ceramic material, pieces of black material of metallic composition were found inside the bundle and below. The metallic material was clearly separated from the ceramic melt. There were more metallic portions in and below bundle B than in bundle C.

Below the heated region of the bundle, an abundancy of various debris was found after the experiments had been performed. In bundle C, however, the amount of fragments that fell off the test section was significantly less compared to bundle B.

Aerosols generated during the heatup periods of each experiment are found deposited on the surfaces of tungsten heater, pellets, and cladding. Video cameras inserted into the bundles showed more aerosol transportation during test B compared to test C.

A detailed description of the posttest appearance is provided with the two following sections. The description can be compared with the cross-sectional photographs of CORA bundles B and C that are compiled in the appendix.

### 3.1 Posttest Condition of Bundle B

The damage to bundle B can be described in the following way:

The upper two thirds of bundle B (from about 370 mm upward) melted away during the test, and the material from this region relocated in the lower third of the bundle. In the lower portion there are extended reaction zones. The material of these zones is identified by a white color and by a high porosity. In the upper section unheated rods have disappeared completely. Also cladding and annular $Al_2O_3$ pellets of the heated rods are gone within a large region leaving the tungsten heaters as remnants. So, the destruction of heated and unheated rods had occurred in the same way. The interaction between $Al_2O_3$ pellets and zircaloy cladding which was responsible for the formation of liquid phases and relocation of material did not stop at the upper end of the heated zone. Interaction can be recognized even in the upmost cross section of 1159 mm (see Fig. A-2, Appendix). The zircaloy grid spacer is as well attacked at this elevation.

Details of the upper cross sections (1141 mm and 1159 mm) indicate deformation of the cladding ("flowering") and regions of different microstructure along the circumference of the cladding due to different stages of oxidation. One part of the cladding looks rather unoxidized while the other part appears strongly oxidized with a large number of cracks. Between the two structures cladding material is missing (Fig. 8 ). This inter-cladding space is a sign of once-molten material which had moved out of this region to lower elevations during the test.

At 900 mm pellets of three corner rods could withstand the temperature transient. Ceramic melt is deposited at some pellet remnants.

In the 500-mm region (axial hot spot) there is nothing left except the eutectic decomposition products $Al_2O_3$ and $ZrO_2$ of the ceramic (Al, Zr, O) melt.

At 200 mm the interaction between pellet and cladding material can be recognized in an advanced stage. In the 100-mm elevation rod claddings are left in the outer regions. In these regions the $Al_2O_3$ pellets appear almost entirely intact. Although the cladding of the outer rods shows the "flowering" effect, no

difference in the material's structure is visible as was observed in the cross sections above the heated zone.

A considerable amount of once-molten material is found solidified at the bottom of the bundle (Fig. 9), at the position of the bottom grid spacer. This ceramic material formed a kind of crucible between 75 mm and -16 mm embedding various debris from 15 mm to 75 mm elevation (see cross section, Fig. 10 , and longitudinal section, Fig. 11) and metallic melt at the bottom of the heated zone (Fig. 12). The metallic melt was identified as an intermetallic phase $Zr_xAl_y$ with a measured Vickers microhardness of MHV 918 compared to MHV 440 of the tungsten heater.

At 0 mm elevation there are some alumina pellets left. They are partly without cladding but embedded in the solidified $Al_2O_3/ZrO_2$ eutectic alloy surrounding the metallic center. In this center position neither cladding nor pellet can be recognized.

At -50 mm (bottom grid spacer) the zircaloy of the grid spacer and the zircaloy of the cladding are baked together. Despite the grid spacer the blockage of this cross section is less than in the area above with a maximum of blocked flow area between + 1 mm and -18 mm.

The various types of rubble deposited below the heated region are depicted in Fig. 13 . In this figure the fragments are characterized by three types of material although the same kind of material can be of different shape. The black, shiny material is metallic, the gray, foamy material is ceramic melt, the third type is debris from embrittled residues of the simulator rods.

An example for aerosol deposition on cladding and pellets is given in Fig. 14 . In this picture the cladding appears brittle and unattacked by the pellets. The cladding in front (rod No. 20) is bent away from the pellets. Lack of contact means prevention of interaction between materials.

### 3.2 Posttest Condition of Bundle C

In bundle C the interaction between materials above 650 mm was less than in bundle B. This fact might be due to a stronger oxidation of the cladding in bundle C (steam flow) compared to bundle B (some steam from evaporation of the water pool below the test section). The major damage to the bundle is

between 200 mm and 600 mm (for comparison see also cross sections of bundle C compiled in the appendix).

Claddings and pellets of all rods are intact above 1094 mm. Between 900 mm and 1094 mm some heated as well as unheated rods have lost their claddings. The alumina pellets, however, appear intact above the top of the heated zone (1000 mm). Below 900 mm there is no cladding intact and some interaction between pellets and cladding had occurred. An enhanced interaction can be observed between 600 mm and 700 mm.

The "region of destruction" lies between 200 mm and 600 mm. In this region the liquefaction process started at about 1350°C as was observed by video cameras during the test. At about 1550°C the rod structures collapsed. In this region there are no materials but the tungsten heaters left. Below this voided region the material from above relocated forming a blockage zone which extends to the very bottom, i.e. below the heated test section. The density of relocated material differs as can be seen in the longitudinal section between 88 mm and 209 mm (Fig. 15 ).

The largest blockage of the cross section in bundle C caused by material relocation lies between 56 and 86 mm. In this section, however, a great portion of the molten material solidified outside the shroud leaving sufficient area for coolant channels.

The shroud of bundle C was extremely brittle. Melt from the bundle was found refrozen at the inside and outside of the shroud. The largest shroud deformation occurred in the region between 300 and 700 mm, i.e. in the region of the axial peak temperature.

An example for the transition from an undamaged state to melt formation is given with Fig. 16 . Rod No. 36, for instance, is intact from the top down to about 710 mm (with the cladding oxidized). From 710 mm to 670 mm the cladding is missing but the $Al_2O_3$ pellets are still intact. Melt droplets can be seen between 670 mm and 650 mm. Rivulets of melt ("Candling") can be observed below 650 mm. So, the transition from intact rods to partly molten pellets occurred on a length of about 60 mm only.

# 4. Metallographic Examination

## 4.1 Investigation of Relocated Materials and Fragments Taken from the Test Bundles

First results on the composition of relocated materials were obtained from samples which were taken off the test bundle prior to encapsulation in epoxy. Fragments of different appearance were taken either directly from the bundle, from remnants that had fallen below the heated test section during the test or dropped into the water pool which was used to keep the lower bundle head cool (Fig. 17).

As already mentioned in chapter 3.1 the various relocated materials and fragments of CORA tests B and C can be classified in three types (see Fig. 13): type A) Ball-shaped foamy ceramic materials, rather light and white looking. Sometimes many particles are attached to each other forming large conglomerates. Type B) Once molten metallic material of black colour with a smooth glass-like surface. This type of material has a higher density than the materials of type A and C, type C) Partially or fully oxidized Zircaloy cladding fragments without or with attached solidified materials. All the materials exhibit different sizes and shapes. Fig. 13 shows various relocated materials taken from Bundle B; Fig. 18 shows a large fragment being taken from Bundle C.

### 4.1.1 Materials Taken from Bundle B

From each of the various types of relocated materials (A, B, C) specimens were taken for metallographic and for analytical scanning electron microscope (SEM) examination with an energy dispersive X-ray system (EDX) or wavelength dispersive X-ray system (WDX) to determine the chemical composition of relocated material and of the reaction products.

**Type A:** The macro- and microstructure of a typical ball-shaped white looking ceramic "droplet" (CORA B-1) is shown in Fig. 19. A cut through this particle (top of Fig. 19) reveals a very porous ceramic material with many radially extended pores indicating large temperature gradients resulting from fast cooldown. The porous nature of this type of particles is the reason for their low density. The microstructure (photos in center and bottom of Fig. 19) indicates an eutectic phase formation. SEM/EDX examinations of specimen CORA B-1 result in a very

fine $Al_2O_3/ZrO_2$ eutectic alloy with large primary $Al_2O_3$ constituents (see chapter 5.2.3). The (Al,Zr,O) melt, which forms due to chemical interactions, decomposes on cooldown at about 1800 °C eutectically (eutectic temperature varies in literature between 1710 and 1850 °C) into $Al_2O_3$ and $ZrO_2$. The average chemical composition of specimen CORA B-1 is about 63 wt.% $Al_2O_3$ and about 37 wt.% $ZrO_2$. Fig. 20 shows the Al and Zr distribution of specimen CORA B-1. The $Al_2O_3$ phase contains no Zr and the $ZrO_2$ phase contains no Al. The gross chemical composition of the particles type A varies from specimen to specimen which can easily be recognized by the different phase portions in the solidified materials (Fig. 21). Fig. 21 shows three different relocated ceramic melts; the microstructure of each material reveals an $Al_2O_3/ZrO_2$ eutectic alloy with various amounts of primary $Al_2O_3$ constituents of typical angular shape. In some cases the primary $Al_2O_3$ constituents grow in a form of dendrites as shown in picture c of Fig. 21. The primary constituents form on solidification first and are in general homogeneously distributed in the eutectic $Al_2O_3/ZrO_2$ alloy, which is sometimes hardly to recognize due to its extremely small phase size (see picture c in Fig. 21). Picture b in Fig. 21 shows in addition two regions with entrained $ZrO_2$ fragments of completely oxidized cladding. Those pieces have been embedded in the eutectic alloy but not yet chemically dissolved in the ceramic (Al,Zr,O) melt at temperature. Sometimes the solidified ceramic melts contain various amounts of metallic inclusions of an (Al,Zr) alloy with some Sn (from the Zircaloy cladding) and W (from the tungsten heaters).

**Type B:** The fragments of black, glass-like appearance as shown in Fig. 13 were identified as once molten metallic materials. Fig. 22 shows the microstructure of specimen CORA B-5 which consists, according to SEM/EDX examinations, of mainly two phases: oxygen stabilized α-Zr(O) and a (Zr,Al,Sn) alloy. Sometimes small $ZrO_2$ precipitates can be recognized in the solidified melt in addition. The average chemical composition of specimen CORA B-5 is about 68 wt.% Zr, 31 wt.% Al, and 1 wt.% Sn. In general, the composition can vary strongly from particle to particle. The formation of a metallic (Al,Zr) alloy is a clear indication for the chemical reduction of $Al_2O_3$ by the Zircaloy cladding. According to the Al/Zr phase diagram first liquid metallic phases have to be expected at about 1350 °C (eutectic between β-Zr and $Zr_5Al_3$, see chapter 5.2) which is in agreement with the physicochemical behavior of Bundle B during heatup which indicated first molten materials at this temperature. The eutectic temperature of the metallic alloy is much lower than the onset of melting for Zircaloy cladding (~ 1760 °C) or the eutectic temperature of the ceramic $Al_2O_3/ZrO_2$ alloy at about

1800 °C. This means the various melts will form and relocate at different temperatures and times. Therefore, solidification occurs at different axial elevations in the test bundle.

**Type C:** The macro- and microstructures of fully oxidized Zircaloy cladding fragments with attached partially molten material are shown in Fig. 23 and 24. Fig. 23 is an illustration of a rod fragment that appears "intact" on the outside and partially molten on the inside of the cladding with attached material. A sequence of microstructures is given for the examined cross section A through B. The outermost structure is the oxidized cladding which did not reach the onset of melting (m.p. of $ZrO_2$: ~ 2700 °C). The large $ZrO_2$ crystalline grains in this region are an indication for the high formation temperatures and the stoichiometric composition of the formed $ZrO_2$. The porosity is due to pieces that were broken out during the metallographic preparation of the specimen. The reaction layer adjacent to the $ZrO_2$ is quite inhomogeneous and consists of an $Al_2O_3/ZrO_2$ eutectic alloy in fine to coarse dispersion and of some patches rich in $Al_2O_3$. This reaction layer results from the interaction between the $Al_2O_3$ pellet and the Zircaloy cladding and/or $ZrO_2$ at temperatures ≥ 1800 °C, the eutectic temperature of the $Al_2O_3/ZrO_2$ alloy. At similar specimens and at much higher magnifications one can recognize the typical eutectic structure of the $Al_2O_3/ZrO_2$ reaction zone (Fig. 24). The next layer can be described as the interaction zone within the original $Al_2O_3$ pellet. Here at least the cores of the $Al_2O_3$ grains have never been in a molten stage, whereas the grain boundary regions have continuously been leached under the attack of liquid material. During solidification the alumina-rich phase either forms an eutectic $Al_2O_3/ZrO_2$ microstructure or crystallizes around the "primary" $Al_2O_3$ crystals, thus leaving the grain boundary regions for the Zr-rich oxidic phase. This layer is porous and contains some metallic inclusions. The next layer towards the inside is the - almost unchanged - alumina pellet with its original grain size and porosity. The innermost layer again results from re-solidified melt. Some $Al_2O_3/ZrO_2$ eutectic alloy must have flown downwards along the inner surface of the annular alumina pellet interacting with it and partly dissolving it along the contact region.

### 4.1.2 Materials Taken from Bundle C

As in test CORA-B, similar molten materials and fragments have formed and relocated in test CORA-C. Beside the three types of materials A, B, and C some shroud fragments were taken and examined to get information of the chemical attack of the Zircaloy shroud by steam and relocated molten materials.

Specimen CORA C-1 (Fig. 25) comprises two shroud fragments taken at 320 mm elevation from the bundle. The microstructural and SEM/EDX examinations of one of them revealed a metallic Zircaloy melt adherent to the external shroud surface; the shroud wall was completely oxidized to $ZrO_2$. Some interaction between the once molten and relocated metallic Zircaloy and the $ZrO_2$ has taken place, e.g. the initally formed $ZrO_2$ was again partially dissolved by the relocated metallic Zircaloy forming a substoichiometric $ZrO_{2-x}$ compound which decomposes on cooldown into $ZrO_2$ + α-Zr(O) (see positions 2 of Fig. 25).

Specimen CORA C-2 (290 mm elevation) is another piece of the embrittled shroud which showed fine crystalline deposits on its internal surface. SEM/EDX analysis resulted in tungsten oxide crystals, beside Zr, as shown in Fig. 26. The crystals showed different shapes and sizes. This observation indicates that after meltdown of the $Al_2O_3$ pellets the tungsten heater reacts with steam and the resulting tungsten oxide evaporates and condenses at colder spots in the bundle. The amounts of evaporated tungsten are very small and have no influence on the overall meltdown behavior of the bundle since the heater degradation begins late in the experiment.

Specimens CORA C-3A and -3B are two other fragments of the shroud (140 mm elevation) which are completely oxidized and show on the inside attached relocated once molten ceramic material forming large "bubbles" on solidification (Fig. 27). The once molten material ($T > 1800$ °C) itself is very porous; the microstructure indicates an $Al_2O_3/ZrO_2$ eutectic alloy with great quantities of large $ZrO_2$ crystals (position 2 in Fig. 27). Wether these large $ZrO_2$ crystals formed on solidification of the ceramic (Al,Zr,O) melt or were present in the melt as solid particles is not clear.

The oxidized shroud of specimen CORA C-3A was in contact with a Zr-rich metallic melt of the α-Zr(O)/$ZrO_2$ eutectic type (Fig. 28) and a ceramic eutectic $Al_2O_3/ZrO_2$ melt (Fig. 29). The metallic melt decomposes on cooldown mainly in

$ZrO_2$ and α-Zr(O); the latter contains in addition some Sn and Al (Fig. 28). SEM/EDX examinations also show ceramic precipitates of complex chemical composition.

All the other fragments or relocated materials taken from bundle CORA C are in agreement with the various types of materials (A, B, C) described in chapter 4.1.1. Specimen CORA C-7 is of type A, a ball-shaped foamy ceramic white looking material which contains various metallic inclusions (Fig. 30). The $Al_2O_3/ZrO_2$ eutectic alloy contains $ZrO_2$ as primary constituents (position 1) but also undissolved $ZrO_2$ cladding fragments. The chemical composition of the metallic inclusions is given in Fig. 30.

Specimen CORA C-6 is a pair of metal droplets which solidified at the 250 mm elevation (Fig. 31). The metallic multi-component liquid alloy decomposes on cooldown into two different phases as shown in Fig. 31. Both phases contain Al which indicates the interaction of the Zircaloy cladding with the $Al_2O_3$. One phase contains some quantities of W reflecting interactions with the heater. The droplets are slightly oxidized on their surfaces and show also some eutectic $Al_2O_3/ZrO_2$ alloy formation.

Specimen CORA C-4, which consists of a metallic and ceramic melt, was taken from a videoscope instrumentation window through the shroud at 100 mm elevation. It is an effluent of a ceramic melt (type A) over which, after its solidification, a small rivulet of molten metallic material (type B) flowed and solidified on top of the ceramic. At the same time some chemical interaction between both materials took place. SEM/EDX investigation indicated for the ceramic material a typical eutectic $Al_2O_3/ZrO_2$ alloy with various amounts of primary $ZrO_2$ constituents and for the metallic material, after solidification, a α-Zr(O) phase and a (Zr,Al,Sn) phase (Figs. 32, 33). The free surface of the metallic melt carries a $ZrO_2$ scale and thin intermediate layers of a (Zr,Al,Sn) alloy and an $Al_2O_3/ZrO_2$ eutectic (Fig. 33). In contact with the ceramic melt the metal was oxidized and a $ZrO_2$ containing interaction layer has formed (see position 1 in Fig. 32). The solidified ceramic material shows a very porous structure.

Specimen CORA C-5 is a piece of partially oxidized cladding of type C from the 650 mm elevation (Fig. 34). The $Al_2O_3$ pellets are not attached any more to the cladding fragment. On the outside and inside of the cladding rather uniform oxide layers have formed which acted as a crucible for the molten metallic part

of the Zircaloy. However, at lower axial locations the oxide layer was breached and some of the molten cladding relocated resulting in a large porous structure after solidification at the examined elevation (Fig. 34). At the cladding/$Al_2O_3$ pellet interface an eutectic $Al_2O_3/ZrO_2$ alloy has formed (about 77 wt.% $ZrO_2$, 23 wt.% $Al_2O_3$). The average metallic composition is about 75 wt.% Zr, 13 wt.% Al, and 12 wt.% Sn; in addition, there are $ZrO_2$ precipitates homogeneously distributed in the solidified metallic material.

## 4.2 Analyses of Cross Sections

After the visual inspection, photographic documentation, and collecting of fragments the test bundles were encapsulated in epoxy and sectioned permitting a detailed examination of the materials behaviour at various elevations.

For the encapsulation of the bundle the epoxy system Rütapox 0273 with the hardener designated LC (Epoxy resin and hardener manufactured by Bakelite GmbH, D-5860 Iserlohn) was chosen.
The bundle was filled from the bottom, through the steam inlet line, to avoid air entrainment in the encapsulant. Approximately 13 kg were required to fill the bundle of 130 by 130 mm to an elevation above the top of the shroud.
The epoxy showed some heating during the curing stage but the shrinkage effect was small. After epoxying the bundle the resin was allowed to harden for one week.

A saw with a 2.3-mm thick diamond blade(mean diamond size 138 µm) of 500 mm OD was used for the sectioning of the epoxy slab. The rotating speed of the saw blade was 3200 rpm. The thickness of one slice from the epoxied bundle resulted in 15 mm corresponding to the distance of the marks of 18 mm (CORA-B) and in 13 mm with the marks being 15 mm apart (CORA-C).

The two bundles were sectioned according to the lists of Tables A-1 and A-2 (Appendix). The sectioning locations of the bundles CORA-B and CORA-C are illustrated in Figs. A-1 and A-8, respectively (also in Appendix).
All sectioning locations are referred to the bottom of the heated zone. In addition to the cross sections longitudinal sections were prepared from blocked bundle regions.

Before grinding and polishing of the samples the selected cross sections were infiltrated by "Araldit" resin to close up residual pores.

The procedure of the preparation for the metallographic examination is given with Table A-3 (Appendix). The steps described in the list were performed using a semi-automatic machine with a closed water circuit for grinding and an automatic lubricant feeder for the polishing steps.

Five cross sections of test bundle CORA-B and nine cross sections of test CORA-C were chosen as metallographic samples.
The metallographic samples of the bundles were:

- Cross section No. B-04 (bottom at -71 mm, top at -55 mm)
- Cross section No. B-07 (bottom at -16 mm, top at 0 mm)
- Cross section No. B-08 (bottom at + 71 mm, top at + 91 mm)
- Cross section No. B-10 (bottom at 235 mm, top at 251 mm)
- Cross section No. B-17 (bottom at 1143 mm, top at 1159 mm)

- Cross section No. C-02 top at - 4 mm
- Cross section No. C-04 top at 26 mm
- Cross section No. C-07 top at 71 mm
- Cross Section No. C-09 top at 224 mm
- Cross section No. C-13 top at 484 mm
- Cross section No. C-14 top at 499 mm
- Cross section No. C-17 top at 664 mm
- Cross section No. C-26 top at 984 mm
- Cross section No. C-27 top at 999 mm.

Three of the nine samples of CORA-C (C-07, C-13, C-26) were investigated in detail. The very samples were examined by SEM (Scanning Electron Microscope) to determine the chemical compositions of the various reaction products.

### 4.2.1 Cross Sections of Bundle B

The macrographs of the cross sections through the bundle (Appendix, Figs. A-2 through A-7) and magnified parts of them illustrate the relative importance of

the different damage mechanisms in their contribution to the overall accidental behavior.

At the elevations of the lower spacer grid (-73 to -53 mm, Fig.A-7) the heated rods (Fig. 35) are cut through their 86 mm thick molybdenum end sections, below the lower level of the heated pellet stack. The unheated annular pellets are essentially intact, although most of them are filled by ceramic melt, one of them (rod 37, Fig. 36) by metallic melt. The space between the rods is mostly blocked by ceramic and metallic melt (Fig. 35, 36). The ceramic melt looks darker in the macrophotos and is characterised by large cavities and numerous fine pores. Different events of melt relocation and re-solidification can be distinguished from the pore distribution. The metallic melt looks lighter in the macrophotos and is characterised as brittle material by a network of cracks. The claddings and the spacer grid have interacted with the melts up to variable degrees. Where surrounded by metallic melt they got at least partly molten and dissolved in it. In contact with ceramic melt the pre-existing scale improved the wetting (by reducing the interfacial energy), but resisted essentially against a dissolution and homogenisation into the melt. In total the cladding and the spacer are partly remaining as thin-walled structures and partly molten at contact zones with molten metal. Open channels through metallic melt are distinguished from closed cavities by their subsequent steam oxidation, during which scales were formed.

At the elevations just below the bottom of the heated zone (-18 to + 1 mm, Fig. A-6) the bundle is almost completely blocked. Solidified ceramic melt is the main component, at the center of the bundle metallic melt is enclosed. Some metallic melt path must also have rinsed down between bundle and shround (cross section 0 mm, Fig. A-6). In the central part of this cross section the cladding material has disappeared to a large extent. It can be assumed that it partly melted as metallic material (Fig. 37) and partly reacted with pellet material (Fig. 38, top). Some other fraction of reacted pellets was possibly dissolved in metallic melt (Fig. 39, bottom). The surrounding rods have retained their claddings, which are steam-oxidized and were partly molten or interacted with pellets (Fig. 40). The pellets of the five central rods are found dissolved almost without discernable residues. The bare tungsten heater rods are embedded in metallic melt without essential interaction (Fig. 39).

The region up to 73 mm is covered by vertical cross sections through the unheated rods (Fig. 41-48). The picture given by that figures is quite informative and self describing. The essential feature is, that the annular pellets are almost unaffected by melting processes within the metallic parts of the neighbouring cladding on the one hand and the contact with the penetrating ceramic melt on the other hand (Fig. A-5). It should be mentioned in addition, that the vertical cross sections C1 and C2 show a lump of metallic material surrounded and covered by ceramic material. This can be taken as an example for an initial relocation of metallic melt and the subsequent deposition of ceramic melt.

The region above 73 mm is characterised by a ceramic "crucible", which was formed by melt, which solidified at the cooler external ring-shaped zone of the bundle. At the lower levels this crucible contains a bed of rubble fragments (Fig. 49). At one corner of the bundle the gap to the shroud is filled by metallic melt. The four corner rods are almost intact (Fig. 50), the others have lost their cladding mostly. Concurring processes are intrinsic cladding melting without essential interaction with the pellet (Fig. 51, bottom) and pellet dissolution into surrounding ceramic melt (Fig. 51, center, 49, rods Nos. 9 and 12).

The levels further above (Fig. A-4) have contributed more to the formation of melts. While the corner rods only show some clad melting, the other rods have lost their claddings either due to metal melting, oxidation-embrittled fracture, or pellet dissolution under formation of ceramic melt (Fig. 52, 53).

Most of the molten material described above originates from even higher elevations (Fig. A-3). At 507 mm only some residues of ceramic and metallic melts are found adherent to the otherwise bare tungsten heaters. In addition, few residues of cladding and pellet are still found attached to the corner rod heaters (Fig. 54).

Towards the cooler upper end of the bundle the amount of damage diminishes again. Around the level of the upper spacer grid (Fig. A-2), where the heated rod end sections are again Zry-clad molybdenum rods, only limited clad melting and pellet/clad reaction can be identified.

Two cross sections have been selected for a detailed microstructural inspection, namely those of the elevations -71 mm (B4), and 0 mm (B7).

**Cross Section B4**

B4, at the level of the lower spacer grid, was already characterized by a considerable fraction of blockage of the flow channels due to re-solidified ceramic and metallic melts. The cladding of the heated rods (Mo end section of the heater at that elevation) and of the unheated rods is comparably damaged by severe oxidation and embrittlement, unimportant dissolution of the scale in contact with the ceramic melt, and partial melting in contact with molten metallic material. The spacer is slightly distorted by oxidation and similarly affected as the cladding. The interaction of pellet and cladding remained relatively weak at this elevation.

Details of the microstructure are depicted in Figs. 55-57: Spacer oxidation took place below 1525°C according to the scale microstructure; oxygen uptake converted the original β-Zr matrix completely to α-Zr(O) (Fig. 55, position 2). Partial melting of heated rod cladding indicates peak temperatures above 1760°C (the melting point of Zircaloy-4) at those positions (Fig. 56, top, left). Some eutectic interaction between the cladding and its scale (Fig. 56, bottom, left) indicates equally high temperatures of the unheated rods. The ceramic melt after solidification reveals its eutectic $ZrO_2/Al_2O_3$ origination. The metallic melt has decomposed into essentially two phases, α-Zr(O) and (Zr, Al, Sn) phase and eutectic distributions of both (Fig. 57).

**Cross Section B7**

The cross section B7 is from the elevation of the most complete blockage. The materials which form the blockage are resolidified ceramic melt (at the outer parts of the bundle) and metallic melt (in the center of the bundle and adhering to one side and the shroud. The ceramic melt encloses large cavities and many small pores, the metallic melt was severely cracked during cooling.

Despite the close contact of ceramic melt and oxidized cladding the scale remains from detectable up to almost undisturbed, even if the melt has filled the flow channel completely (Fig. 58, bottom, left). Oxygen-poor internal parts of the metallic cladding had been molten and partly relocated to leave the respective cavities within the cladding, which later on continued to oxidize. This partial melting indicates corresponding oxygen profiles through the cladding wall, which prove, that also internal oxidation of the cladding has occurred (Fig. 60 to

62, above, left). A barrier layer of oxide (Fig. 60,62, bottom, left) should have diminished the rate or stopped the reaction with the aluminia ring pellets, which are often looking undisturbed (Fig. 58, above, right). Where ceramic melt found its way into the annular alumina pellet it reacted and dissolved into the ceramic melt of the eutectic $Al_2O_3/ZrO_2$ system. One type of metallic melt decomposed during solidification into at least two phases of the Al-Zr-system (with minor contents of Mo, W and Sn). The other type is α-Zr (O) (Fig. 59, bottom, left and middle). Sn rich metallic residues are found frequently within the ceramic matter (Fig. 61, bottom, right).

A vertical cross section through the bundle between the elevation 1 and 73 mm is shown in Fig. 64. It shows the residues of two unheated fuel rods, whereas the third, in the middle which is the central rod of the bundle, is missing. At the lower levels the center is filled by metallic melt, the surrounding area by ceramic melt, which forms a crucible, that reaches to the higher levels, where it contains fragments of rubble. Fig. 65 shows in more detail the three types of material found, $Al_2O_3/ZrO_2$ eutectic, Al/Zr eutectic and rubble. The rubble bed (Fig. 66) consists of solidified droplets of ceramic eutectic melt (see Fig. 67), and more or less oxidized pieces of cladding. With respect to the materials interaction processes Fig. 68 illustrates, that ceramic melt has not been able to dissolve the oxidized cladding from its external side, whereas the cladding was protected by an internal scale from pellet interaction. The pellet has reacted with ceramic melt attached to its internal surface along a smooth front of interaction (Fig. 68, bottom, right).

### 4.2.2 Cross Sections of Bundle C

The macrographs of the cross sections through the bundle are given in the Appendix as Figs. A-9 through A-23.

At the lower end of the bundle, around the elevation of the grid spacer and slightly above (Figs. A-22 and A-23), the fuel rods look almost unaffected by the melt, which, after penetrating downward, has re-solidified there. The porosity of the melt indicates its ceramic character. Only some metallic melt, identified by its dense or cracked structure has reached the spacer. Some melt even found its way downward within the annular pellets of unheated rods (No. 37 and 17).

At the elevations above, covered by Figs. A-20 and A-21, most of the melts have solidified. The flow channels are roughly half blocked by ceramic melt together with comparable amounts of metallic melt. The latter looks darker in Fig. A-20, in which pins No. 20, 21, 22 and 28 are in contact with it. Ceramic melt is also found outside the flow shroud. The examination of the cross sections allows to distinguish different lumps of melt, which have relocated in separate events.

With increasing elevation the deterioration of the pins is increasing, partly due to interaction with contacting melt, and partly due to incipient melting from rod intrinsic interaction processes. More detailed information gives a vertical cross section through the bundle between the elevations 88 and 209 mm, by which it is divided into the halfpieces b1 and b2 (Fig. 69). At the 88 mm elevation the bundle is mostly blocked by ceramic melt, which attacks the oxidized cladding fragments and the alumina pellets (Fig. 69). At 211 mm elevation only the tungsten heater rod and some residual melt or fragments of pins and shroud are found to remain. So the vertical section covers a most interesting transition region (Fig. 70). The both sides of the cut and the detail of halfpiece b2 (Fig. 71) illustrate the blockage by porous ceramic melt, on top of which rubble particles have accumulated after the re-solidification of the melt. The rubble consists of melt droplets and mainly of cladding and shroud fragments, embrittled by serious steam oxidation.

The next higher cross sections (Fig. A-19) also show some rubble particles as additional constituents. Essentially no metallic melt can be distinguished at those elevations and above.

The extent of damage to the core still increases further upward, as shown by Figs. A-18 and A-17. The corner rods, here No. 3 and 26, as the relatively coolest ones, had been the last to loose their structure, although good insulation of the bundle resulted in a flat temperature profile.

The center grid spacer has disappeared without much residues. (Some can be distinguished at the 499 mm level (Fig. A-17)). They and the remnants of the cladding show heavy distortion by oxidation-induced stresses. Due to the "flowering" process the cladding of the external rods had often got contact with the surrounding shroud. Fragments of it are fixed to the shroud via re-solidified melt, which is of ceramic character and shows good wetting of the oxidized clad and shroud pieces.

The upper half of the bundle begins with an essentially void zone, which was not cut, because no information on the damage mechanisms were expected. The next zone (from 621 to 724 mm), in contrast, was subdivided by several cuts as illustrated by Figs. A-17 to A-13, because it promised information on the formation steps of the already described melts. Figs. A-16 and A-15 can be roughly described by the following statements: The annular alumina pellets are mostly present, at least as remnants of melting and cracking processes, mostly attacked by heavy reaction with the cladding on the whole circumference or part of it. Some of them even look partly unaffected. The cladding has mostly disappeared, has formed droplets of metallic melt, or contributed to the interaction with the pellets and the resulting formation of ceramic melt, or even has remained as wall structures of heavily embrittled oxide scale. The described aspects are indicated on Fig. 72, a detail of a cross section, which is included as example.

The features of Fig. A-14 can comparably be described: At the somewhat lower temperature level of the higher elevations more remnants from clad melting and oxidation and more products of pellet reaction remain discernible (Fig. 73).

Further above (Fig. A-13 to A-9) the cross sections can be described by the summarizing statements: Going upward, the effect of clad melting can no longer be distinguished, so that this effect seems to be the first to disappear. Compared to that, the reaction of cladding and pellet remains further upward as the main damage mechanism. Cladding without good pellet contact has the final chance to disappear by breaking into rubble fragments after being embrittled from steam oxidation. The same happened to the upper spacer grid. Less embrittled or more slowly oxidized cladding further upward remains at place (Fig. 74).
Three cross sections have been selected for a detailed microstructural inspection, namely those of the elevations 71 mm (C 7) 484 mm (C 13), and 984 mm (C 26).

**Cross Section C 7**

At the elevation of cross section C7 some pins remain isolated, others are in contact with metallic or oxidic melt (Fig. 75). In Fig. 76, both types of solidified melt, the eutectic Al-Zr alloy, consisting of α-Zr(O) phase and (Zr, Al, Sn) phase and the eutectic distribution of the $Al_2O_3$ and $ZrO_2$ phases are shown, together

with the cross section through an oxidized cladding wall. Internal oxidation of this indicates some oxygen uptake from the contacting pellet. Fig. 77, showing similar microstructures from pellet-cladding reaction, indicates one reason of enhanced interaction: molten cladding is able to fill the original gap to the pellet, and the resulting different wall thicknesses around the circumference of the cladding are indicating the intimate contact. By interaction with the alumina pellet the Zry enriches in oxygen and dissolves aluminum. Fig. 78 illustrates the more complex case of internal pellet interaction and external contact of the cladding with ceramic melt. The contact zone between pellet material and ceramic melt at another position is further shown. In case of considerable interaction with alumina, the Zry is always analyzed to contain Al, the maximum determined content being 17 wt-%. A further case, the external interaction of oxidized cladding with metallic melt together with the internal pellet interaction is depicted in Fig. 79.

**Cross Section C 13**

At cross-section C 13 (484 mm) remaining pieces of completely oxidized and thus embrittled cladding have been microstructurally resolved by growing magnification (Fig. 80). It was found that the $ZrO_2$ from the cladding has been in contact with ceramic melt, in which even some interaction with the tungsten heater rod was identified. Remnants of melt adhering to tungsten heater rods have been analysed to consist of (Zr, Al, Sn) alloy, the $ZrO_2$ phase or the $ZrO_2$-$Al_2O_3$ eutectic and a dispersed tungsten phase (Fig. 81). So, under extreme conditions, even the heater rods are subjected to an interaction.

**Cross Section C 26**

At cross-section C 26 the $Al_2O_3$ attack by molten Zry was studied in more detail, at the positions indicated in Fig. 82. At one position of localized pellet attack, Fig. 83, the originally present metallic melt, presumably of Zircaloy, develops porosity, enriches in aluminum and oxygen from the interaction with the $Al_2O_3$ pellet and finally tends to get oxidized. The observed duplex microstructures of metallic and oxidic phases indicate the respective oxygen content.

Figs. 84 and 85 illustrate again that the reaction between cladding and pellet is often restricted to localized interaction zones around the circumference of the pellet. The reaction products, mainly $ZrO_2/Al_2O_3$ eutectic melt, in contrast, are

found to have reached widespread distribution through the bundle and further interaction with the contacting materials has taken place.

## 5. Materials Interaction Processes; Separate Effects Tests

To describe the complex material behavior of integral tests, like the CORA experiments, it is necessary and important to perform in parallel separate effects tests under well controlled boundary conditions and to use these results for the interpretation. The elevated temperatures during the CORA tests cause a variety of changes in the bundle materials resulting in typical metallographic structures for the solid and liquid reaction products. These phenomena include phase transformations, type and extent of oxidation, formation of precipitates, Zircaloy cladding and $Al_2O_3$ melting, $Al_2O_3$ and/or $ZrO_2$ dissolution, and the solidification of melts. Since most of these phenomena leave characteristic patterns in the resulting microstructures of the various phases, these microstructures can be compared with those obtained in well defined annealing or interaction experiments. This is one of the tools which can be used in parallel to chemical analytical examinations and available phase diagram informations to analyze what may have happened in the bundle during the test.

The separate effects tests performed in connection with the CORA tests B and C are described below. The results of Zircaloy cladding oxidation experiments in steam up to the melting point of Zircaloy-4 (~ 1760 °C) and above are described in chapter 5.1. The essential results of $Al_2O_3$/Zircaloy and $Al_2O_3/ZrO_2$ interaction experiments are described in chapter 5.2. The interpretation of the CORA B + C post test examination results is given in chapter 5.3.

### 5.1 General Behavior of Zircaloy Cladding Exposed to High-Temperature Oxidation

The behavior of Zircaloy cladding during oxidation by steam, will be described in this chapter on the basis of experience and results from extensive separate effects investigations [5]. The influence of alumina ($Al_2O_3$) pellets on the chemical behavior of the cladding is intentionally neglected in the following description since it will be explained in chapter 5.2.

During the high-temperature cladding oxidation by steam or oxygen the metallic Zircaloy is transformed into various other oxygen containing metallic and ceramic compounds which form different layers. Starting from the cladding outside a layer of tetragonal $ZrO_2$ is followed by a layer of cubic $ZrO_{2-x}$ (stable above 1525 °C), a layer of oxygen-stabilized α-Zr(O), and the original β-Zircaloy

matrix (Fig. 86). This layer sequence is in agreement with the binary (Zr-O) phase diagram (Fig. 87).
In the following the Zircaloy cladding oxidation going on in the course of a temperature excursion is discussed with a sequence of mechanisms, which are illustrated (Figs. 88 to 93) by micrographs taken from an earlier investigation on the oxidation kinetics of inductively heated cladding tube sections [6].During oxidation the β-phase enriches in tin (the initial Sn content in Zry-2 and Zry-4 is about 1.5 wt.%) leading to low-temperature melting eutectics. Neglecting this eutectic Sn/Zr phase formation the melting of the oxygen-poor as-received β-Zr matrix is the first phase change during heatup at about 1760 °C. The onset of melting increases with increasing oxygen content up to about 1940 °C, the peritectic temperature (decomposition of β-Zr into a liquid phase and α-Zr upon heating). As shown in Fig. 88 (right picture), cavities may form in partially oxidized Zircaloy cladding if the onset of melting of the remaining metallic part is reached and it relocates. The cavities of a round shape, however, have to be distinguished from artifacts (pullouts) caused during metallographic preparation of the specimen and from cracks in the embrittled cladding which form on cooldown.

Fig. 89 illustrates at the boundary between the once liquid and solid phase that the oxygen stabilized α-Zr(O) layer between the β-Zr and $ZrO_2$ disappears during melting of the β-Zr and that solidification can lead to precipitation of an oxidic $ZrO_2$ phase in the metallic (Zr,O) melt. This oxidic phase originates from an oxygen saturation of metallic Zircaloy. In cases where the metallic portions of the partially oxidized cladding are completely molten, the metallic melt can relocate and form large cavities as depicted in Fig. 90. By approaching 1900 °C the still solid oxygen-stabilized α-Zr(O) absorbs quickly oxygen from the adjacent $ZrO_2$ layer by dissolving it. This results in a thinning of the oxide layer as shown in Fig. 91 (upper picture). Above the α-Zr(O)/$ZrO_2$ eutectic temperature of about 1900 °C the contact region ($ZrO_2$) starts to melt and the reaction rate increases. The melt can penetrate the oxide layer by completely dissolving it or by breaching the thinned oxide layer due to the forces created by the melt formation which is combined with a volume increase of about 10 %. The melt is then ejected as shown in Fig. 91 (lower picture).

In some cases pieces of $ZrO_2$ are broken off the oxide layer and are transported into the metallic (Zr,O) melt where they will be subsequently liquefied and/or dissolved well below its melting point of about 2700 °C, Fig. 92. Examples of

α-Zr(O)/$ZrO_2$ eutectic microstructure are shown in Fig. 93. The microstructural appearance of the eutectic system depends on composition and solidification (cooldown) rate. Sometimes dendritic microstructures form as can be recognized in the right picture of Fig. 93.

## 5.2 Chemical Interaction between $Al_2O_3$ and Zircaloy

Altogether three different types of single effects interaction experiments have been performed to study the resulting reaction products and partly also the reaction kinetics: a) solid $Al_2O_3$/solid Zircaloy interaction experiments, b) liquid $Al_2O_3$/liquid Zircaloy interaction experiments, and c) $Al_2O_3/ZrO_2$ interaction experiments.

### 5.2.1 Determination of the Reaction Kinetics Between $Al_2O_3$ and Zircaloy

$Al_2O_3$ is thermodynamically not stable with respect to Zircaloy cladding, therefore, chemical interactions have to be expected if the materials are in close contact. To determine the reaction kinetics annealing experiments have been performed with Zircaloy crucibles containing $Al_2O_3$ powder up to 1550 °C and maximum annealing times of 25 hours. A detailed description of the experiments and results is given in [7, 8]. The essential results are shown in Figures 94, 95 . The chemical interactions between $Al_2O_3$ and Zircaloy can be described by a parabolic rate law (Fig. 94 ). The plot of the $Al_2O_3$/Zircaloy reaction zone growth rates as function of reciprocal temperature shows clearly that as soon as a liquid phase forms (≥ 1350 °C) the reaction rate increases (Fig. 95). Reaction experiments at 1600 °C and higher were not possible since the specimens were liquefied during heatup at about 1550 °C as a result of fast $Al_2O_3$/Zircaloy chemical interactions. These results are in agreement with the experimental observations during the CORA tests B and C where first relocation of molten material could be noticed at about 1500 °C.

The chemical interaction of $Al_2O_3$ with Zircaloy results in the exchange of oxygen from the ceramic to the metallic phase under the formation of α-Zr(O) since zirconium has a higher affinity to oxygen than aluminum; $ZrO_2$ does not form under solid state conditions.. According to the (Al-O) phase diagram (Fig. 96 ) the extraction of already small amounts of oxygen from $Al_2O_3$ results in the formation of aluminum, which is liquid above 660 °C. $Al_2O_3$ has practically no homogeneity range. However, aluminum will not be released as an element but

transferred to the metallic (Zr,Al,Sn) phase which contains also some oxygen. This lowers the onset of melting of Zircaloy toward the $\beta$-$Zr/Zr_5Al_3$ eutectic temperature of 1350 °C. The $\beta$-$Zr/Zr_5Al_3$ eutectic is the richest in Zr and thus the pertinent eutectic system in the (Zr-Al) phase diagram (Fig. 97). A liquid phase around 1350 °C was observed in the single effects tests which resulted in an increase of the reaction zone growth rate.

An oxygen uptake of the $\beta$-$Zr/Zr_5Al_3$ eutectic melt will raise its solidification temperature range in which it decomposes into an alumina rich and an alumina poor phase. An increasing oxygen content of the still metallic Zr/Al melt improves the wettability with respect to the ceramic $Al_2O_3$ pellets and by this increases the contact area between the melt and the solid which increases apparently the reaction rate. On the other hand, an increasing oxygen content of the Zircaloy decreases the driving force for the oxygen exchange.

### 5.2.2 Liquid $Al_2O_3$/liquid Zircaloy Interaction Experiments

The question was how Zircaloy and $Al_2O_3$ behave if both are molten, e.g. at temperatures above 2050 °C, the melting point of $Al_2O_3$. For this reason $Al_2O_3/Zr$ mixtures of various ratios were melted in an arc furnace and then the resulting reaction products were determined in the solidified materials []. Depending on the $Al_2O_3/Zr$ ratio either a homogeneous or a heterogeneous (two immiscible melts) melt forms. Fig. 98 depicts the macroscopic material behavior after solidification in dependence on the $Al_2O_3$ content. Up to about 20 wt.% $Al_2O_3$ can be dissolved by the metallic Zircaloy before a heterogeneous melt forms. The homogeneous (Al,Zr,O) melt decomposes on cooldown into $\alpha$-Zr(O) and an (Al,Zr) alloy which contains in addition some oxygen. In the solidified metallic melt $ZrO_2$ precipitates can be recognized at higher oxygen ($Al_2O_3$) contents which sometimes form a dendritic structure. The ceramic melt decomposes on cooldown into an $Al_2O_3/ZrO_2$ eutectic with various amounts of primary $Al_2O_3$ or $ZrO_2$ constituents, depending on the initial $Al_2O_3/Zr$ ratio. Typical microstructures of the ceramic and/or metallic melts are shown in Fig. 99. The solidification temperature for the ceramic phase is about 1800 °C ($Al_2O_3/ZrO_2$ eutectic temperature) and that for the metallic phase at about 1350 °C ($\beta$-$Zr/Zr_5Al_3$ eutectic temperature). As a result, a separation of the two melts has to be expected. Since in the CORA bundle test B a strong radial temperature gradient existed, beside the axial temperature gradient, a type of ceramic crucible formed within the destroyed lower bundle region containing the

subsequently solidified metallic material in its center at the bottom of the crucible. A detailed description of the $Al_2O_3$/Zr material behavior is given in [7].

### 5.2.3 $Al_2O_3/ZrO_2$ Interaction Experiments

As a result of the cladding oxidation $ZrO_2$ forms which may chemically interact with the $Al_2O_3$ pellets. The chemical interaction between $Al_2O_3$ and $ZrO_2$ results in a decrease of the melting temperatures of both oxides as shown in Fig. 100 [7]. $Al_2O_3$ and $ZrO_2$ form an eutectic system with an eutectic temperature that varies, according to the literature, between 1710 and 1850 °C. Below that temperature there exists no miscibility between both oxides, which have to precipitate during cooling as fine particles.

Depending on the $Al_2O_3/ZrO_2$ ratio the homogeneous (Al,Zr,O) melt decomposes on cooldown in $Al_2O_3$ or $ZrO_2$ primary constituents and an eutectic $Al_2O_3/ZrO_2$ phase mixture. The microstructures of molten $Al_2O_3/ZrO_2$ specimens of various composition are shown in Fig. 101. SEM/EDX examinations clearly indicate that the primary constituents are pure single phase $Al_2O_3$ (Fig. 102) or $ZrO_2$ compounds (Fig. 103).

## 5.3 Interpretation of the CORA Results

It is particularly important to emphasize that many complex phenomena occurred simultaneously or in series during the CORA test transient, due to large variations in individual rod temperature and local steam flow rate, and also because of cladding and $Al_2O_3$ relocation. The resultant solid and liquid phases encompass a wide range of initial and final chemical compositions. Therefore, what can be identified through posttest metallographic examinations at room temperature is only the chemical and physical state of the reaction products that were present when quenching, or cooldown, of the rod bundle occurred. In a few cases, the time-dependent material behavior during the accident scenario may be postulated.

It is also important to keep in mind the fact that the microstructure (number of phases) of the components of reaction products at room temperature may be different from that existing under the physical and chemical conditions at test temperature. A microstructure that looks multiphase at room temperature may be single-phase at high temperatures. This can have an influence on some

physical properties, such as the meltdown behavior of liquid phases determined by the wetting properties between the melt and the solid substrate. Furthermore, as a result of the fast cooldown rate, the phases may not be under equilibrium conditions. For this reason, the application of available phase diagram information is limited.

In all materials interaction processes both the thermodynamic consideration of free enthalpy changes going along with the possible reactions as well as kinetic considerations of the rates of concurring interactions have to be combined. The above described knowledge on the different processes is incomplete, since especially kinetic data are lacking. So the CORA results have to be analyzed in order to decide on the processes which are pertinent in reality. The following summary can be deduced from the observed behavior of the bundles (Fig. 104):

Both, the incipient melting of the cladding and the melt formation by its interaction with the alumina pellets have occurred. Some pellets have been attacked only locally, by which an often waved reaction front resulted. It can be assumed that relatively low temperatures and only spotwise contact have limited the extent of reaction. Increasing oxygen content in the reaction zone could have diminished the driving force of further reaction and increased the solidus temperature of the melt, below which the reaction rate is comparatively low. During the transient the described rate limiting trends and the temperature increase are counteracting.

Contact regions grown at higher temperatures had more chance to spread and to attack the pellet at the whole circumference. The eutectic melt could relocate by penetrating through any gap, by candling along the surfaces of cladding and shroud, or even by free falling to lower core regions. In contact with pellet or cladding it often changed its composition. Further oxidation could lead to fully oxidized eutectic melt.

Where cladding/pellet contact was not provided up to higher temperatures, incipient melting of the cladding occurred. This must have started from the oxygen poor $\beta$-Zry and spread toward the $\alpha$-Zr(O) phase. Melt relocation has left the observed cavities in the cladding, was the origin of the observed metallic Zircaloy melt, or was equally well the reason for thus-initiated pellet contact and interaction. Where some internal cladding oxidation had previously occurred, the cladding was decoupled from the presence of the pellet. The clad melting

could proceed with increasing temperatures. Above the $\alpha$-Zr(O)-$ZrO_2$ eutectic temperature the oxide scales were more and more consumed, thus loosing their capability to confine the molten cladding. Remnants of them broke into pieces under thermal stresses and fell finally down as rubble fragments.

Since the post-test investigations mainly characterize the final status of the system, some aspects of the initial, low-temperature phase of the tests might remain obscure. For the same reason no information on the directions and velocities of melt progression can be deduced. Thus the interpretation of the post-test evaluation remains incomplete. Additional information on the tests is expected from the analysis of the real-time response of the system to the given test parameters.

## 6. Summary and Conclusions

- The tests CORA B and CORA C have been performed to simulate the high-temperature behavior of "burnable poison rods" and to demonstrate the successful operation of the test facility.

- Uncontrolled temperature escalation started from the upper half of the test bundles, spread along the flux of hot steam and relocated melt, and resulted in peak temperatures around 2000 °C.

- Low-temperature failure of burnable poison rods is due to melt initiation around 135O °C and fast melt relocation around 1500 °C. The metallic (Zr, Al, O) melt is the result of $Al_2O_3$ pellet/Zry cladding reaction.

- Another type of metallic melt is formed above 1760 °C by molten Zircaloy and a third, ceramic type by $ZrO_2/Al_2O_3$ eutectic melting around 1800 °C.

- The melt relocation processes are candling and free droplet falling.

- The relocated and solidified melts form large blockages in the lower region of the bundle. The considerable porosity of the ceramic melt contributes to the high degree of flow channel blockage.

- The crust of re-solidified material acts as a catcher for embrittled bundle fragments which are terminating the materials relocation.

- The early failure of burnable poison rods in a reactor core is expected to induce premature fuel rod degradation, since the cladding and the $UO_2$ fuel can be dissolved or liquefied by contacting melts already below the melting point of Zircaloy.

## 7. Acknowledgements

Various kinds of support of the experimental program and its evaluation is gratefully acknowledged.
The test rods were assembled by Mr. E.Mackert, as were the test bundles by Messrs. H.Giesmann and Ph. Pfann. The authors would like to thank Messrs. K.Vogel, H.Benz, O.Heil, W.Rötzel, and H.J.Röhling for the preparations of the test and for the test conduct. Messrs. H.Malauschek and K.P.Wallenfels are acknowledged for arrangement of camera and video systems to observe the bundle behavior during the transient test. Mr. W.Rötzel's effort in the post-test photography is greatly appreciated. A special acknowledgement is due to Mr. H.Benz for the encapsulation procedure of the tested bundle. The authors thank Mr. L.Anselment for the sectioning of the bundle and for the preparation of the metallographic samples, Mr. H.Metzger for the investigation of the metallographic samples by optical microscope, Mr. J.Burbach for the SEM investigations, and Mrs. B.Bennek-Kammerichs for a contributation to the microstructural investigation. Thanks also to Mr. W.Hering for the critical review of this report.

## 8. References

/1/ A. Fiege, "Severe Fuel Damage Investigations of KfK/PNS", KfK 3431B, 1983

/2/ S. Hagen, K. Hain, "Out-of-pile Bundle Experiments on Severe Fuel Damage (CORA-Program): Objectives, Test Matrix, and Facility Description", KfK 3677, 1986

/3/ S. Hagen, W. Hering, K. Vogel, "CORA Scoping Test B, Test Results Report, KfK 4171, (to be published)

/4/ S. Hagen, W. Hering, K. Vogel, "CORA Scoping Test C, Test Results Report, KfK 4312, (to be published)

/5/ S. Leistikow, G.Schanz, "Oxidation Kinetics and Related Phenomena of Zircaloy-4 Fuel Cladding Exposed to High Temperature Steam and Hydrogen-Steam Mixtures Under PWR Accident Conditions", Nuclear Engineering and Design 103 (1987) 65 - 84.

/6/ S. Leistikow et al., "Untersuchungen zur Hochtemperatur-Wasserdampf-Oxidation an Zircaloy-Hüllrohren", in Jahresbericht 1980, Projekt Nukleare Sicherheit, KfK 2950, 4200/43-69, 1981

/7/ P.Hofmann, M.Markiewicz, "Chemische Wechselwirkungen zwischen $Al_2O_3$ und Zircaloy", in Annual Report 1987, Section 12.07.01/03A, KfK 4450 (1988)

/8/ P.Hofmann, M.Markiewicz, J.Spino, "Reaction Kinetics between $Al_2O_3$ and Zircaloy", to be published at Journal of Nucl. Materials

## 9. List of Figures

## Appendix

## 10. List of Tables



Appendix:

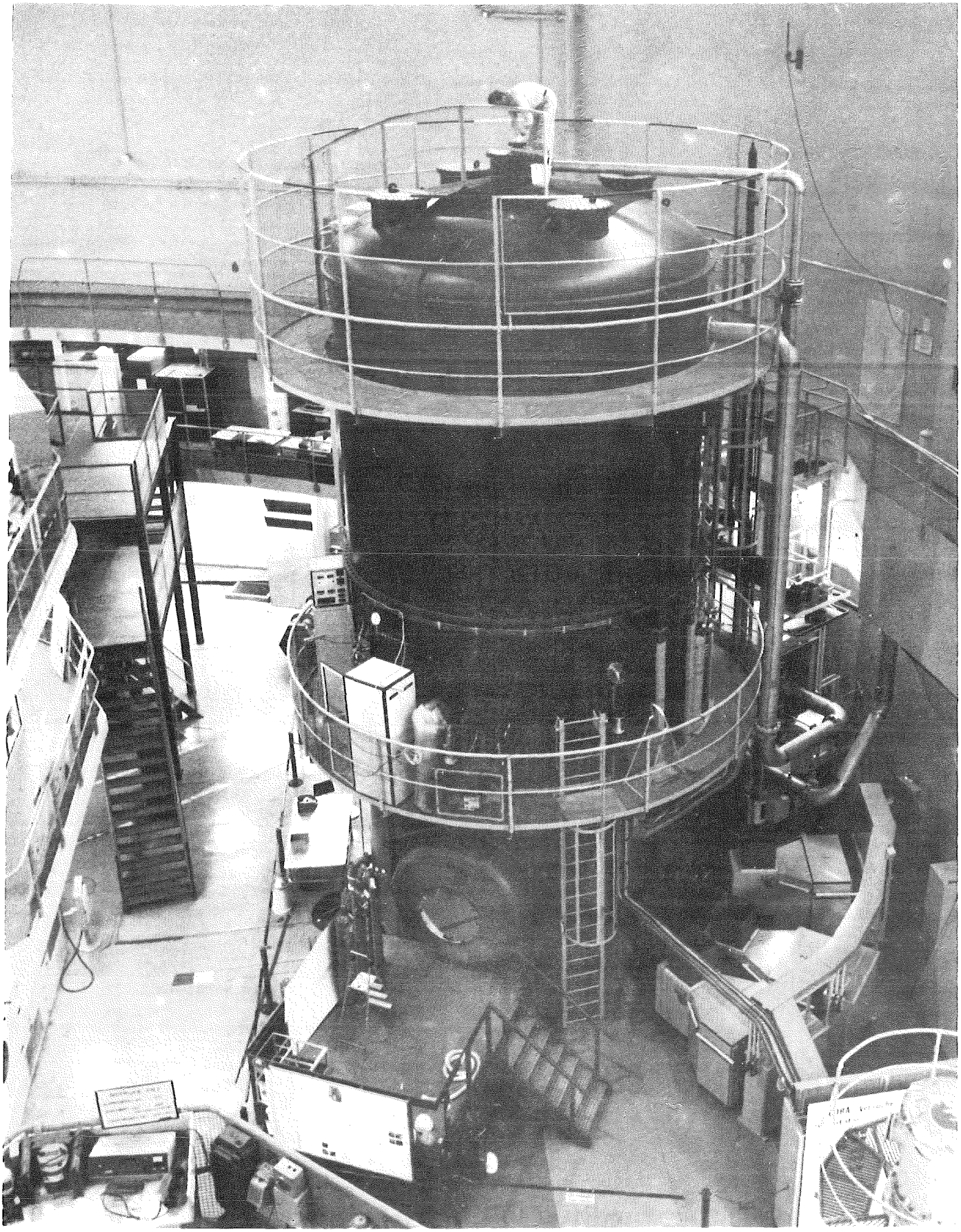

Fig. 1. CORA test facility;

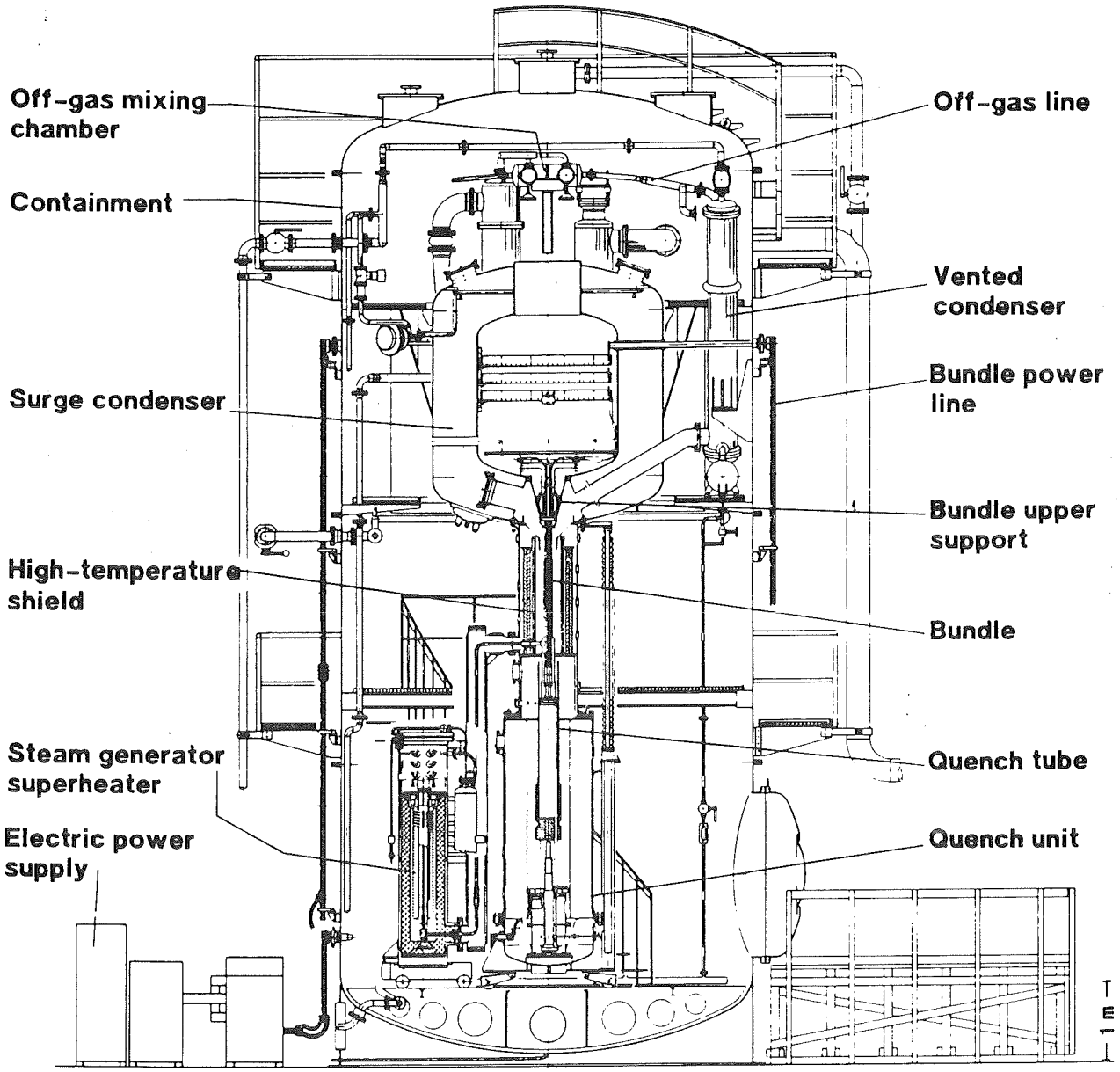


Fig. 2. SFD test facility CORA, schematic

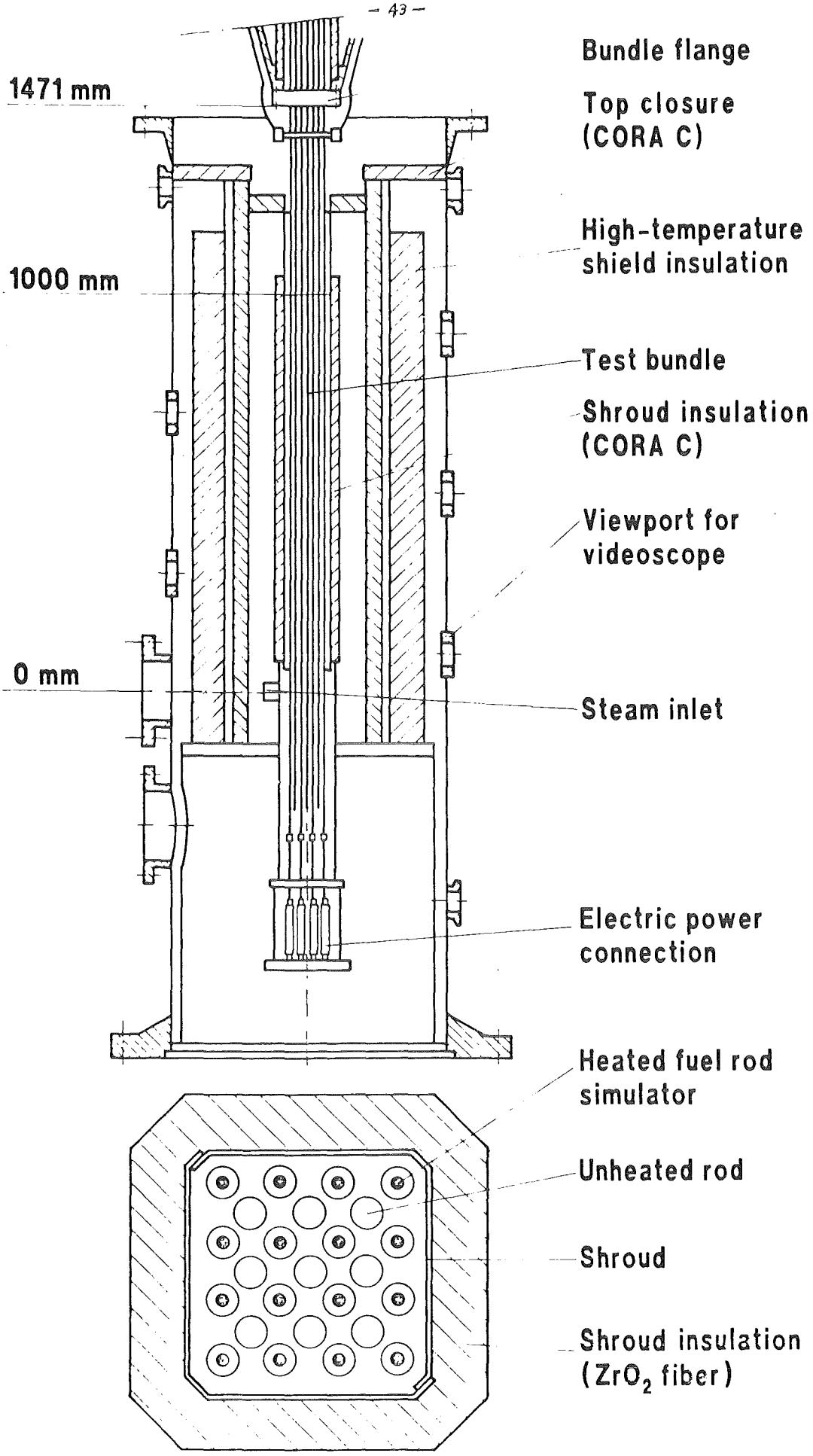


Fig. 3. Test section (schematic) for CORA Tests B and C and test rod array

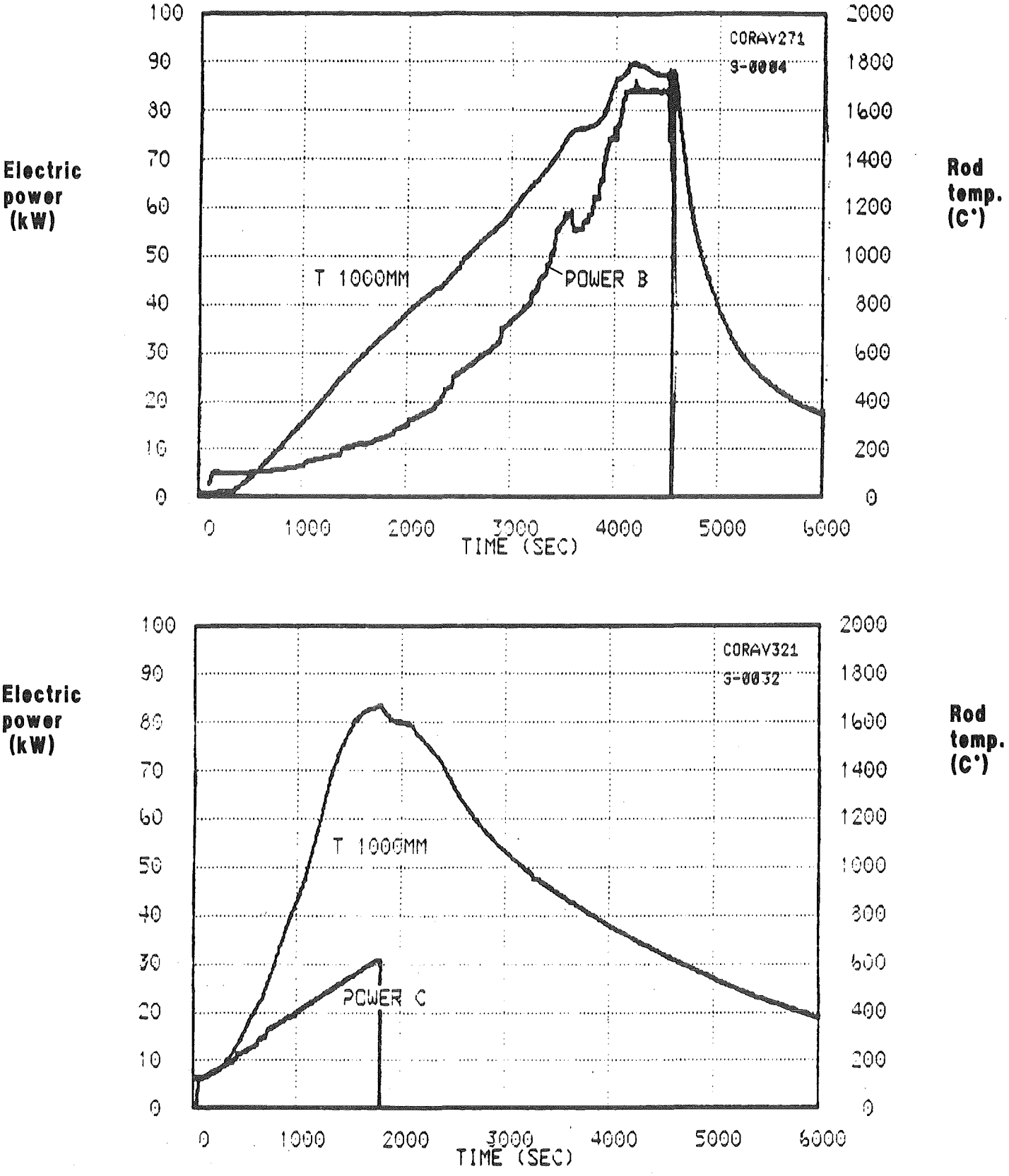


**Fig. 4. Comparison of power and rod temperature at 1000 mm elevation for CORA Tests B and C**

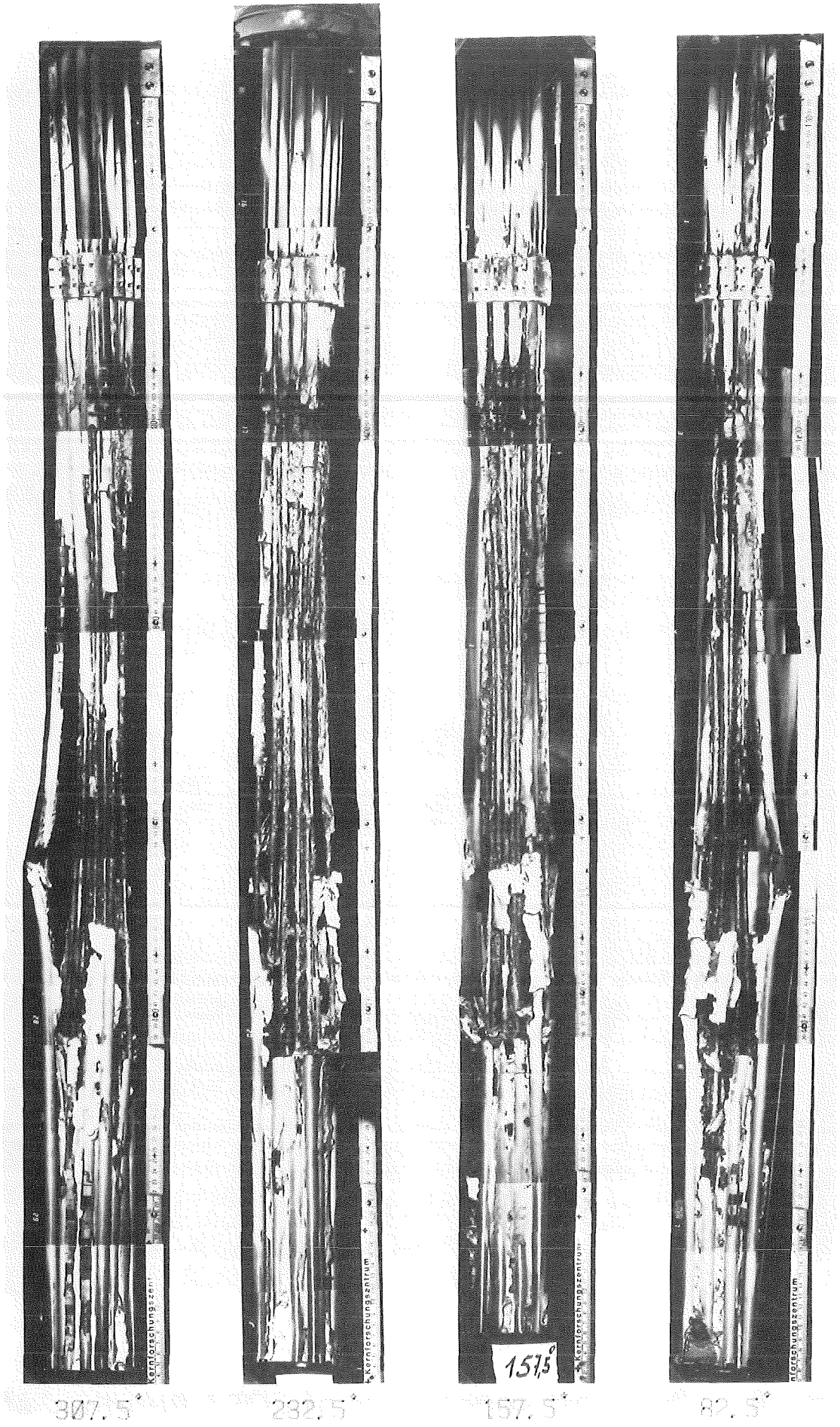


**Fig. 5. Post-test appearance CORA Bundle B**

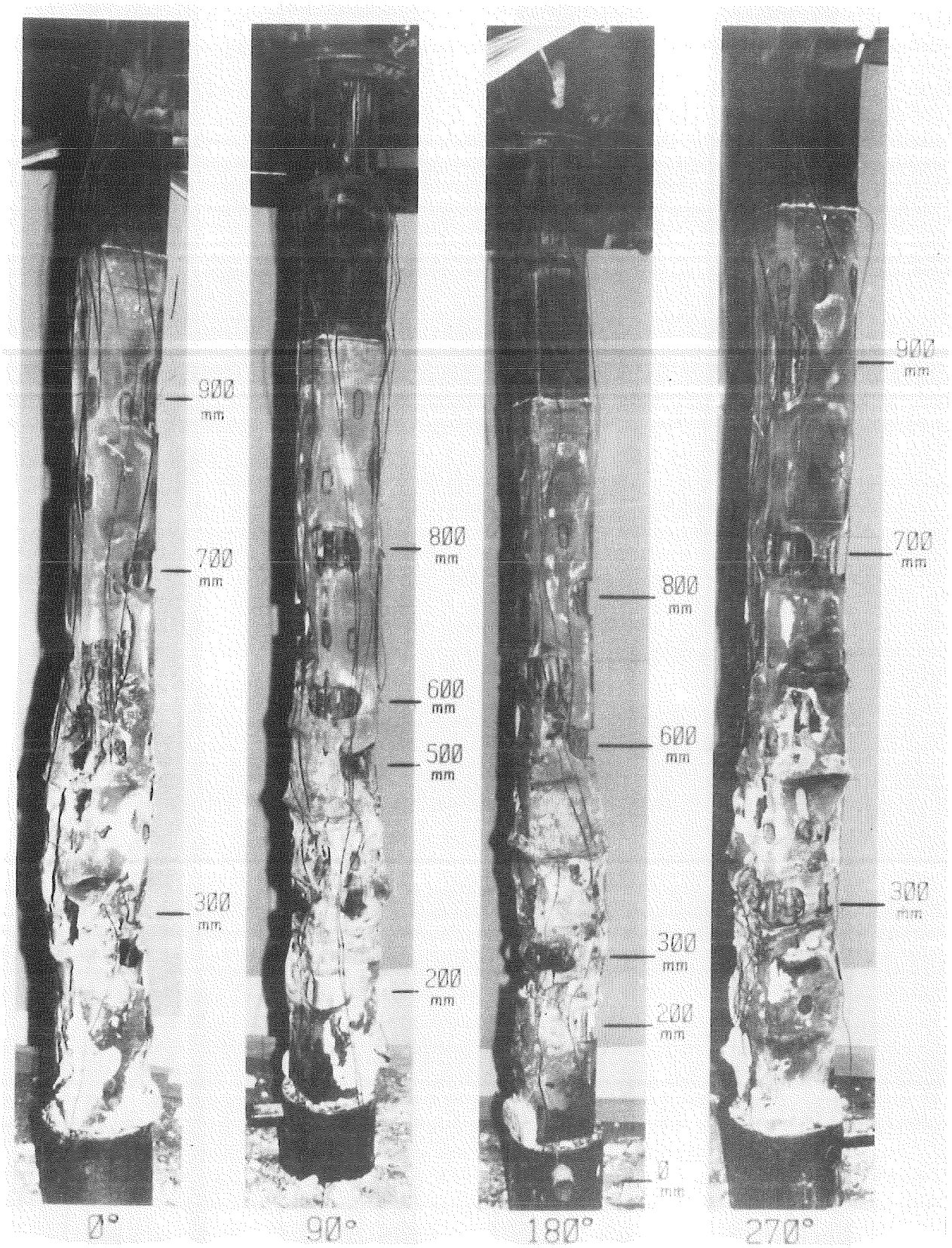


**Fig. 6. Post-test appearance of CORA Bundle C after removal of shroud insulation**

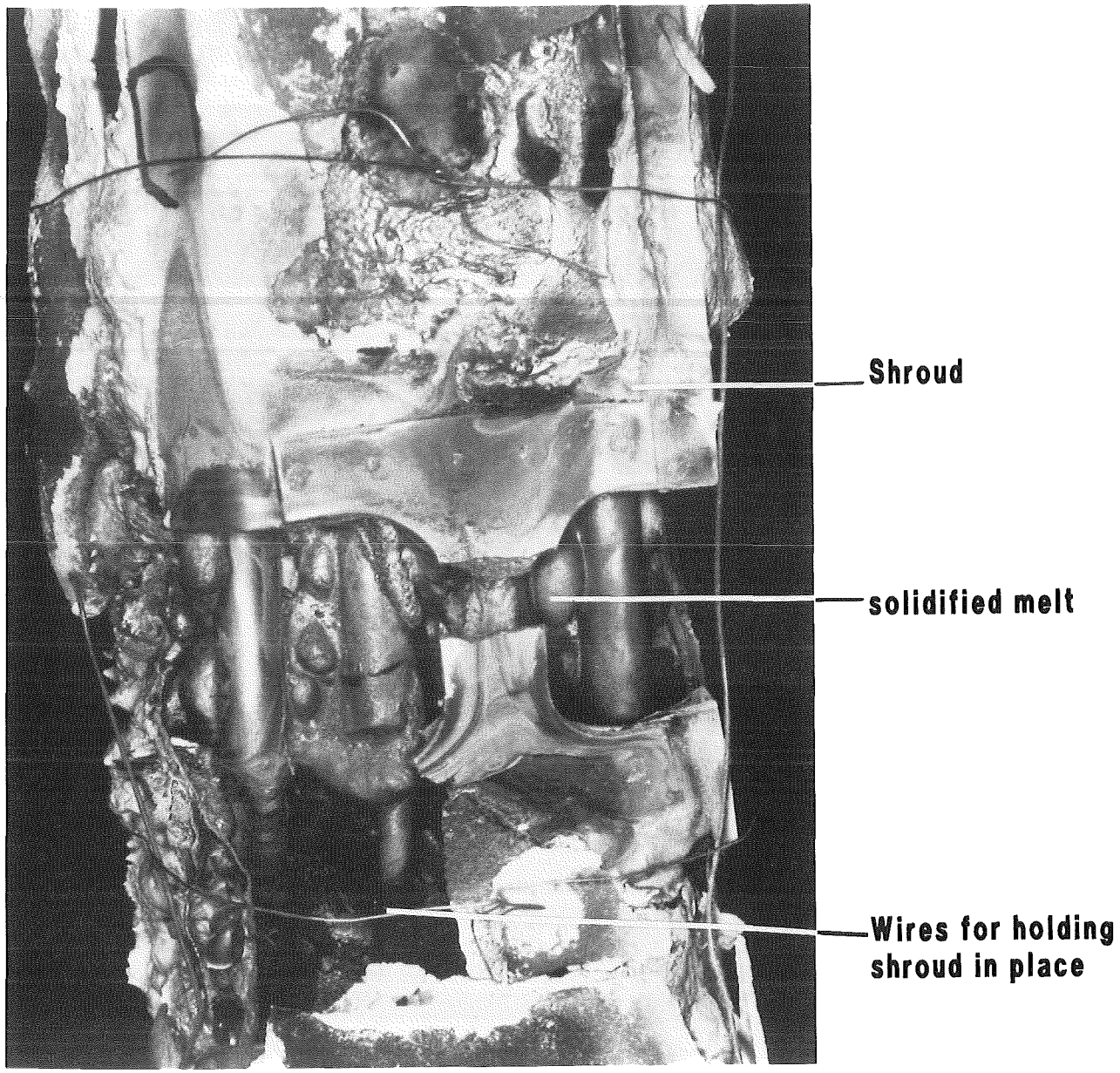


Fig. 7. Influence of shroud insulation on local solidification (CORA Bundle C, 250 - 430 mm, 260°)

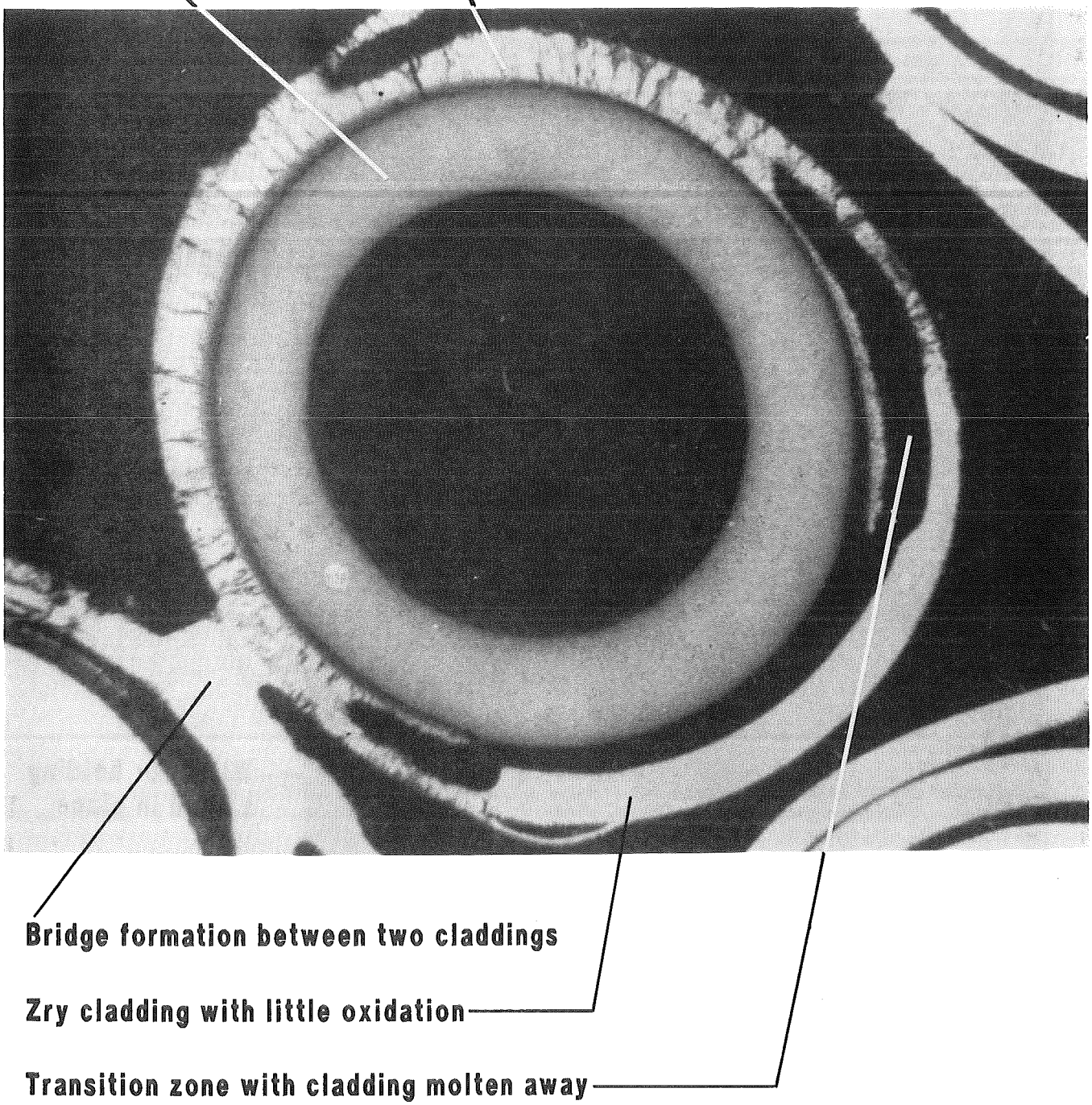


Fig. 8. Detail of unheated rod, CORA-B-16 (1141 mm)

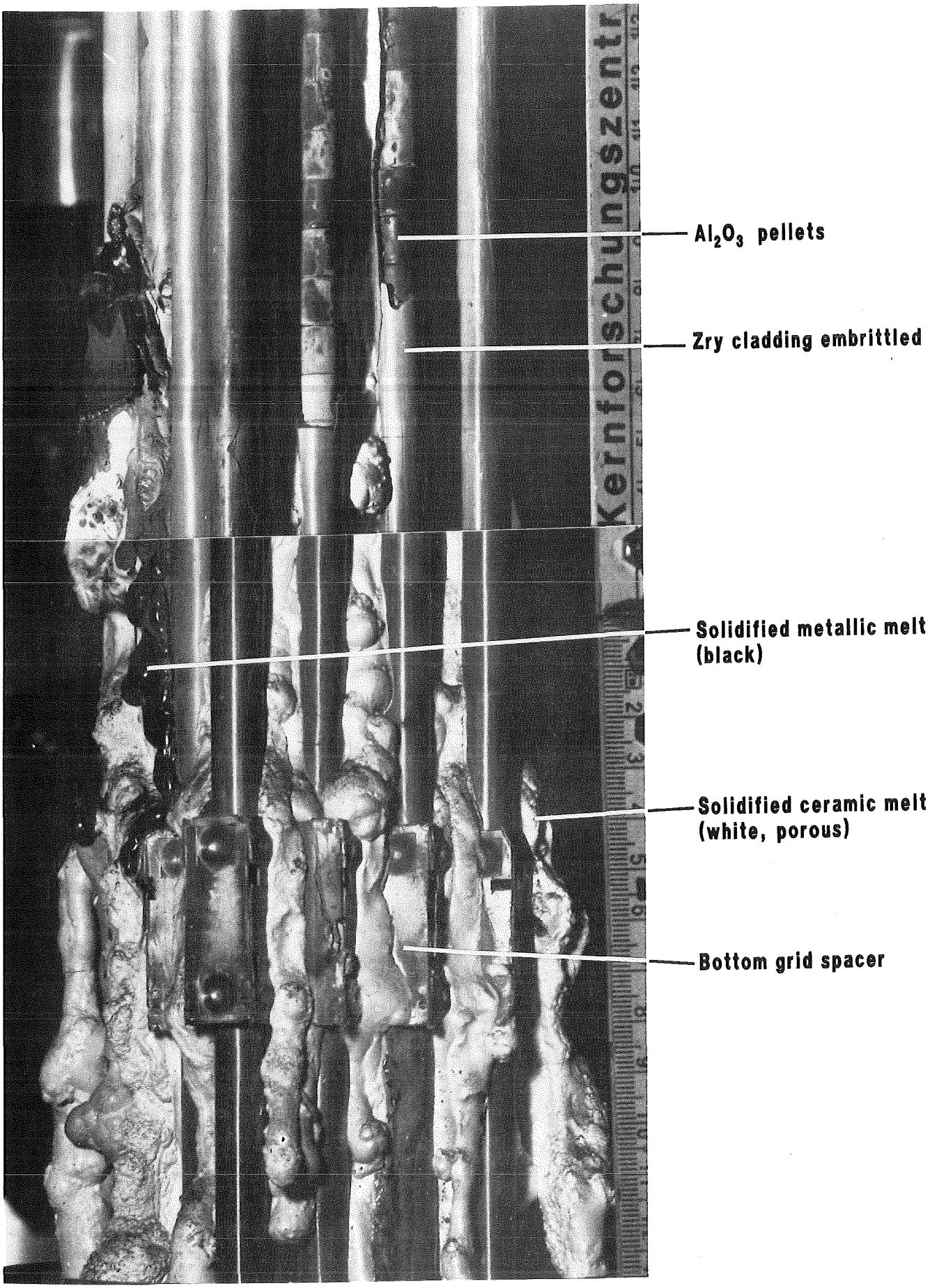


Fig. 9. Solidified melt at lower end of CORA Bundle B (0°)

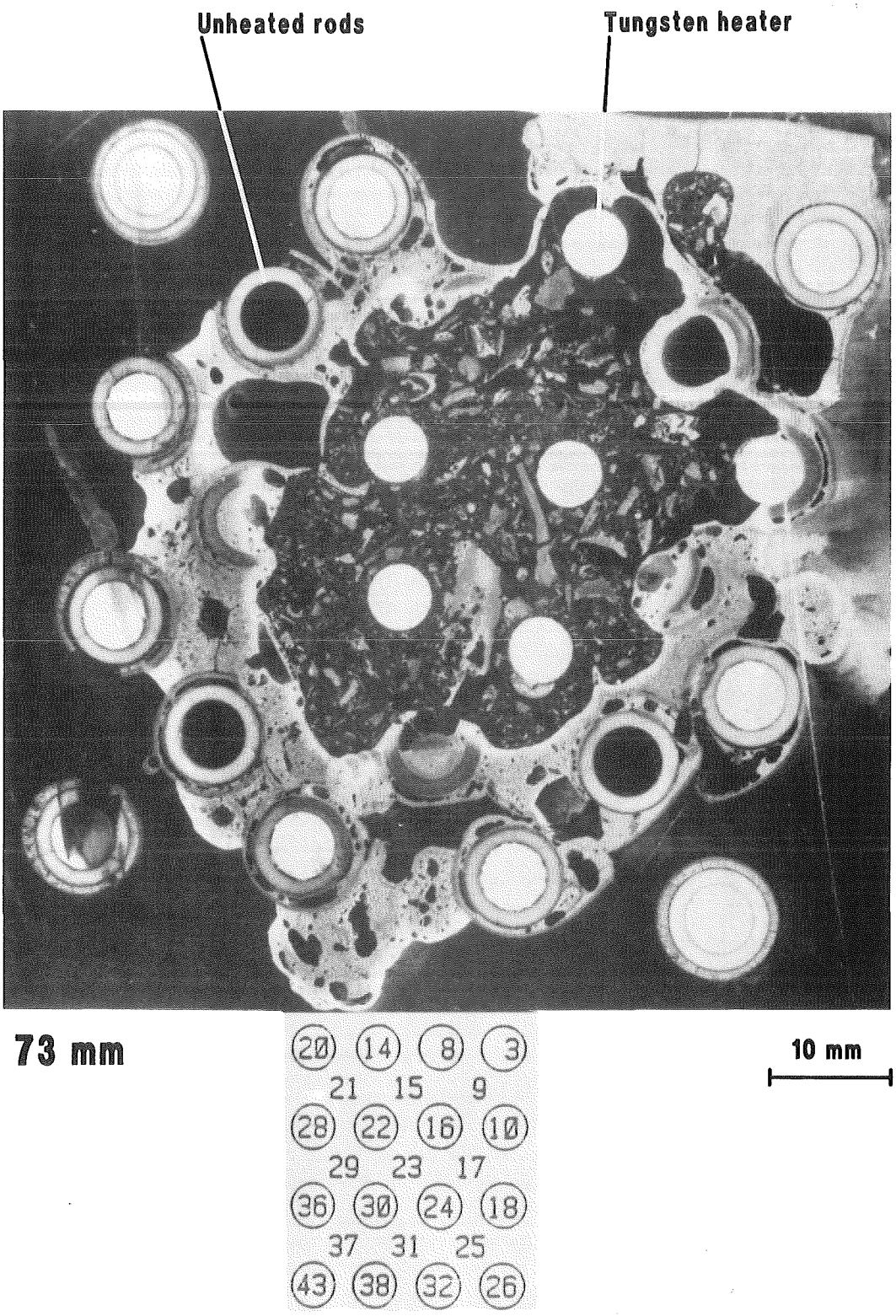


Fig. 10. Cross section of CORA Bundle B at 73 mm elevation; various debris surrounded by foamy ceramic material

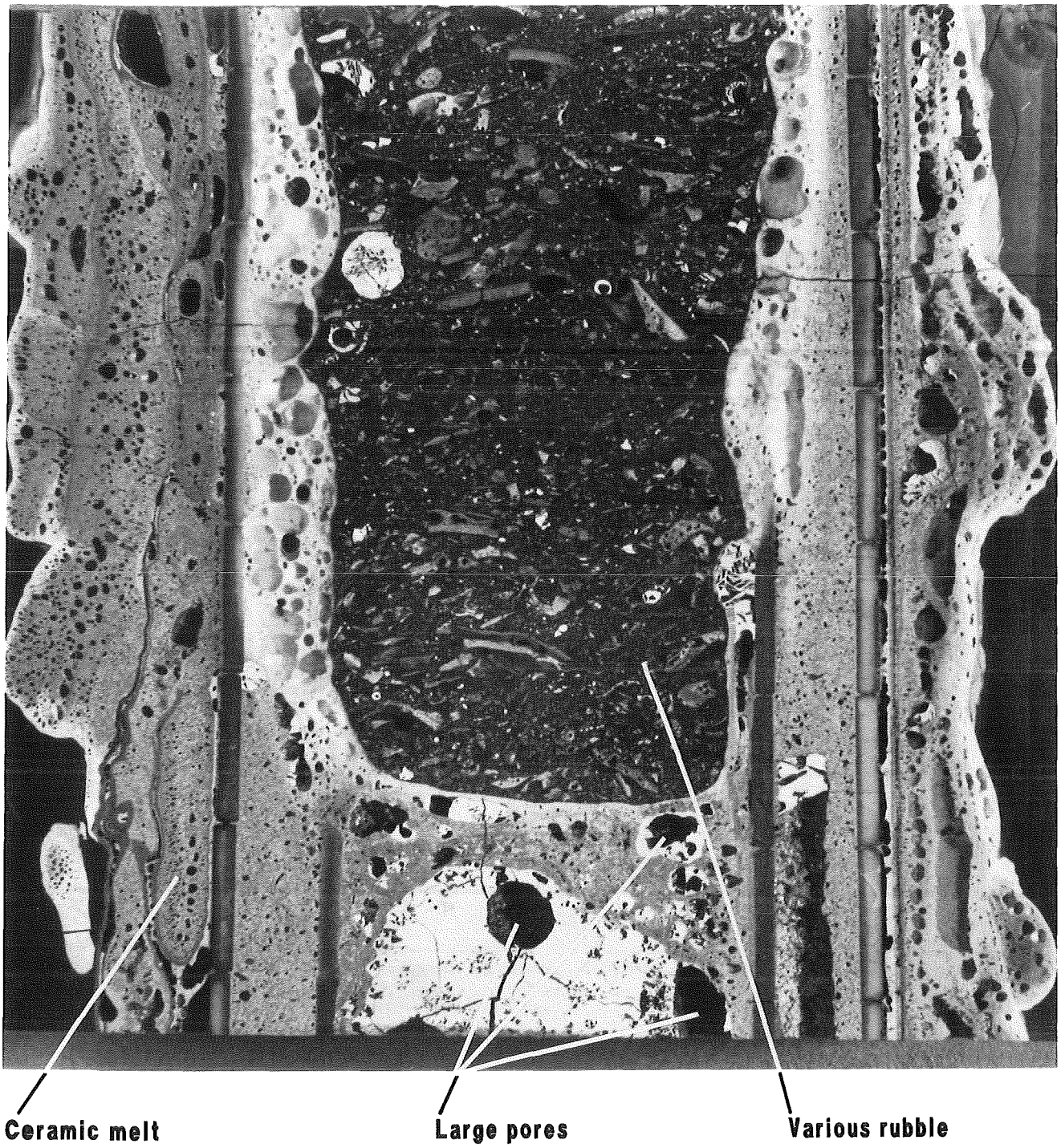


Fig. 11. Vertical cross section c2 between 1 and 73 mm elevation (CORA Bundle B)

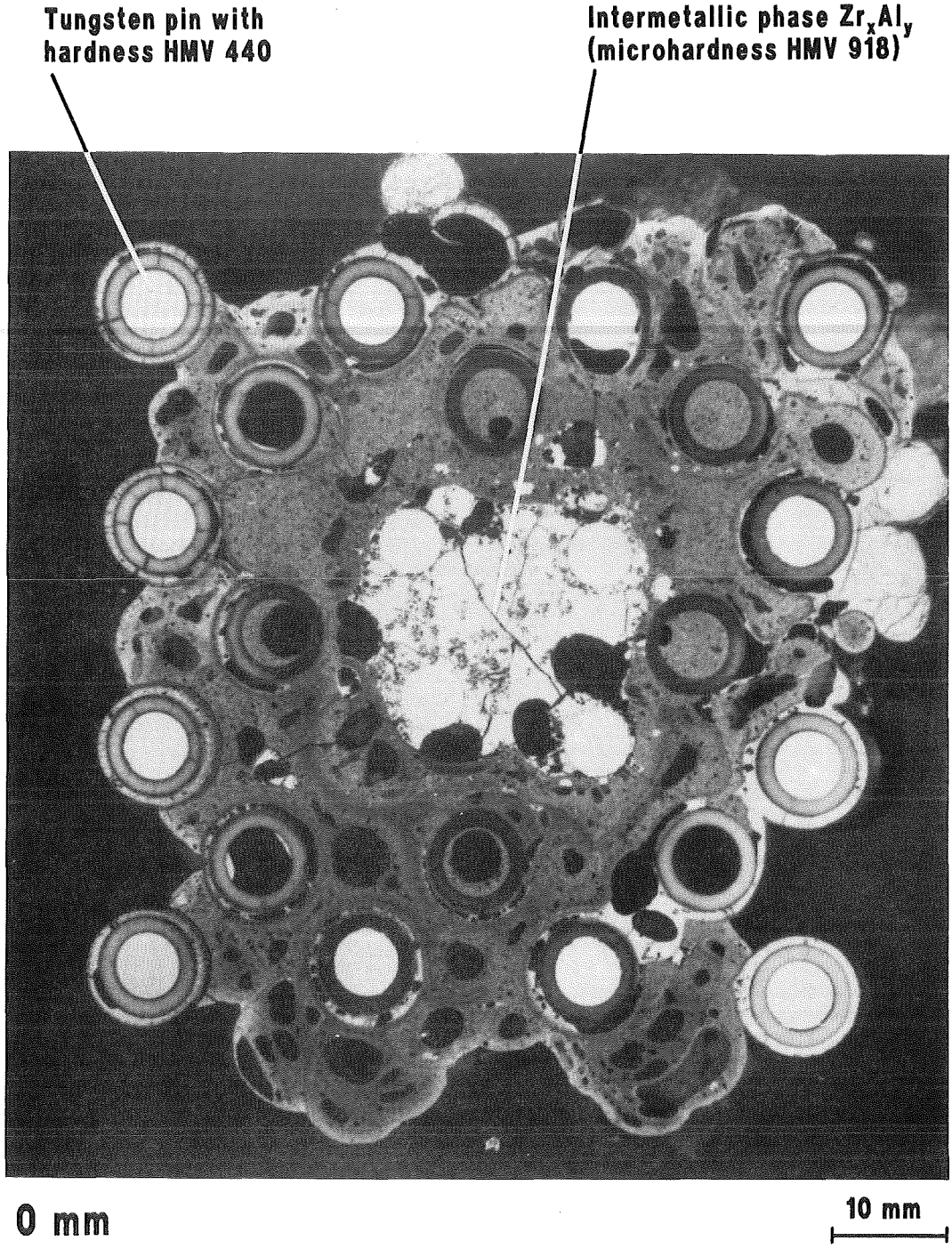


Fig. 12. Cross section of CORA Bundle B at 0 mm elevation

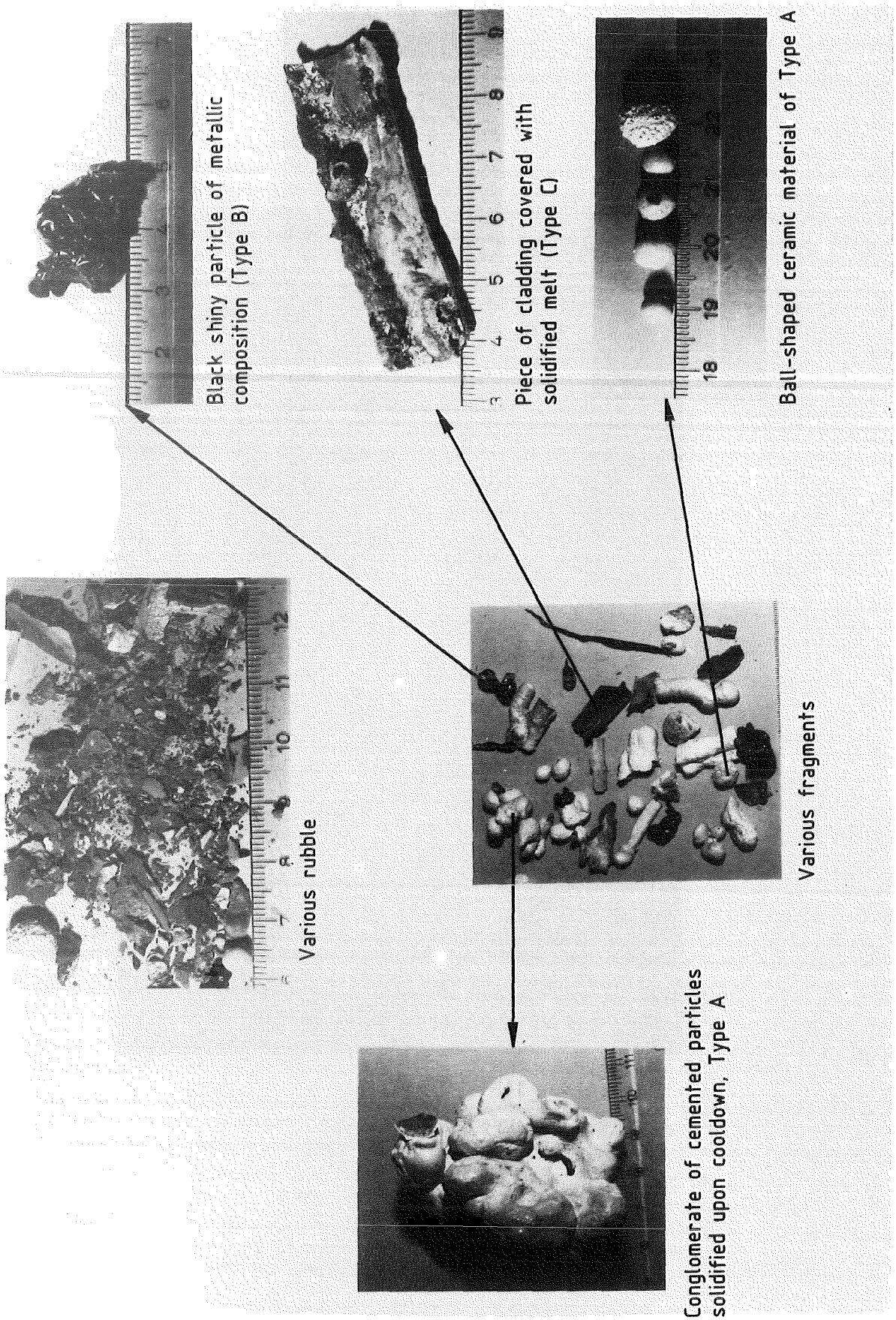


Fig. 13. Fragments and solidified melts found below the test section after CORA Test B

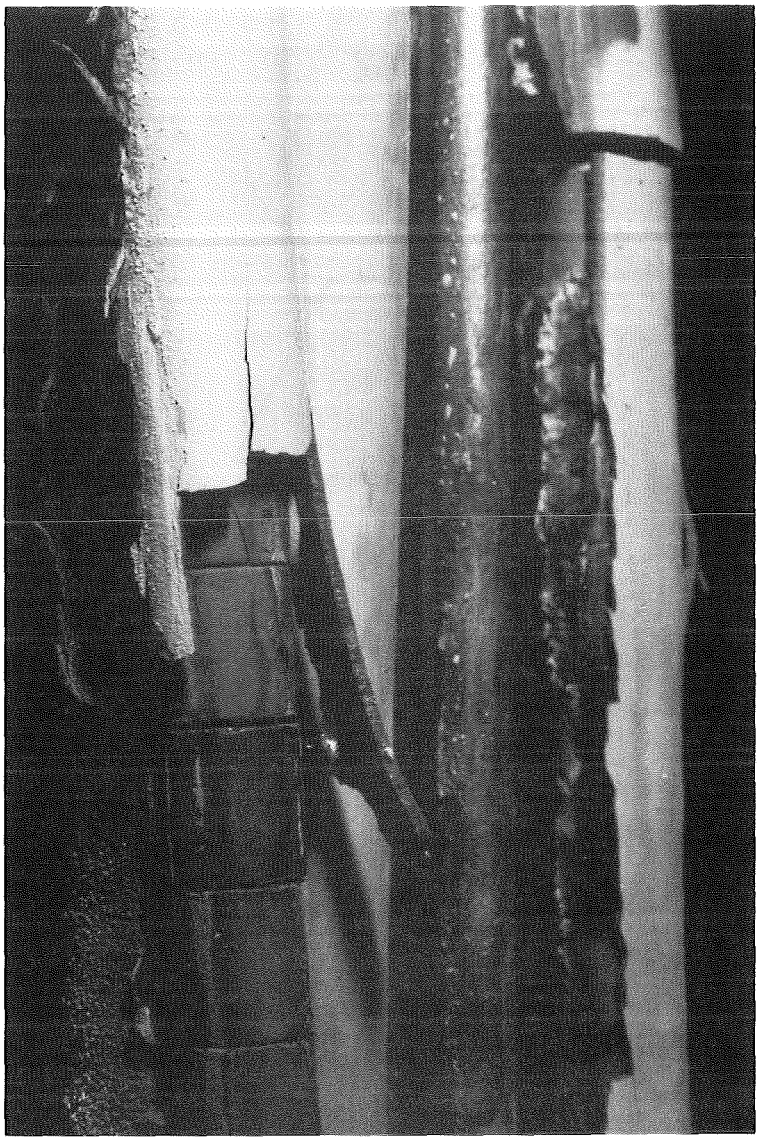

**Fig. 14. Details of middle region of CORA Bundle B (880 mm, 37.5°)**

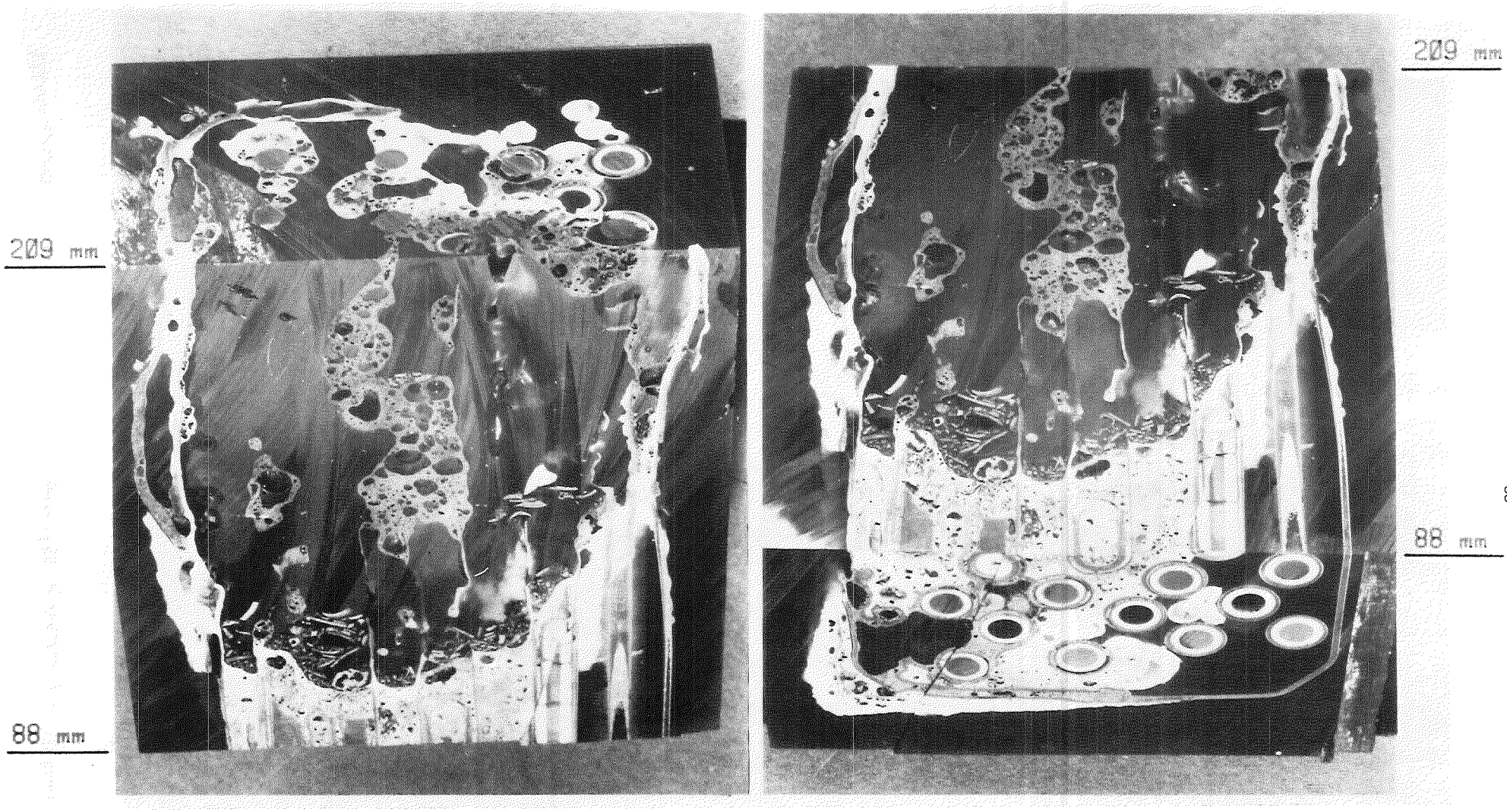


**Fig. 15. Vertical cut through block b2 of CORA Bundle C (88 - 209 mm)**

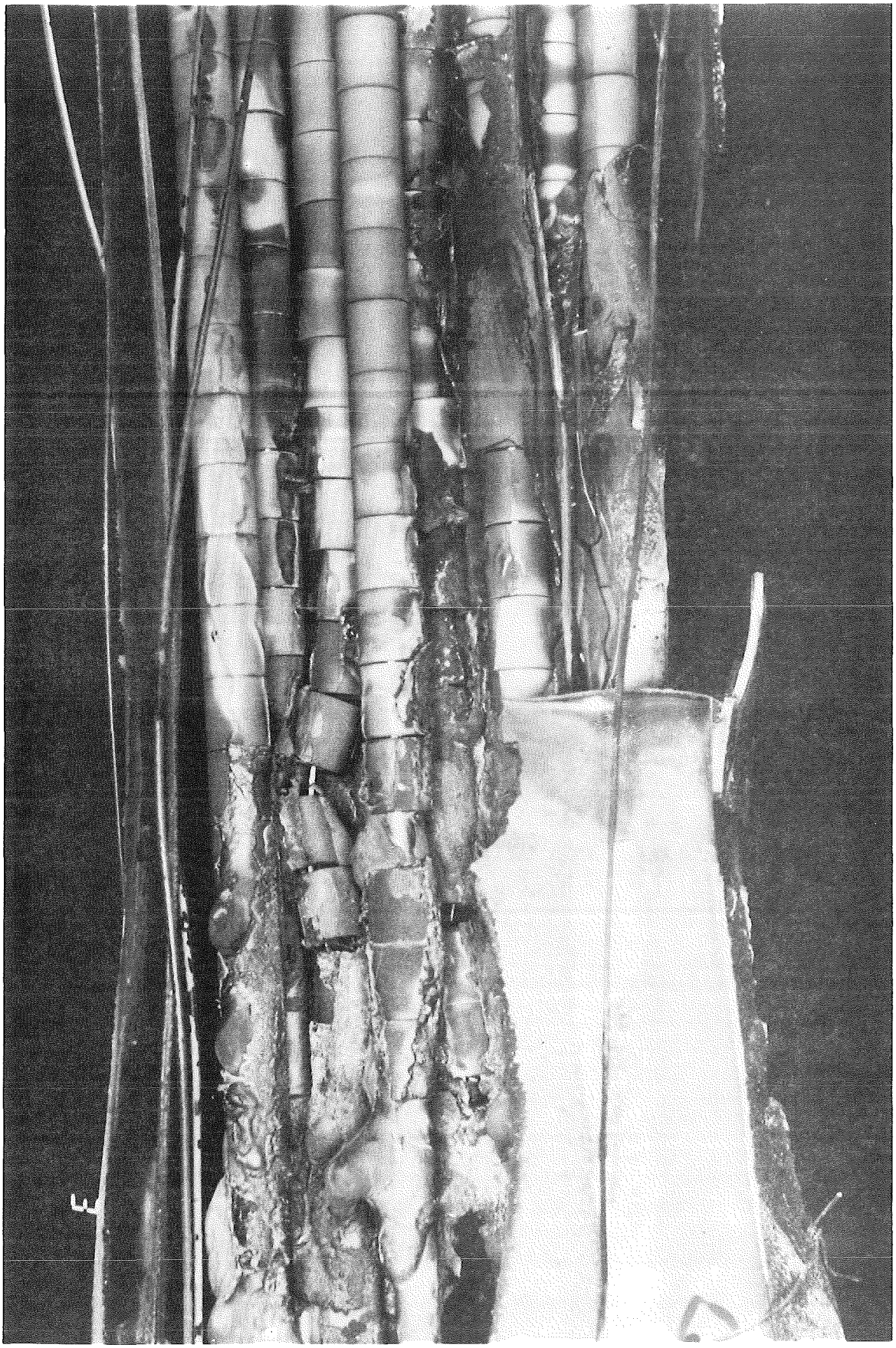

Fig. 16. Details of CORA Bundle C at 610 mm to 800 mm elevation (340°)

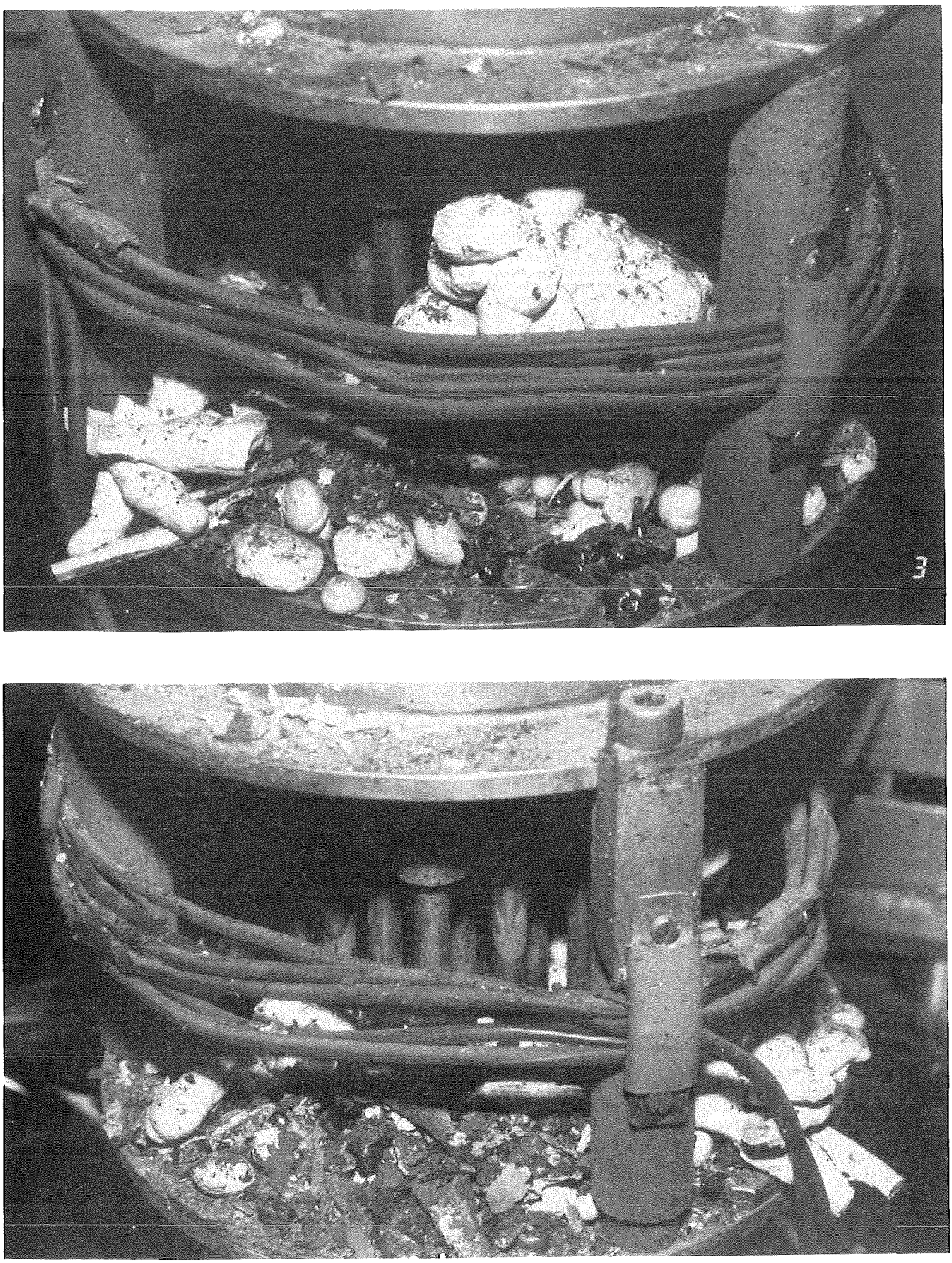


Fig. 17. Rubble collection at bottom of CORA bundle B

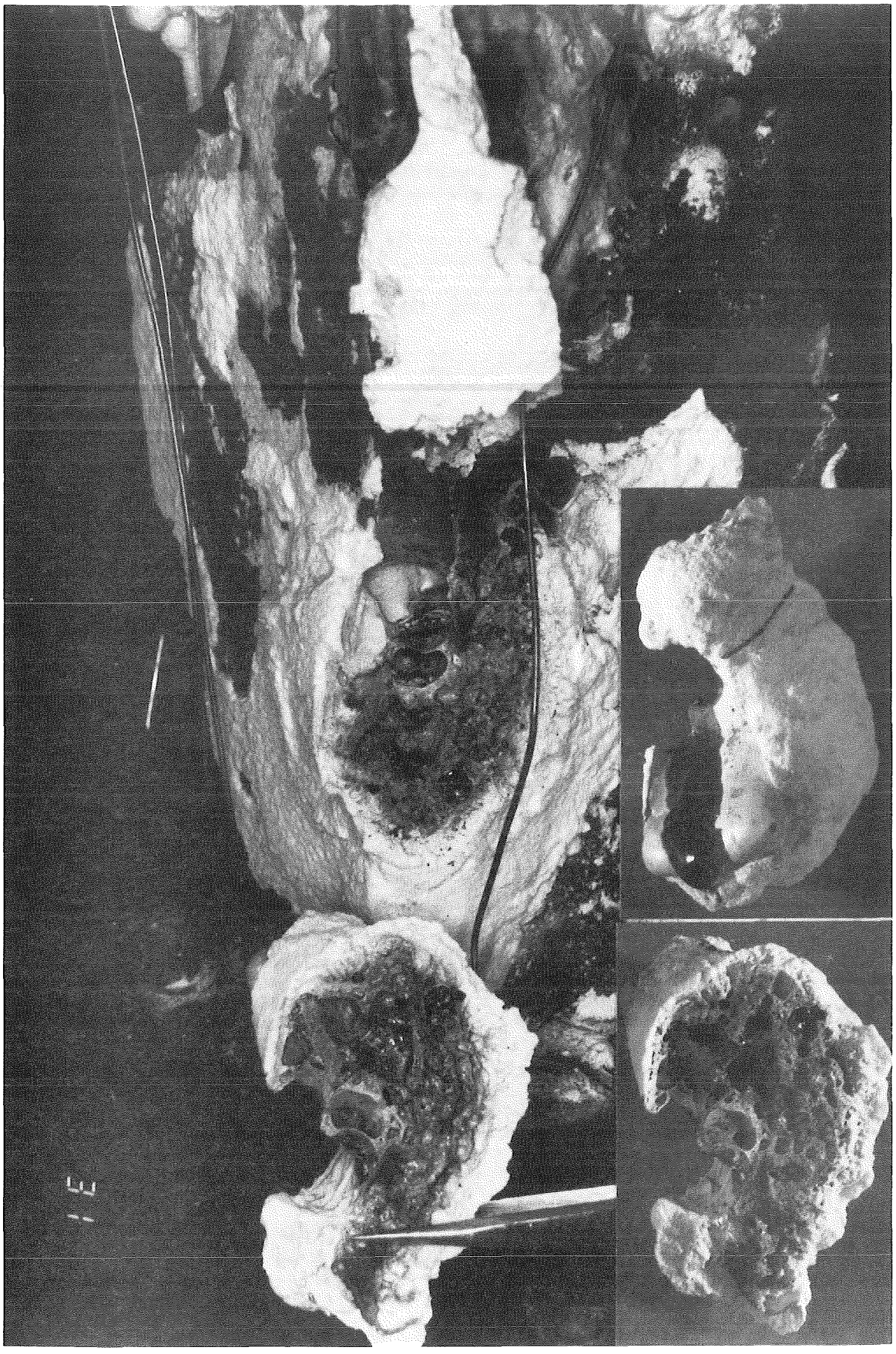

Fig. 18. Sample 4 taken from CORA Bundle C at 100 mm elevation, 30°

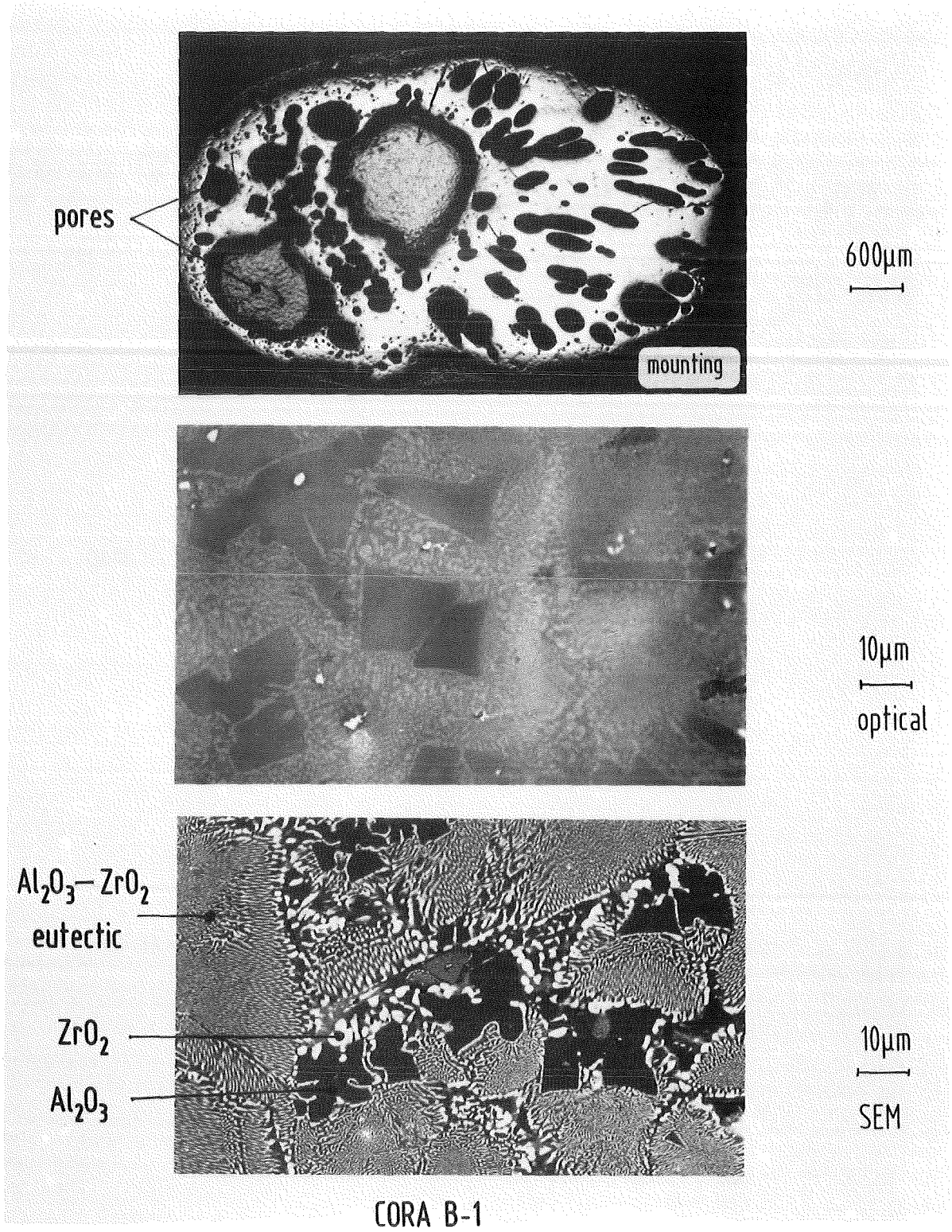


**Fig. 19. Microstructure of a ceramic "droplet" (CORA Bundle B)**

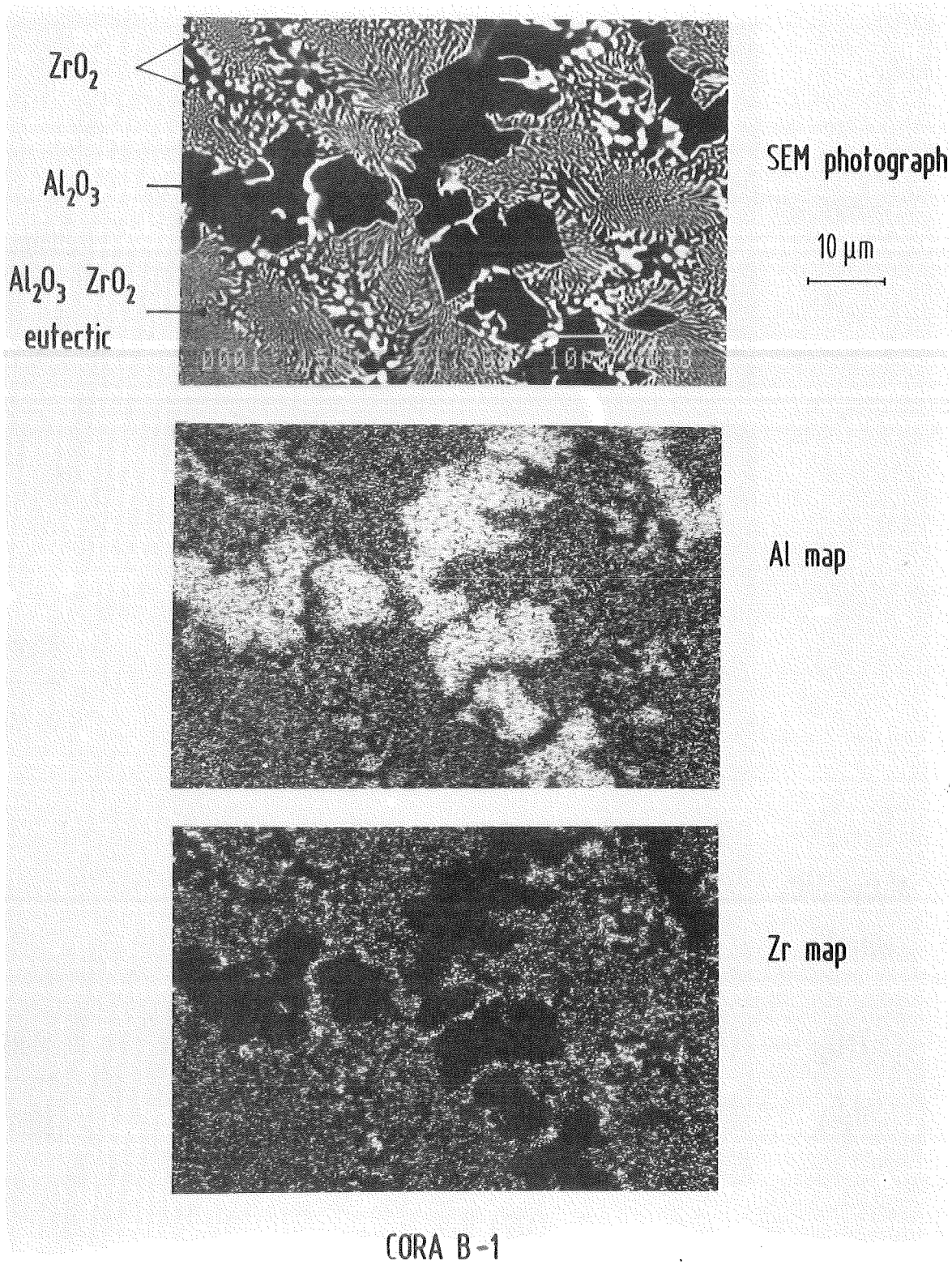


**Fig. 20. SEM-EDX analysis of specimen CORA B-1**

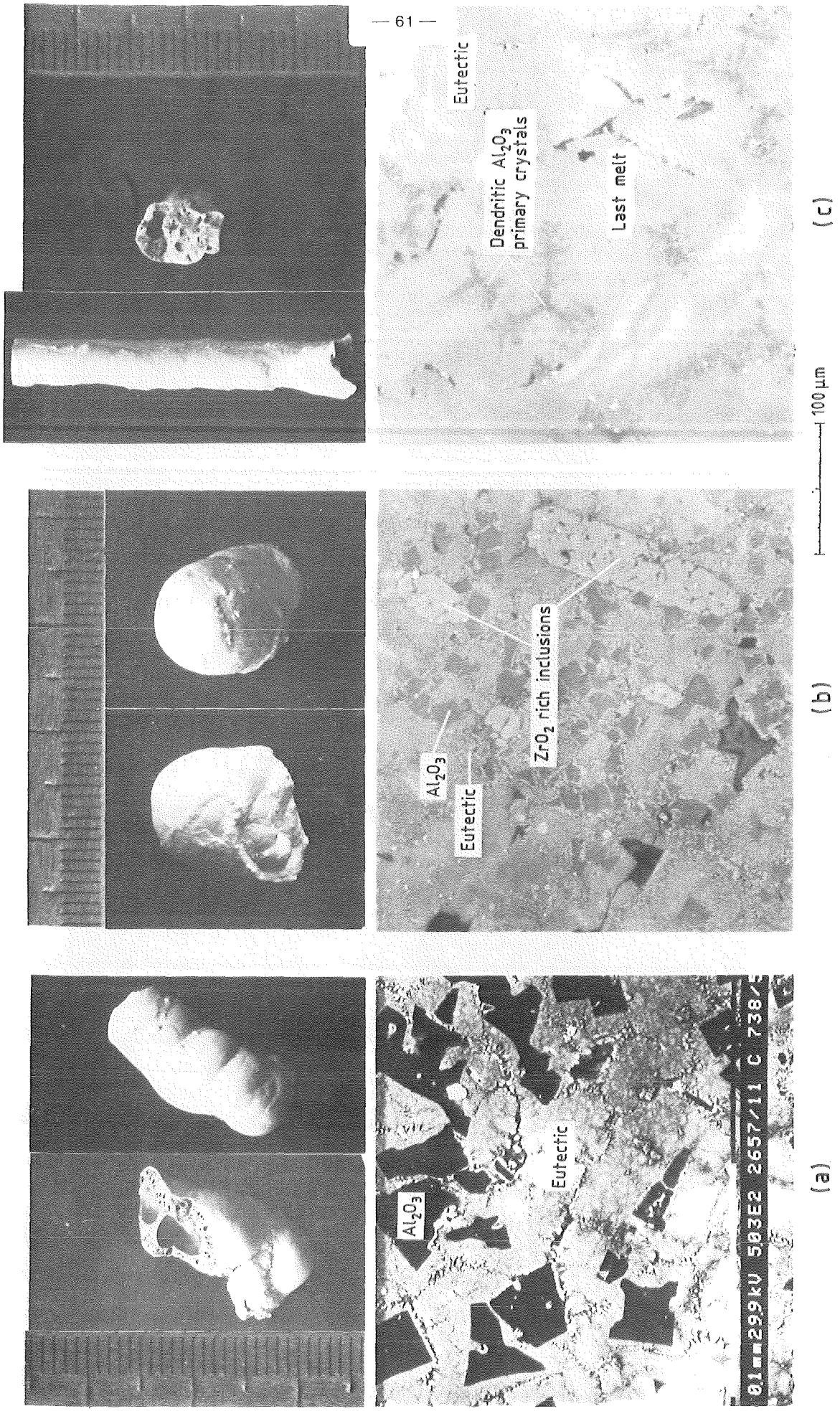


**Fig. 21.** $ZrO_2/Al_2O_3$ eutectic melt identified in three different fragments collected from CORA B

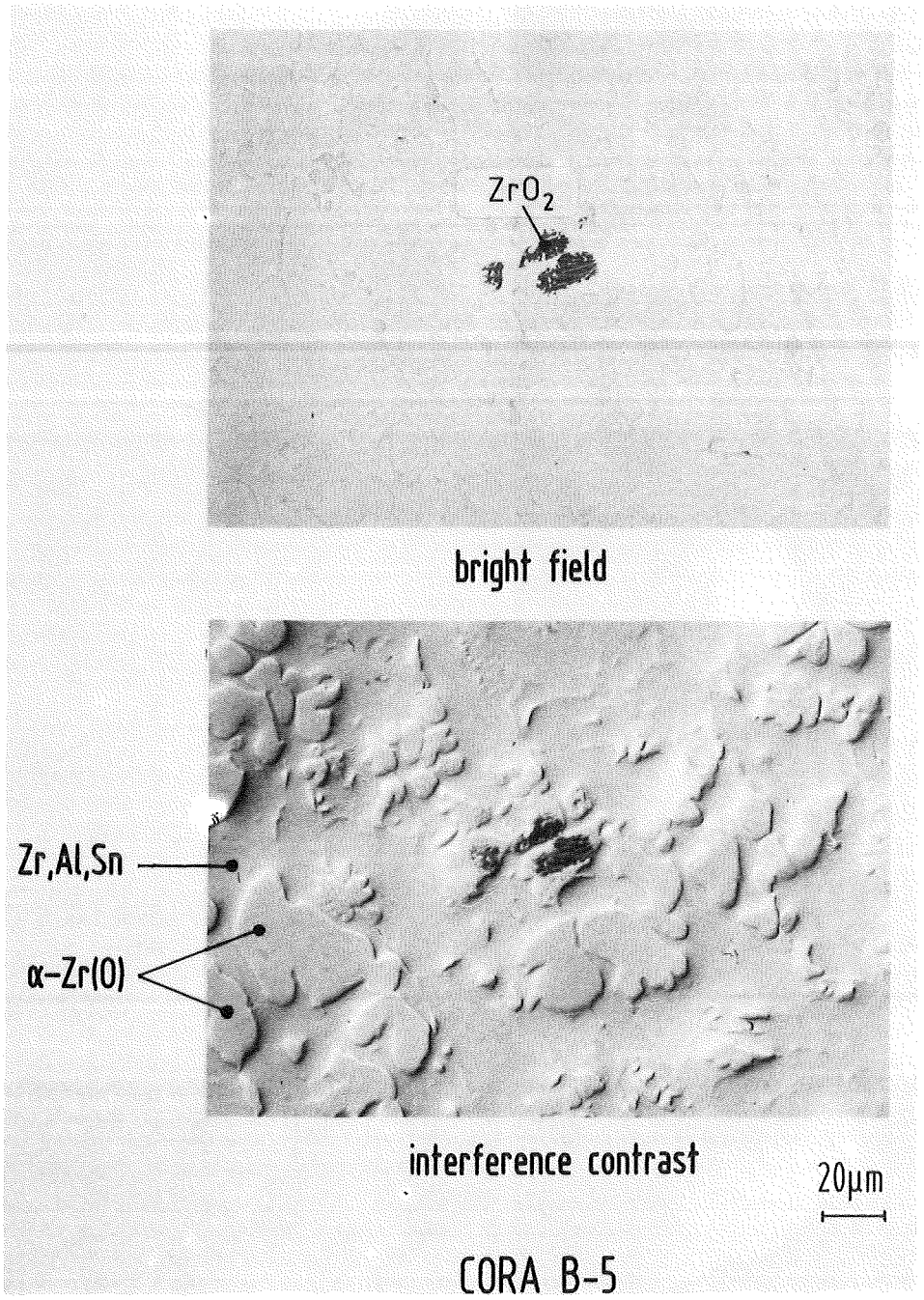


**Fig. 22. Microstructure of a metallic "droplet" (CORA bundle B)**

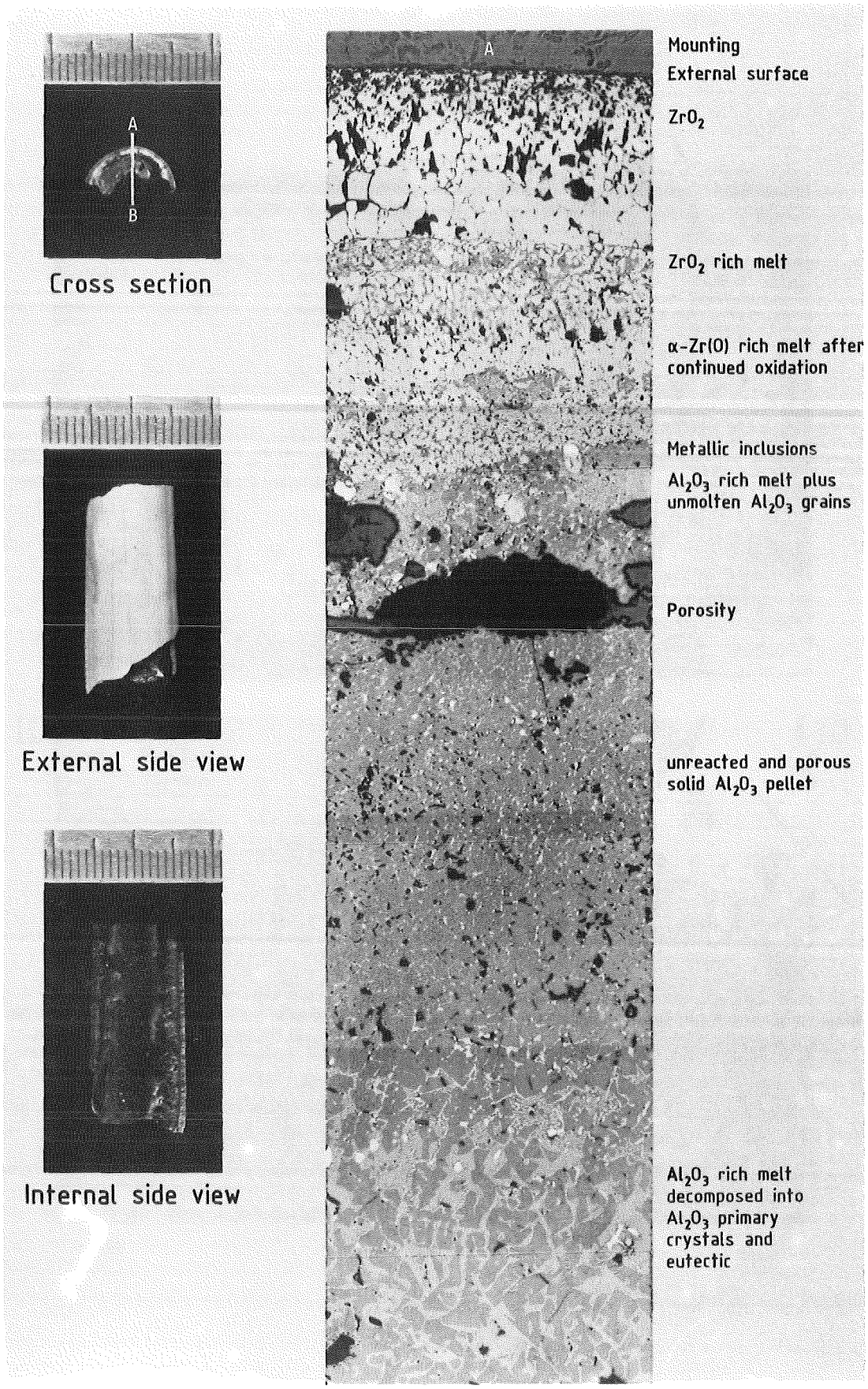


**Fig. 23. Microstructure across a rod fragment after Zircaloy-4 cladding /$Al_2O_3$ pellet eutectic melting (CORA B)**

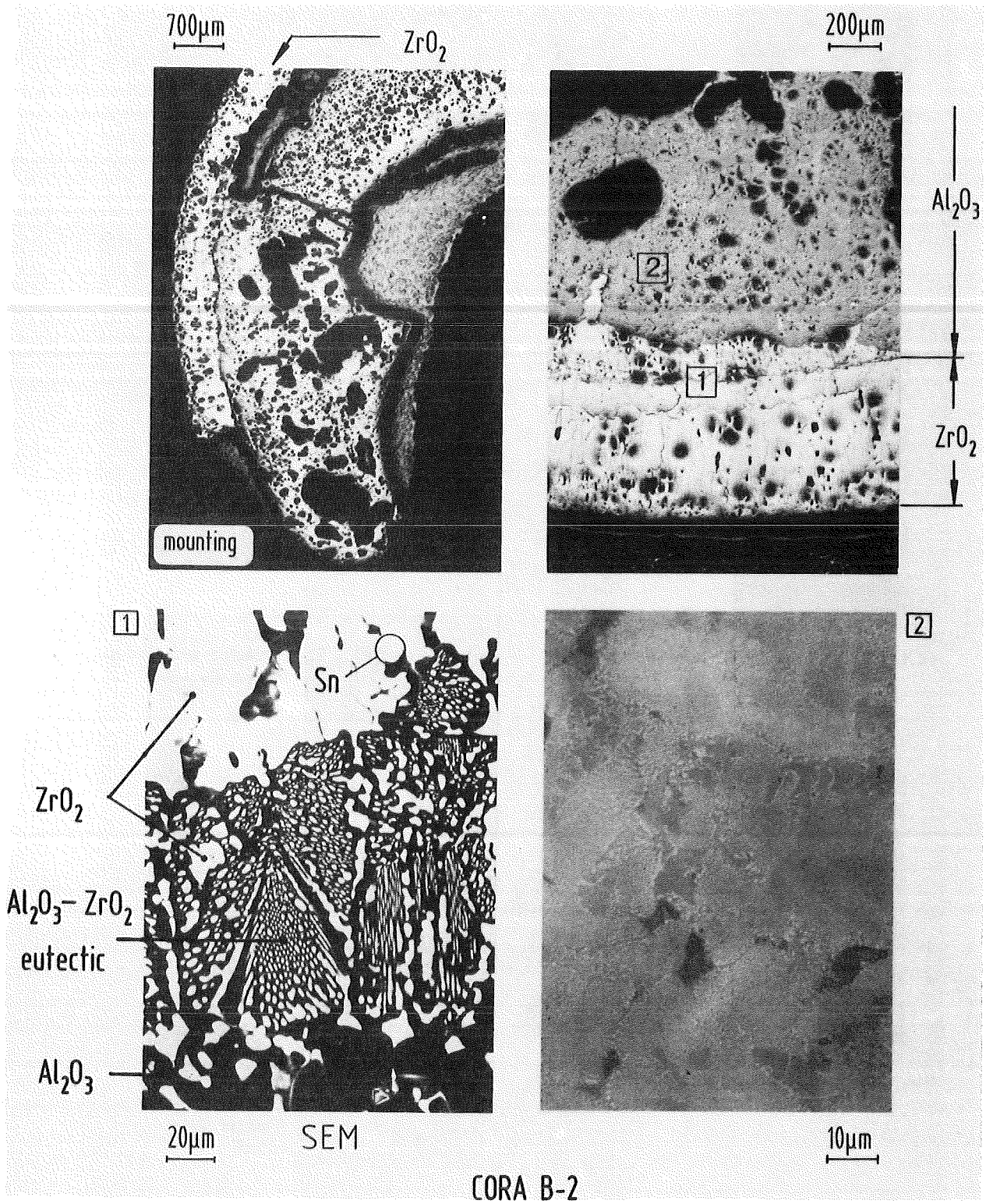


**Fig. 24. Microstructure of a fuel rod fragment (CORA bundle B)**

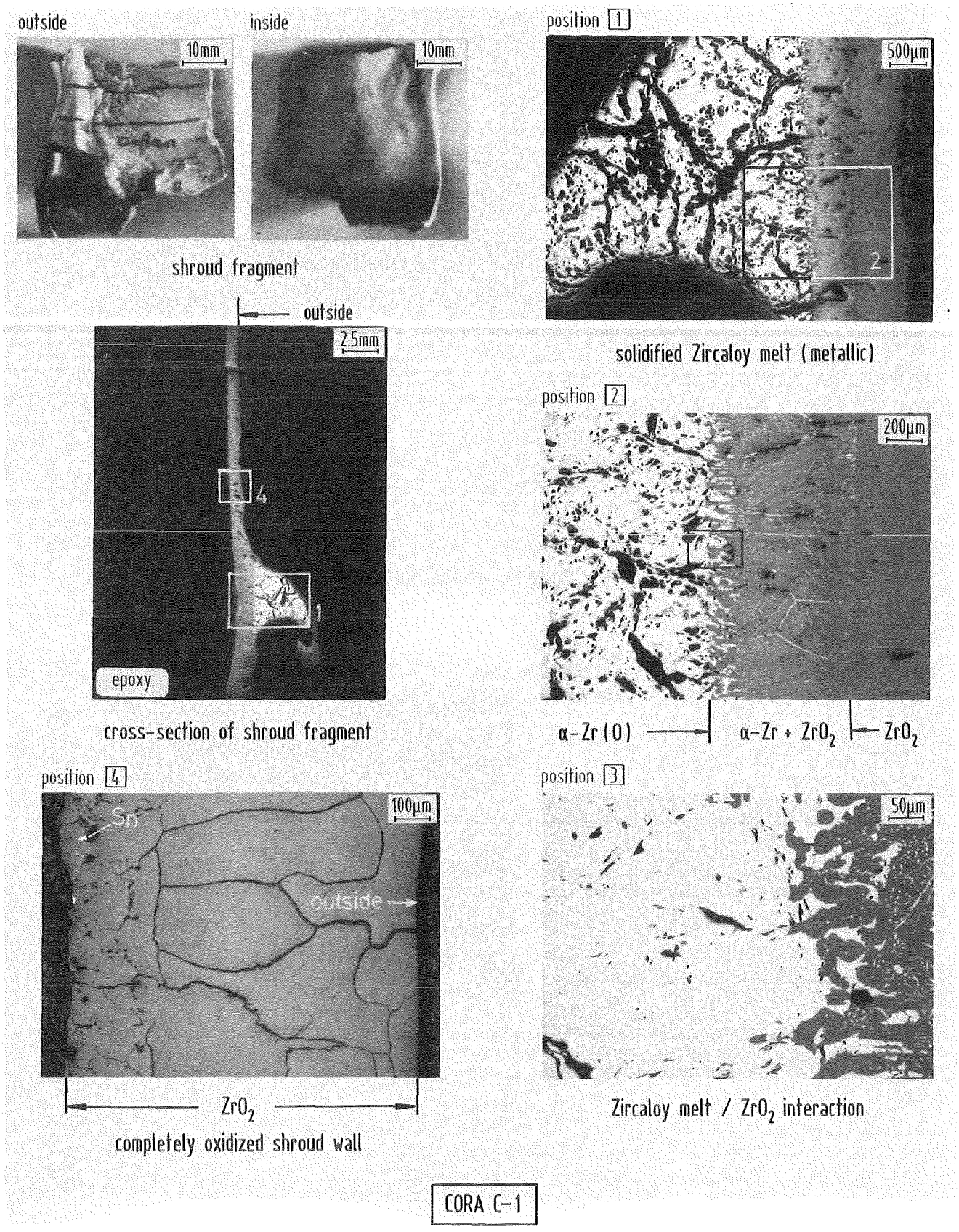


**Fig. 25. Microstructures of shroud fragment # 1 (CORA bundle C)**

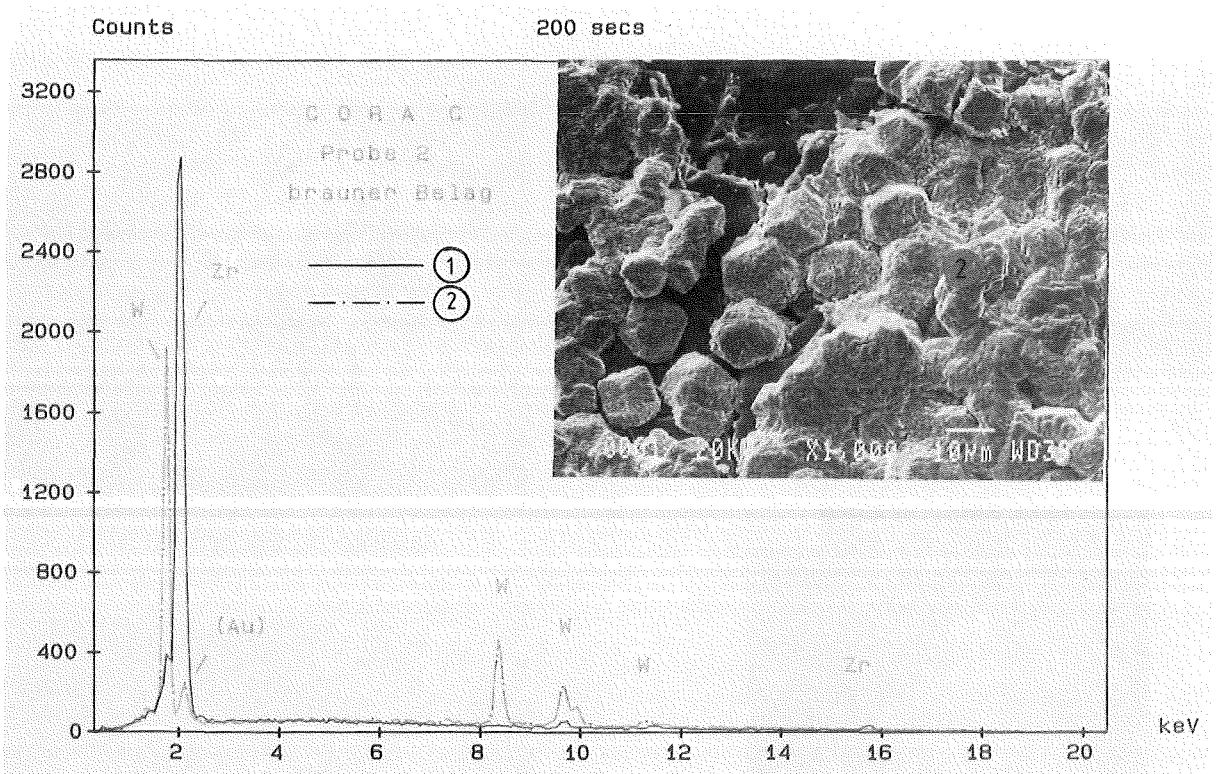


SEM-EDX analysis of inner shroud surface ( CORA C-2 )

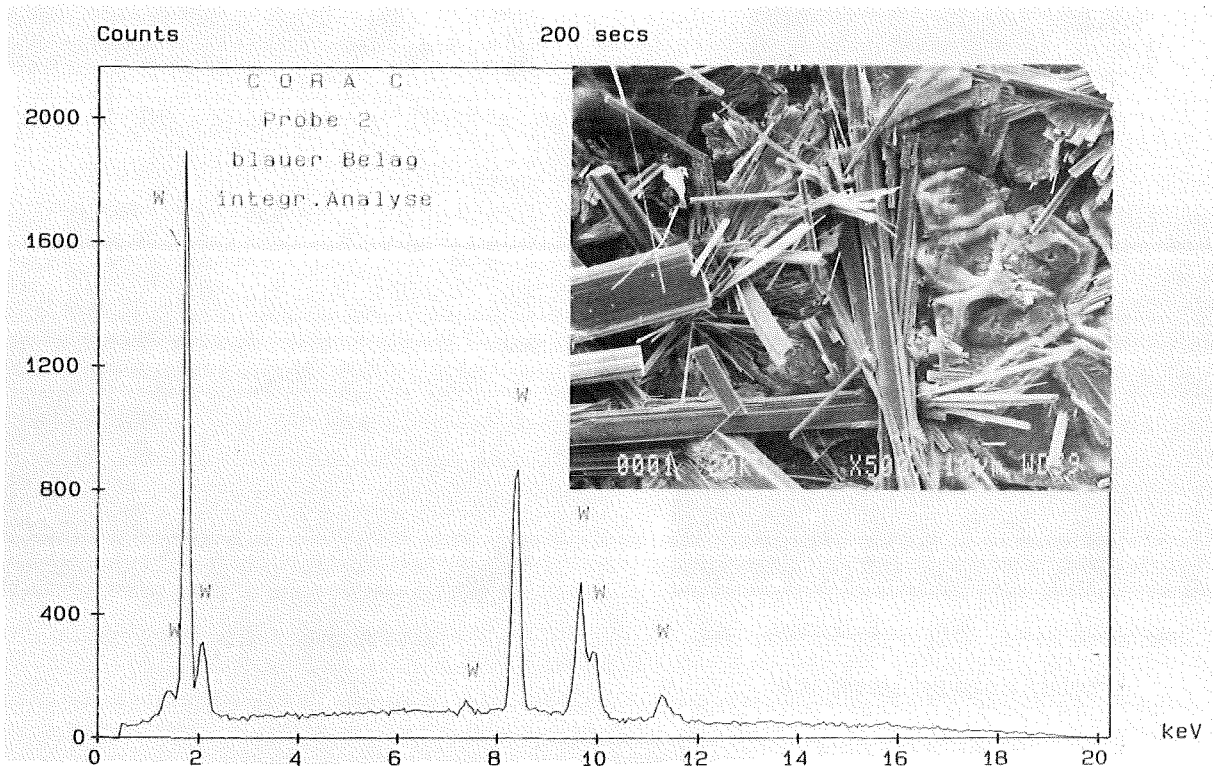


**Fig. 26. SEM-EDX analysis of inner shroud surface (CORA C-2)**

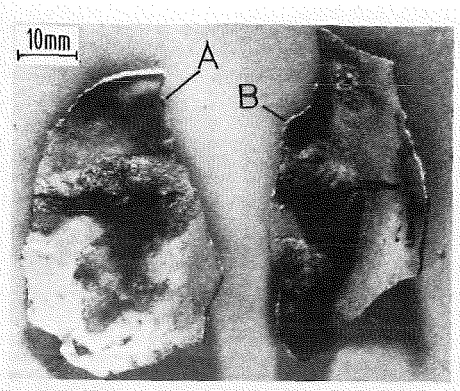


shroud fragments (inside)

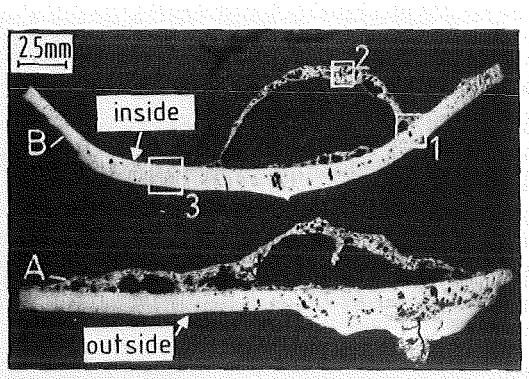


cross-section of shroud fragments

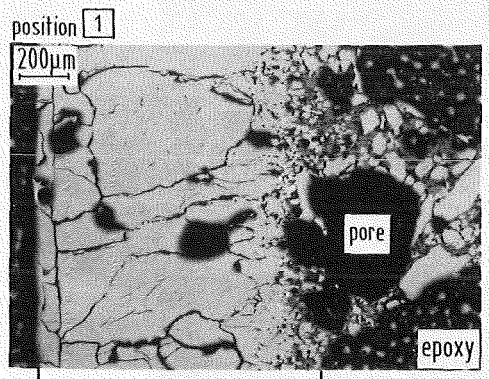


oxidized shroud wall
$ZrO_2$

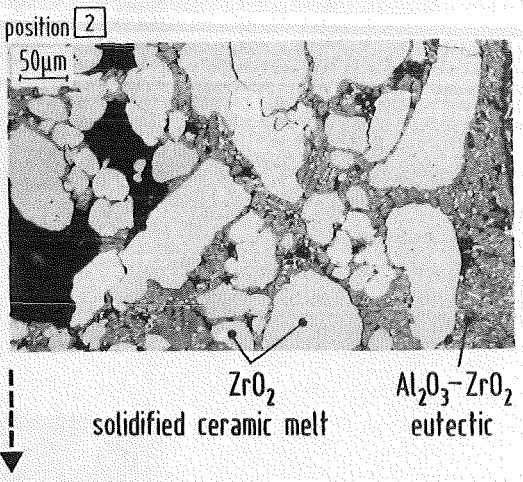


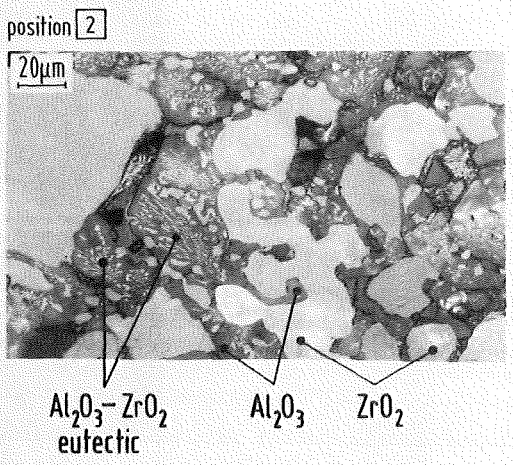


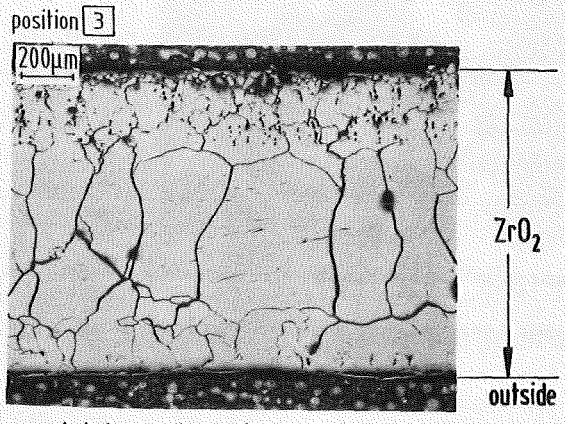


completely oxidized shroud wall

CORA C-3

**Fig. 27. Microstructures of shroud fragment # 3 (A, B) (CORA bundle C)**

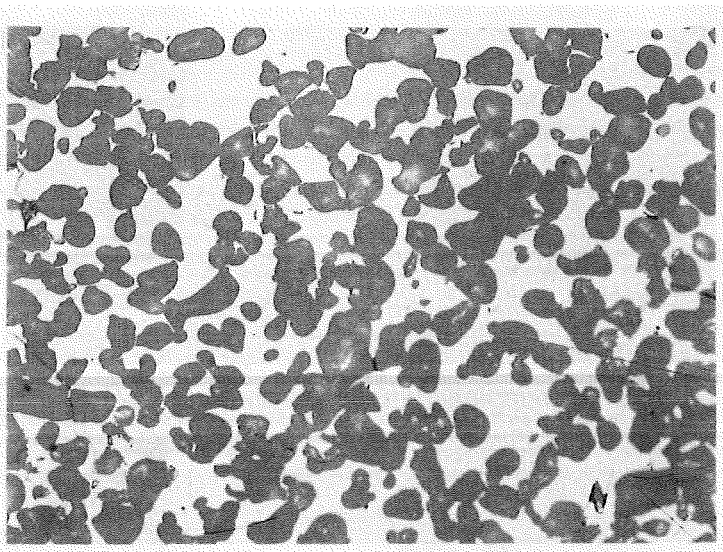

optical
20µm

Zr : 65wt.%
Al : 7wt.%
Sn : 28wt.%

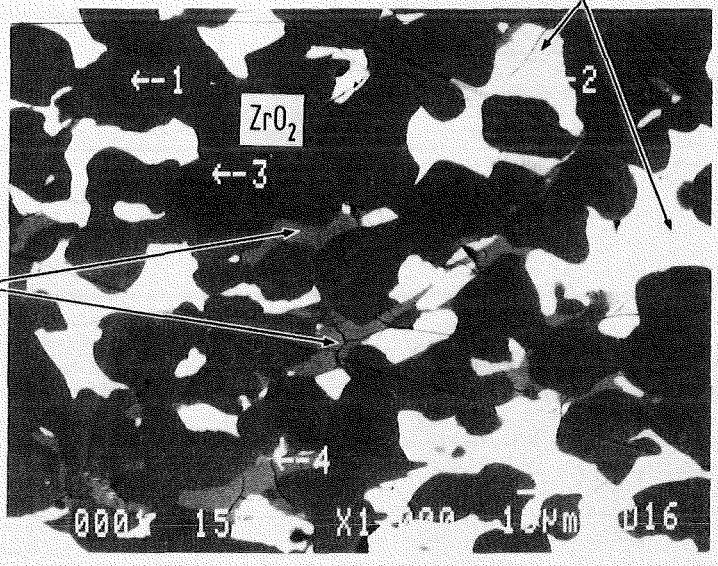


$ZrO_2$ : 48wt.%
FeO : 20wt.%
$Al_2O_3$ : 15wt.%
$Cr_2O_3$ : 12wt.%
$WO_3$ : 5wt.%

SEM
10µm

solidified "metallic" melt with
various ceramic precipitations

CORA C-3

**Fig. 28. Microstructures of shroud fragment # 3A (CORA bundle C)**

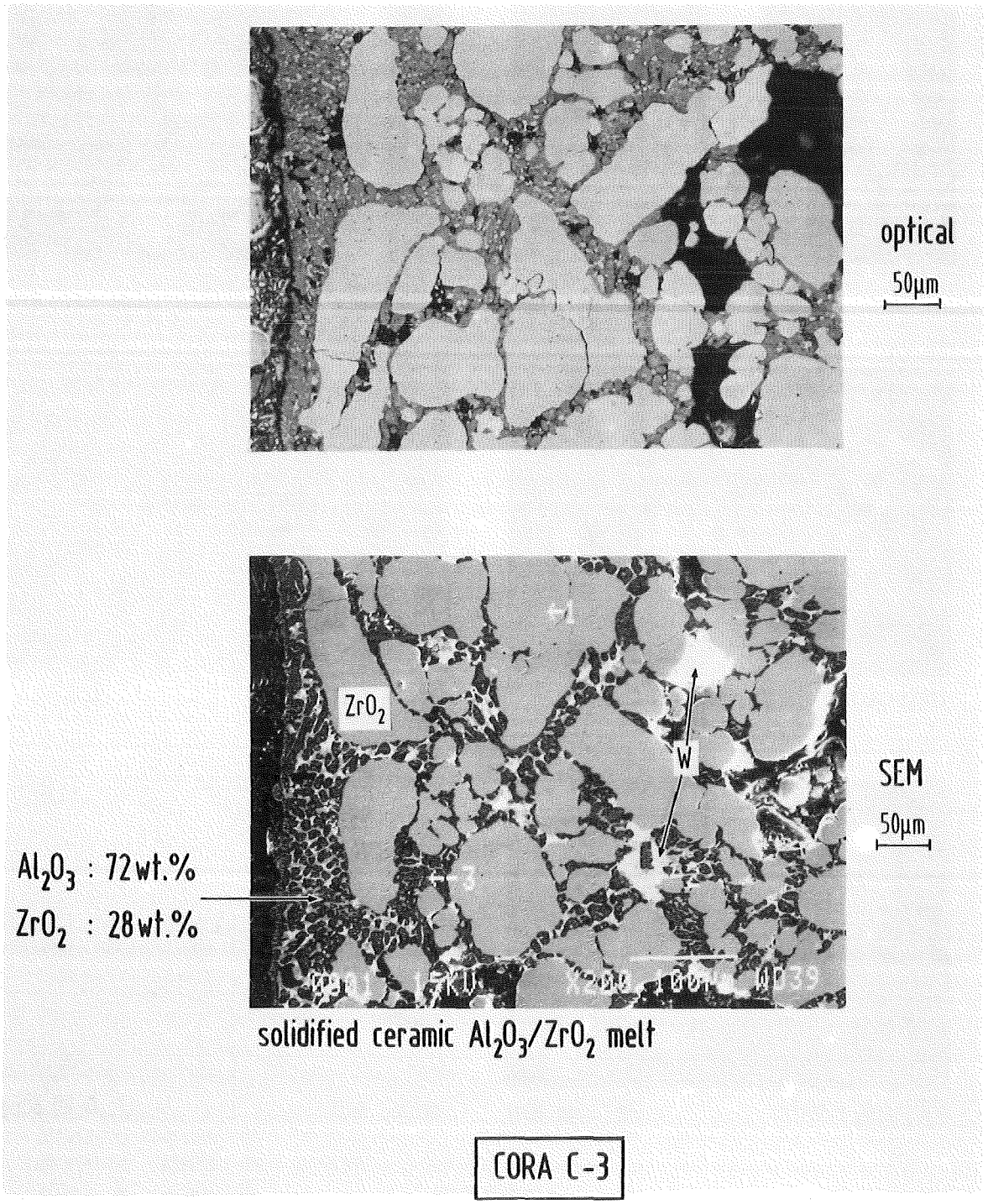


**Fig. 29. Microstructures of shroud fragment # 3A (CORA bundle C)**

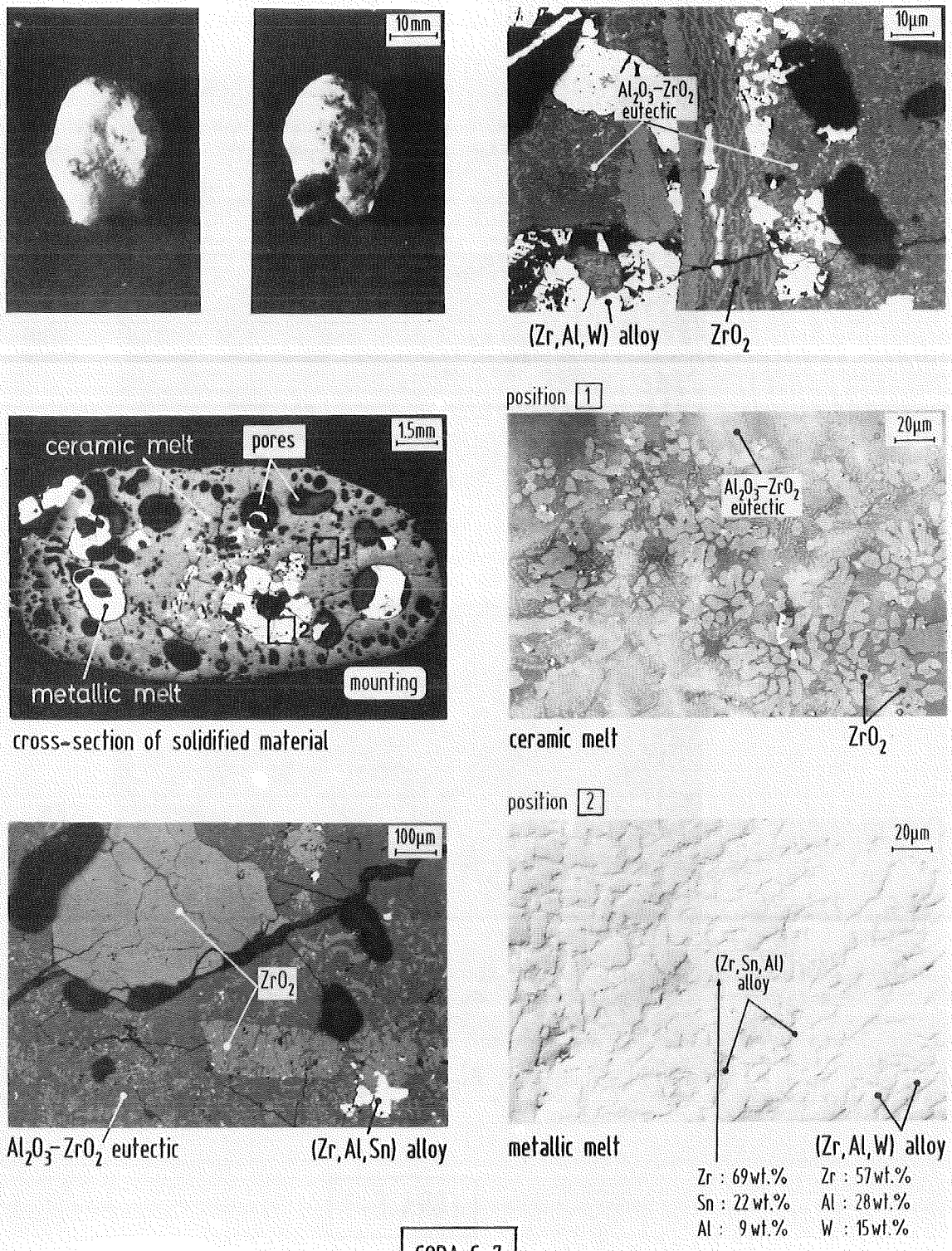


**Fig. 30. Microstructures of molten ceramic and metallic material (CORA bundle C)**

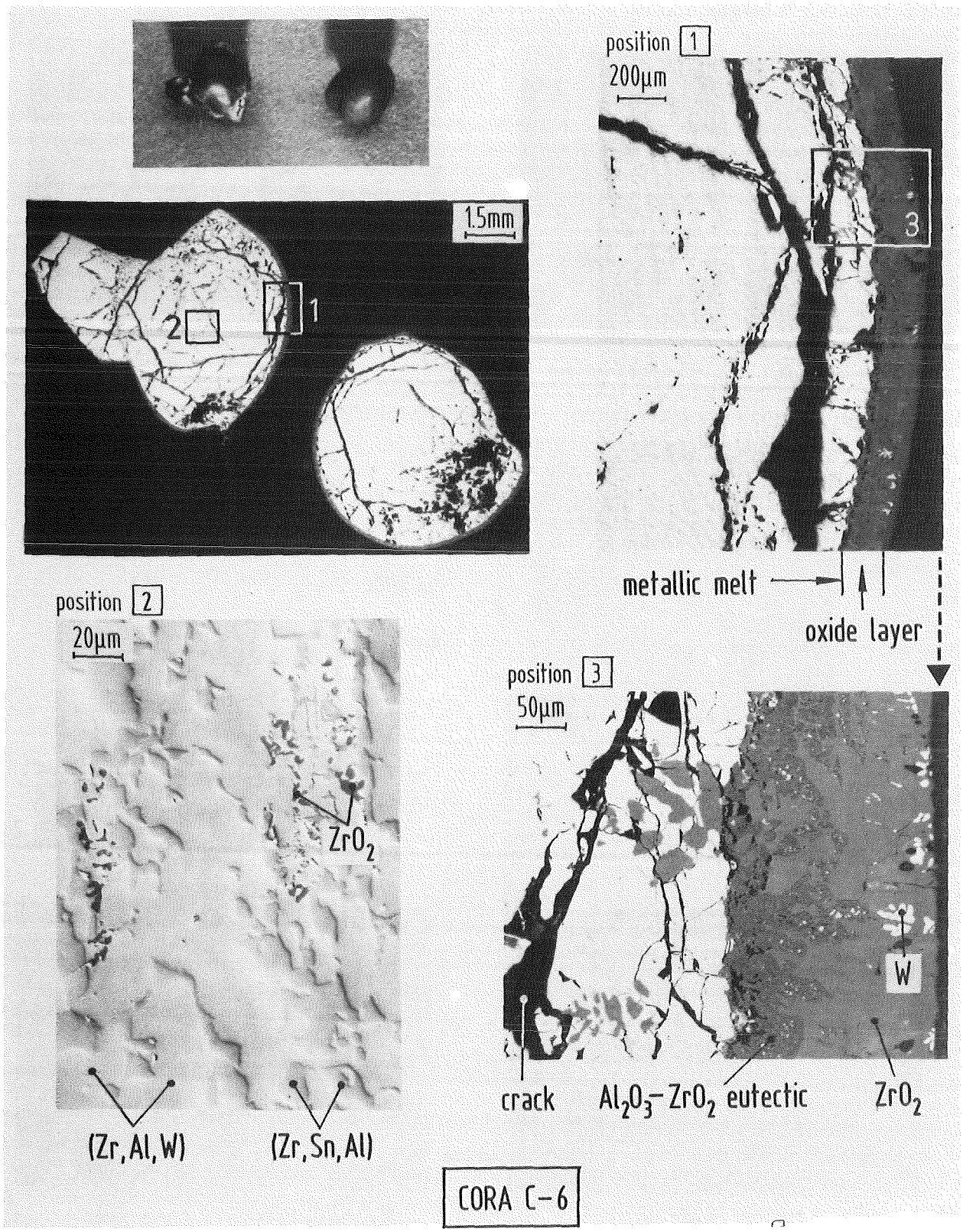


**Fig. 31, Microstructures of molten metallic "droplets" (CORA bundle C)**

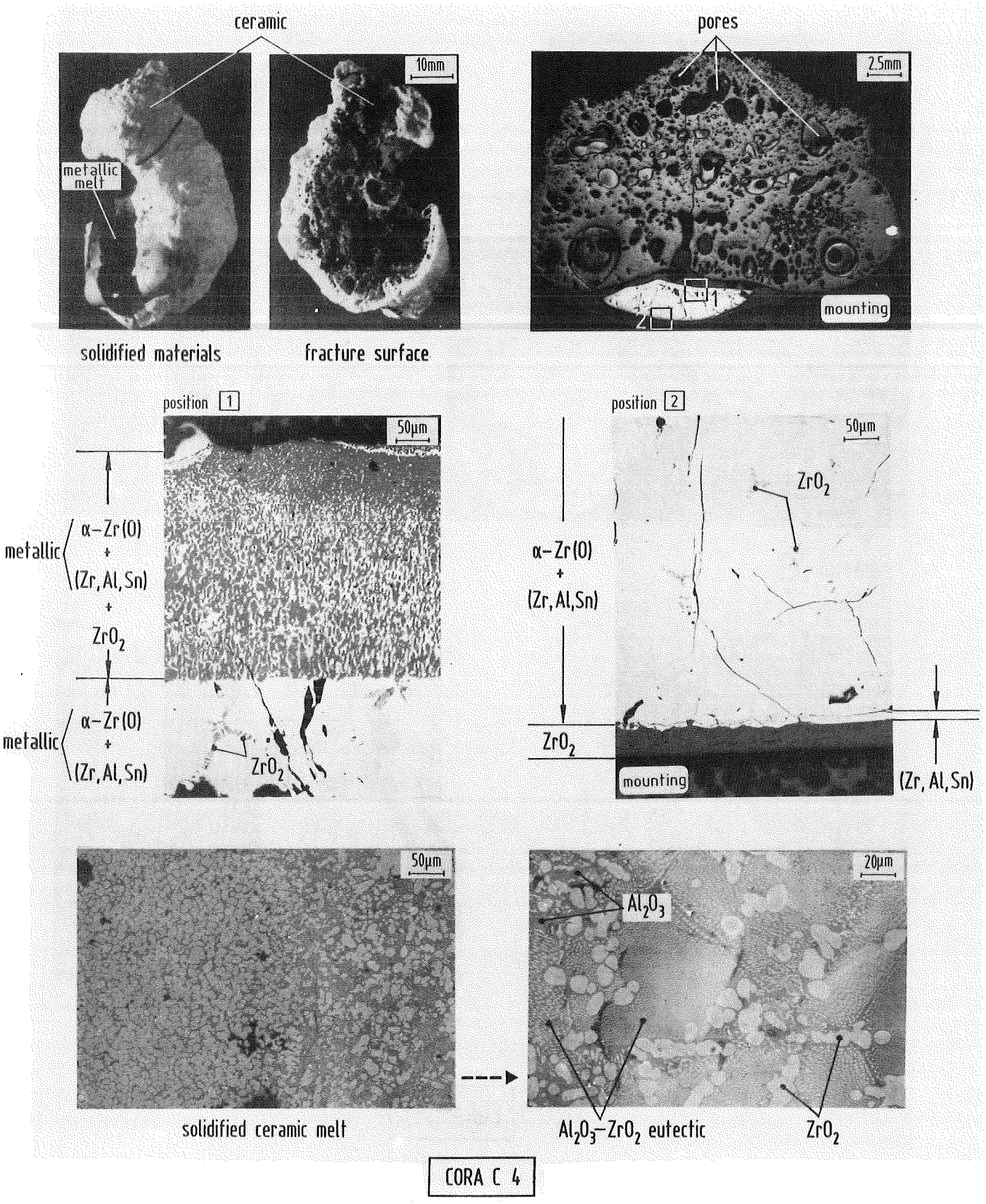


**Fig. 32. Microstructures of a solidified ceramic and metallic melt (CORA bundle C, 4)**

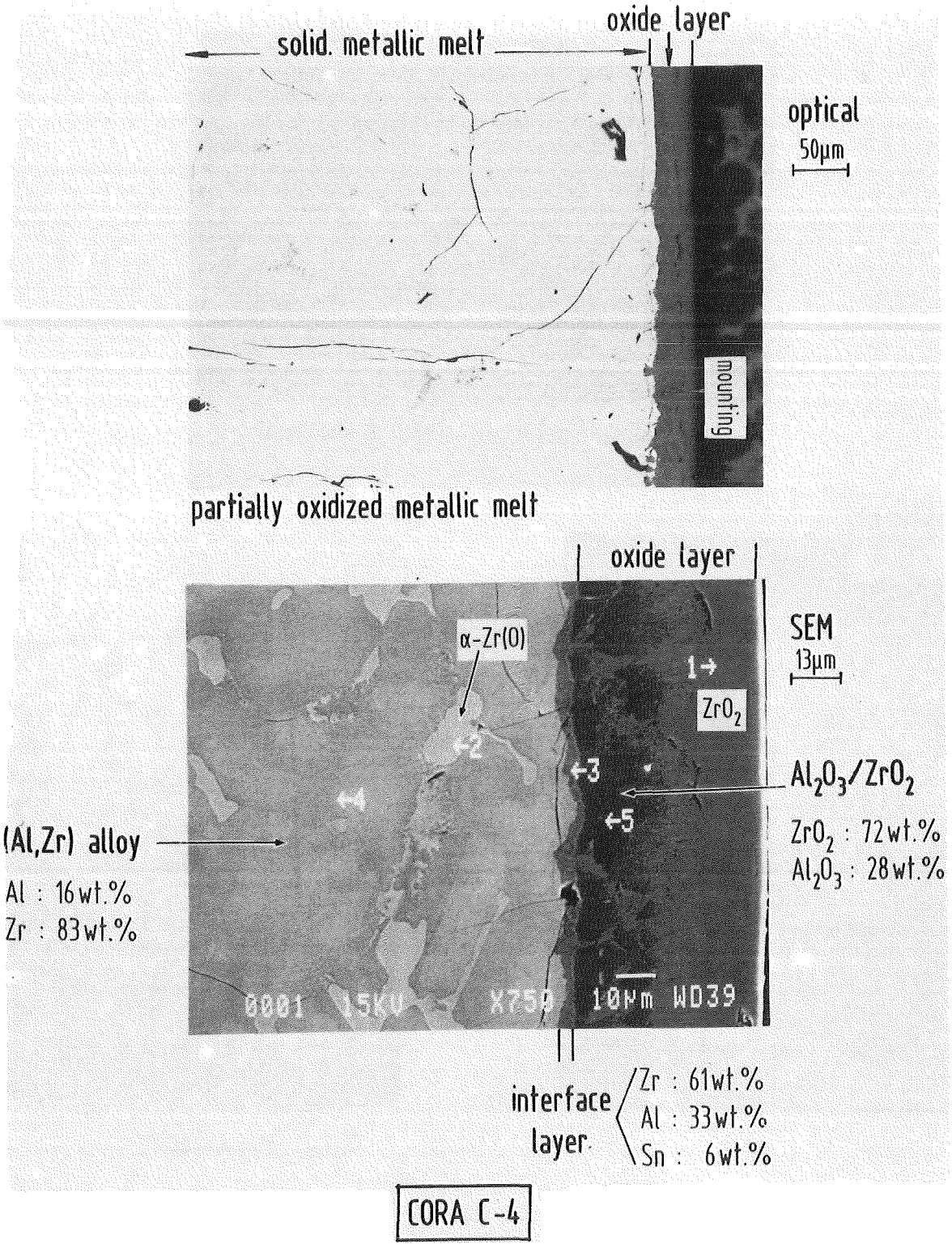


**Fig. 33. Microstructure of solidified metallic melt (CORA bundle C)**

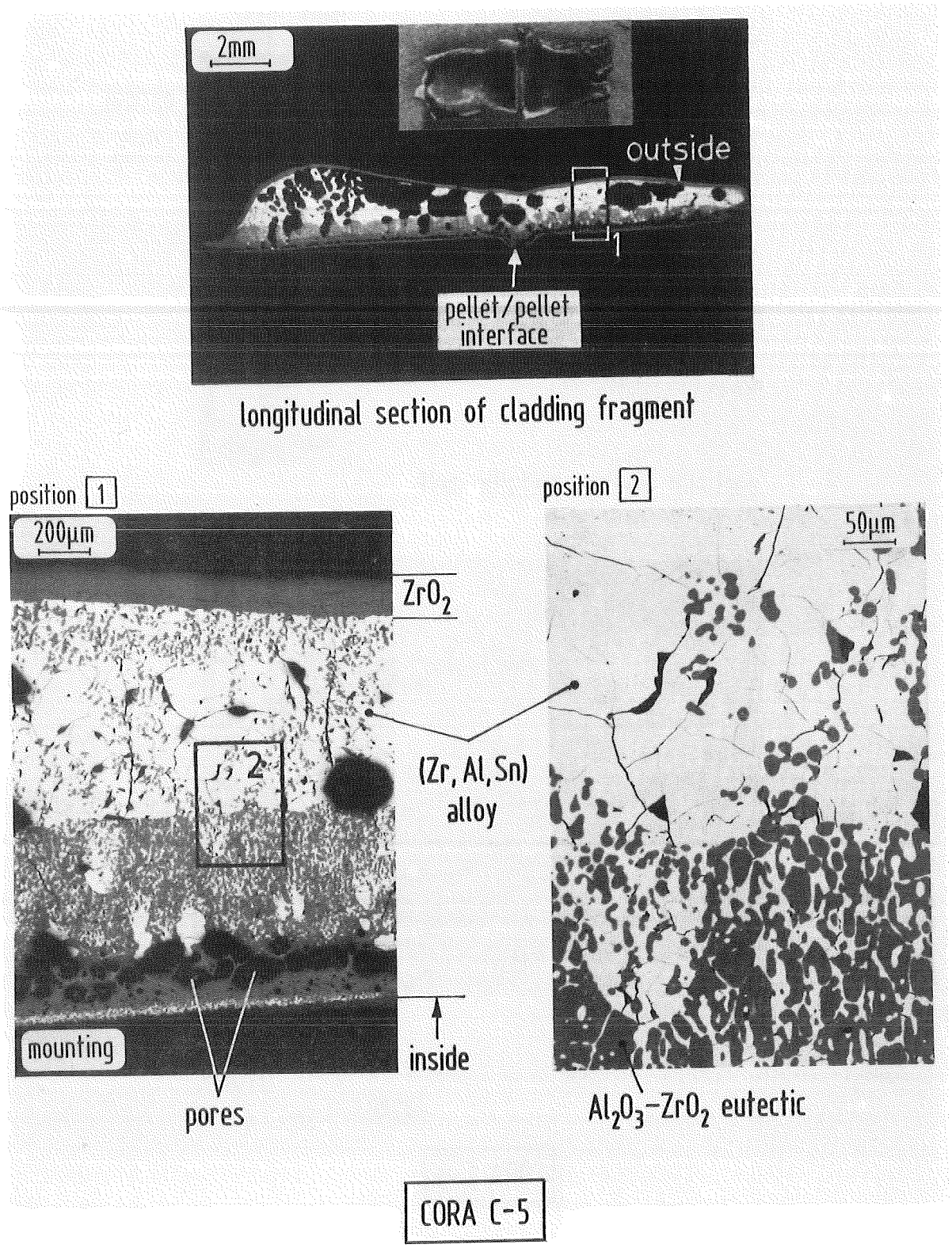


**Fig. 34. Microstructures of molten cladding fragment (CORA bundle C)**

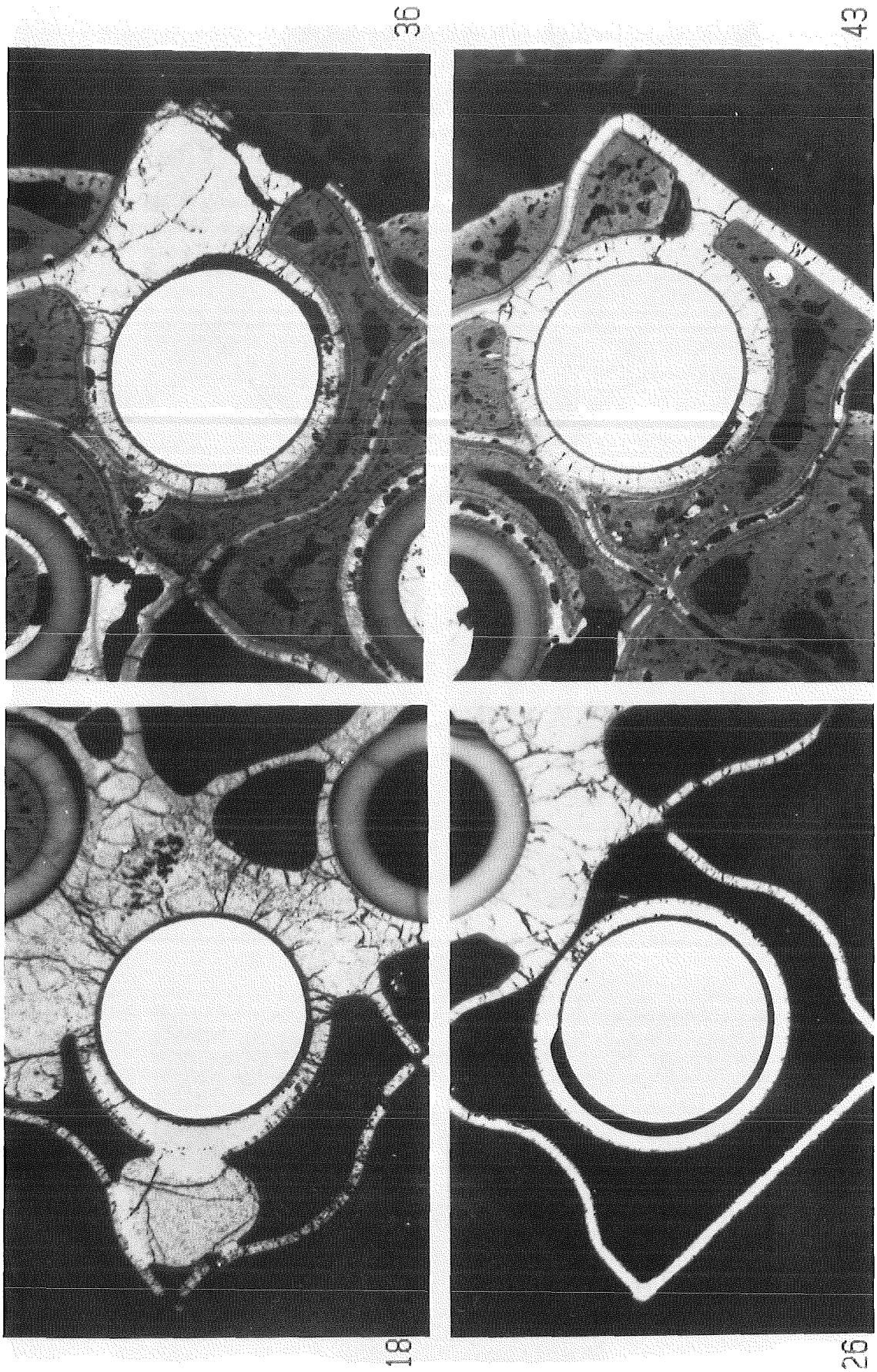


Fig. 35. Enlarged cross sections of heated rods at -71 mm elevation (CORA bundle B)

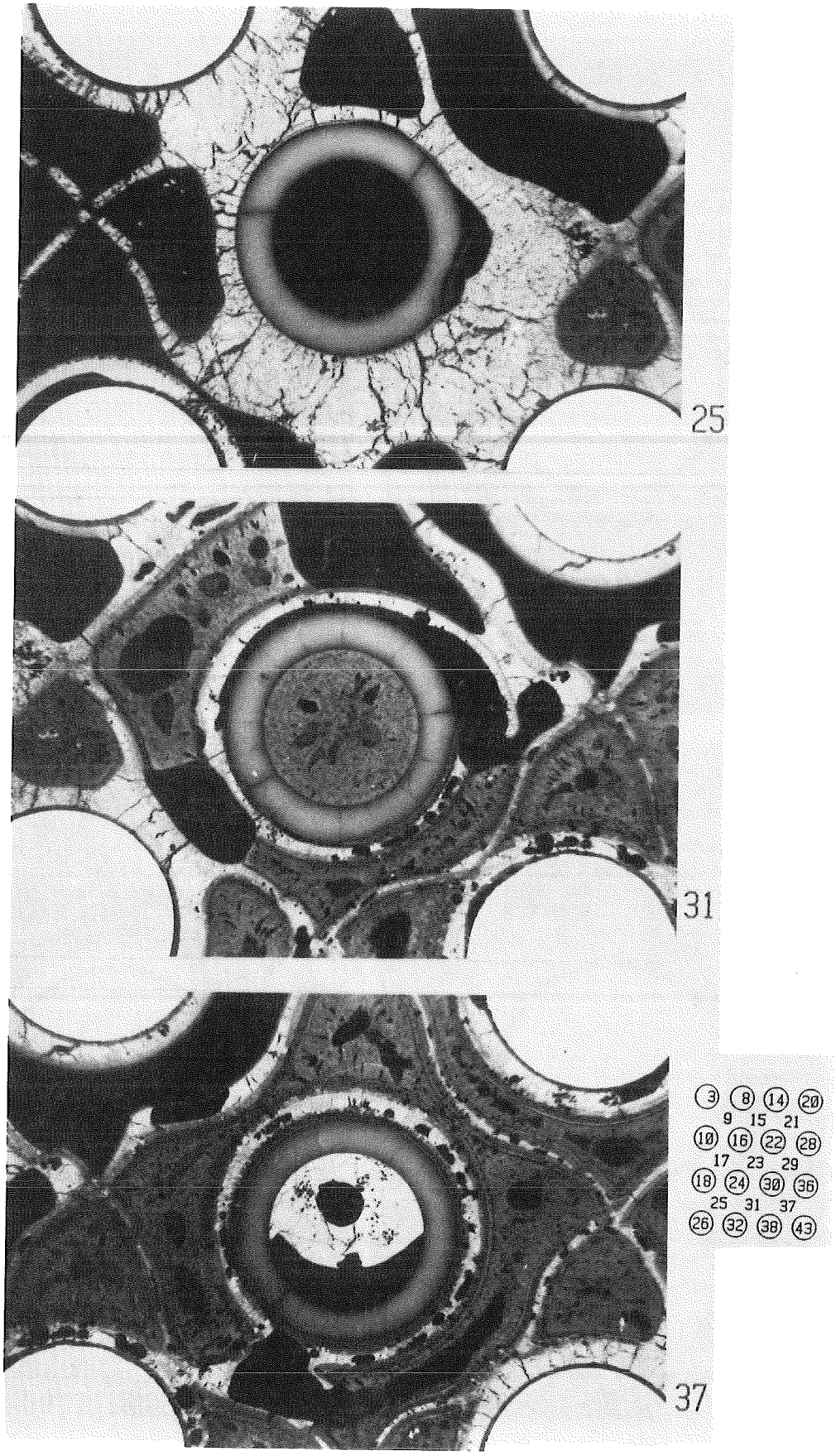


**Fig. 36. Enlarged cross sections in region of unheated rods at -71 mm elevation (CORA bundle B)**

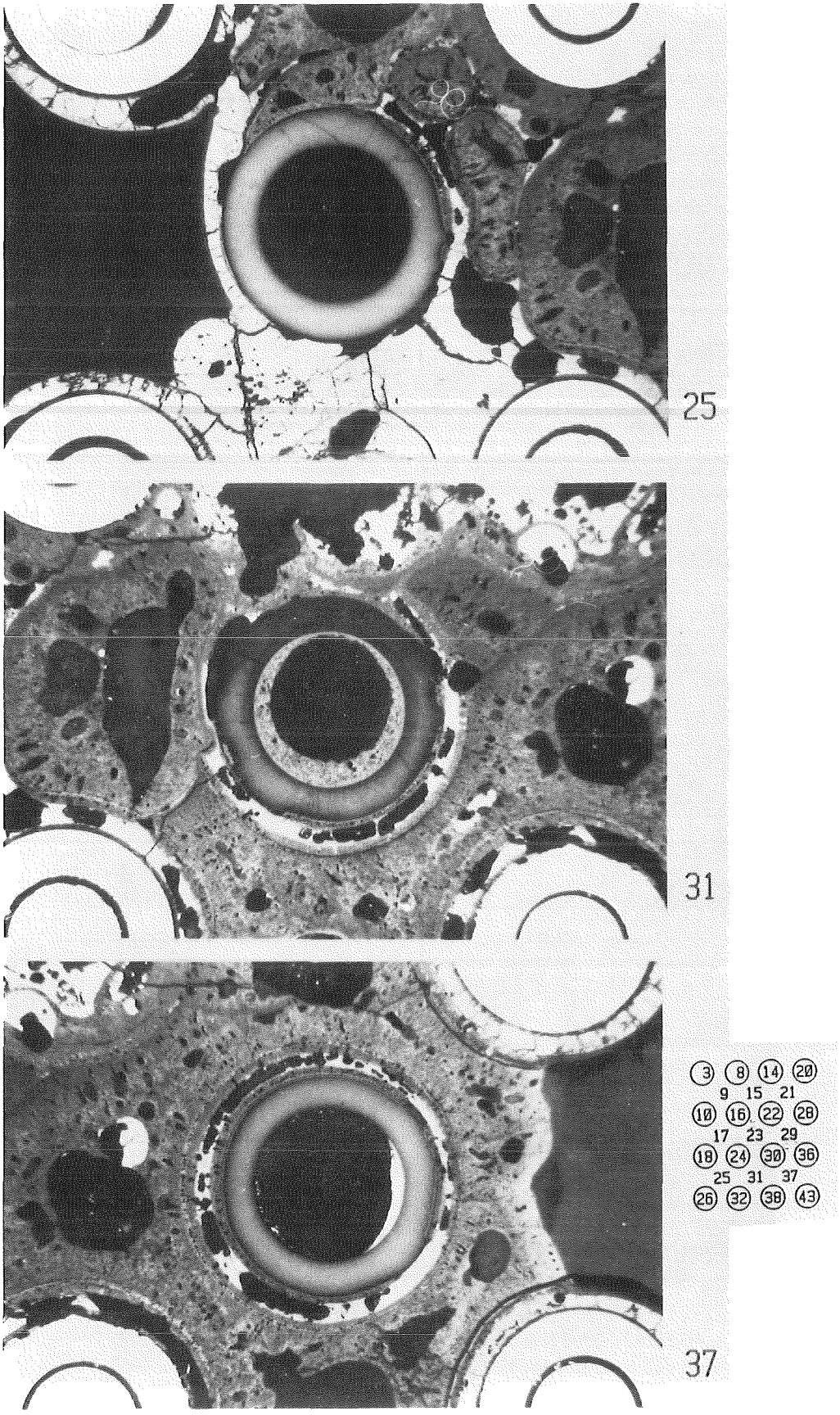


Fig. 37. Enlarged cross sections in region of unheated rods at -16 mm elevation (CORA bundle B)

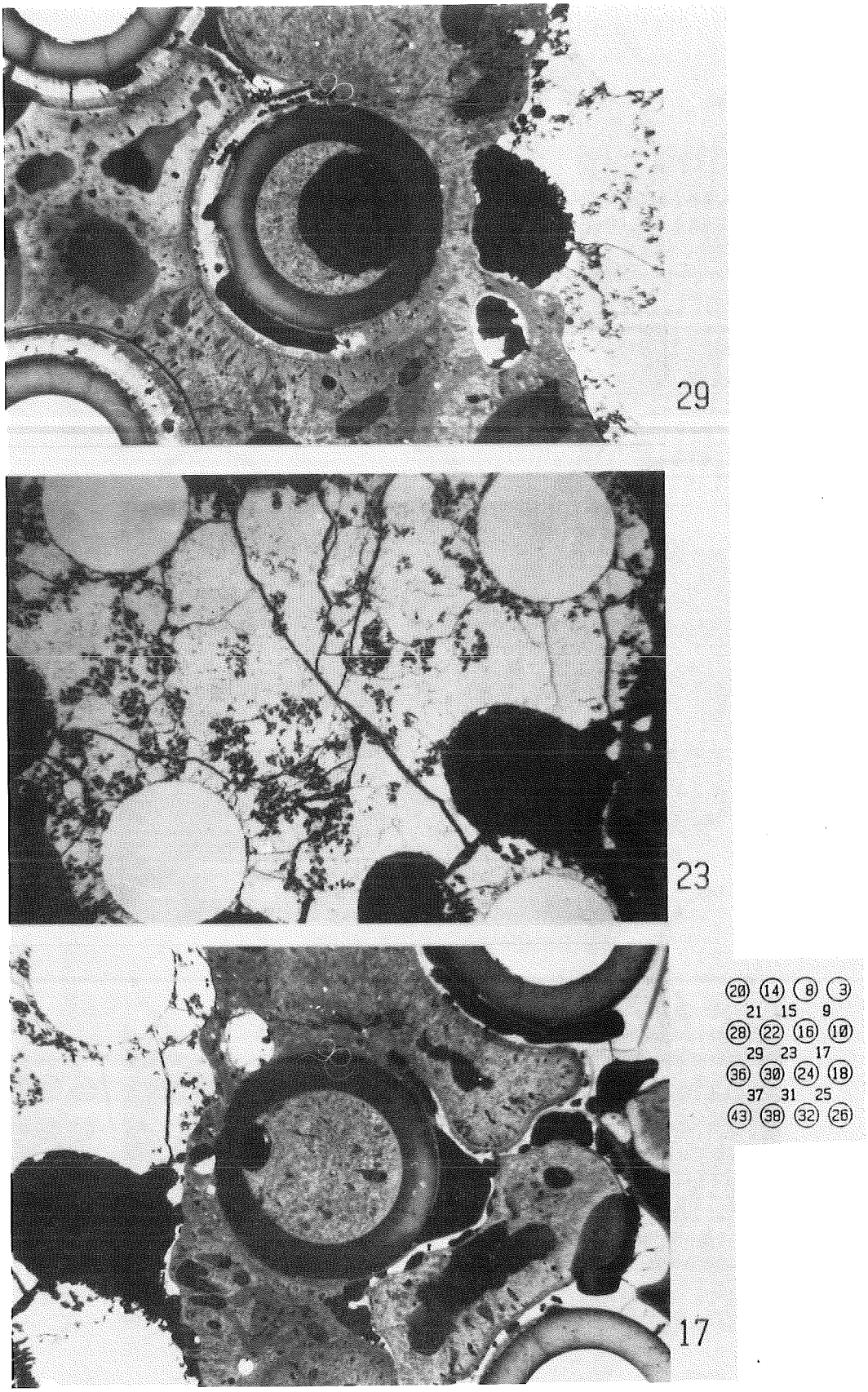


**Fig. 38. Enlarged cross sections in region of unheated rods at 0 mm elevation (CORA bundle B)**

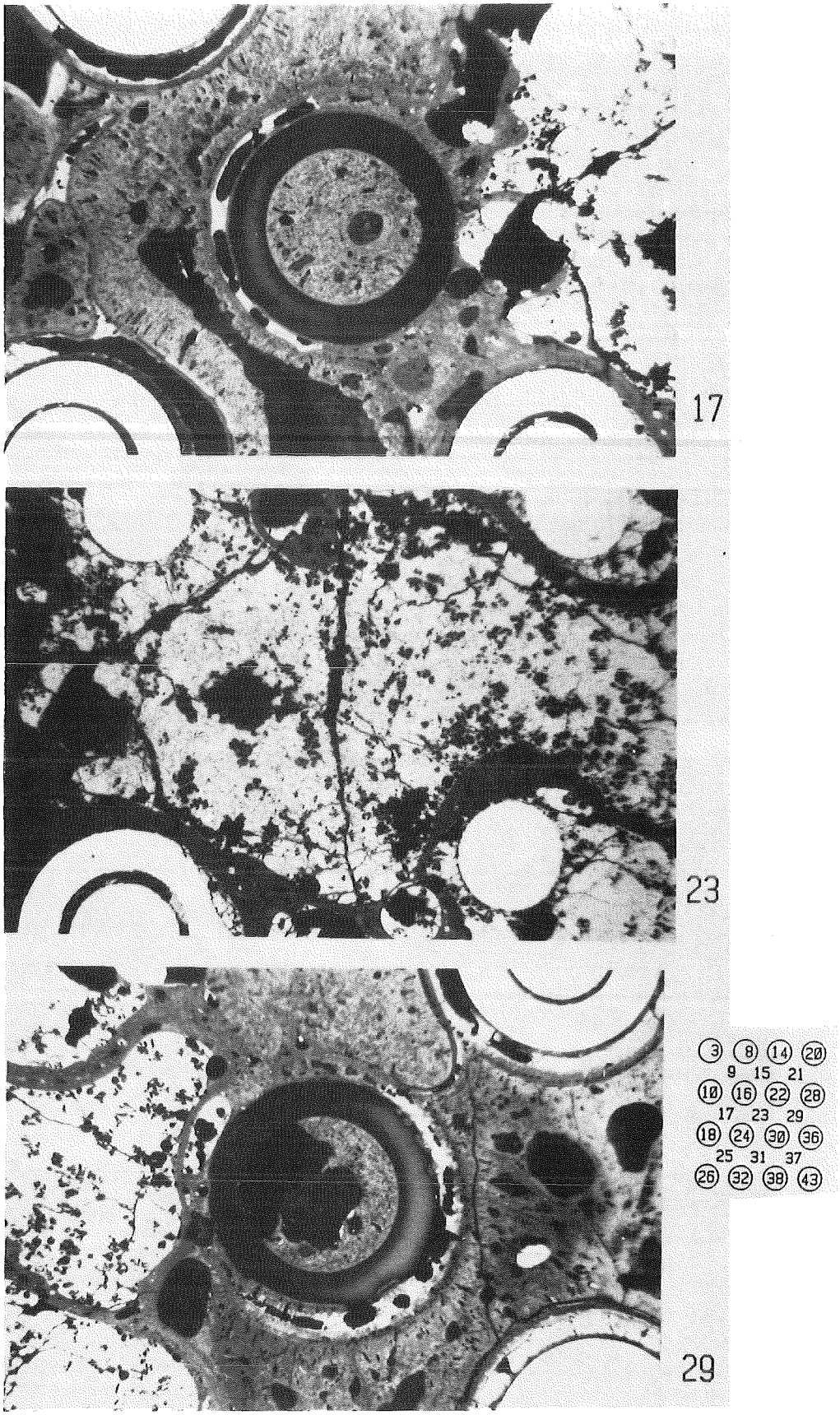


**Fig. 39. Enlarged cross sections in region of unheated rods at -16 mm elevation (CORA bundle B)**

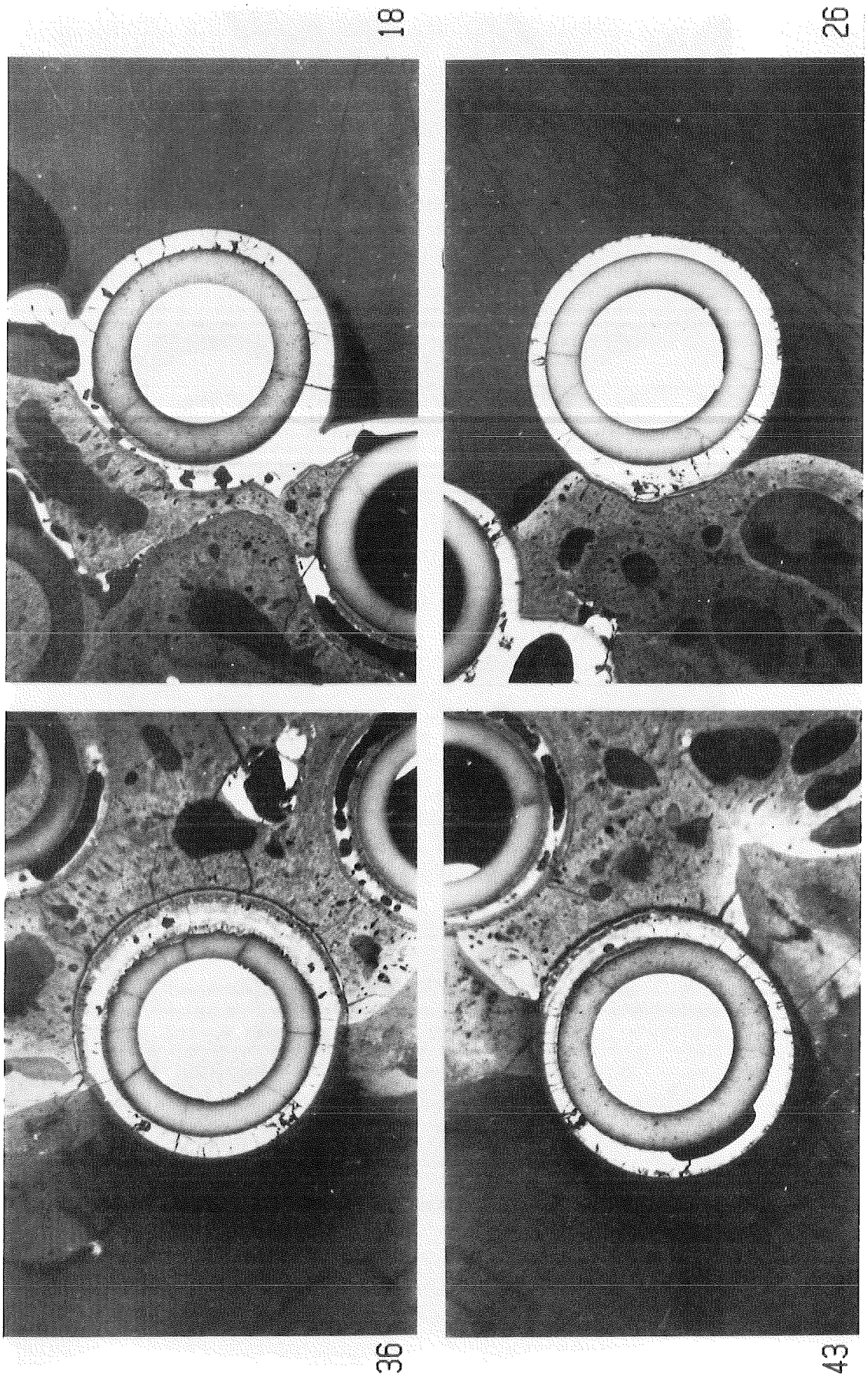


**Fig. 40. Enlarged cross sections of unheated rods at 0 mm elevation (CORA bundle B)**

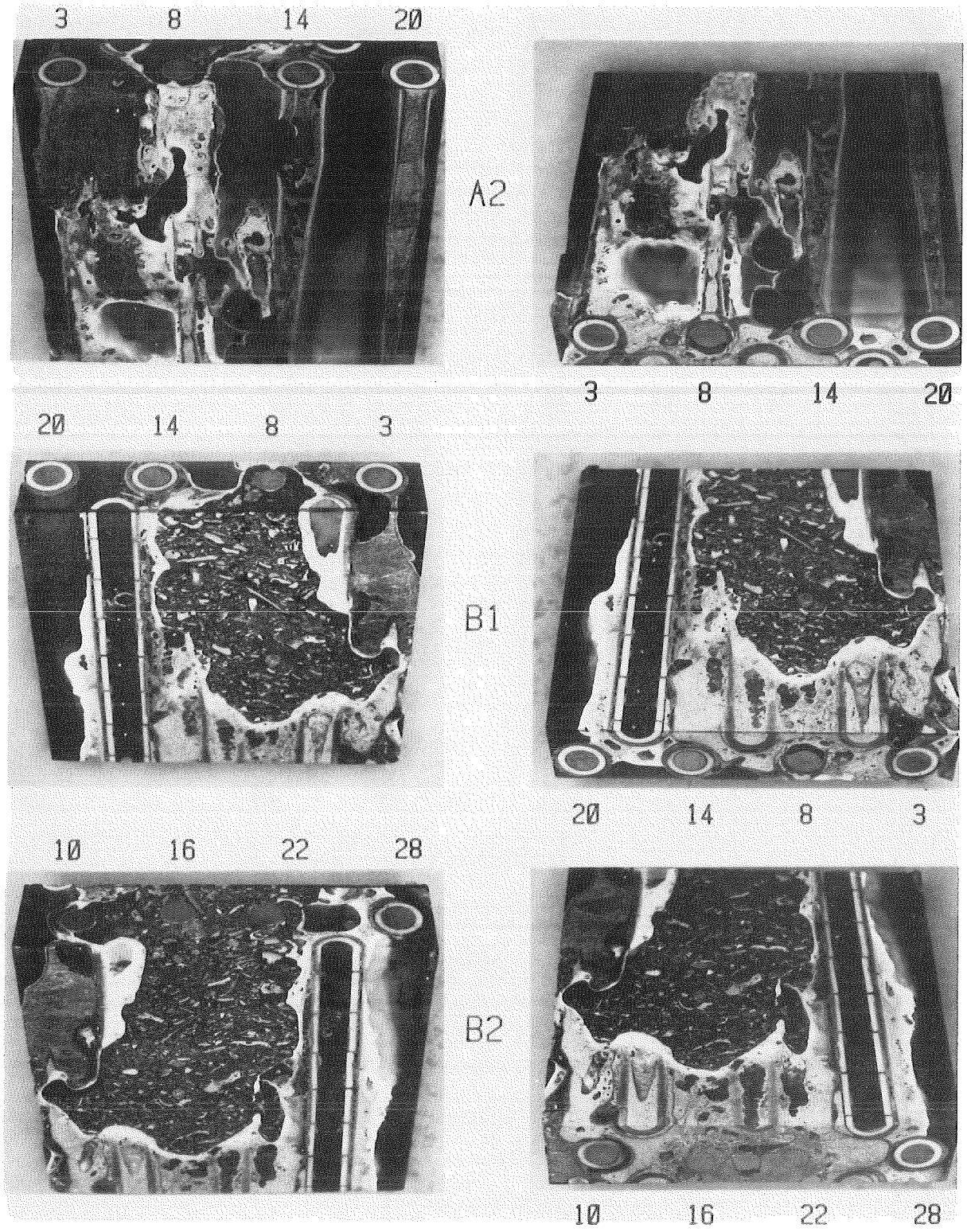


**Fig. 41. Vertical cross sections of CORA bundle B between 1 mm and 73 mm elevation**

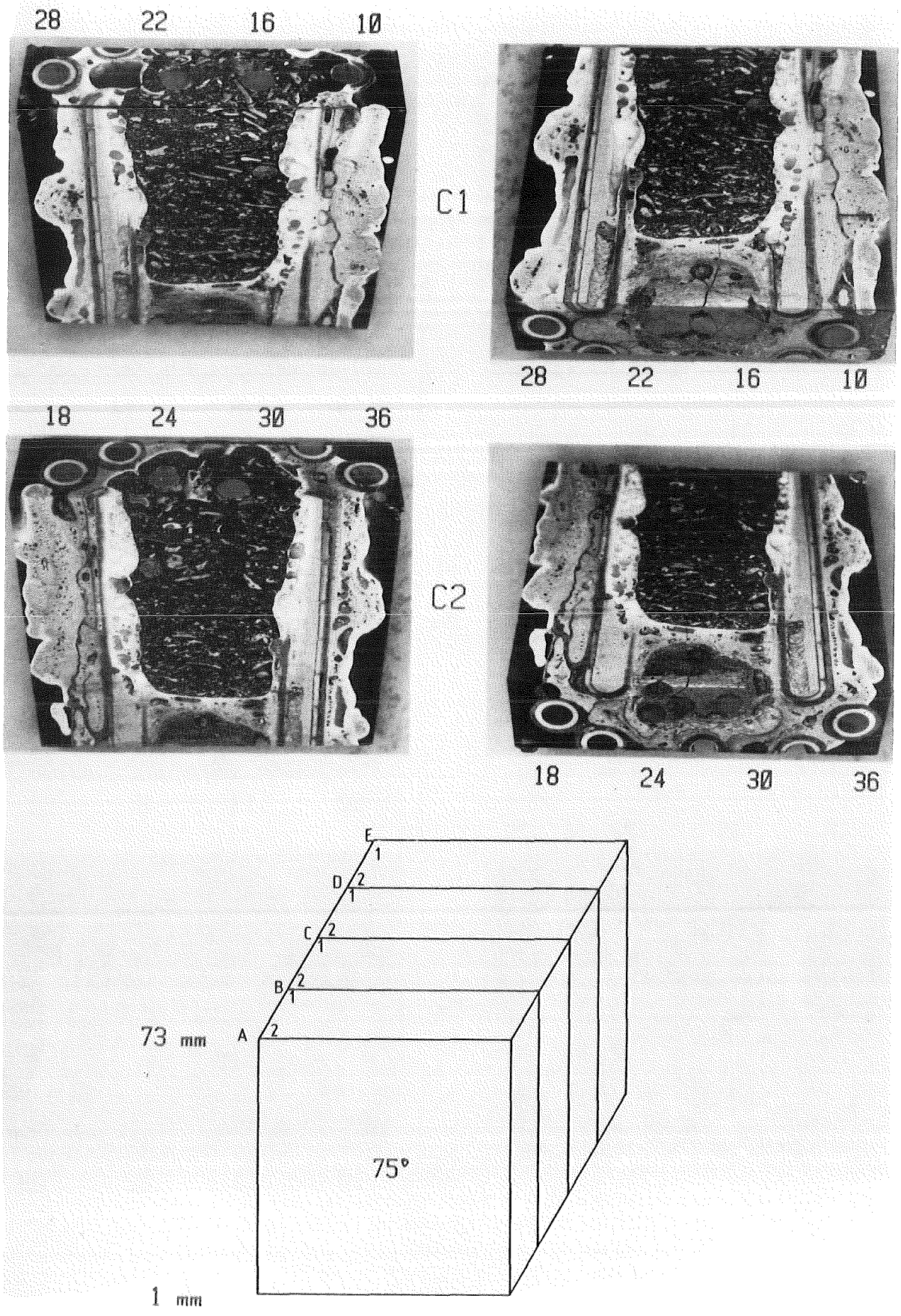


**Fig. 42. Vertical cross sections of CORA bundle B between 1 mm and 73 mm elevation**

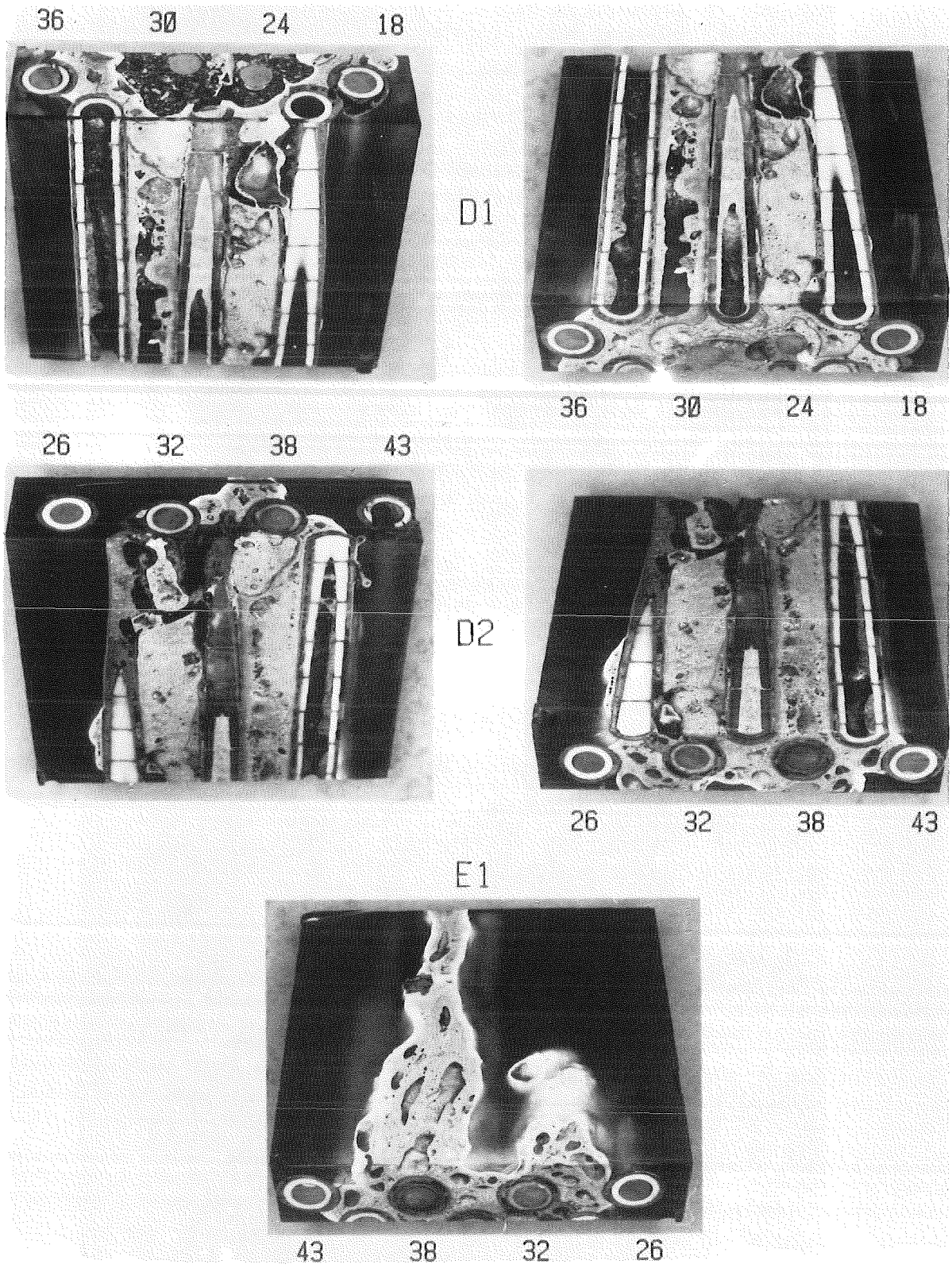


**Fig. 43. Vertical cross sections of CORA bundle B between 1 mm and 73 mm elevation**

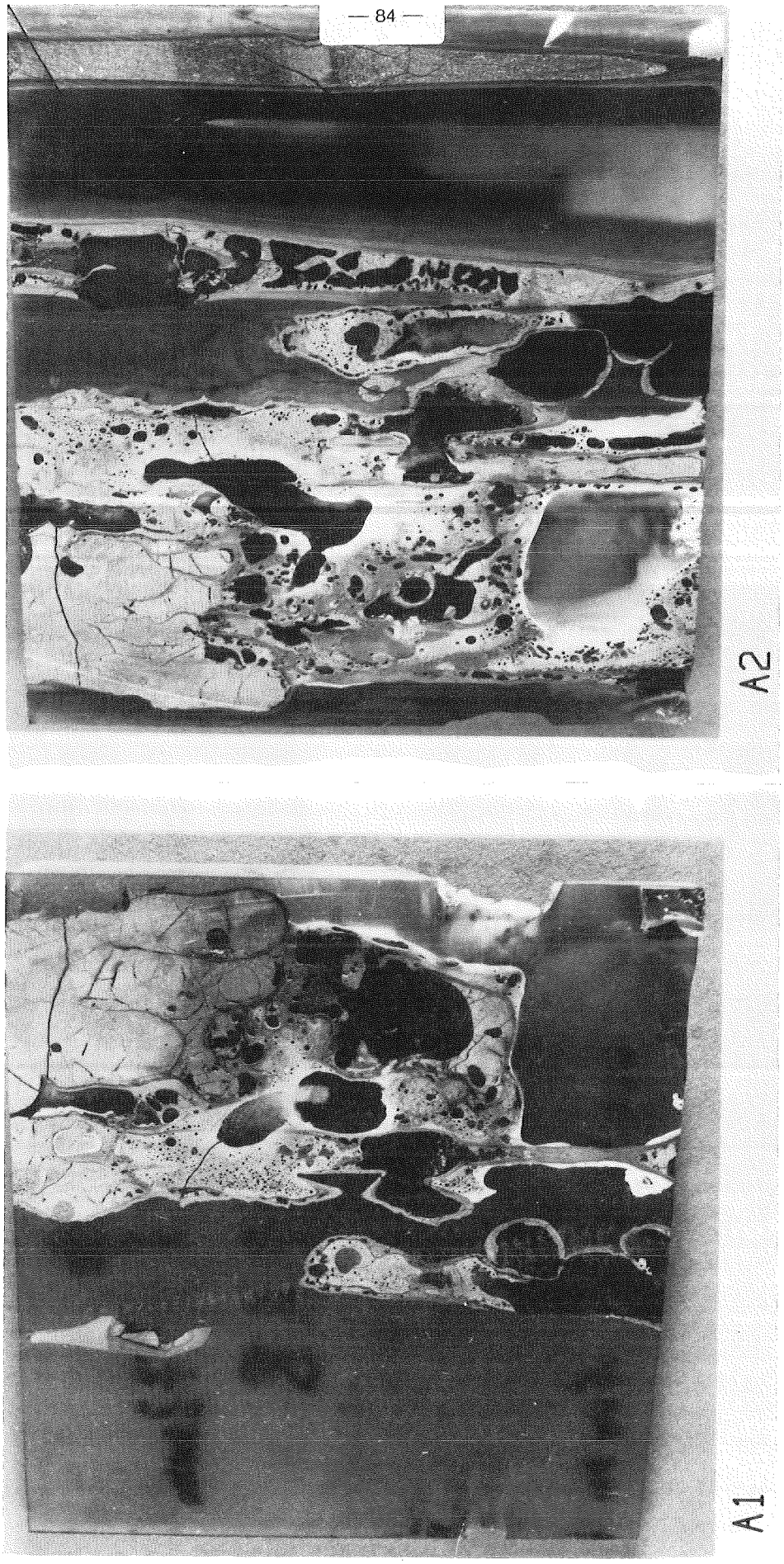


**Fig. 44. Vertical cross sections of CORA bundle B between 1 mm and 73 mm elevation**

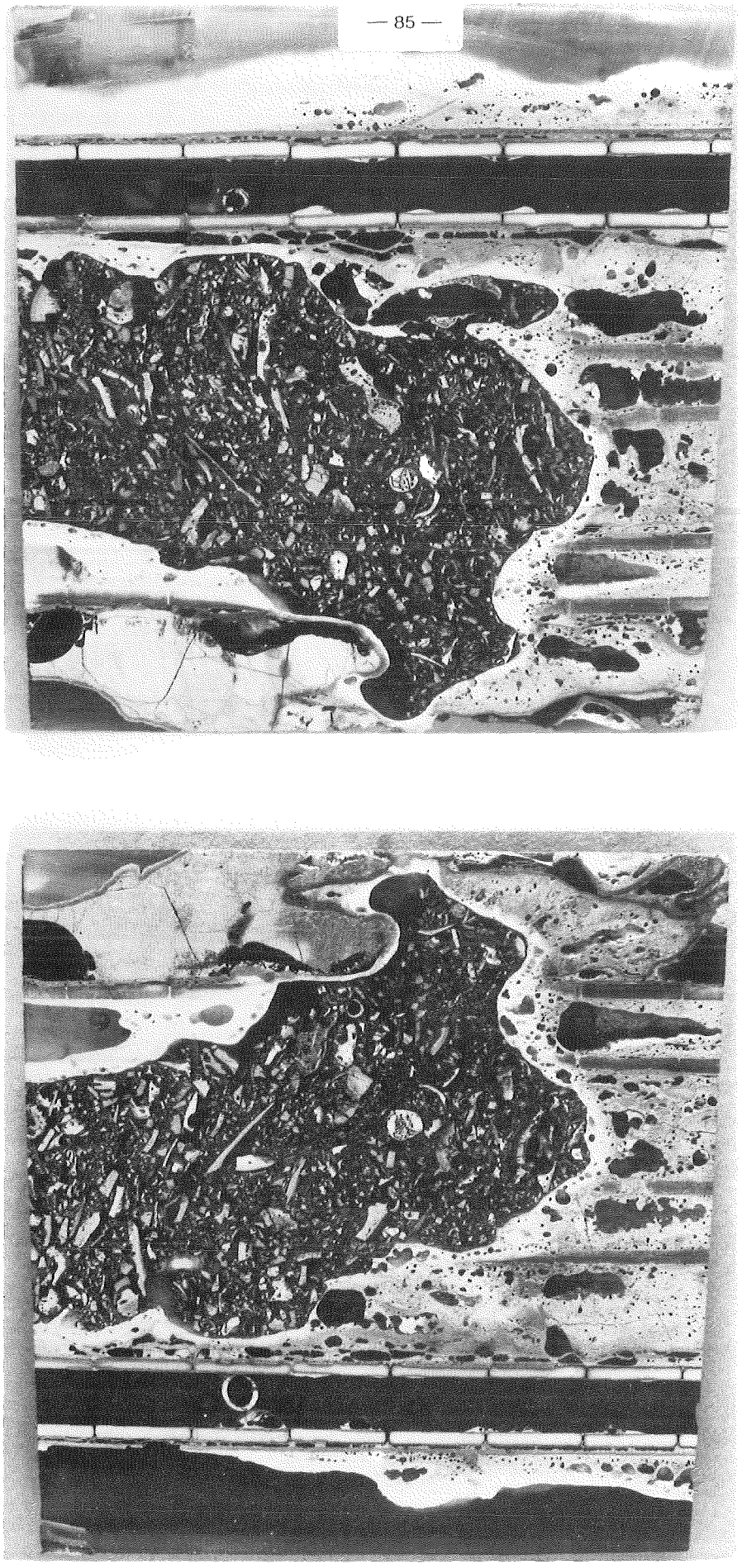


Fig. 45. Vertical cross sections of CORA bundle B between 1 mm and 73 mm elevation

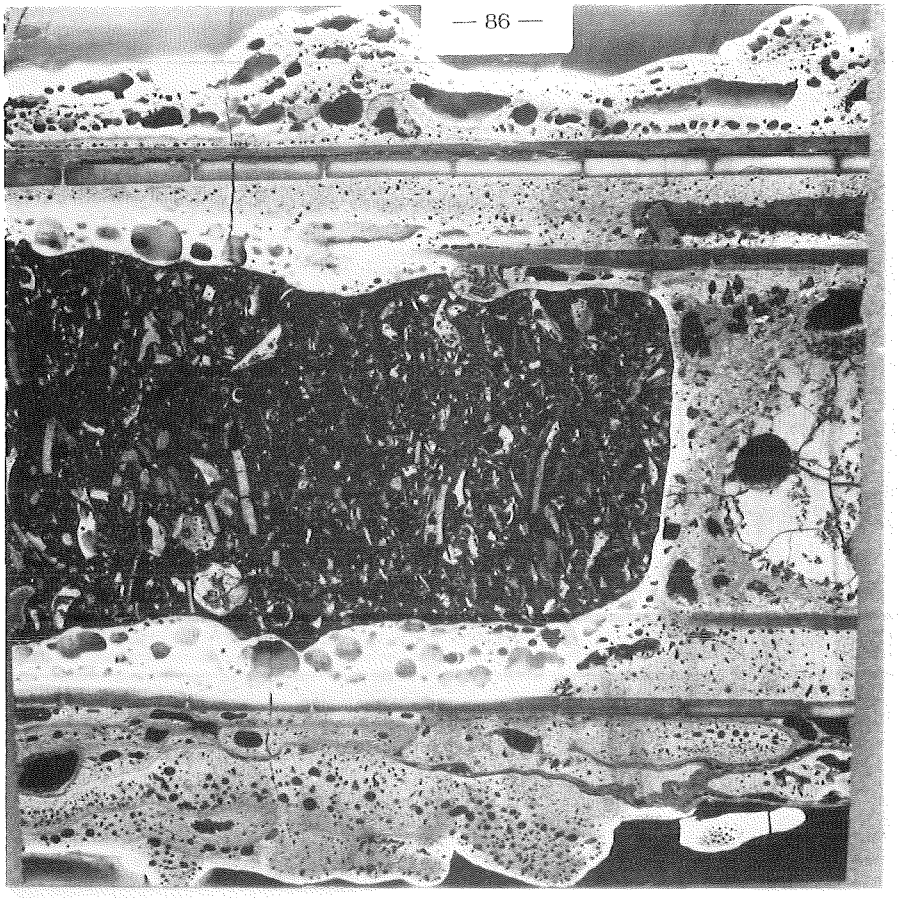

C2

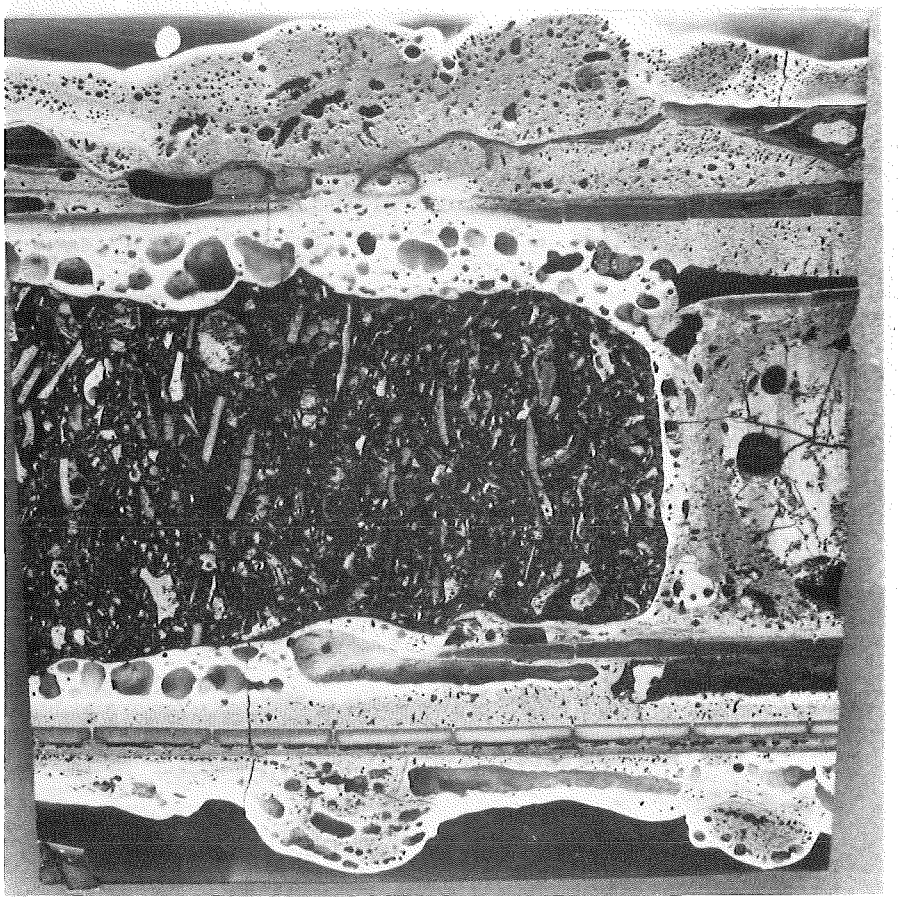

C1

**Fig. 46. Vertical cross sections of CORA bundle B between 1 mm and 73 mm elevation**

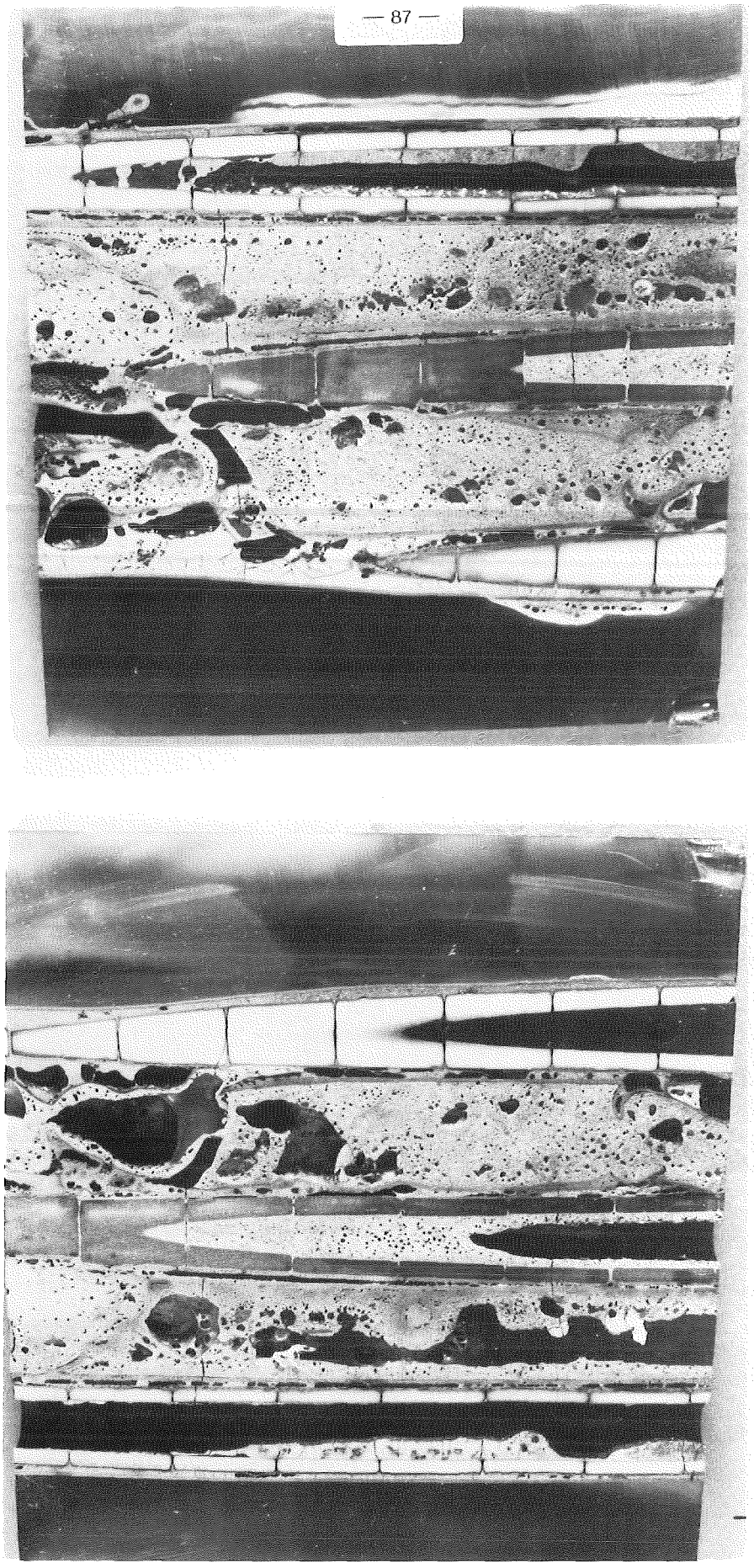


Fig. 47. Vertical cross sections of CORA bundle B between 1 mm and 73 mm elevation

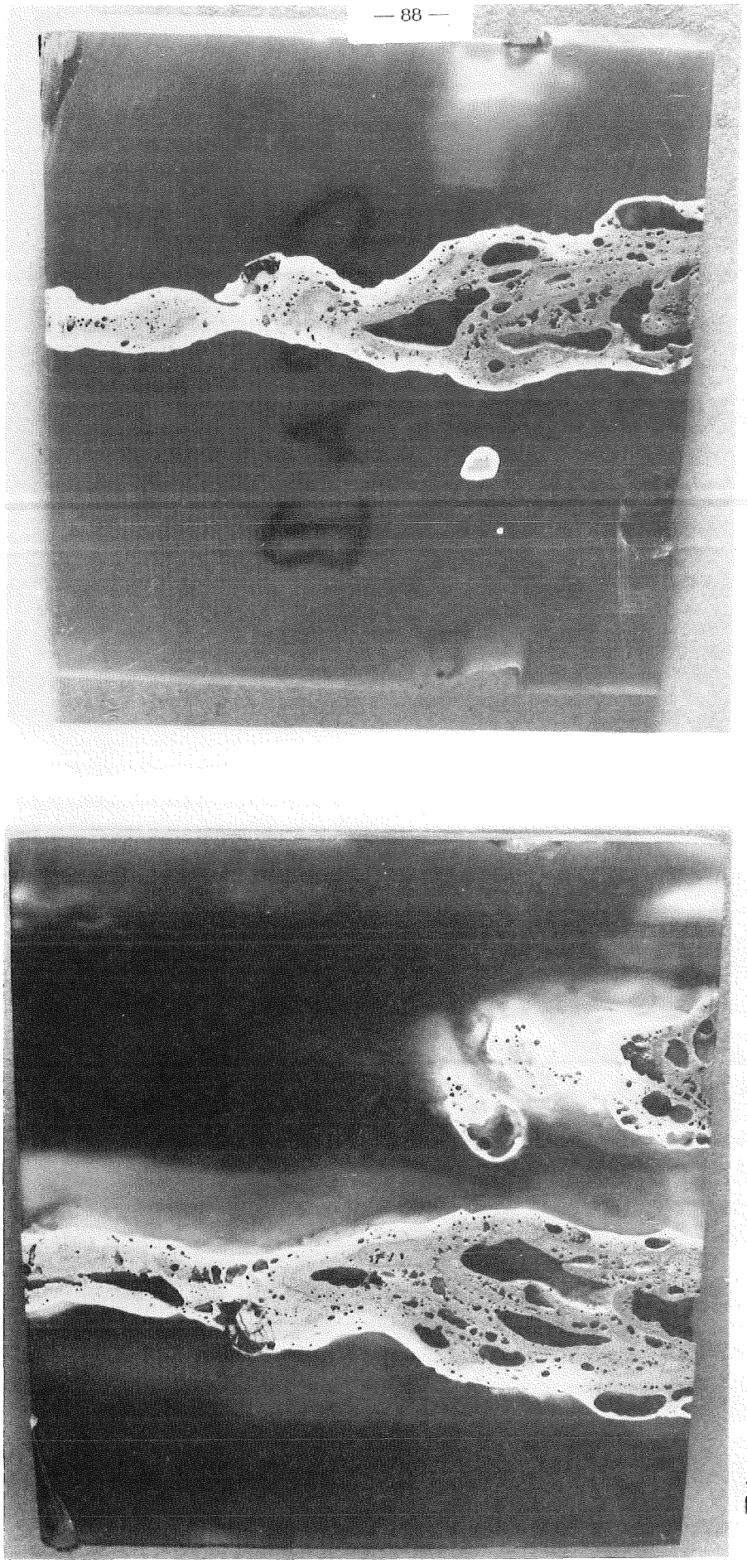


**Fig. 48. Vertical cross sections of CORA bundle B between 1 mm and 73 mm elevation**

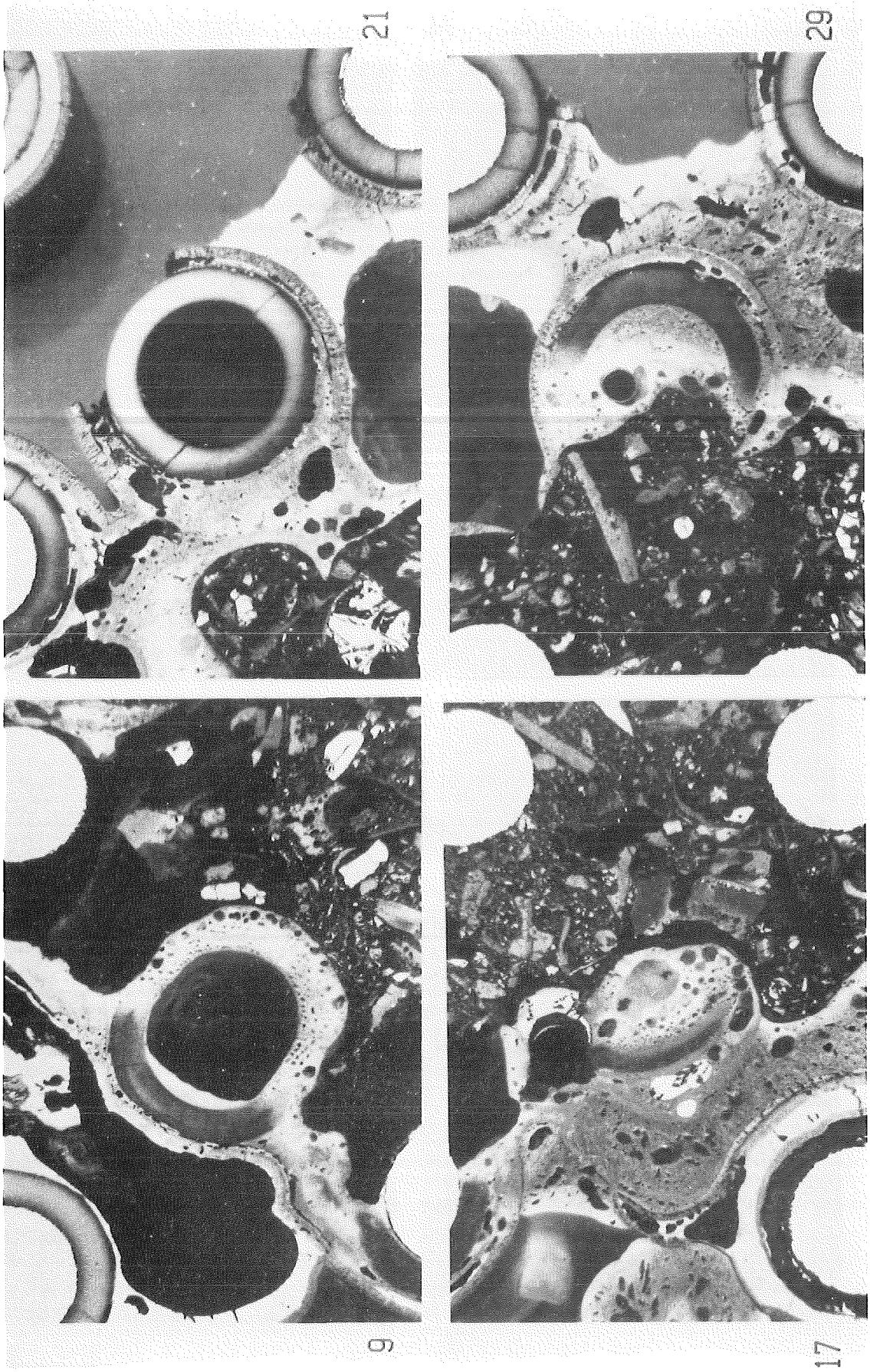


**Fig. 49.** Enlarged cross sections in region of unheated rods at 75 mm elevation (CORA bundle B)

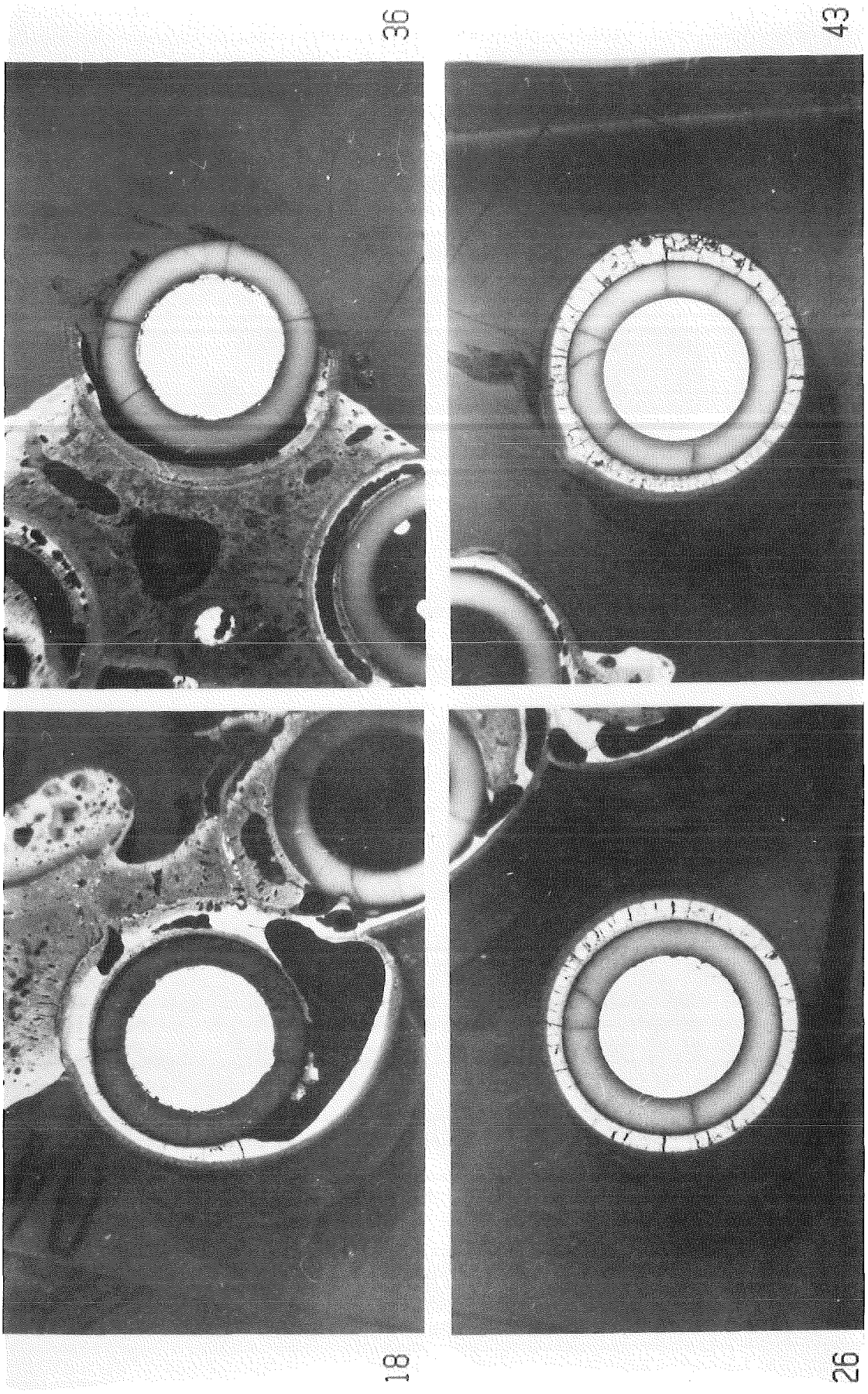


**Fig. 50. Enlarged cross sections of heated rods at 92 mm elevation (CORA bundle B)**

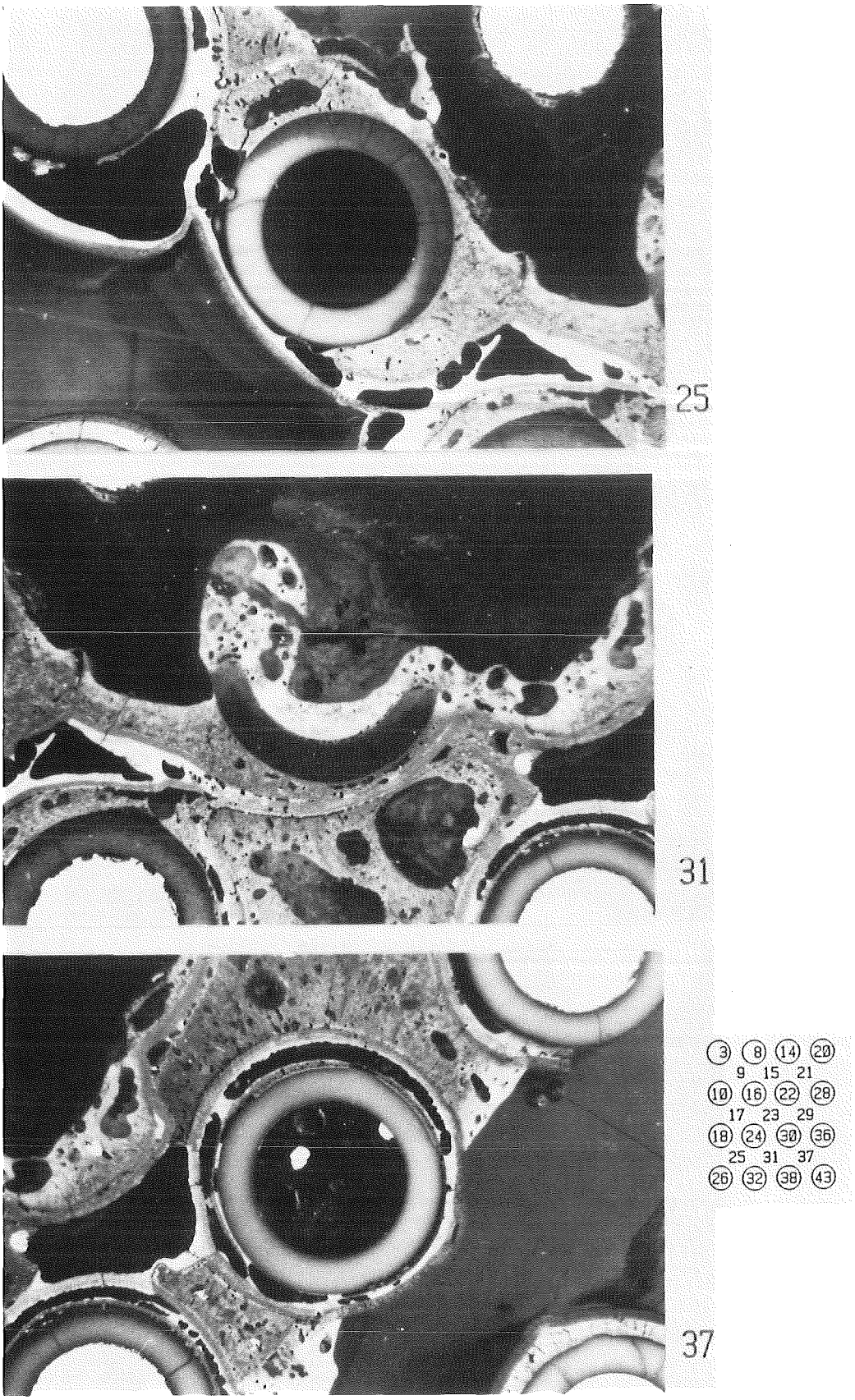


**Fig. 51. Enlarged cross sections in region of unheated rods at 93 mm elevation (CORA bundle B)**

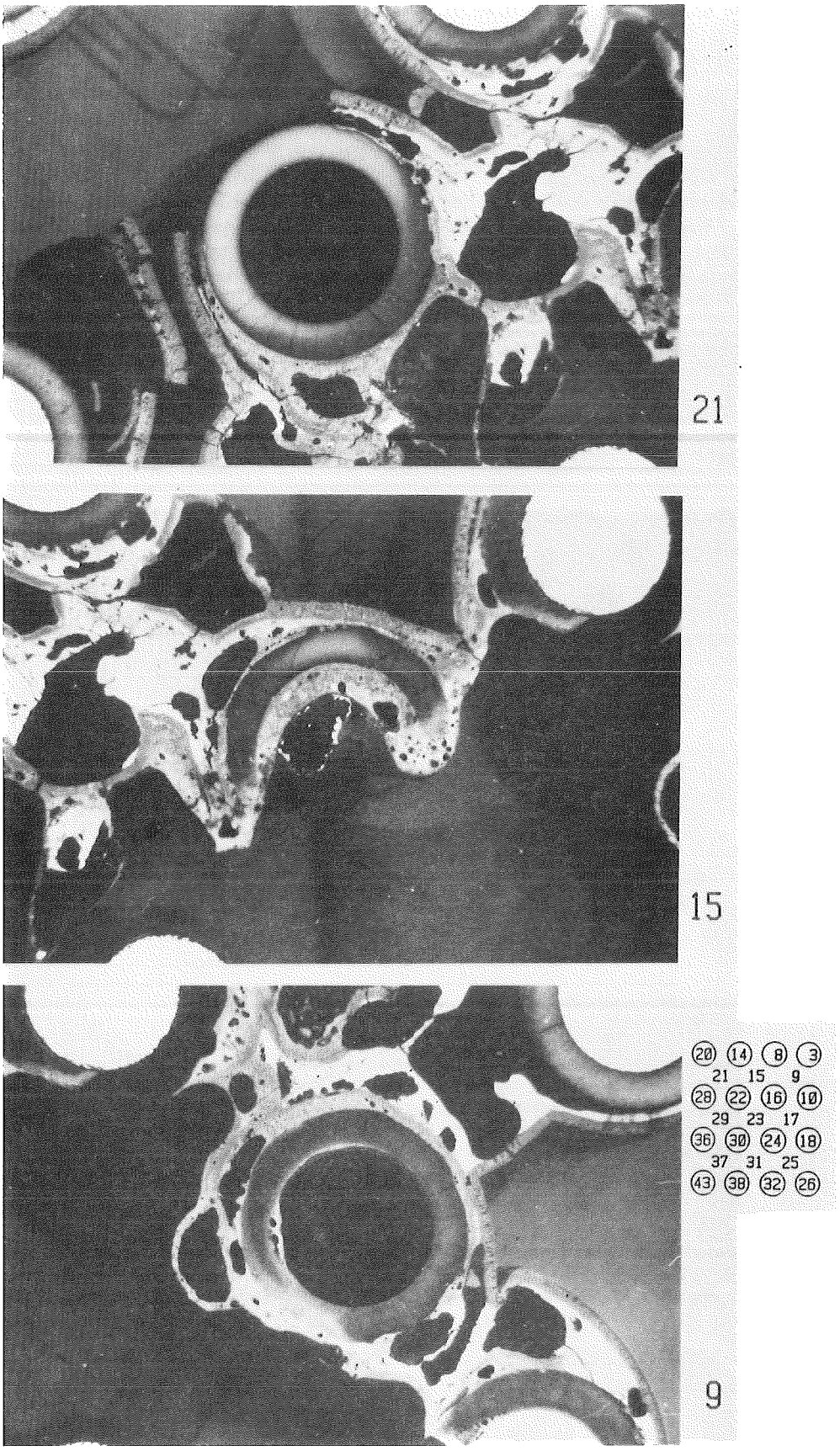


**Fig. 52.** Enlarged cross sections in region of unheated rods at 109 mm elevation (CORA bundle B)

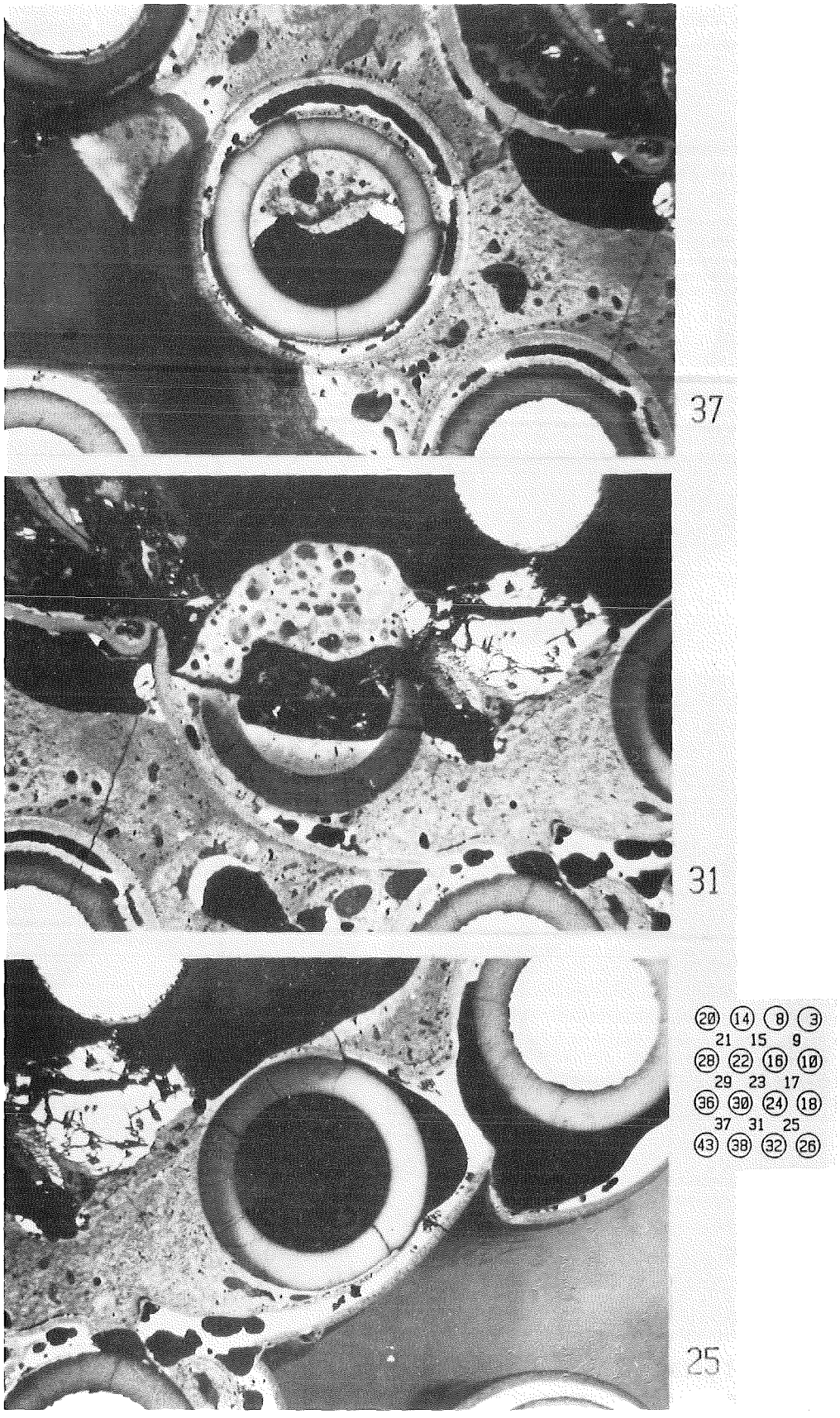


**Fig. 53. Enlarged cross sections in region of unheated rods at 109 mm elevation (CORA bundle B)**

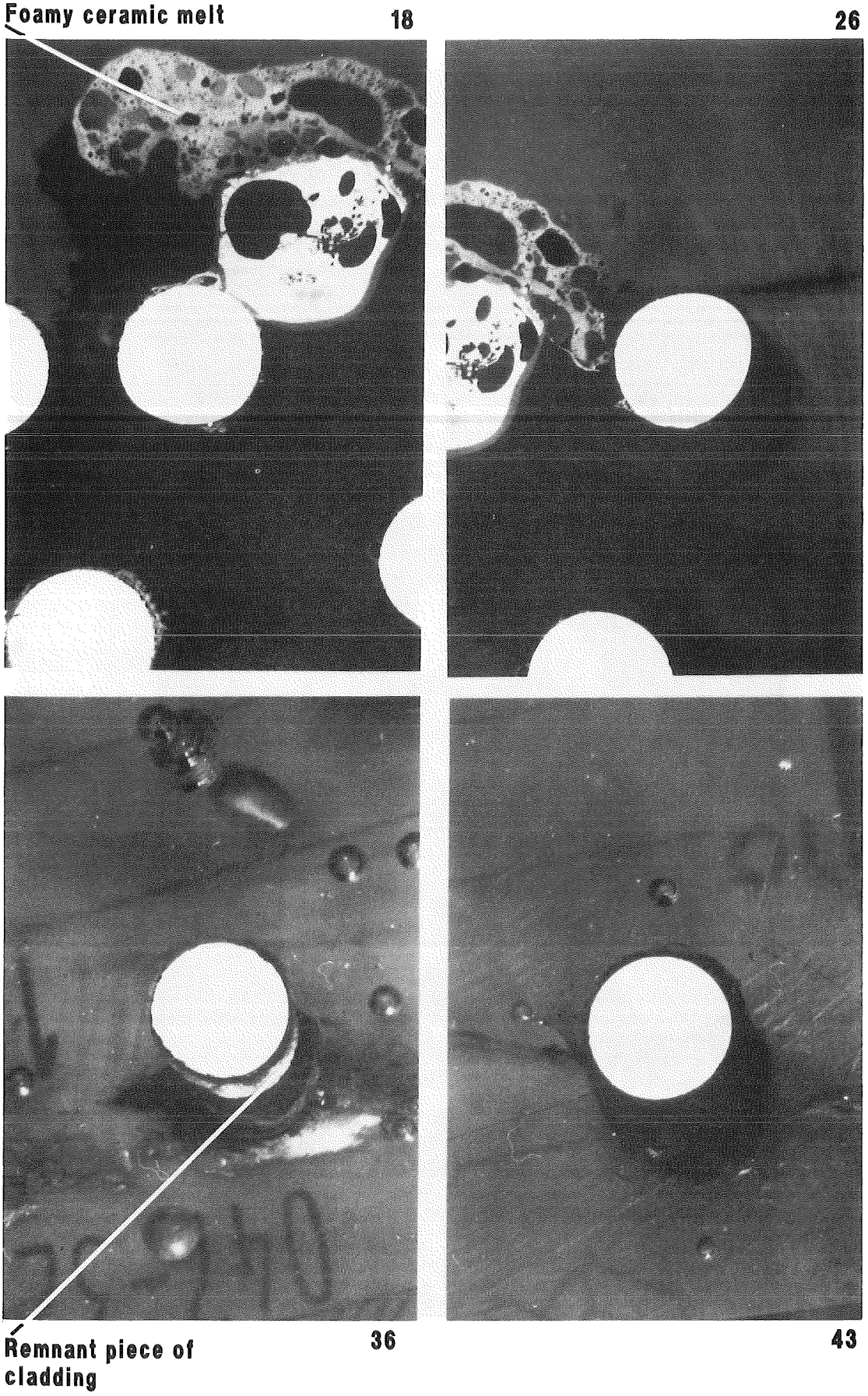


Fig. 54. Enlarged cross sections of heated rods at 507 mm elevation (CORA bundle B)

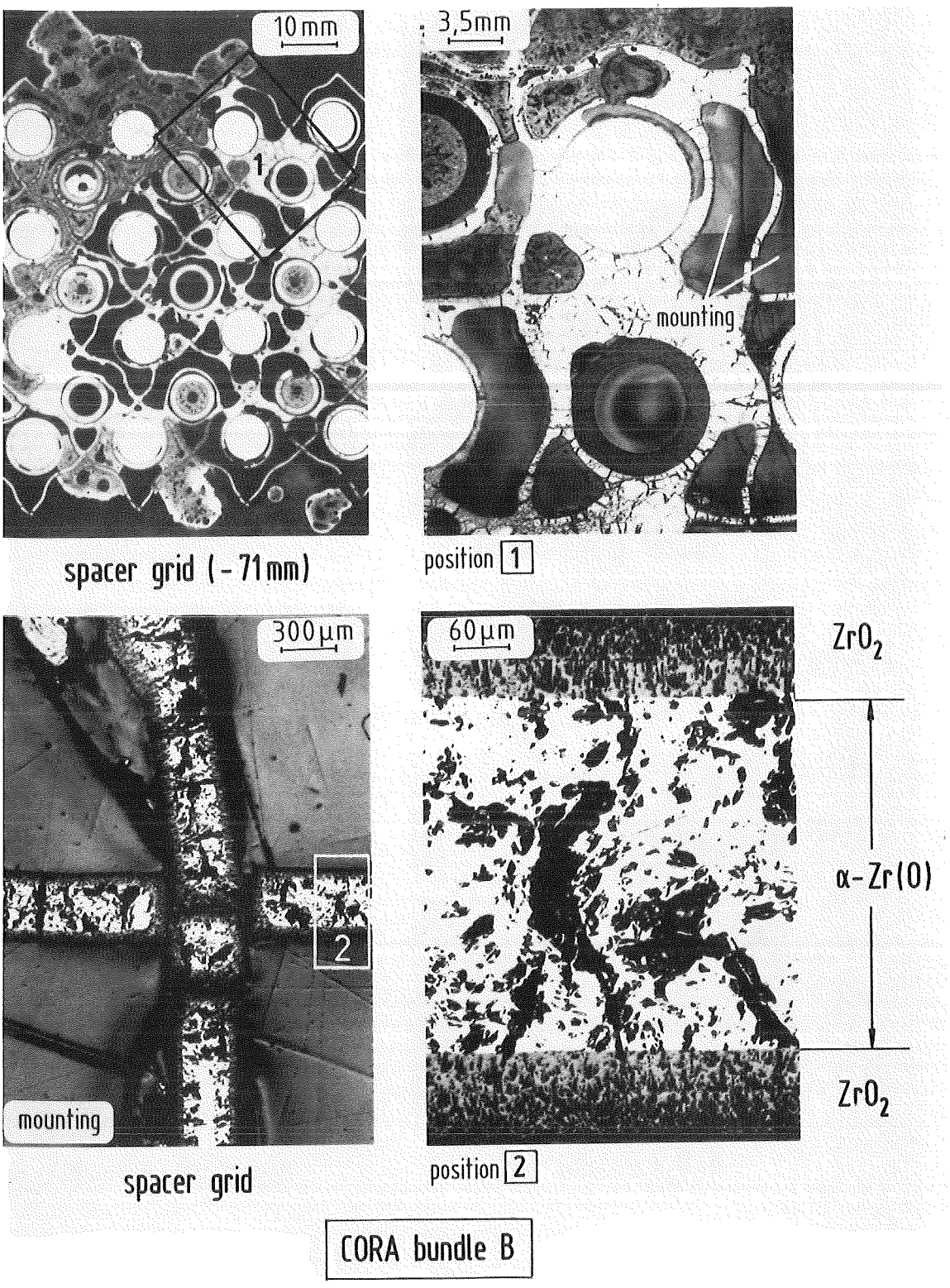


Fig. 55. CORA bundle cross-section B 4 (- 71 mm)

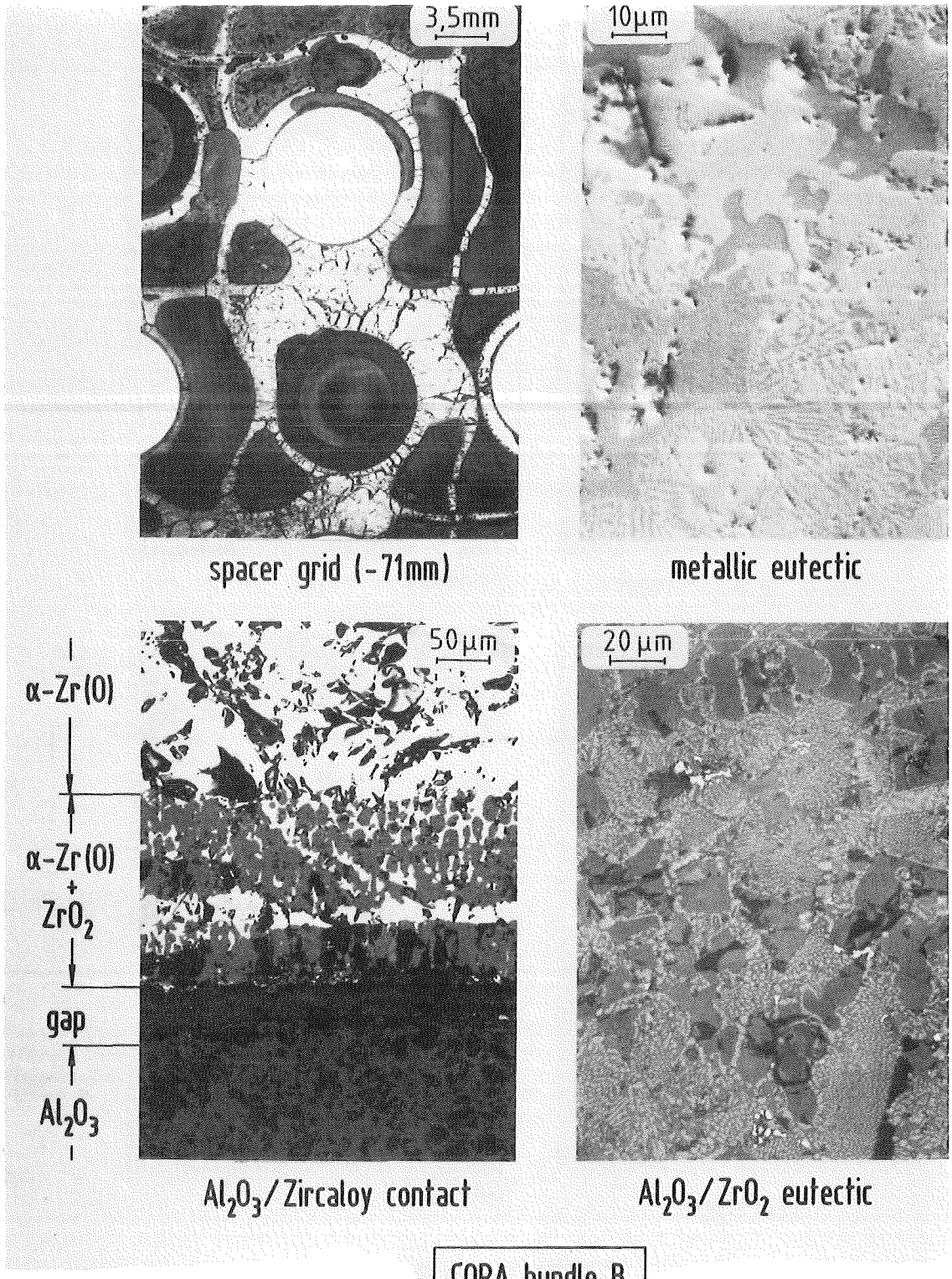


**Fig. 56. Microstructures of the. CORA bundle cross-section B 4 (- 71 mm)**

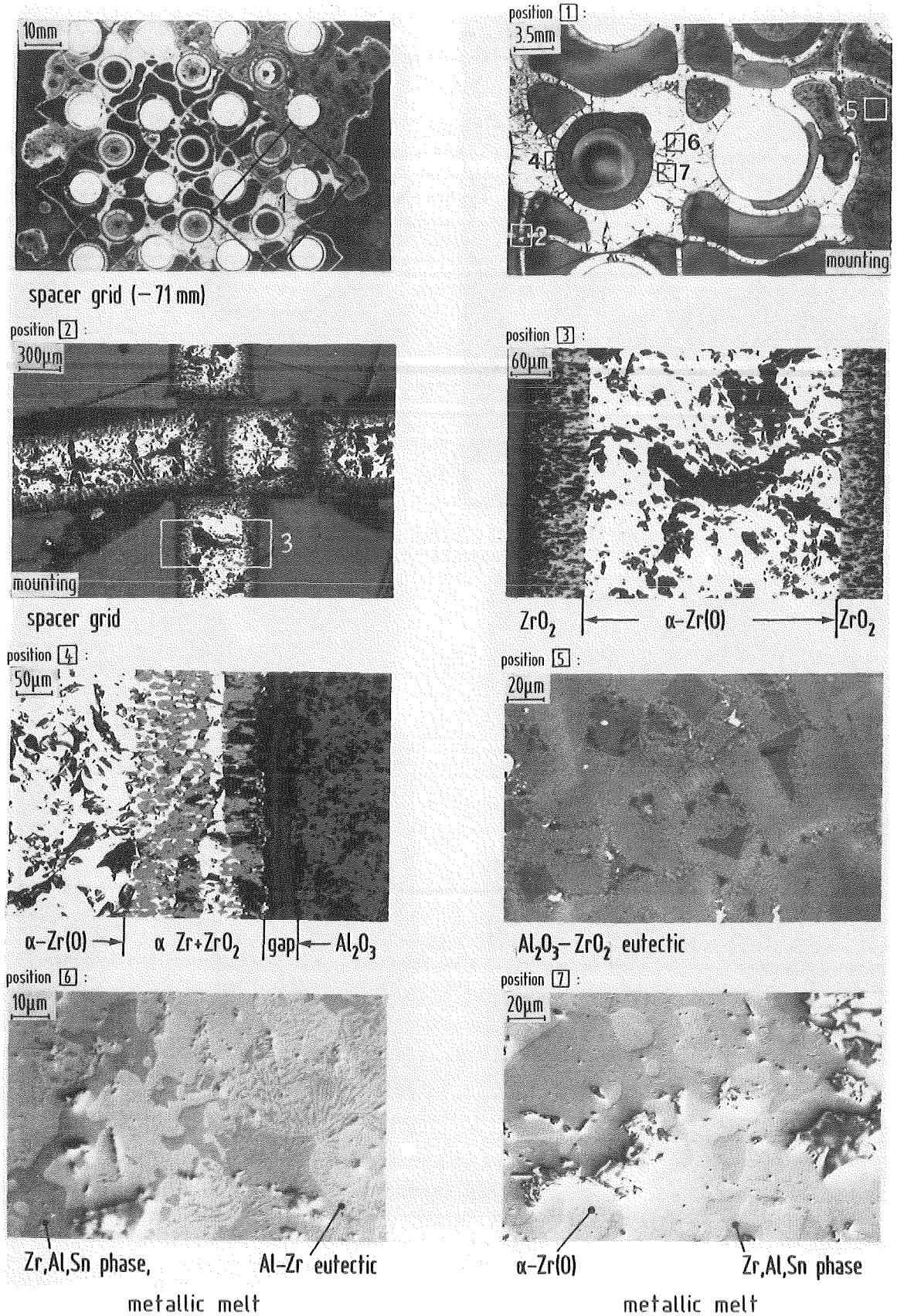


**Fig. 57. Microstructures of the CORA bundle cross-section B 4 (- 71 mm)**

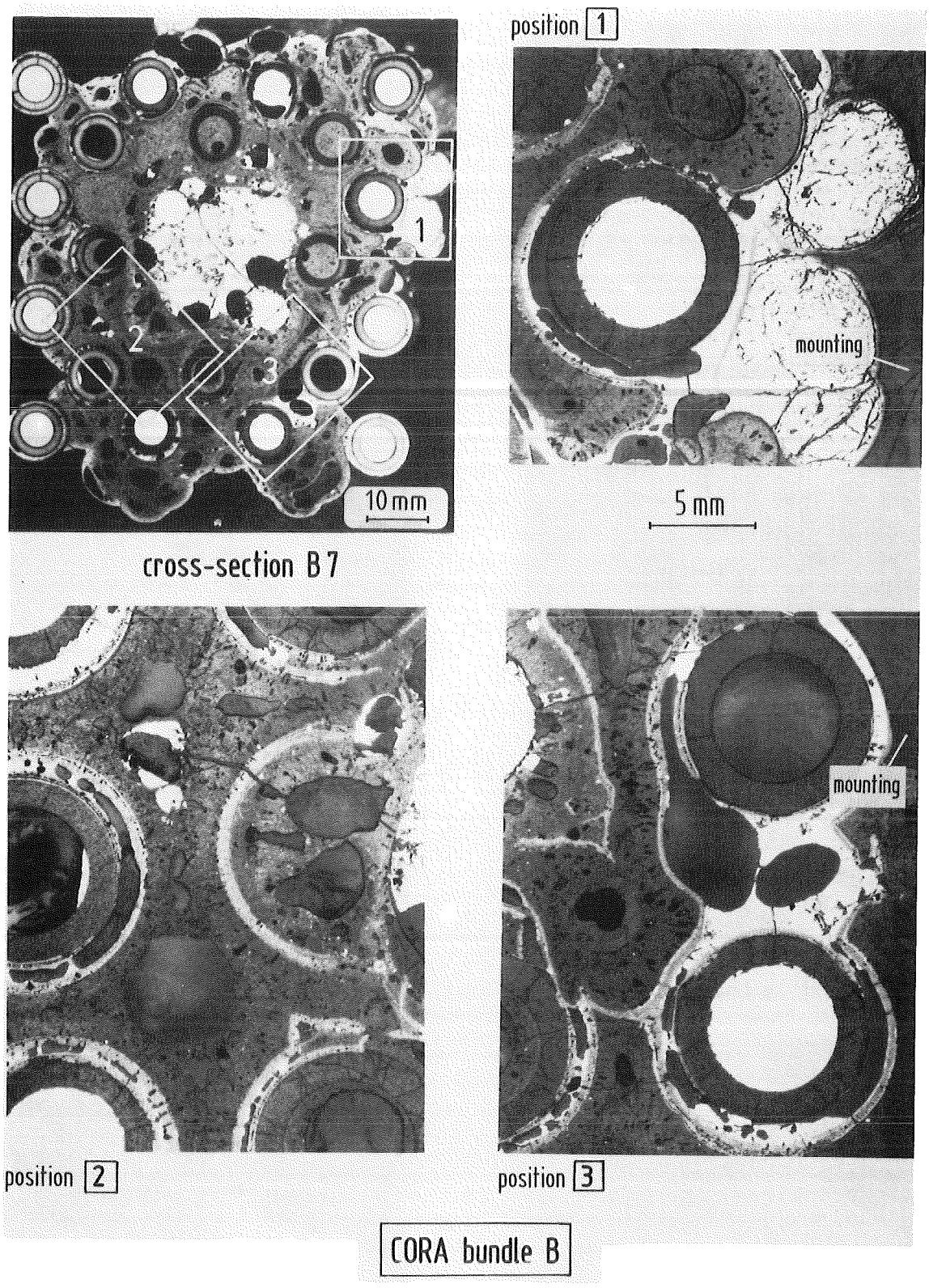


**Fig. 58. CORA bundle cross-section B 7 (0 mm)**

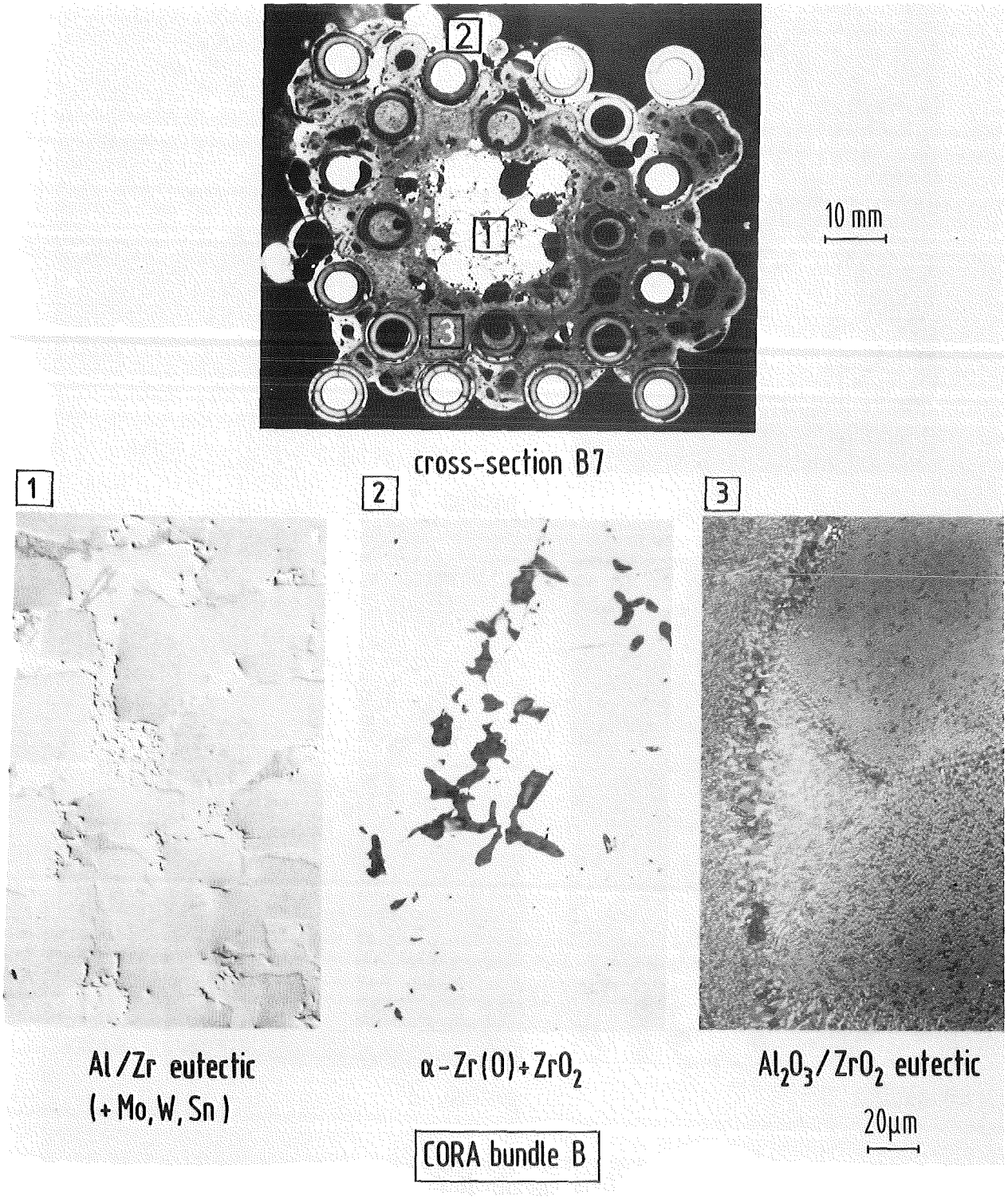


**Fig. 59. Typical microstructures of CORA bundle cross-section B 7 (0 mm)**

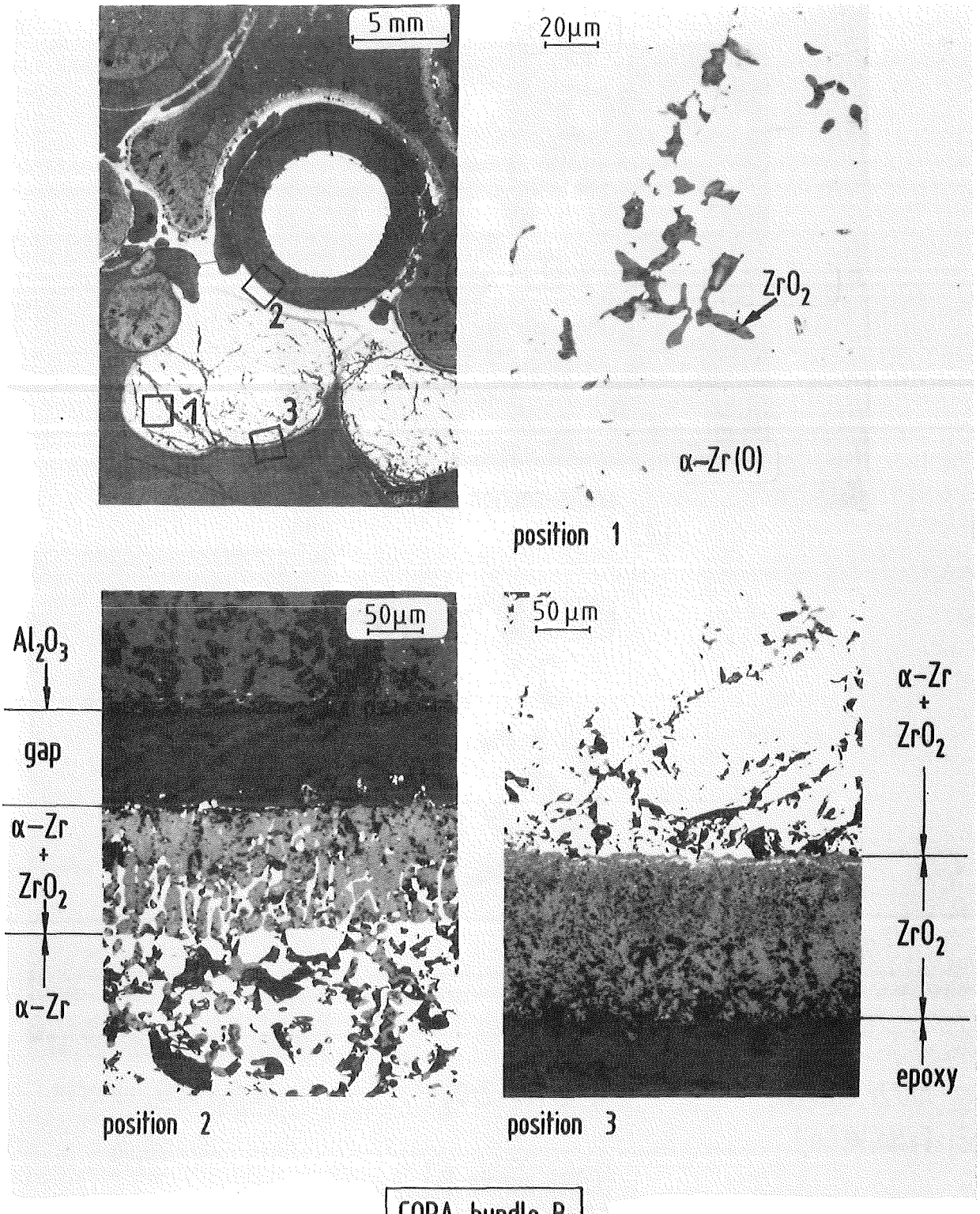


**Fig. 60. Microstructures of solidified metallic melt at CORA bundle cross-section B 7 (0 mm)**

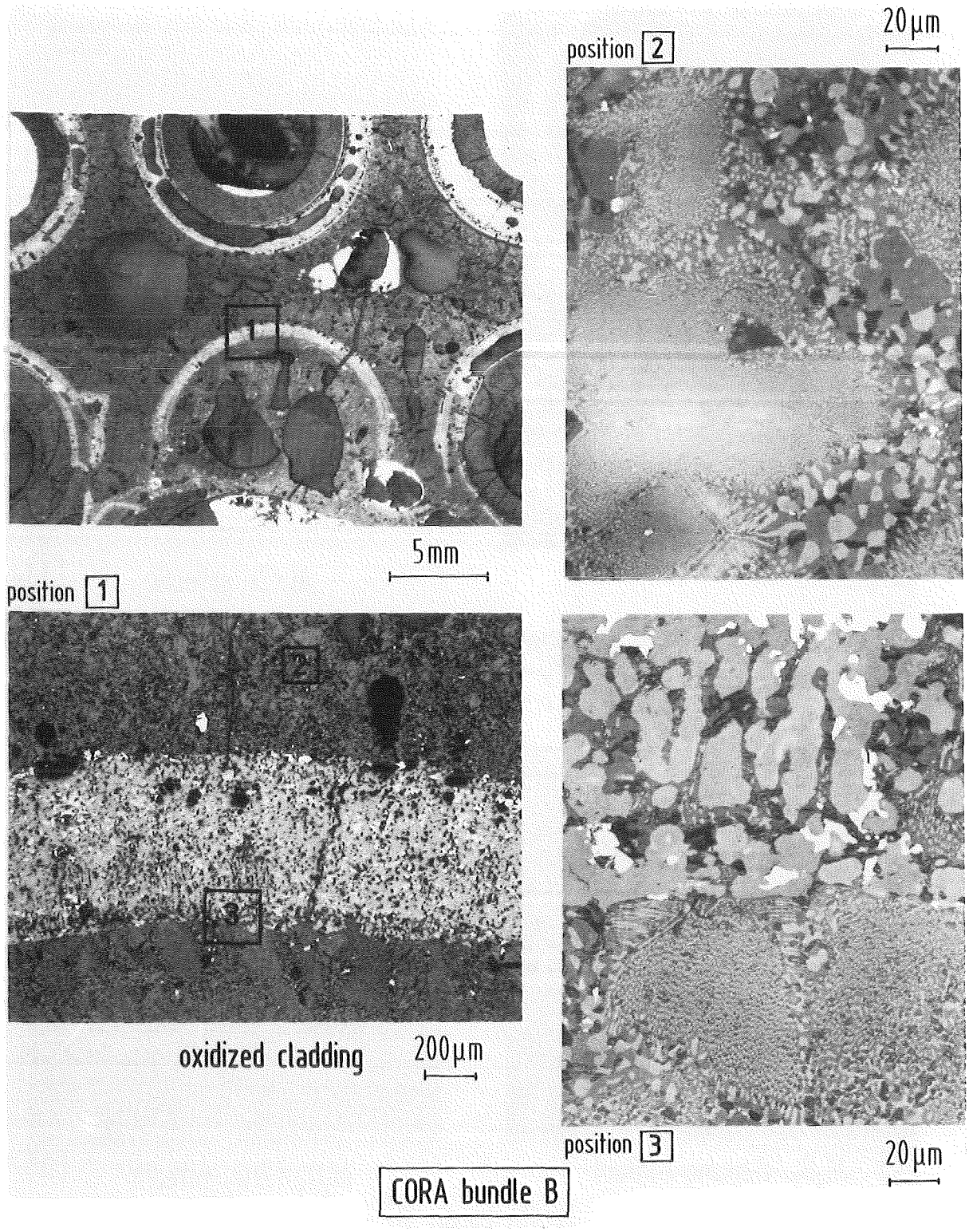


**Fig. 61. Microstructures of CORA bundle cross-section B 7 (0 mm)**

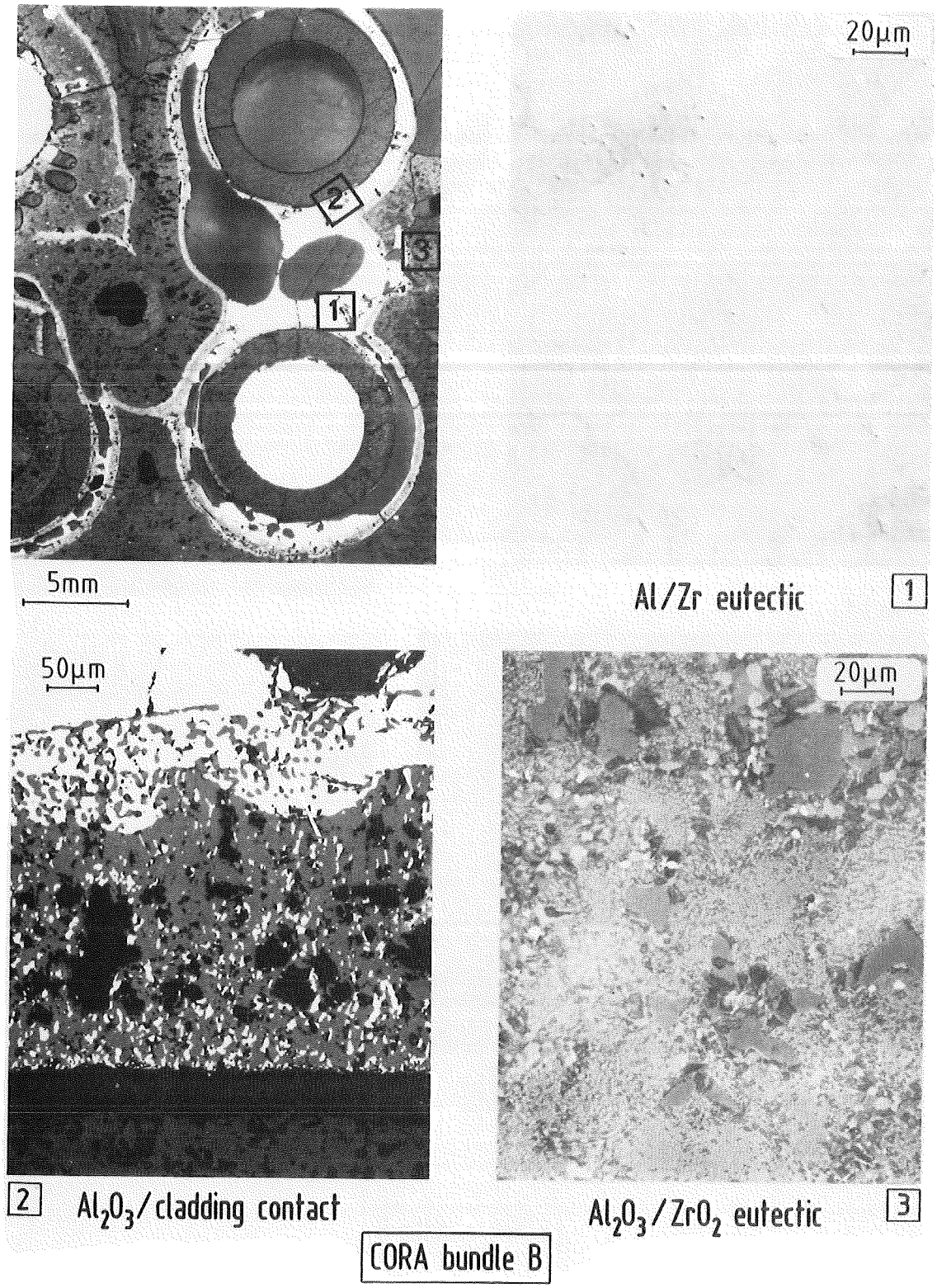


**Fig. 62. Microstructures of CORA bundle cross-section B 7 (0 mm)**

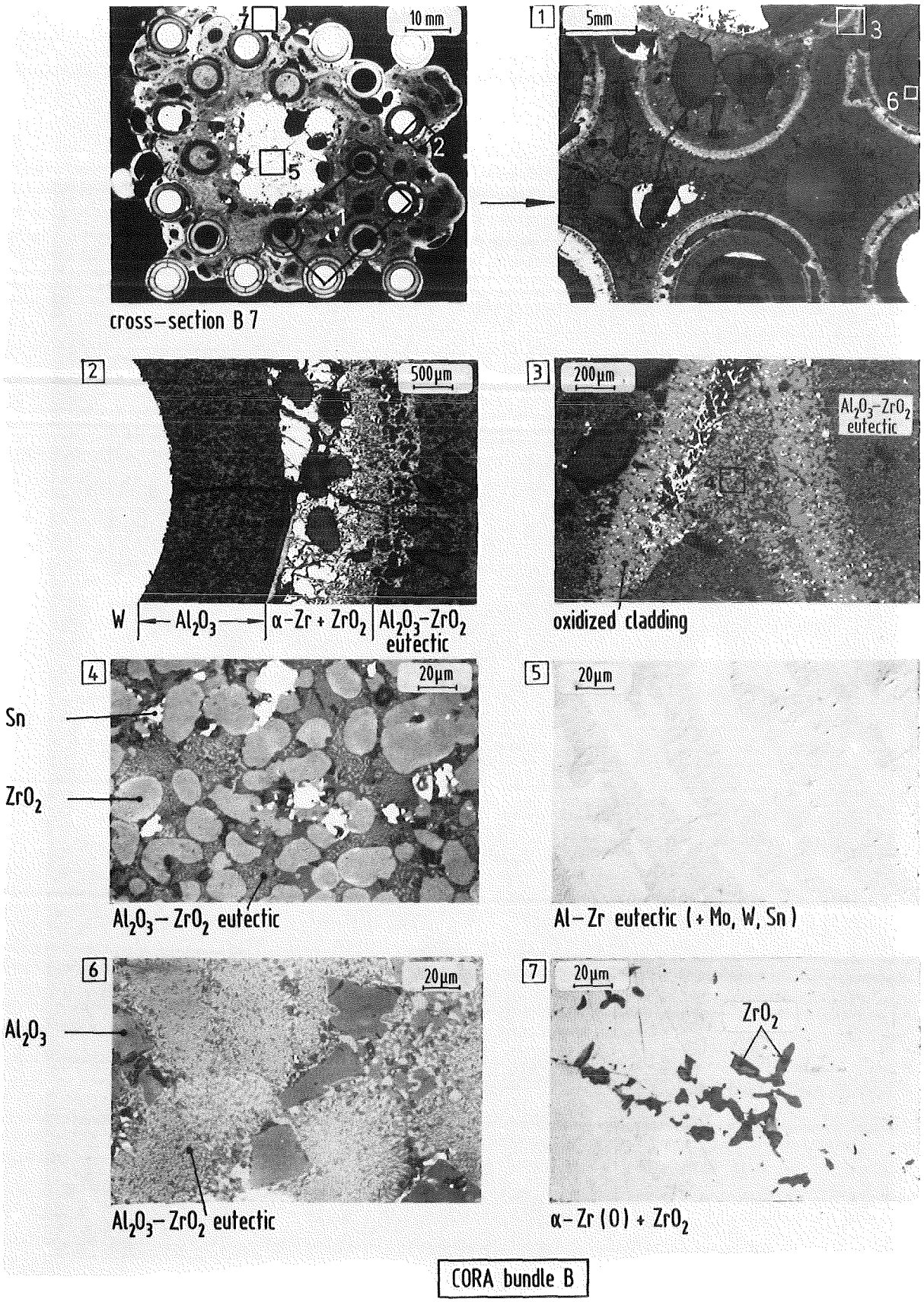


**Fig. 63. Microstructures of CORA bundle cross-section B 7 (0 mm)**

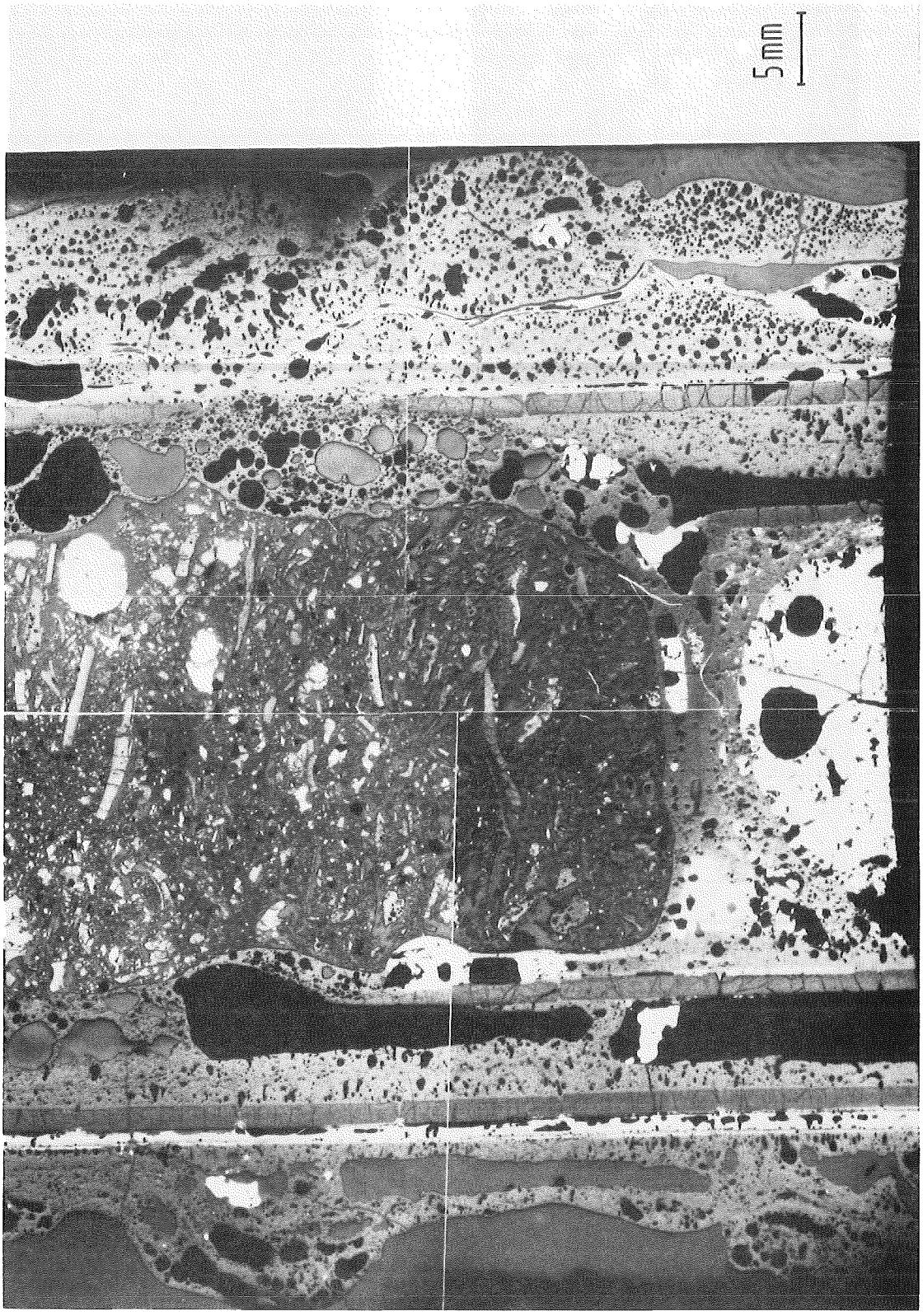


Fig. 64. Vertical cross section of CORA bundle B between 1 and 73 mm elevation

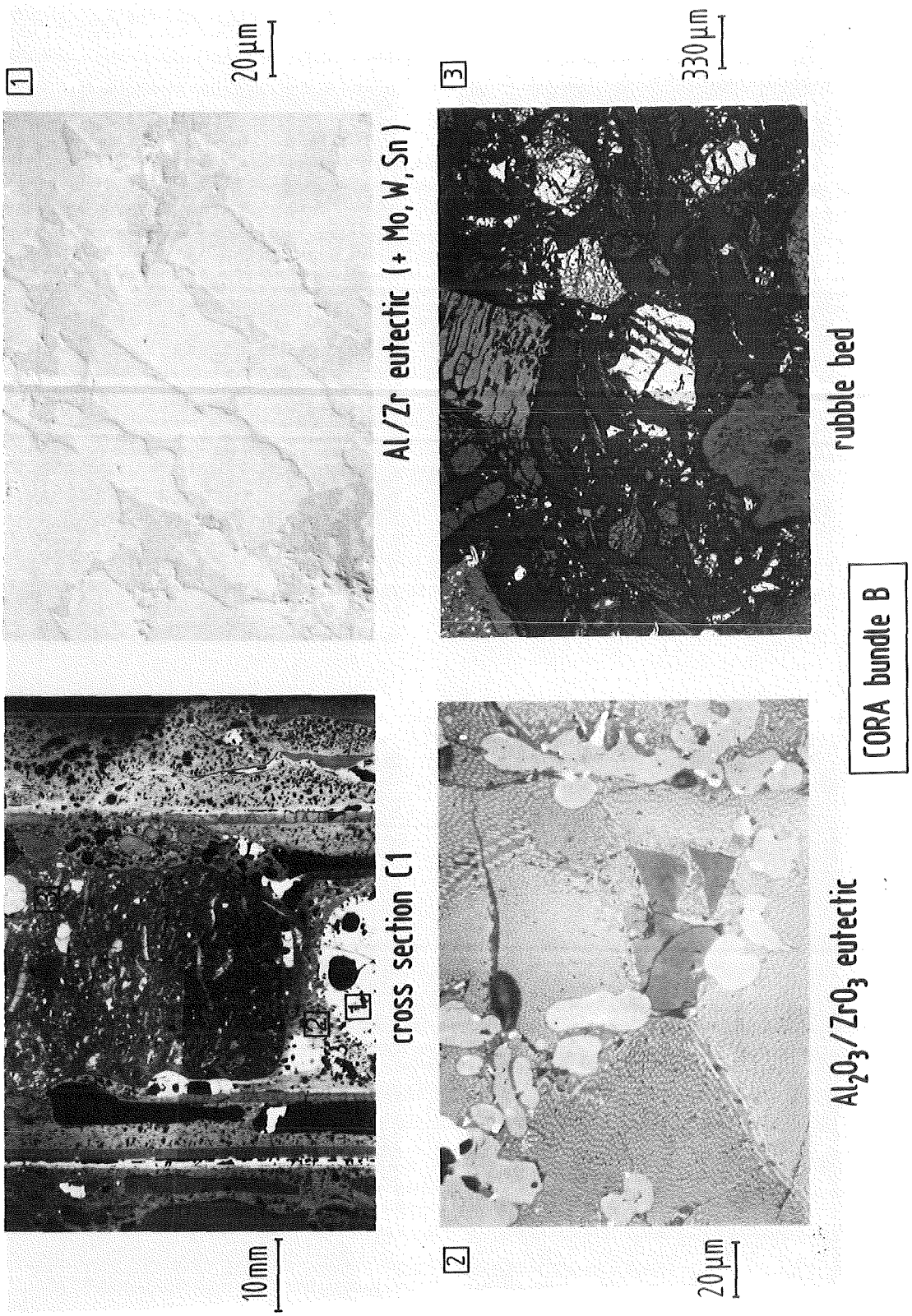


**Fig. 65. Microstructures of CORA bundle B. Vertical cross section C1 (1-73 mm)**

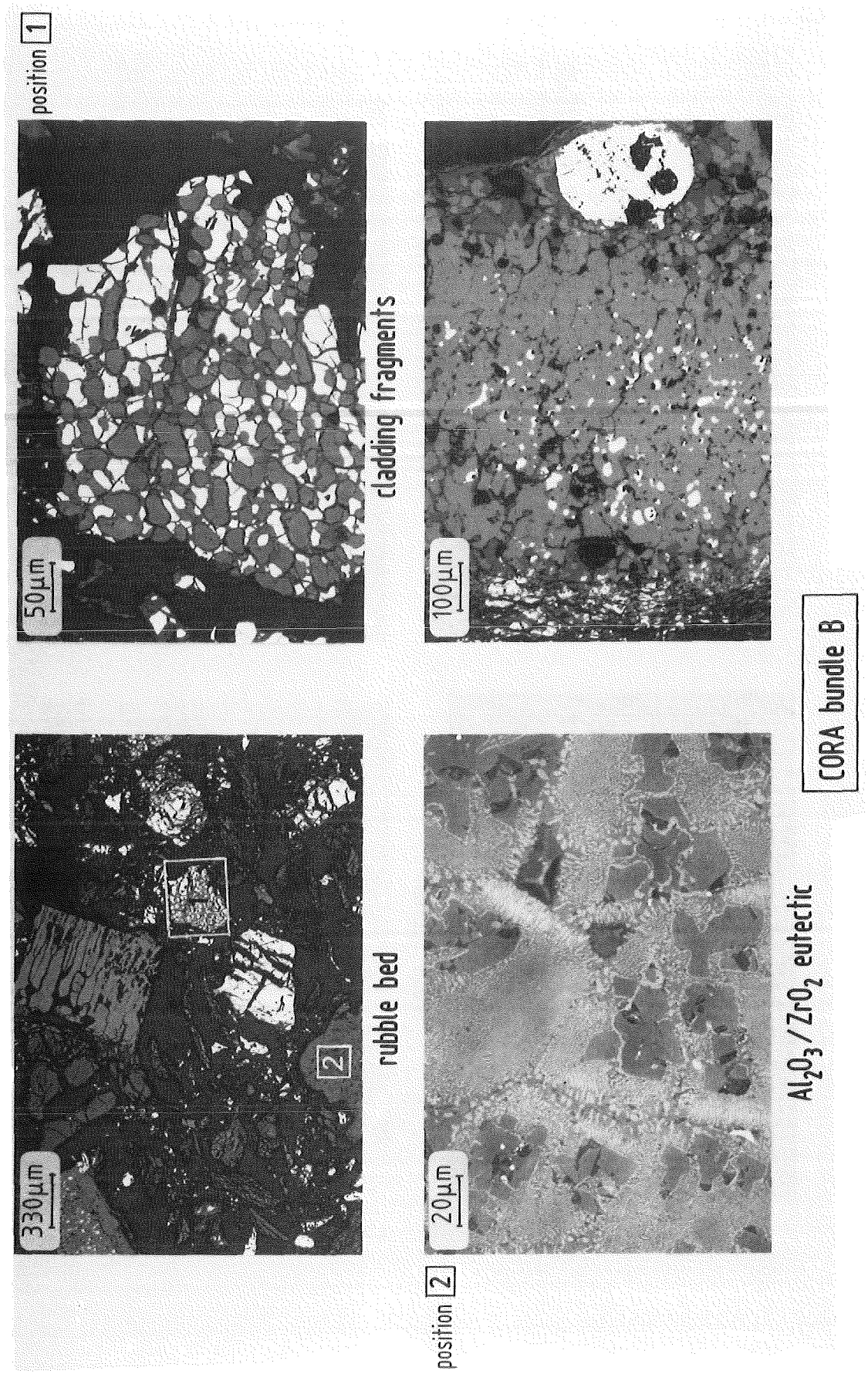


**Fig. 66. Microstructures of CORA bundle B. Vertical cross section C1 (1-73 mm)**

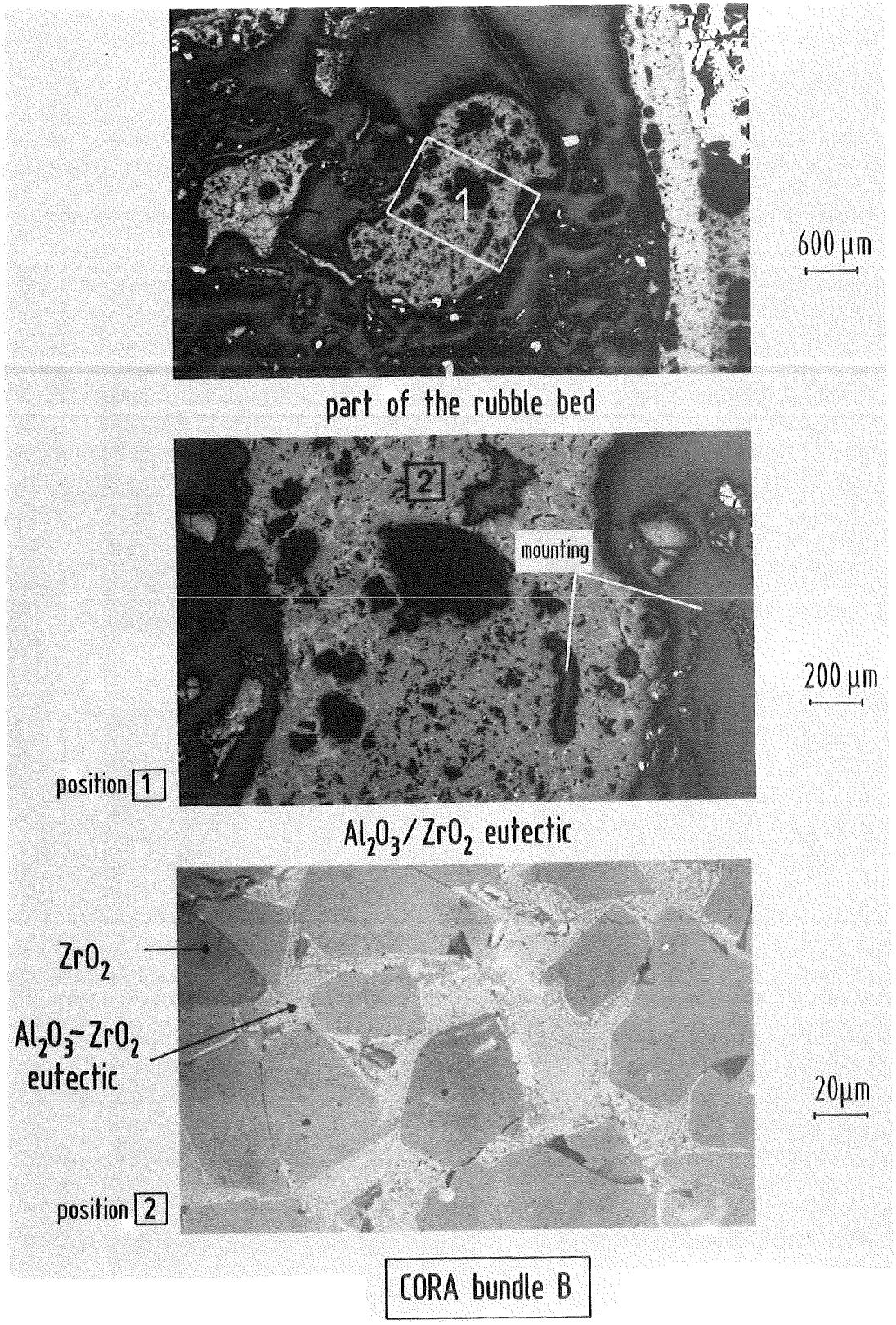


**Fig. 67. Microstructures of the rubble CORA bundle B, vertical cross-section C1 (1-73 mm)**

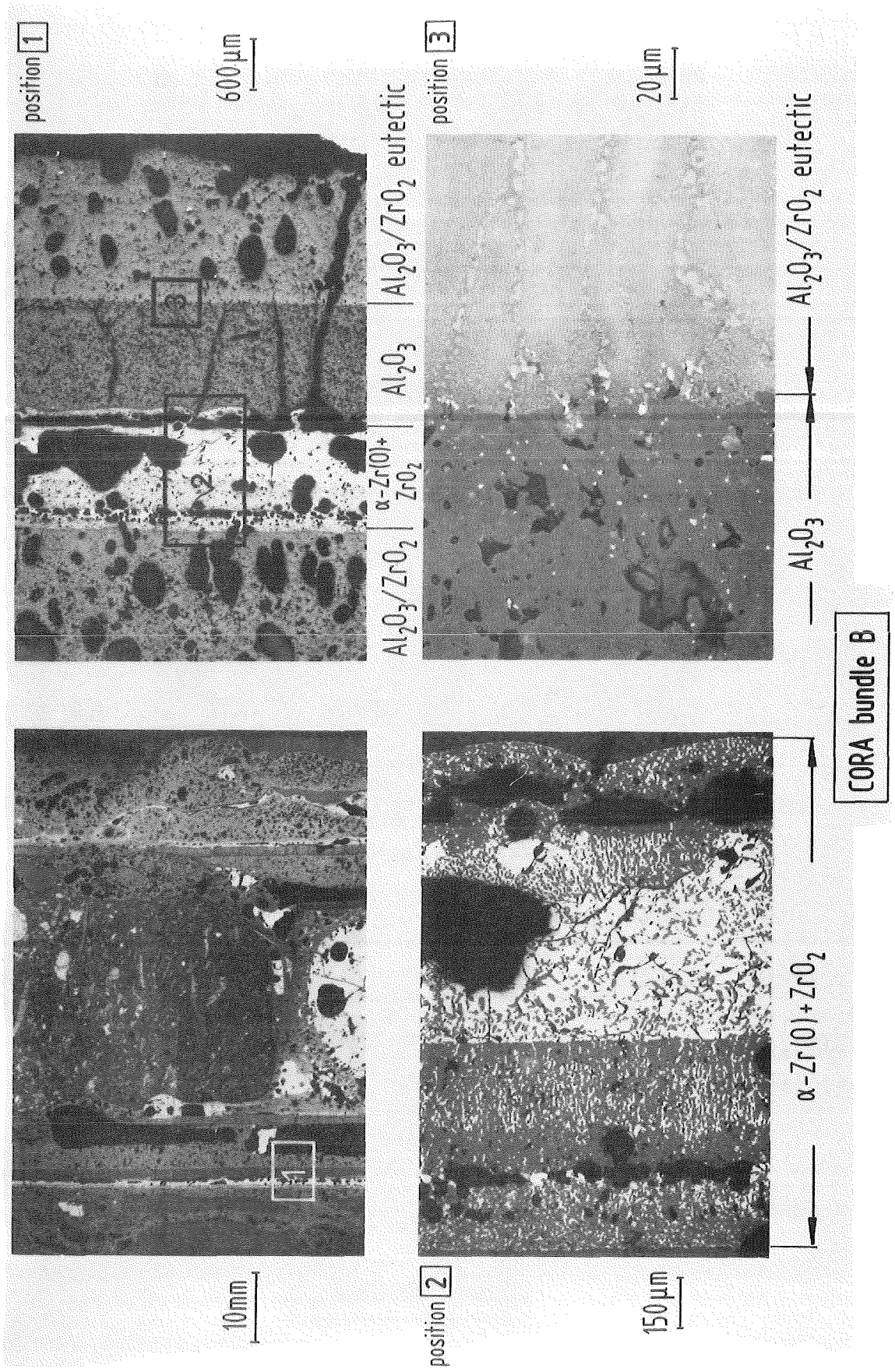


**Fig. 68. Microstructures of CORA bundle B. Vertical cross-section C1 (1-73 mm)**

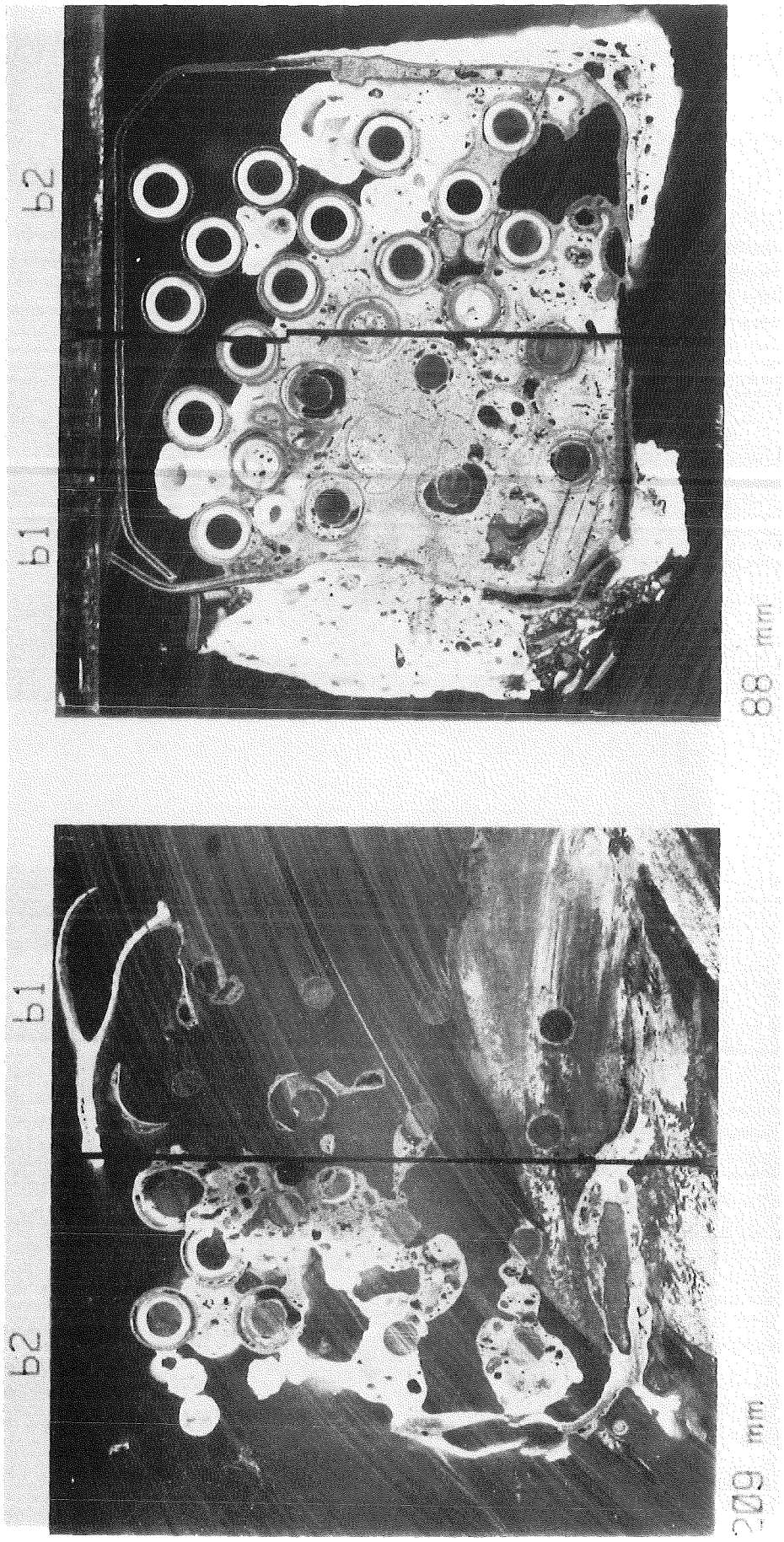


**Fig. 69.** Horizontal cross sections at 88 mm and 209 mm showing the position of the vertical cross sections b1 and b2 (CORA C)

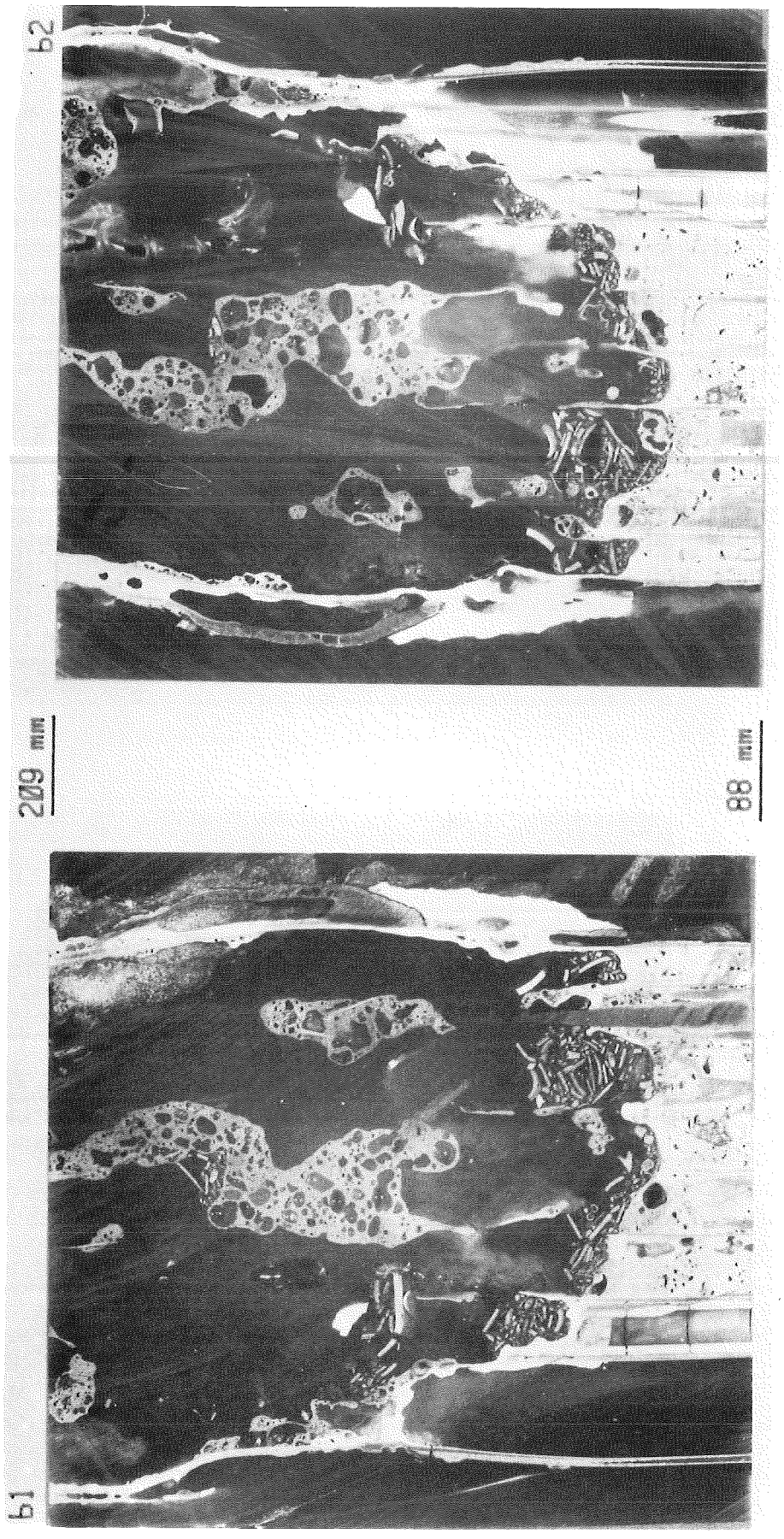


**Fig. 70.** Vertical cross sections b1 and b2 between 209 mm and 88 mm elevation (CORA C)

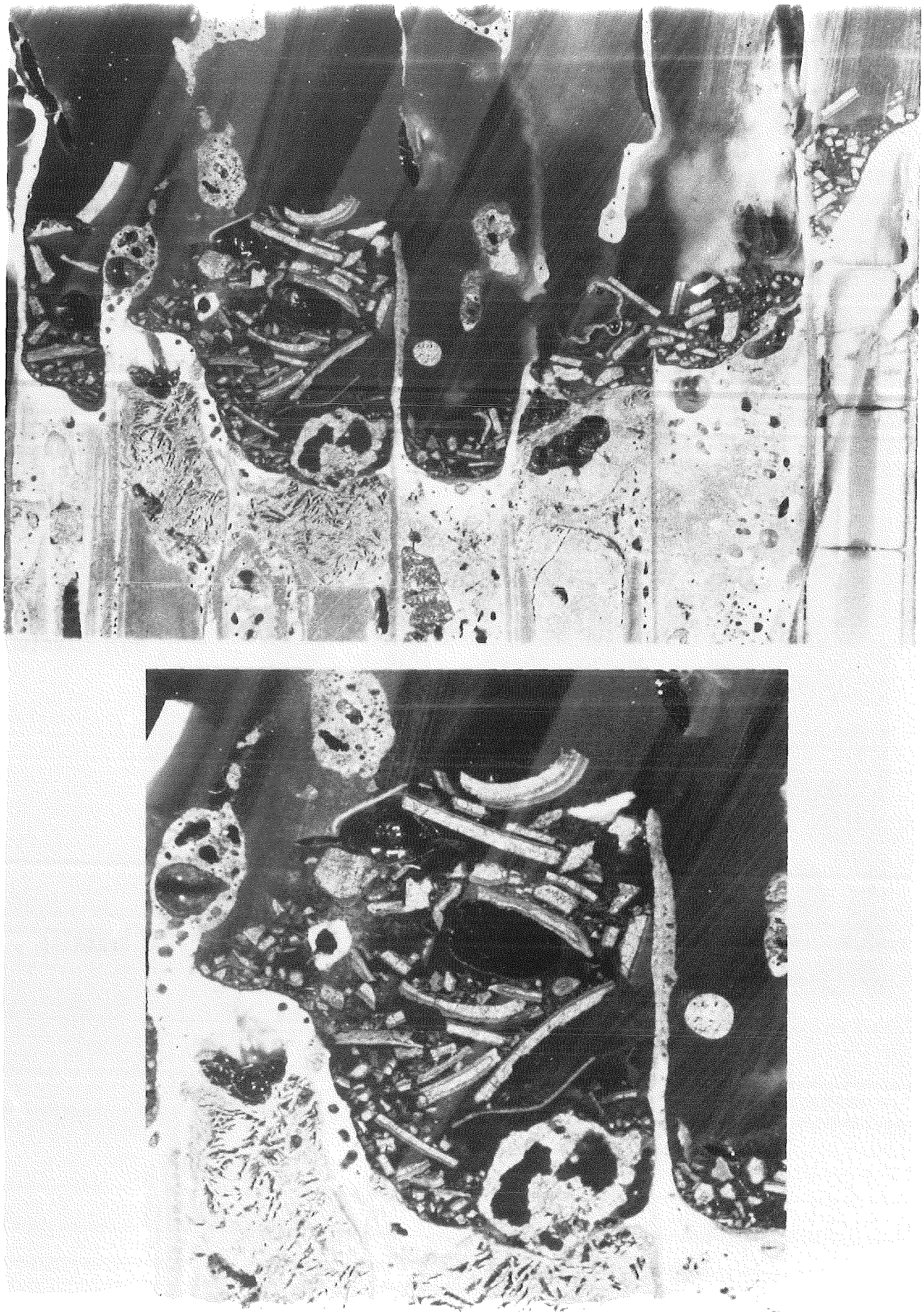

Fig. 71. Details of vertical cross section b2 between 209 mm and 88 mm elevation (CORA C)

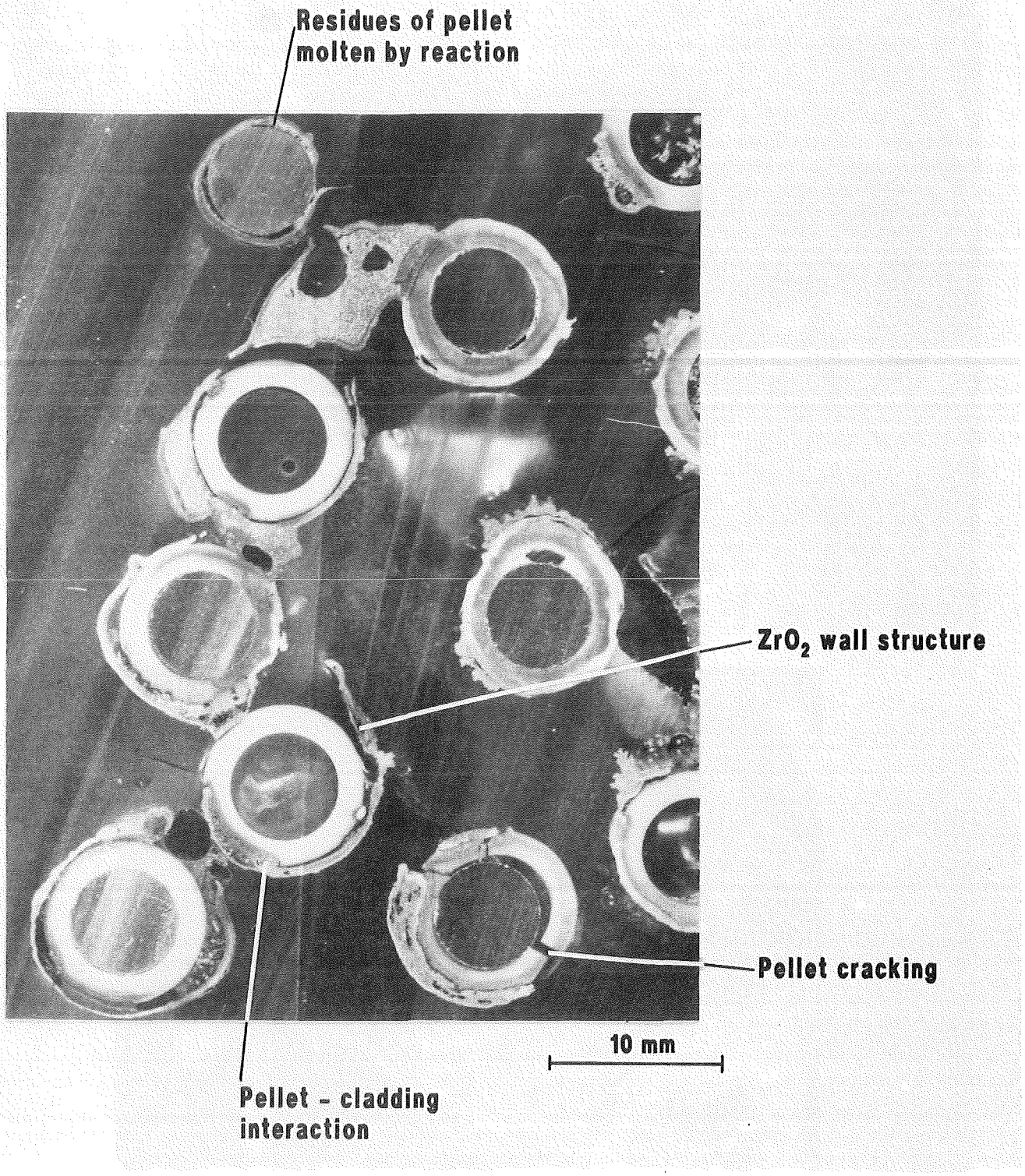


Fig. 72. Details of cross section at 666 mm elevation (CORA C)

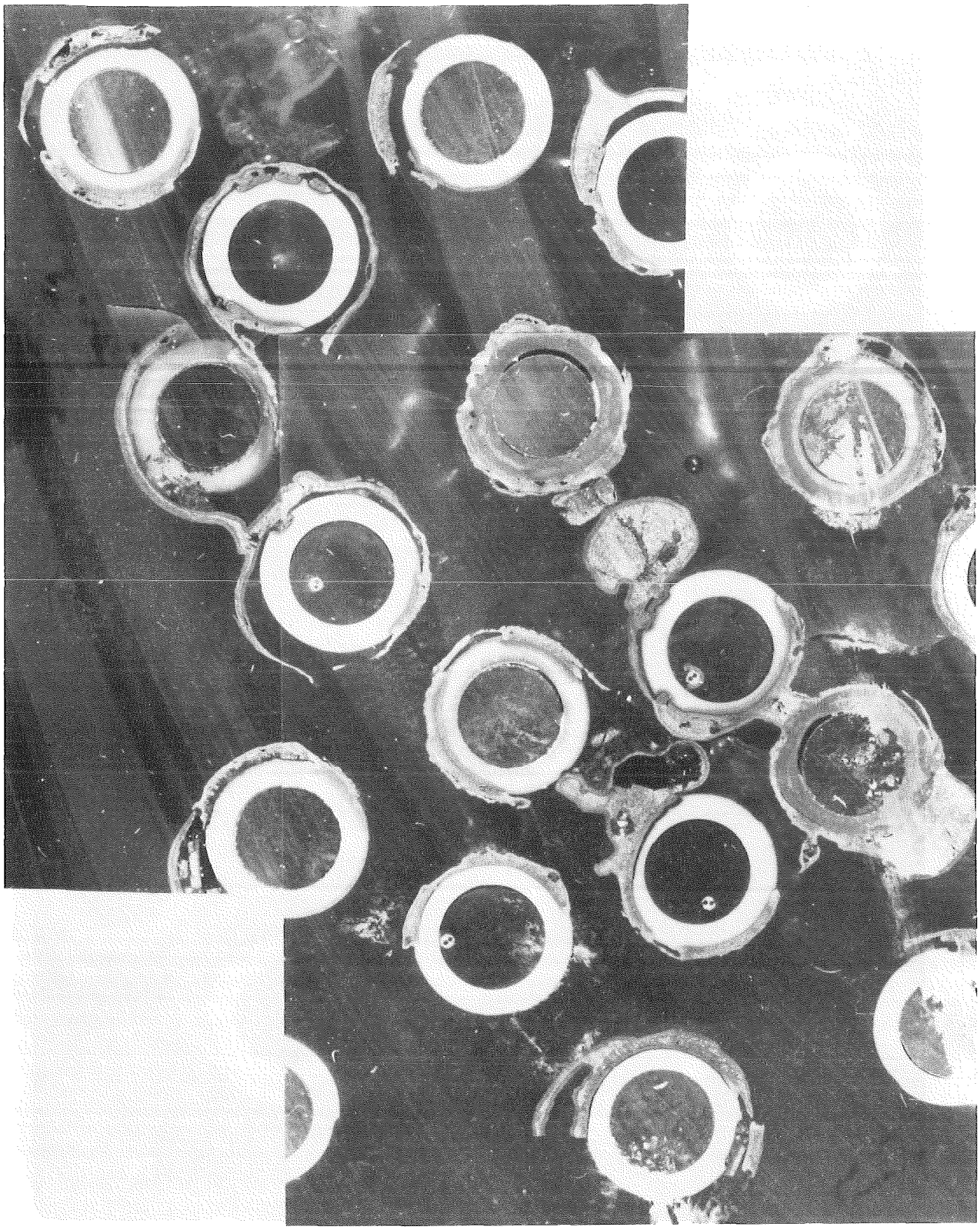

Fig. 73. Enlarged cross section at 694 mm elevation; CORA C

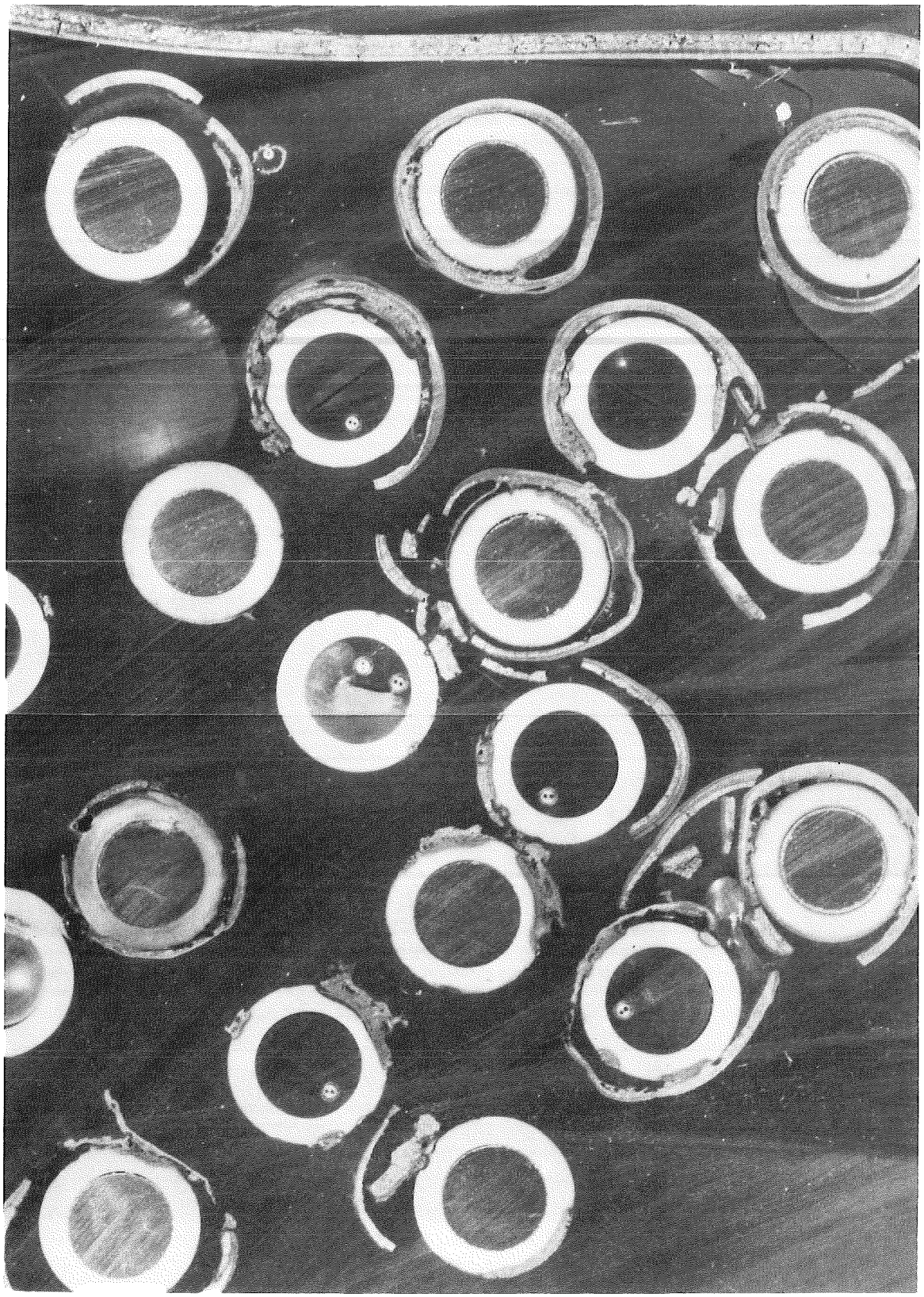

**Fig. 74. Enlarged cross section at 984 mm elevation; CORA C**

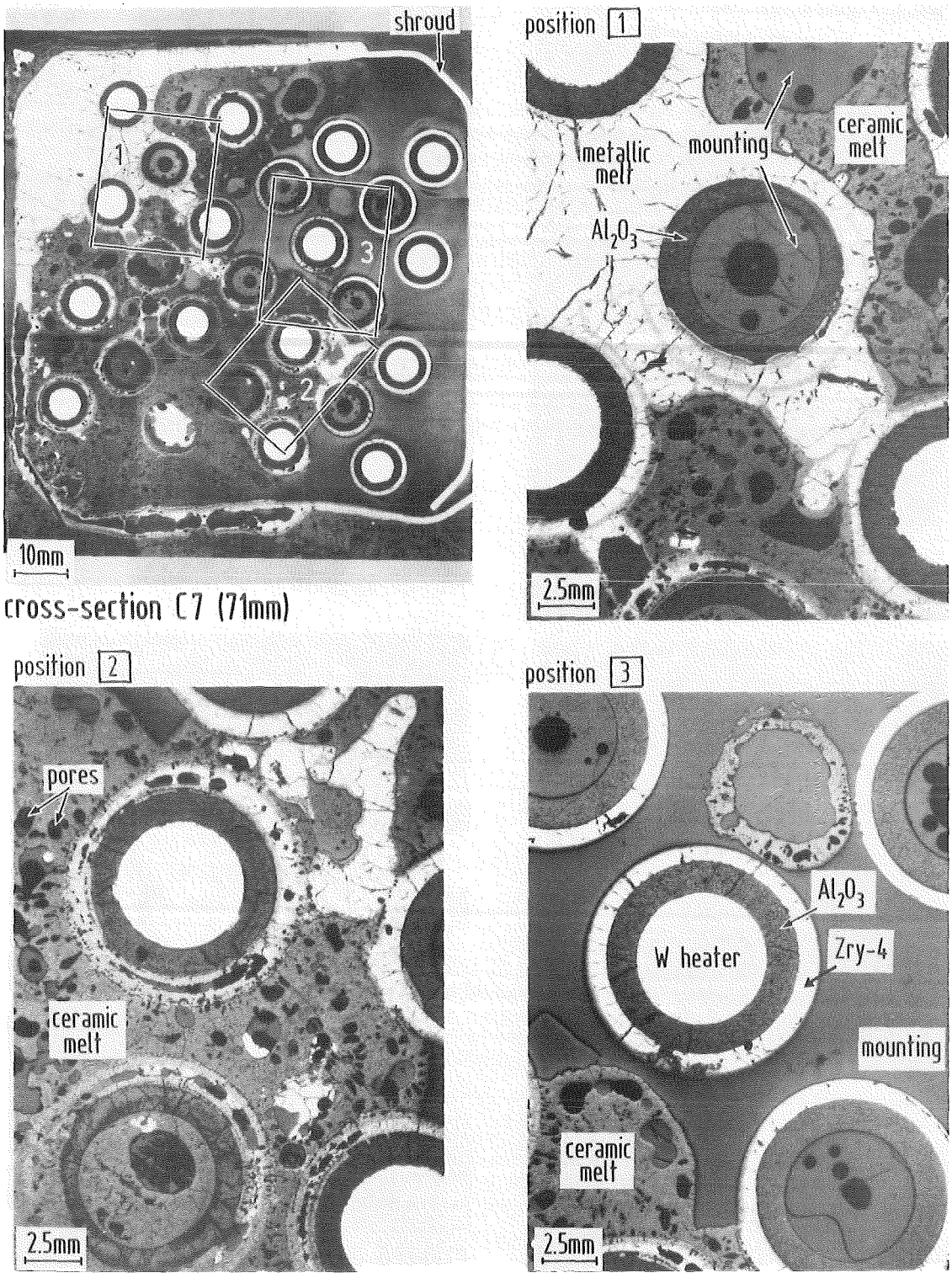


Fig. 75. Macrostructures of CORA bundle cross-section C7 (71 mm)

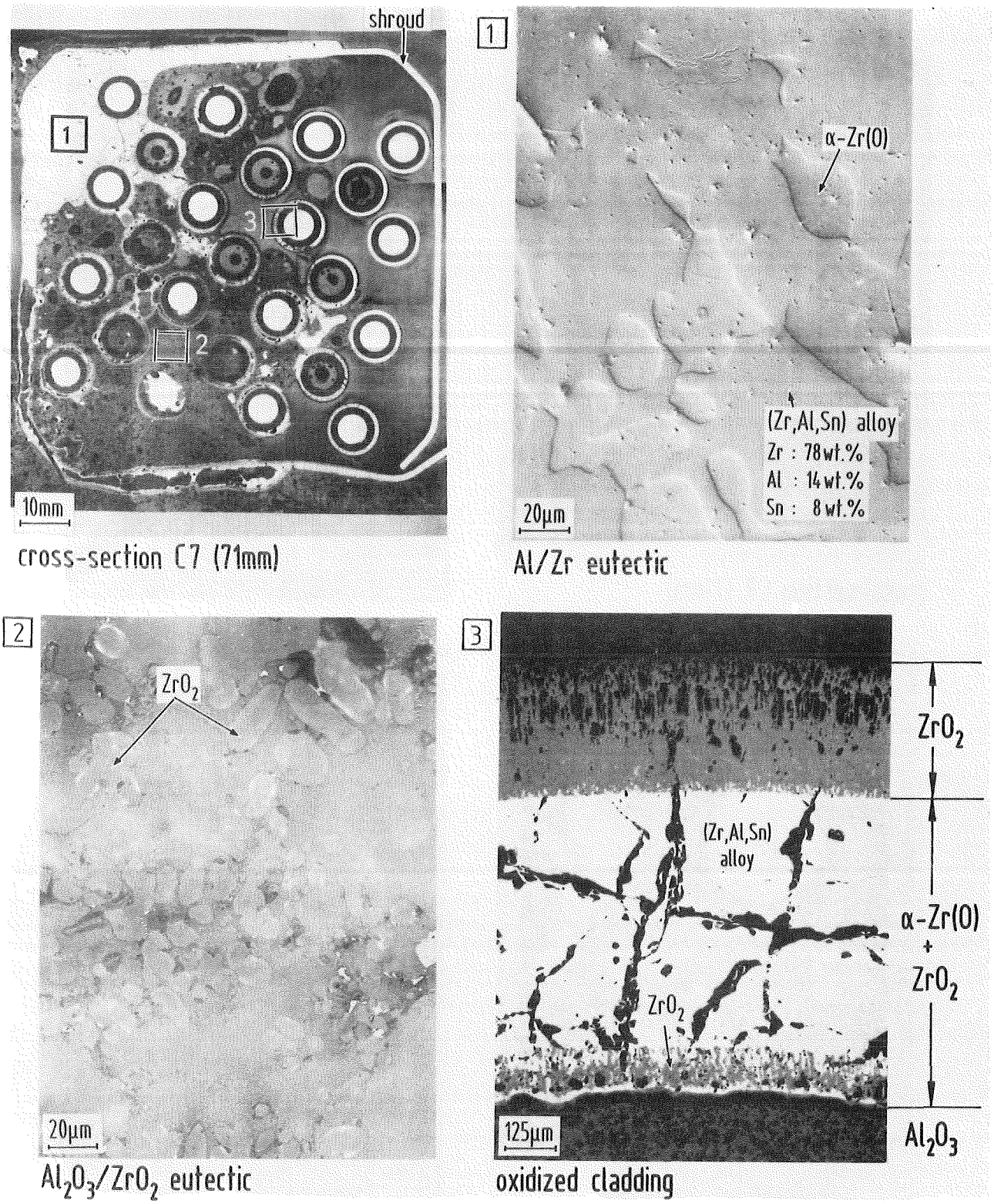


**Fig. 76. Microstructures of CORA bundle cross-section C7 (71 mm)**

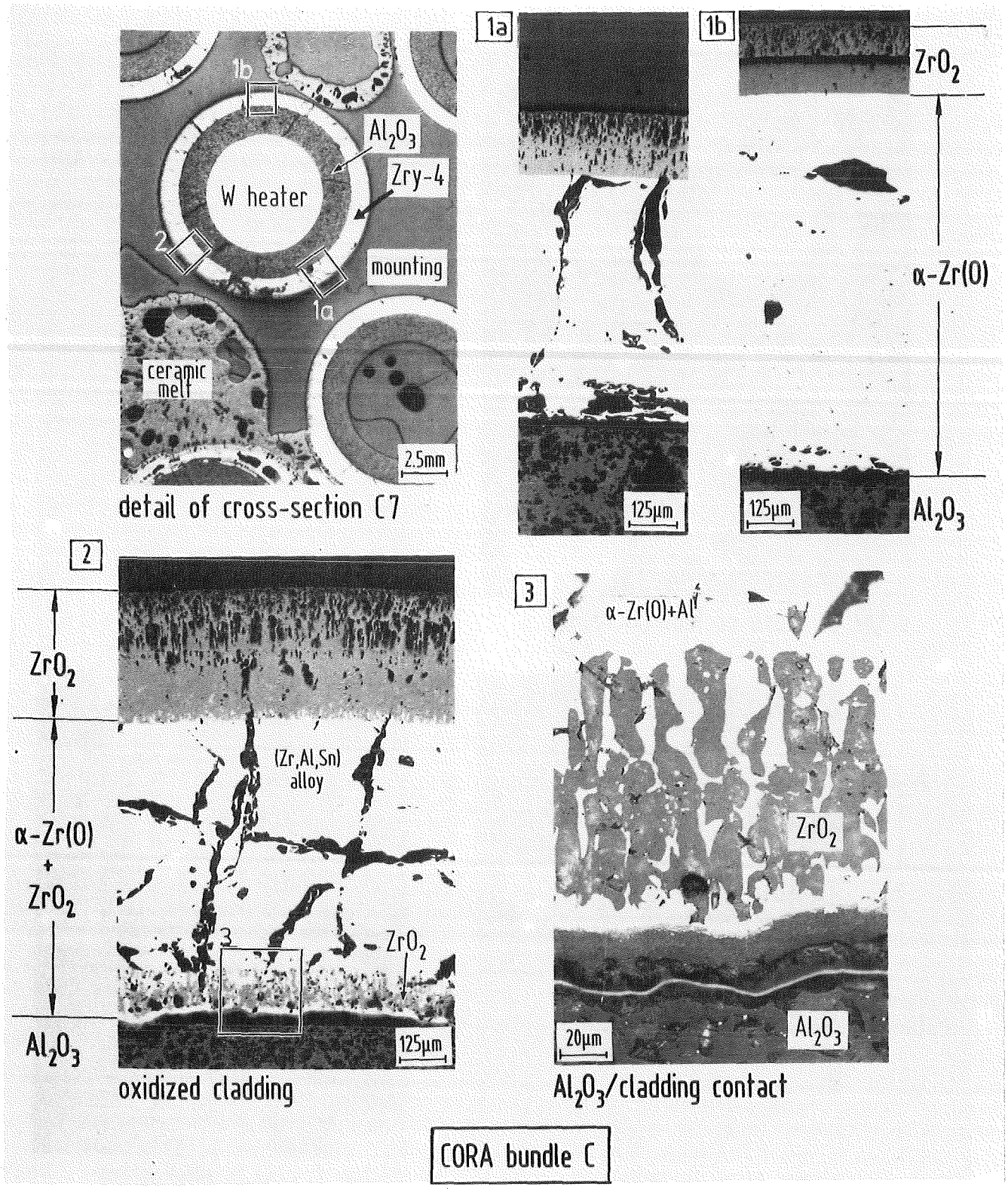


**Fig. 77. Microstructures of CORA bundle cross-section C7 (71 mm)**

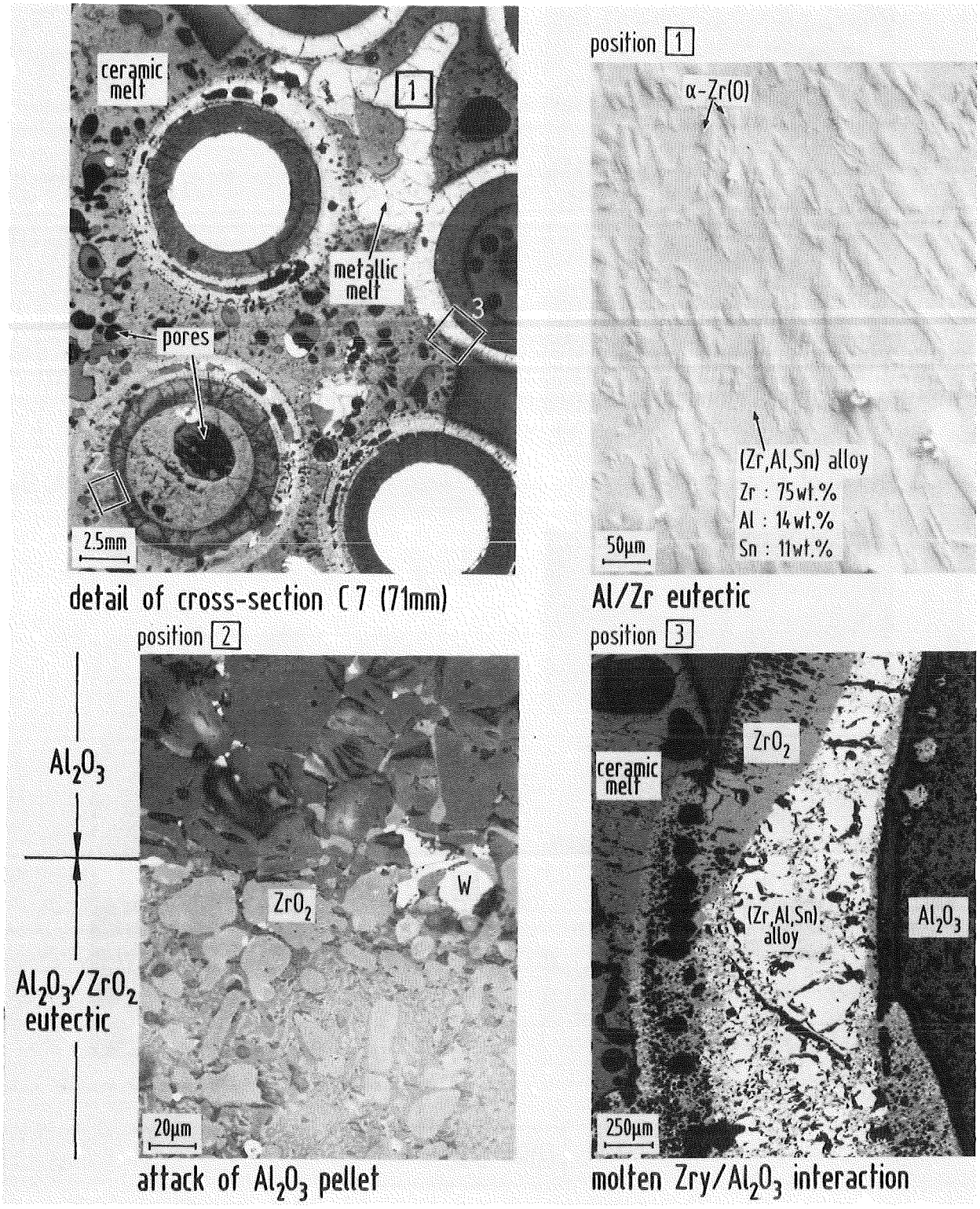


**Fig. 78. Microstructures of CORA bundle cross-section C7 (71 mm)**

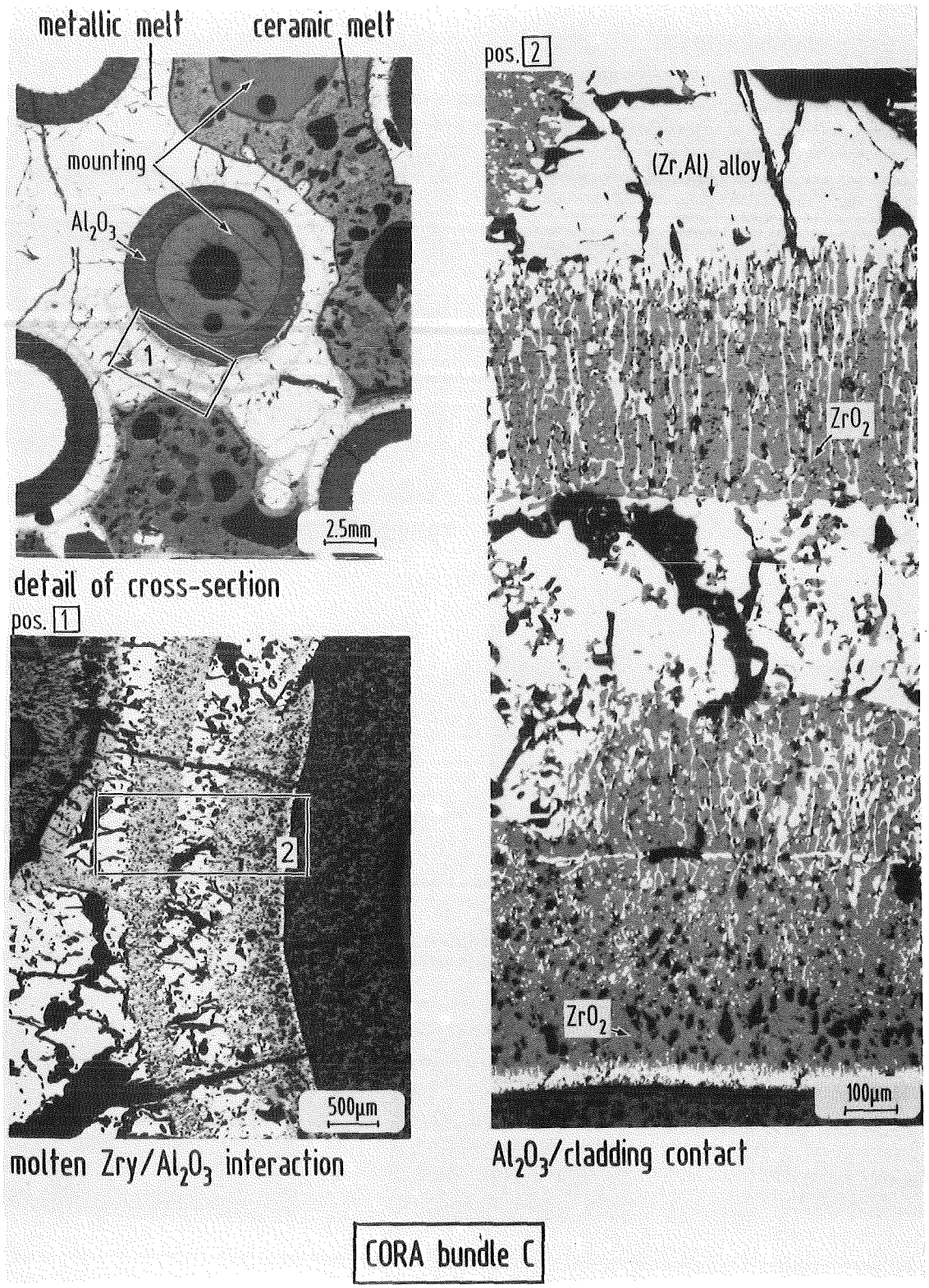


**Fig. 79. Microstructures of CORA bundle cross-section C7 (71 mm)**

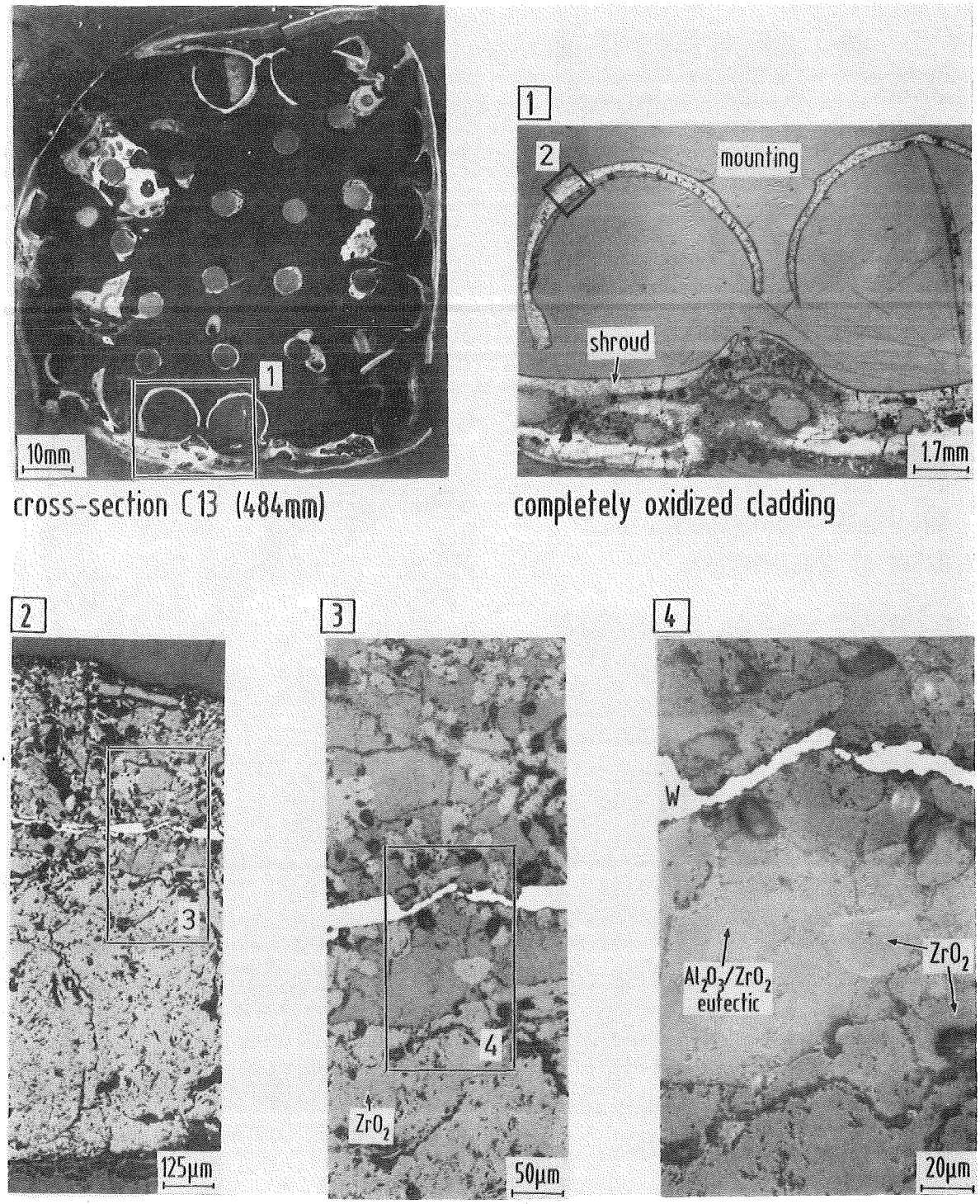


**Fig. 80. Microstructures of CORA bundle cross-section C13 (484 mm)**

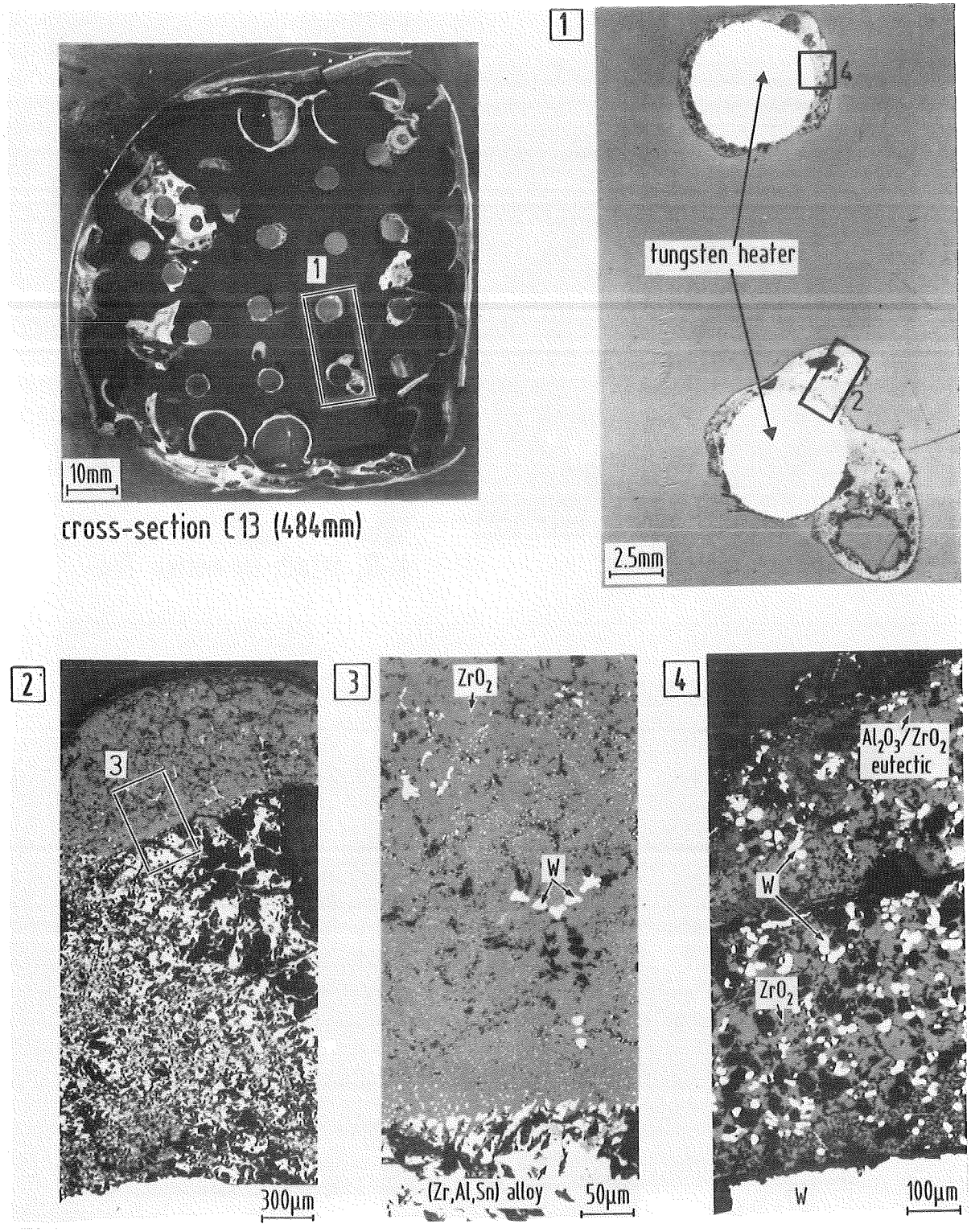


**Fig. 81. Microstructures of CORA bundle cross-section C13 (484 mm)**

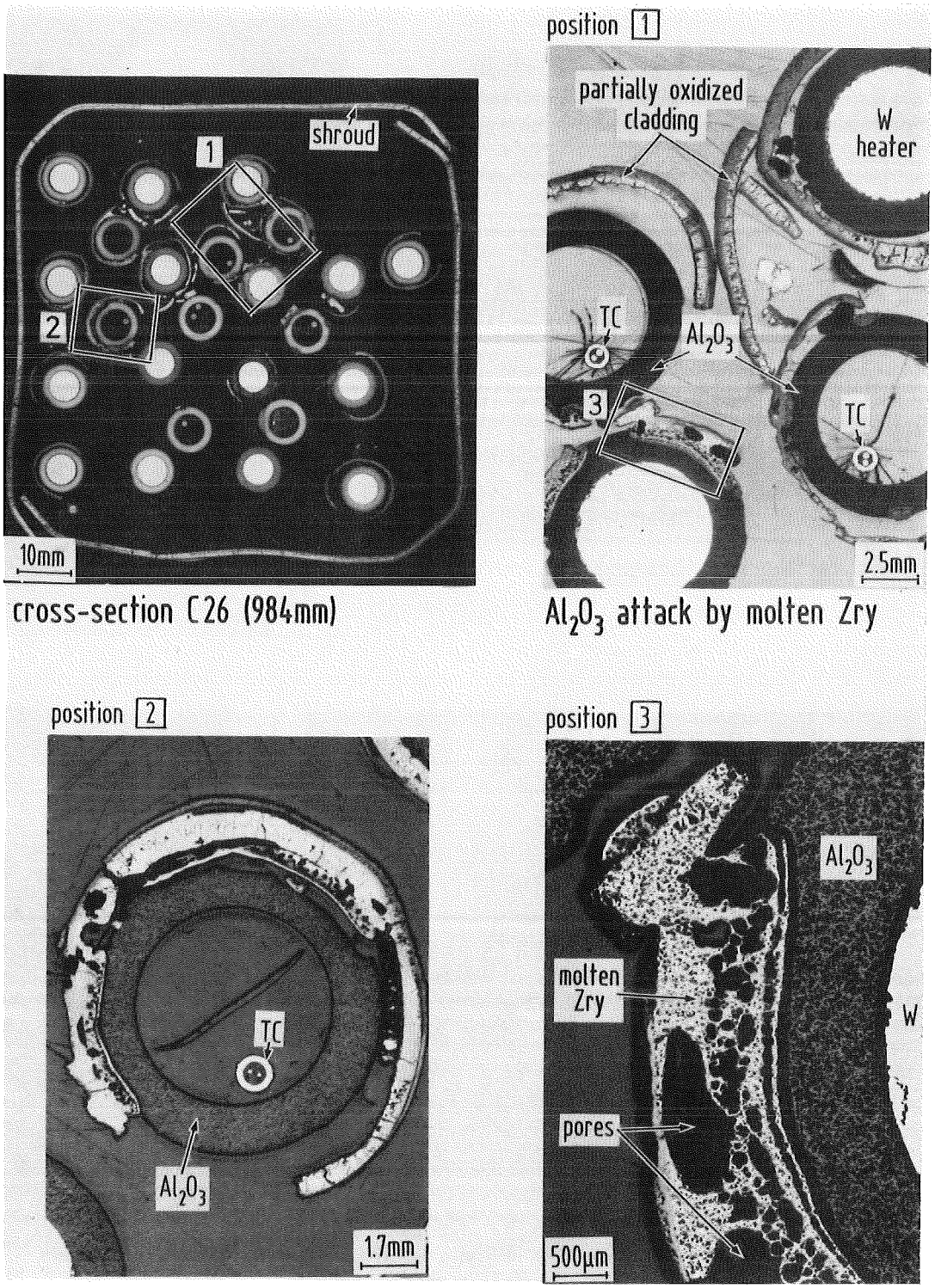


**Fig. 82. Macrostructures of CORA bundle cross-section C26 (984 mm)**

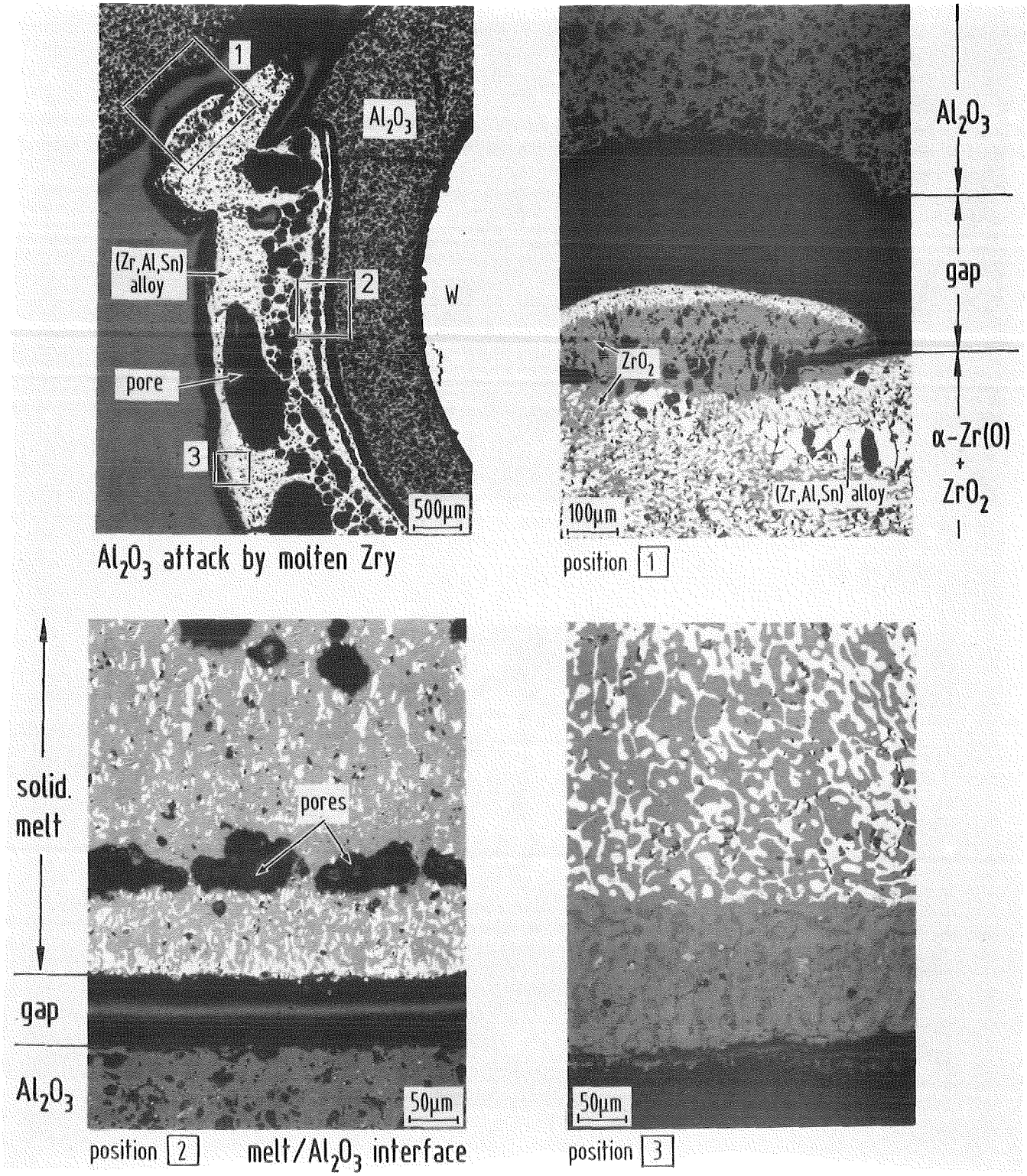


**Fig. 83. Microstructures of CORA bundle cross-section C26 (984 mm)**

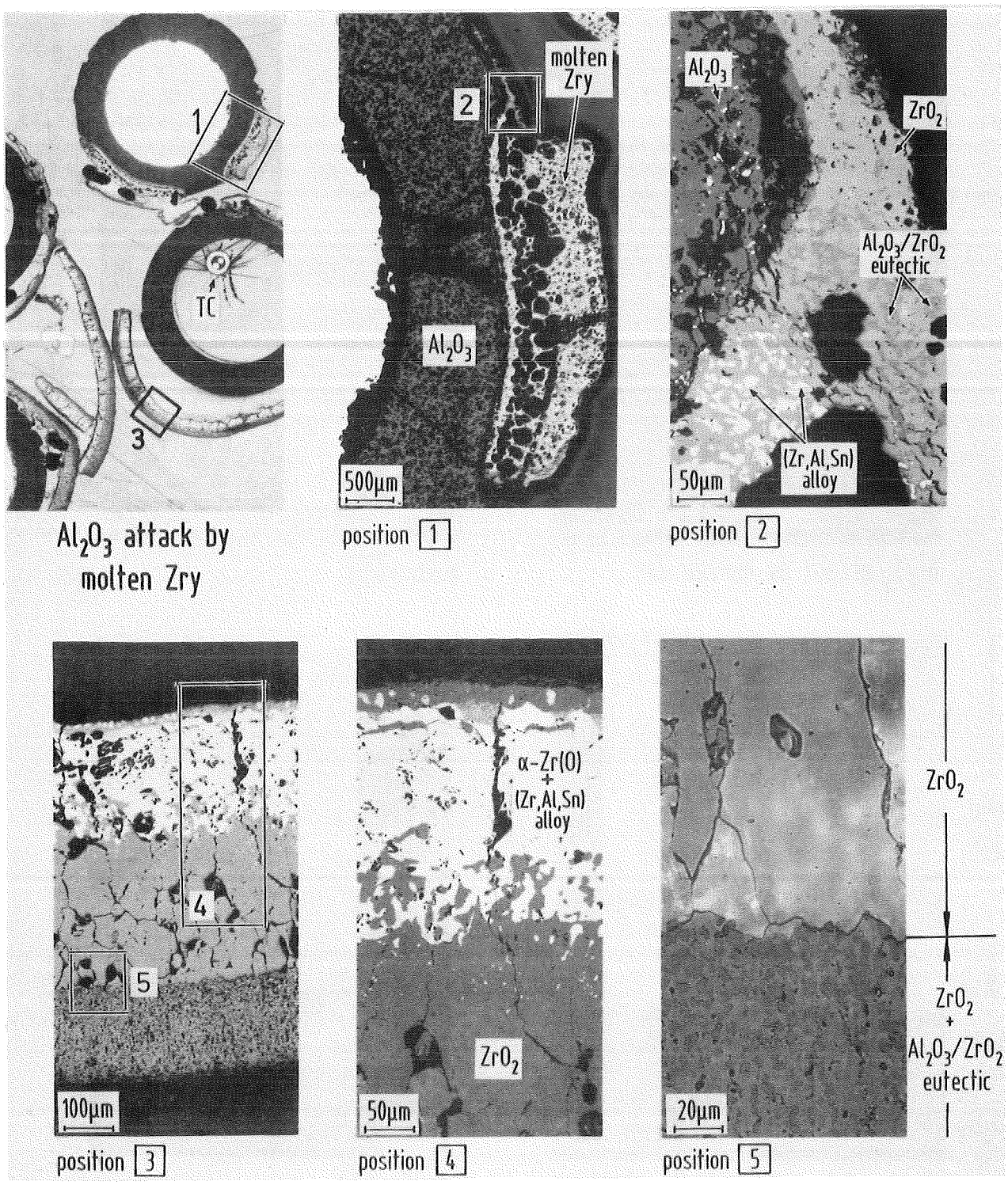


**Fig. 84. Microstructures of CORA bundle cross-section C26 (984 mm)**

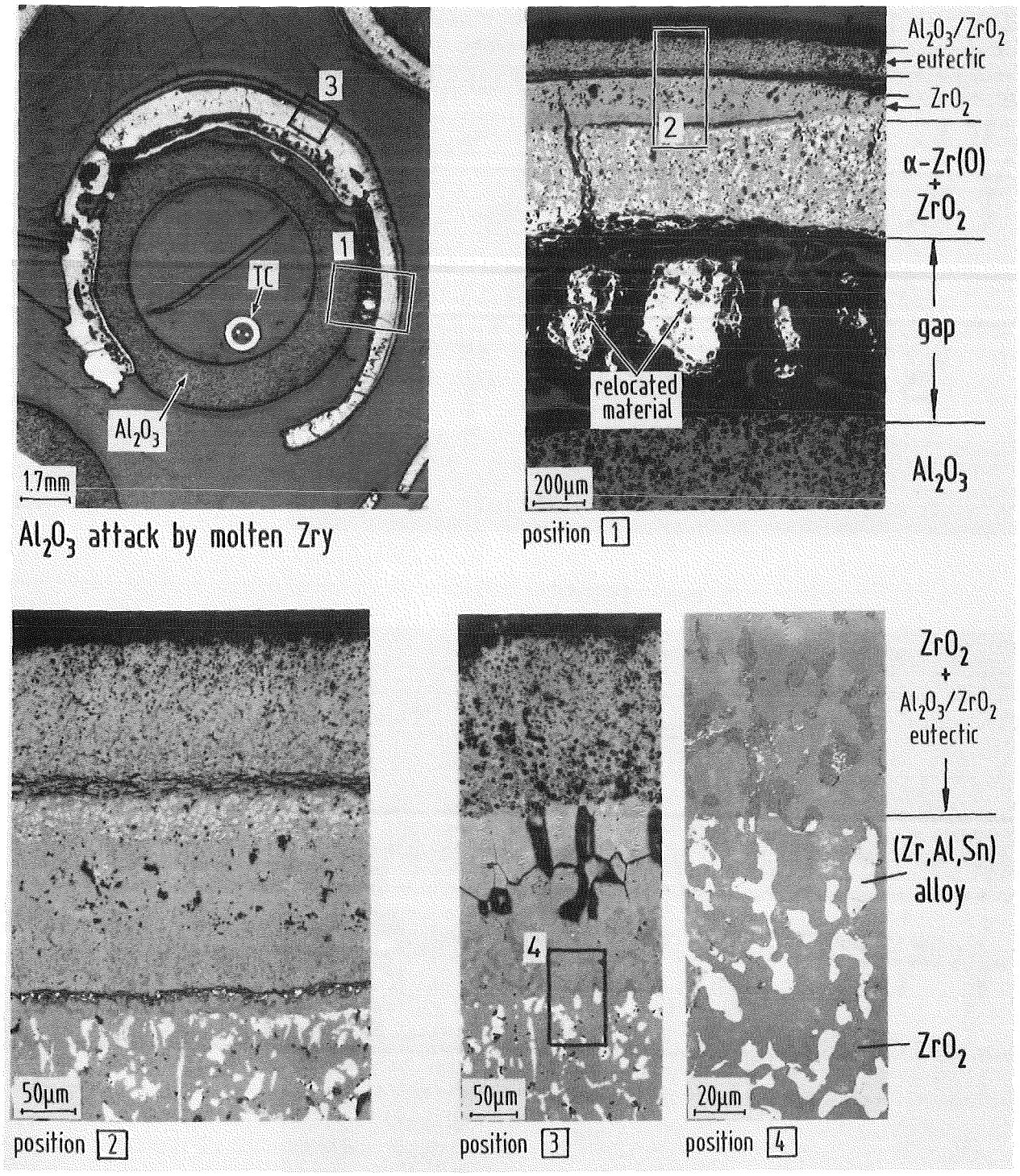


**Fig. 85. Microstructures of CORA bundle cross-section C26 (984 mm)**

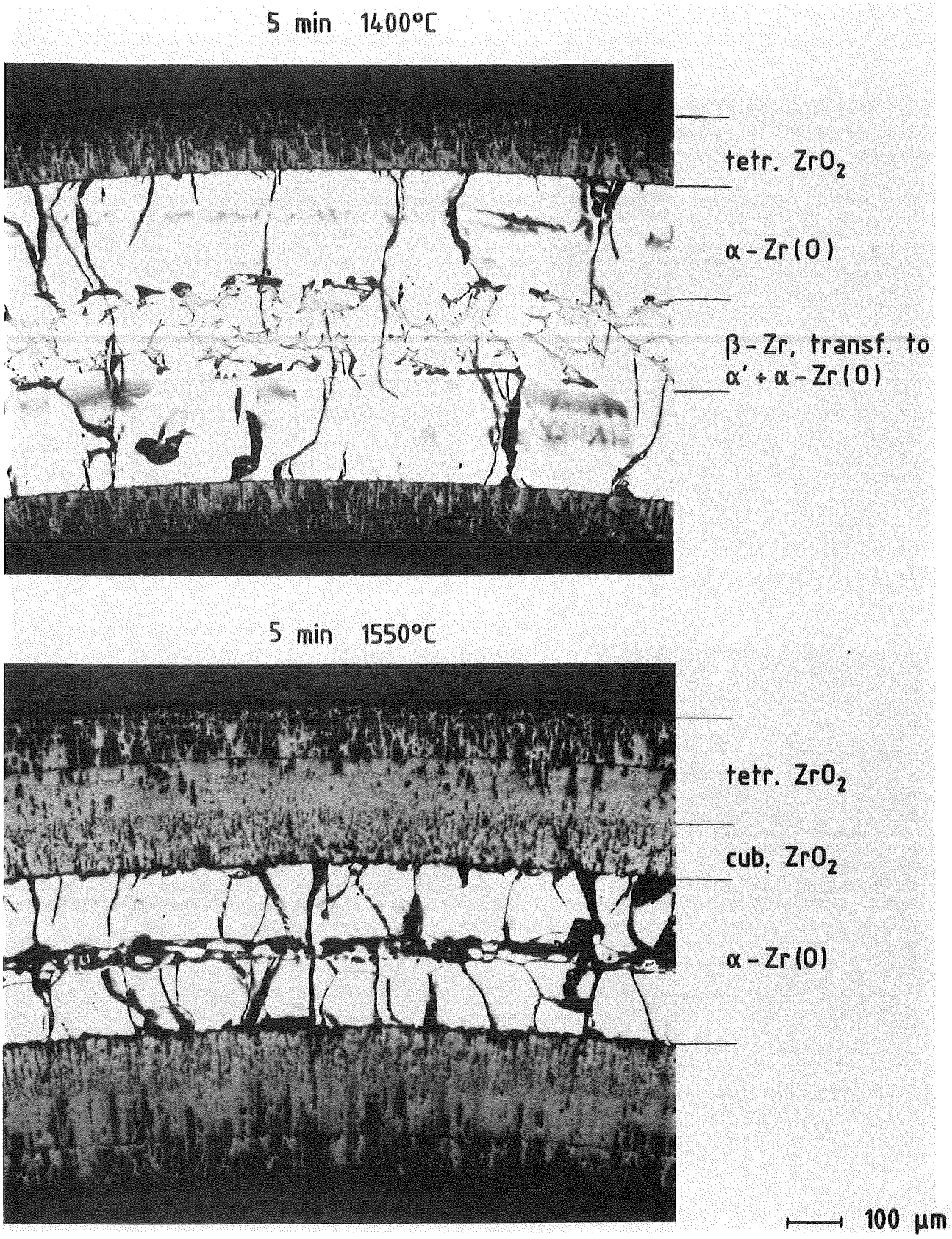


Fig. 86. Zircaloy 4/steam high-temperature oxidation

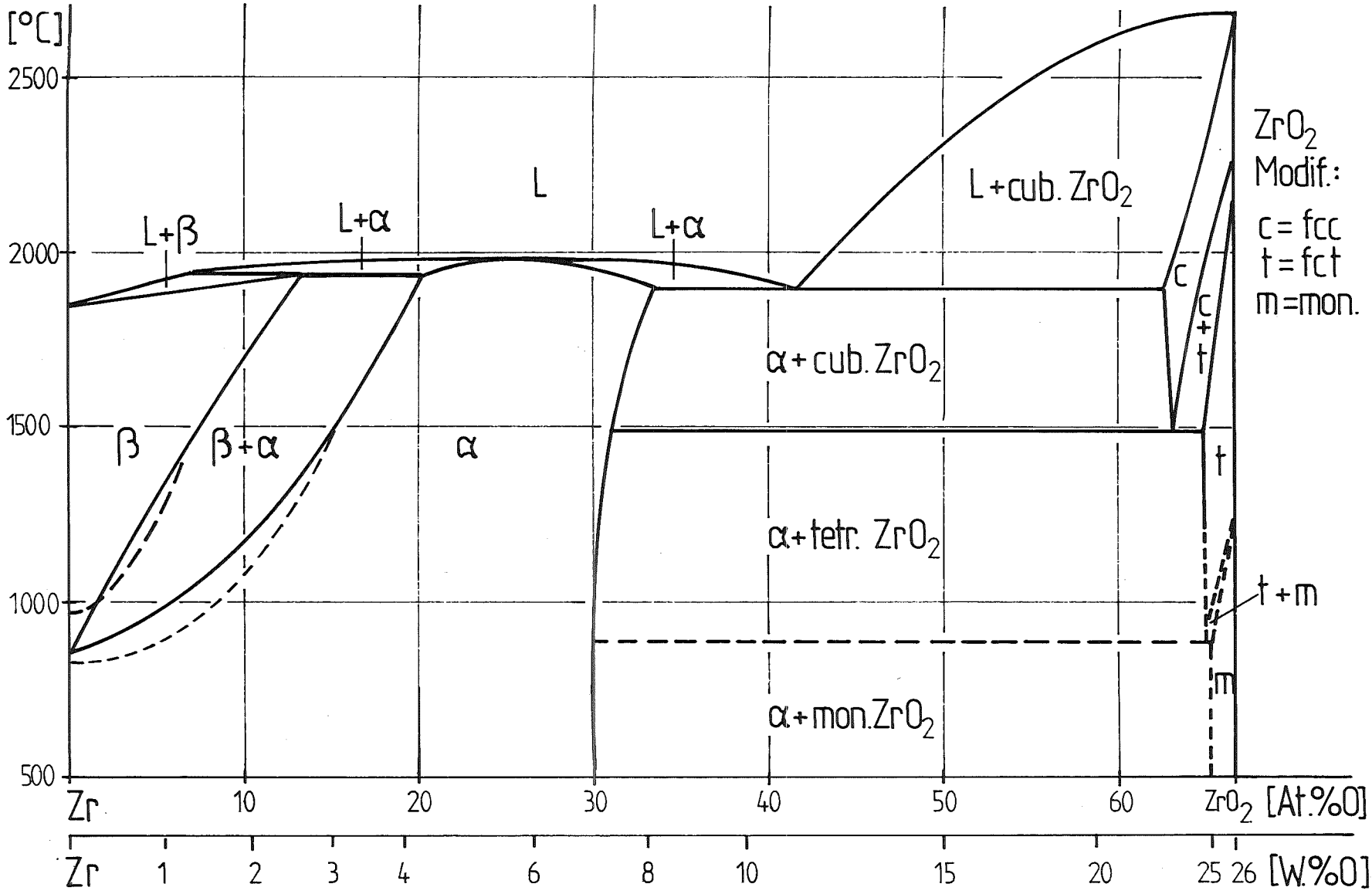


Fig. 87. Zirconium-oxygen phase diagram

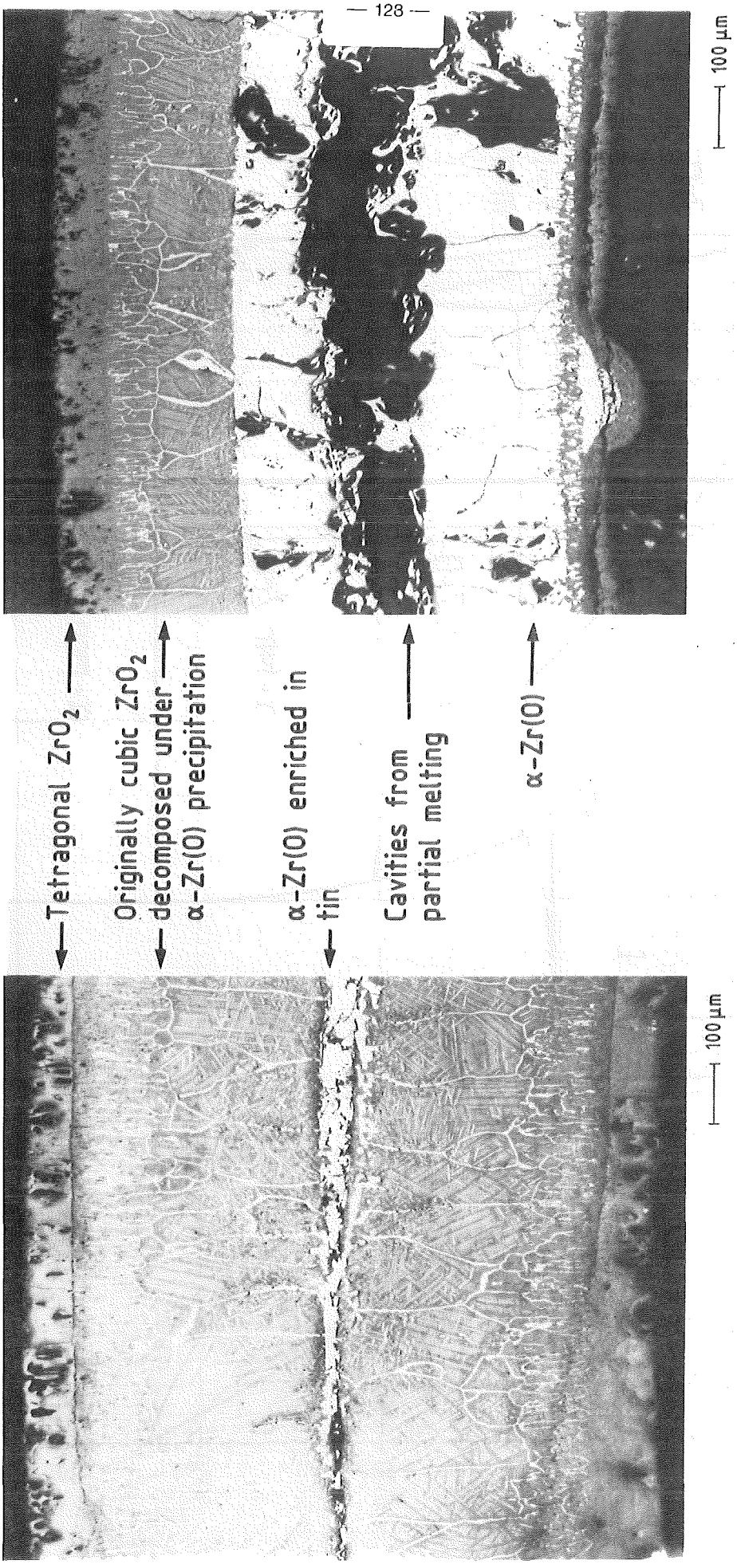


Fig. 88. HT oxidation of Zircaloy-4 without and with formation of metallic melt

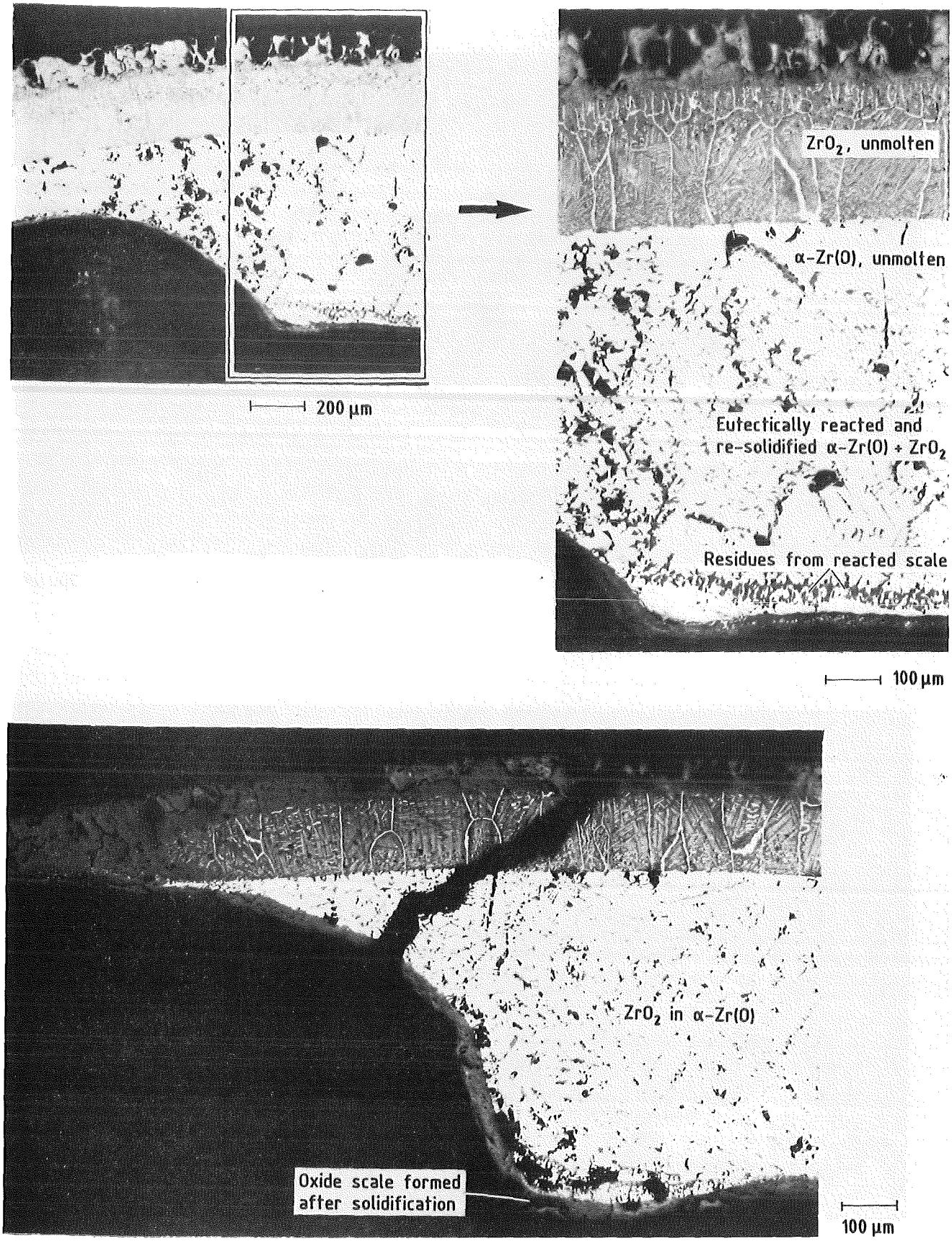


**Fig. 89. Boundary region between unmolten and re-solidified Zircaloy-4 cladding**

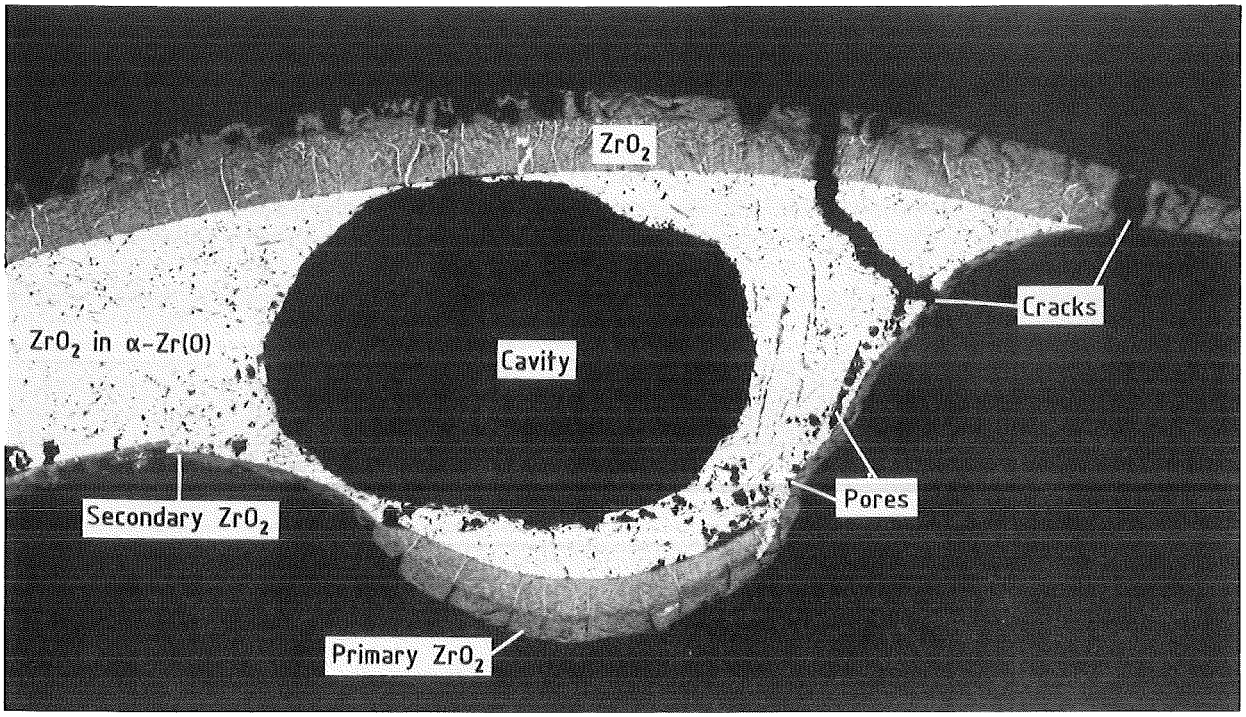


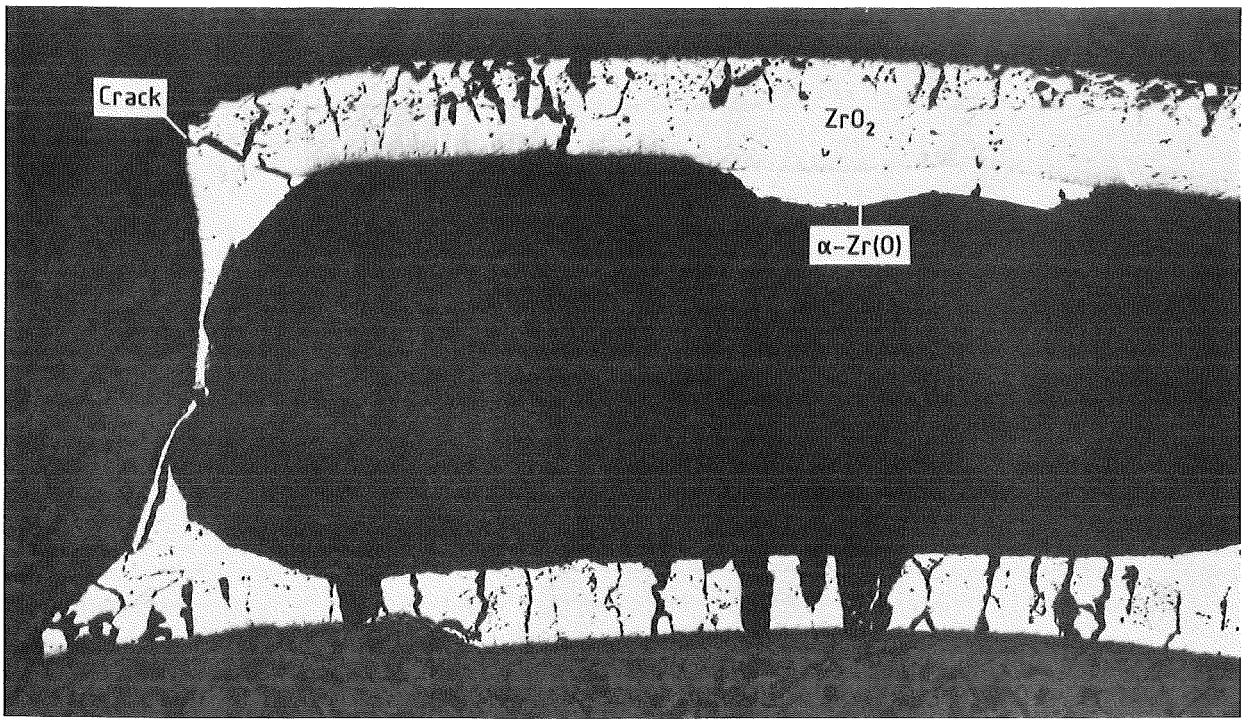


Fig. 90. Relocation of Zircaloy-4 melt

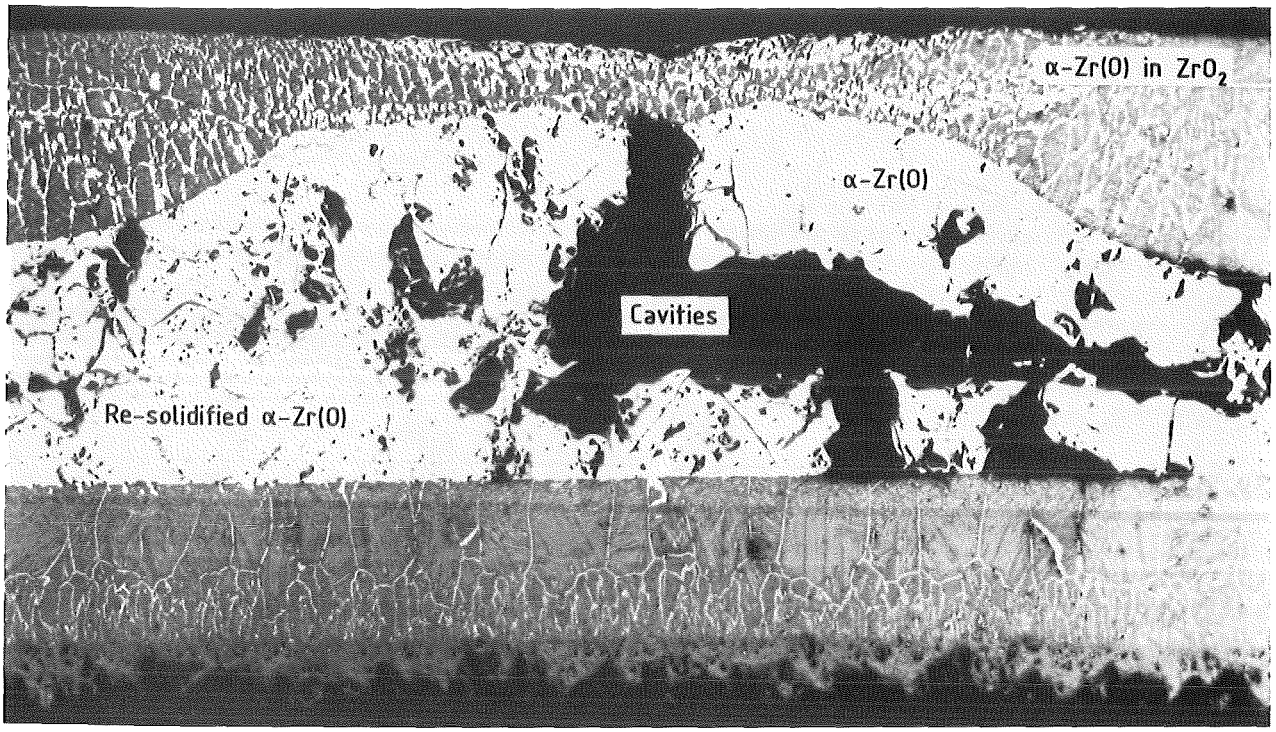


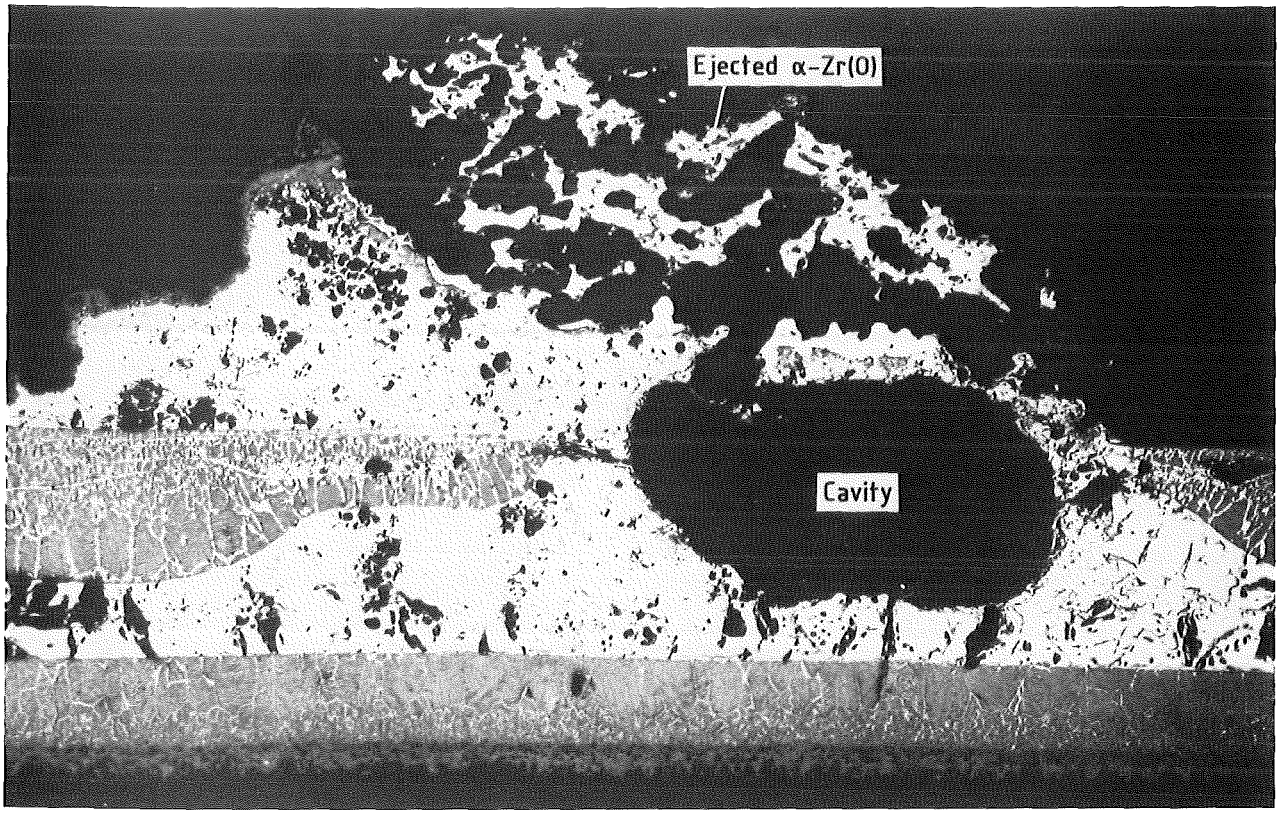


Fig. 91. Penetration of Zircaloy-4 melt through dissolved oxide scale

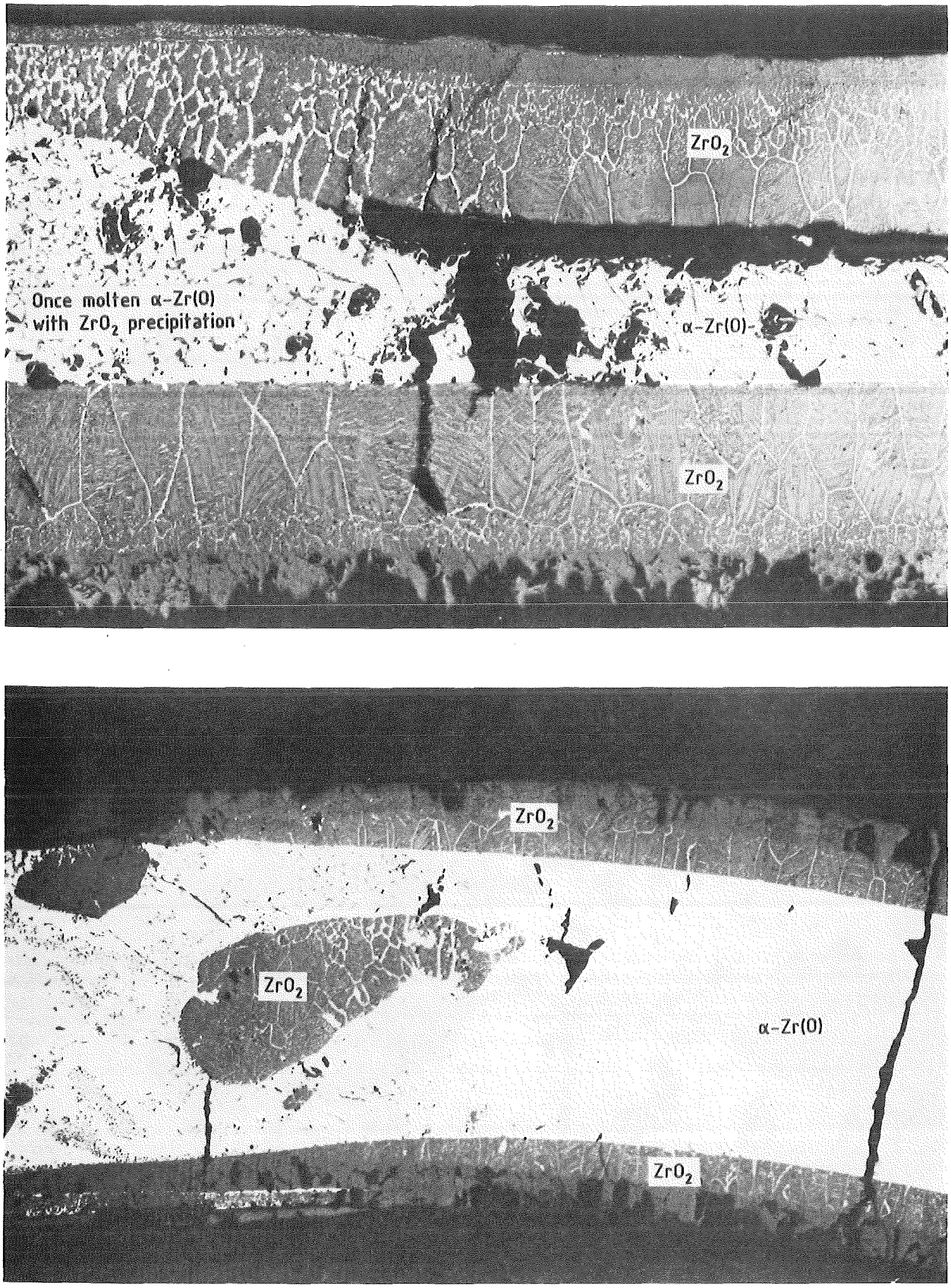


Fig. 92. Liquefaction of $ZrO_2$ scale by eutectic formation with metallic Zircaloy-4

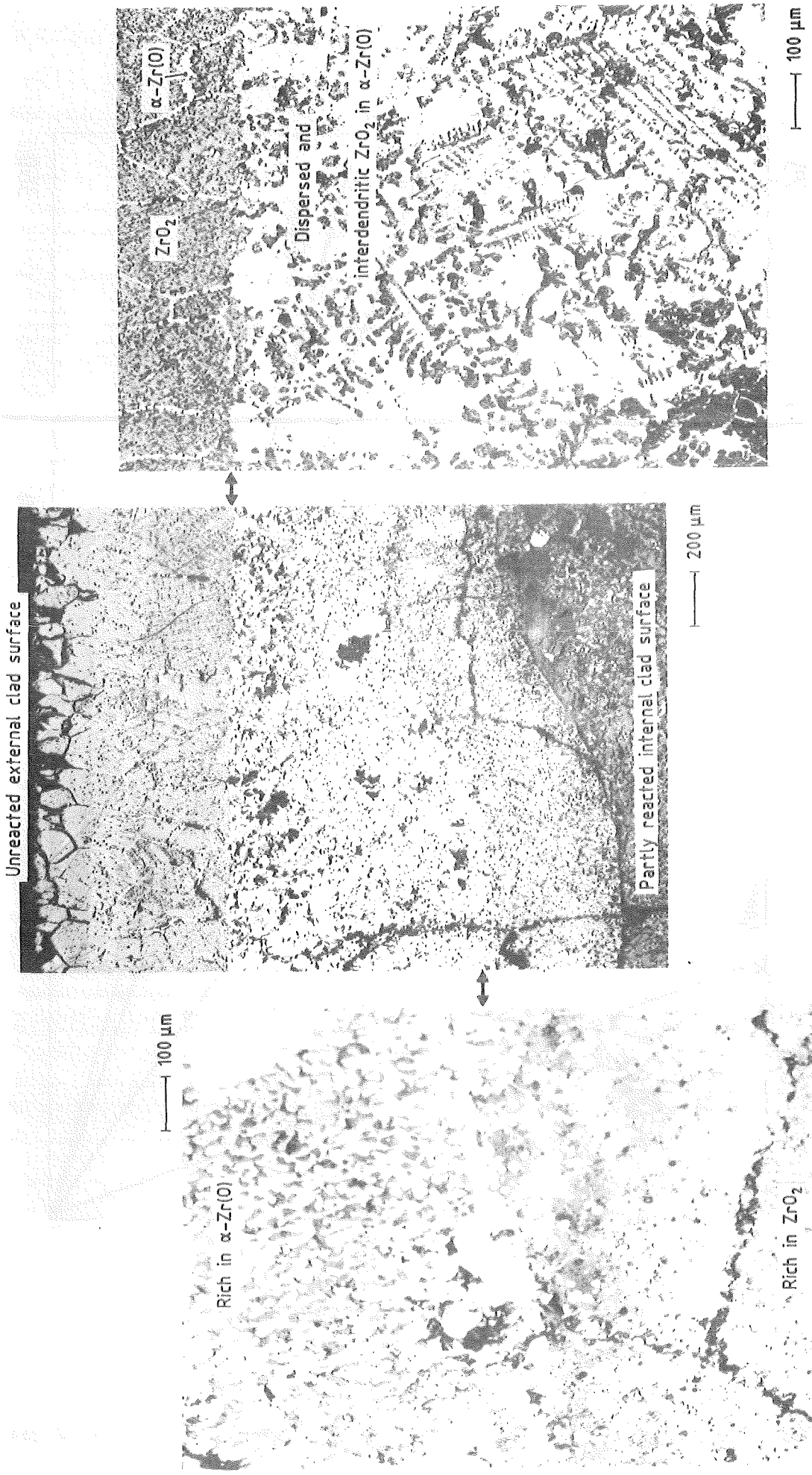


**Fig. 93. Microstructure of the α-Zr(0)/$ZrO_2$ eutectic**

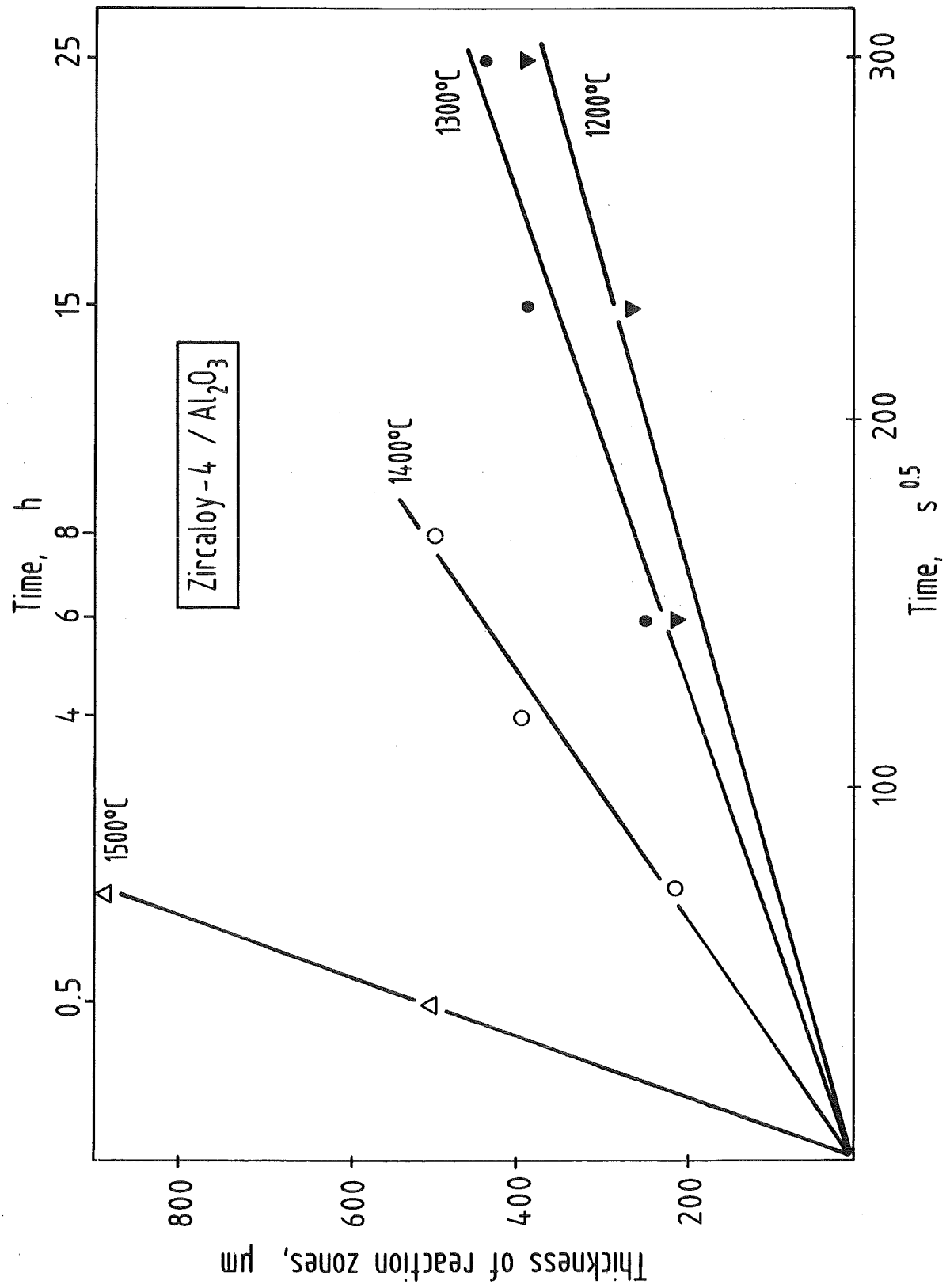


**Fig. 94. Chemical reaction of $Al_2O_3$ with Zircaloy-4 as function of $\sqrt{t}$**

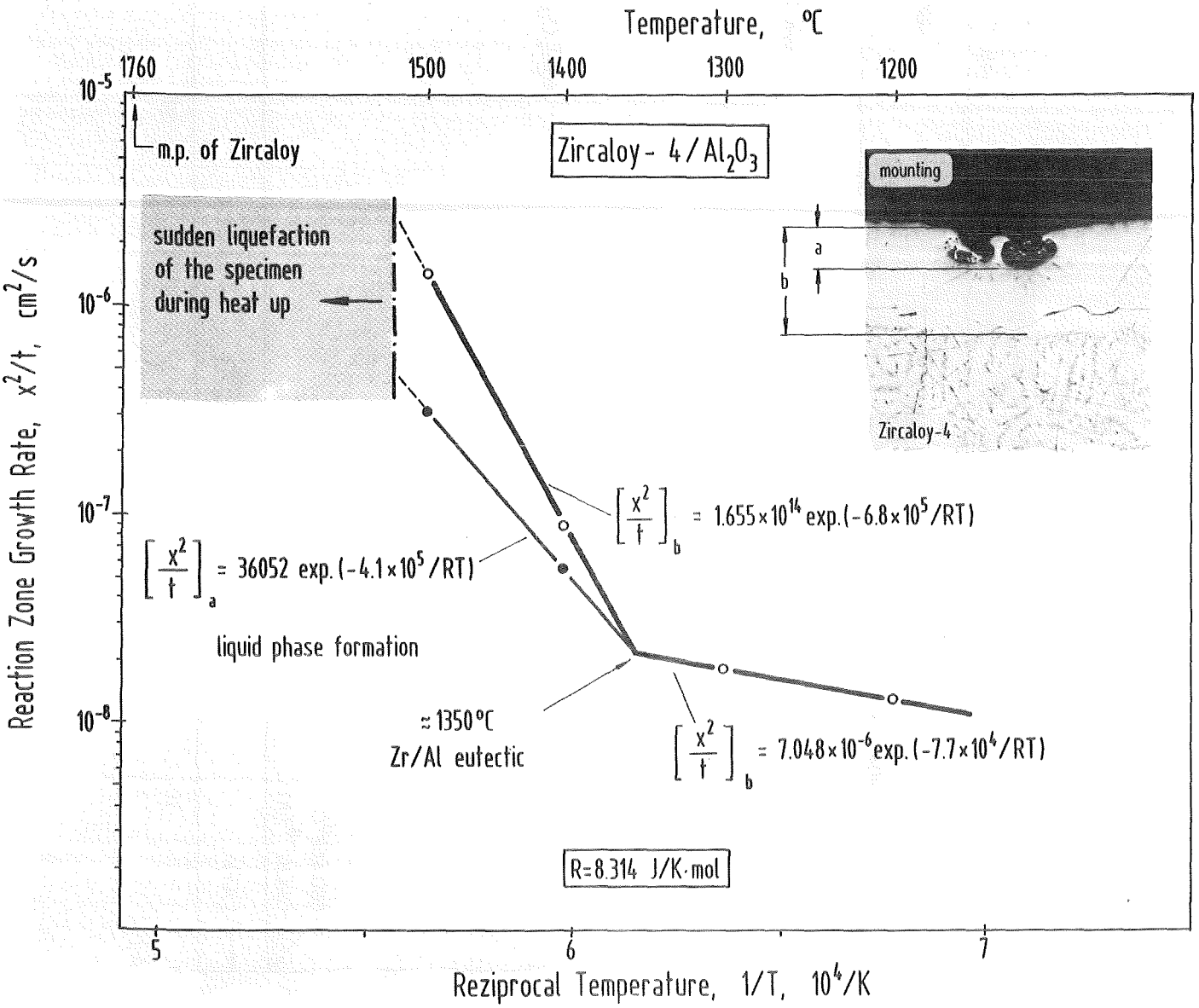


**Fig. 95. Zircaloy-4/$Al_2O_3$ reaction zone growth rates as function of reciprocal temperature**

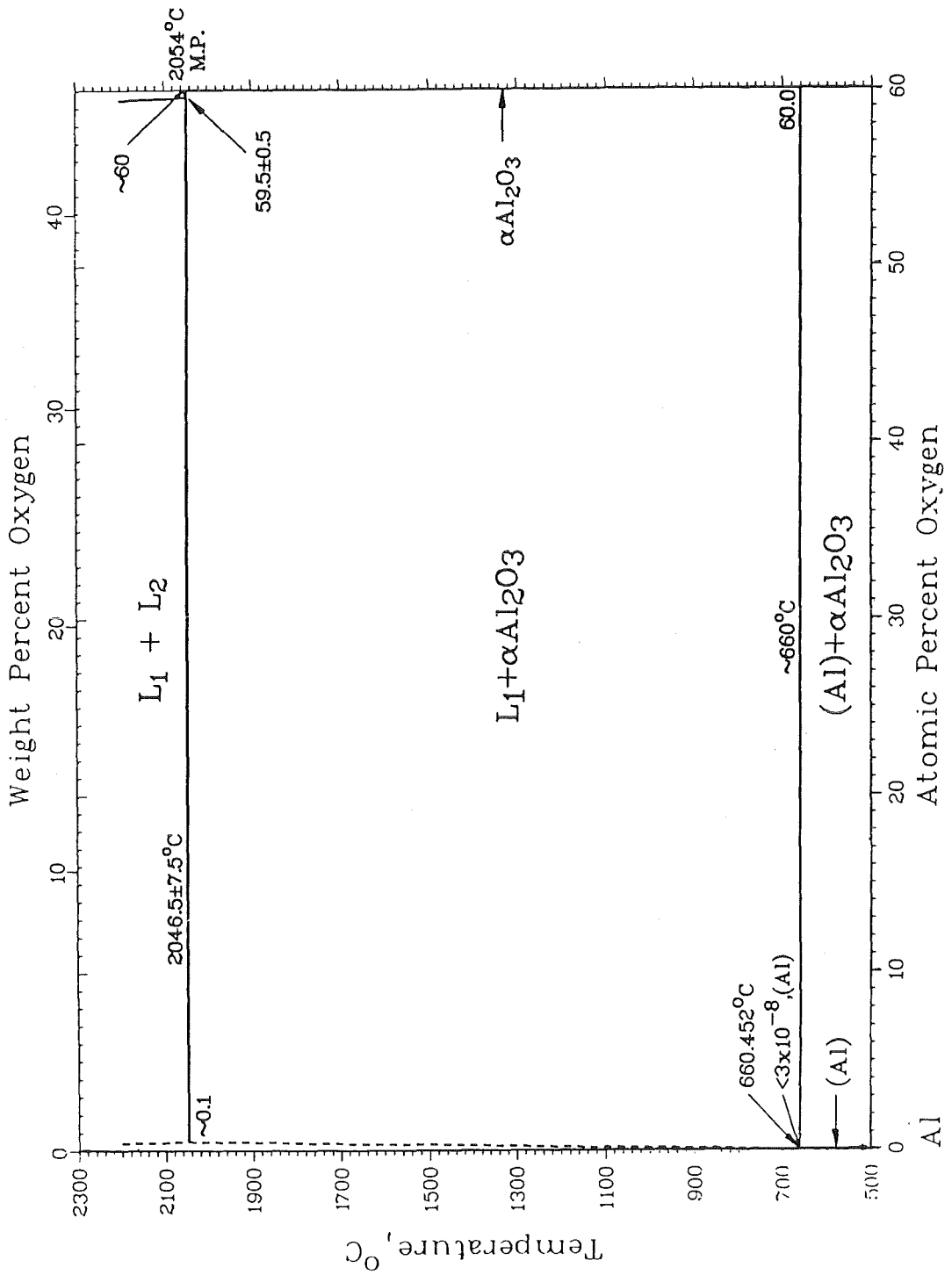


**Fig. 96. Equilibrium phase diagram of the system Al-0**

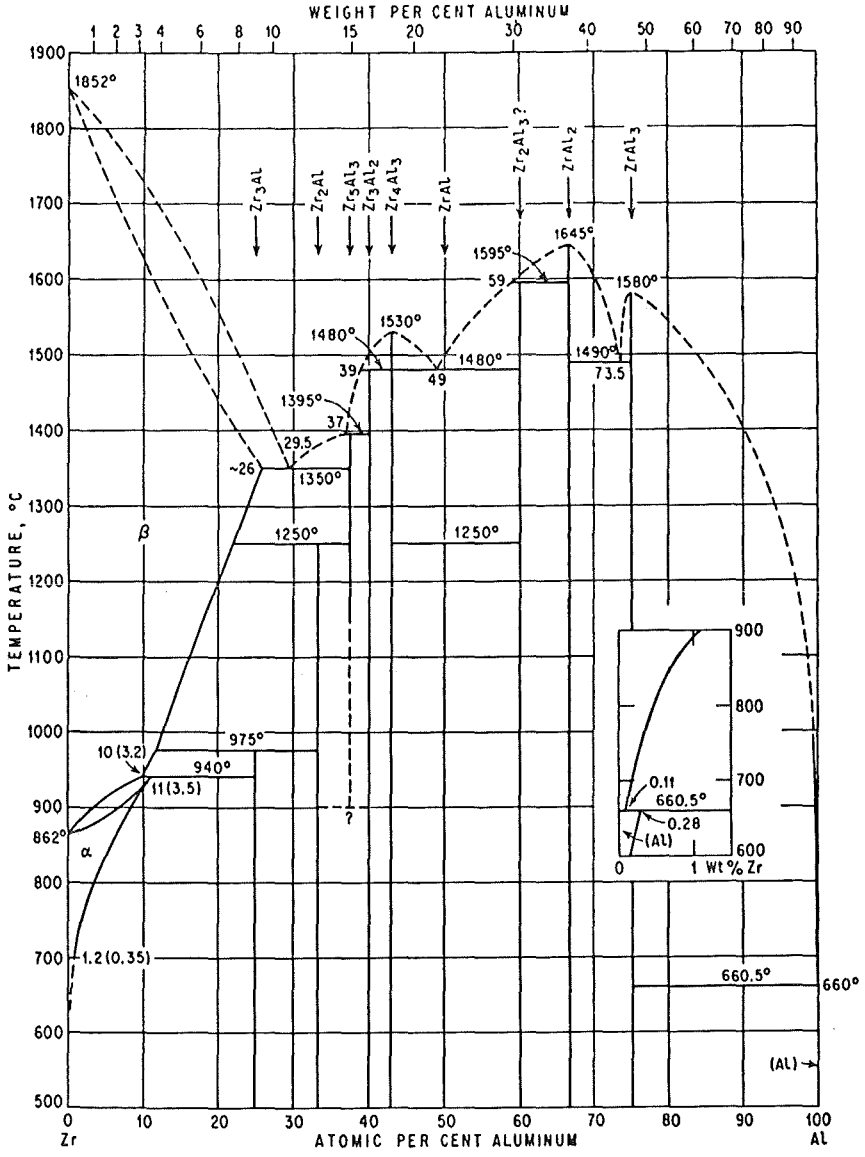


**Fig. 97. Eutectic system Zr-Al**

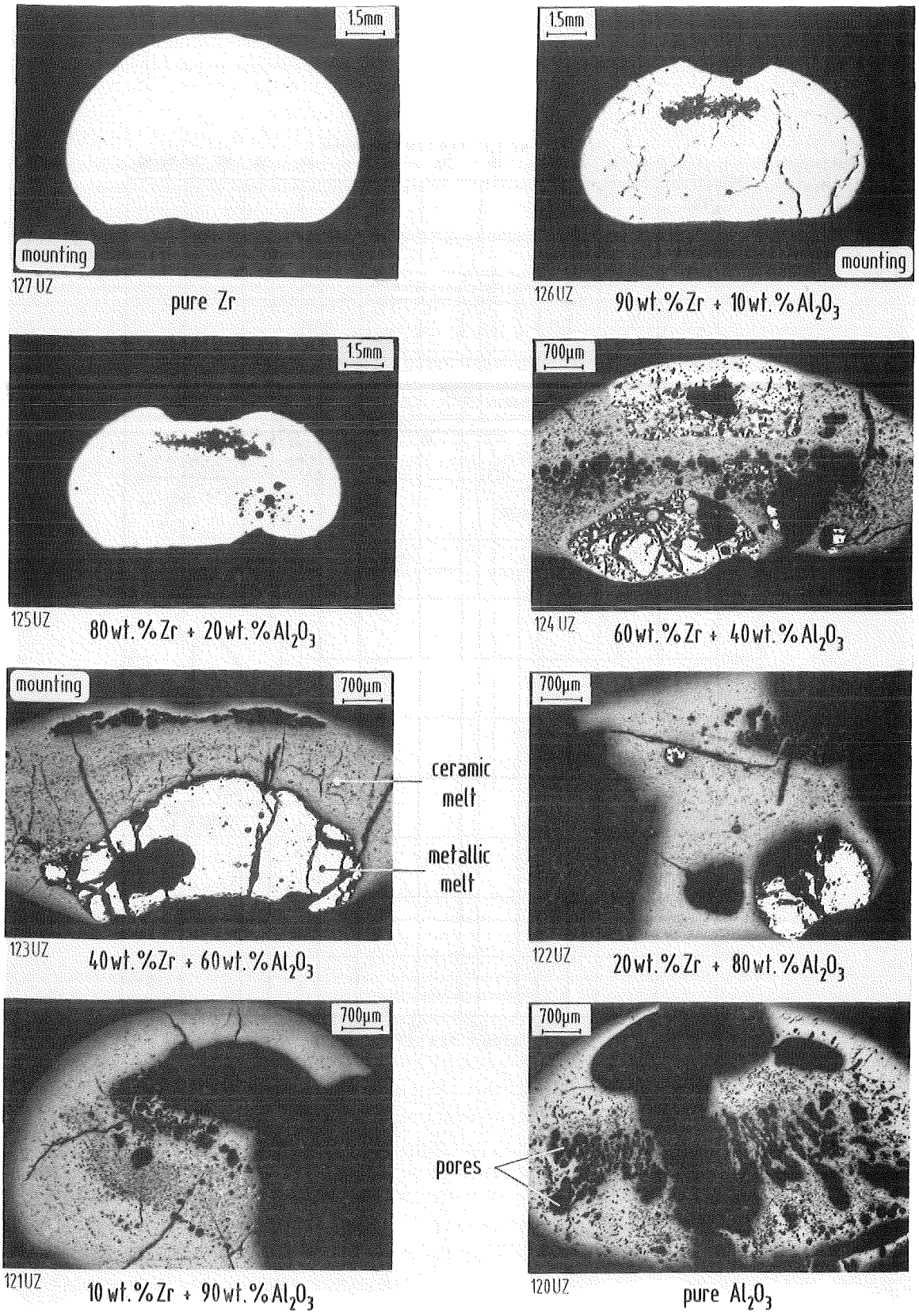


**Fig. 98. Macrostructure of molten (Zr + $Al_2O_3$) specimens in dependence on the initial composition**

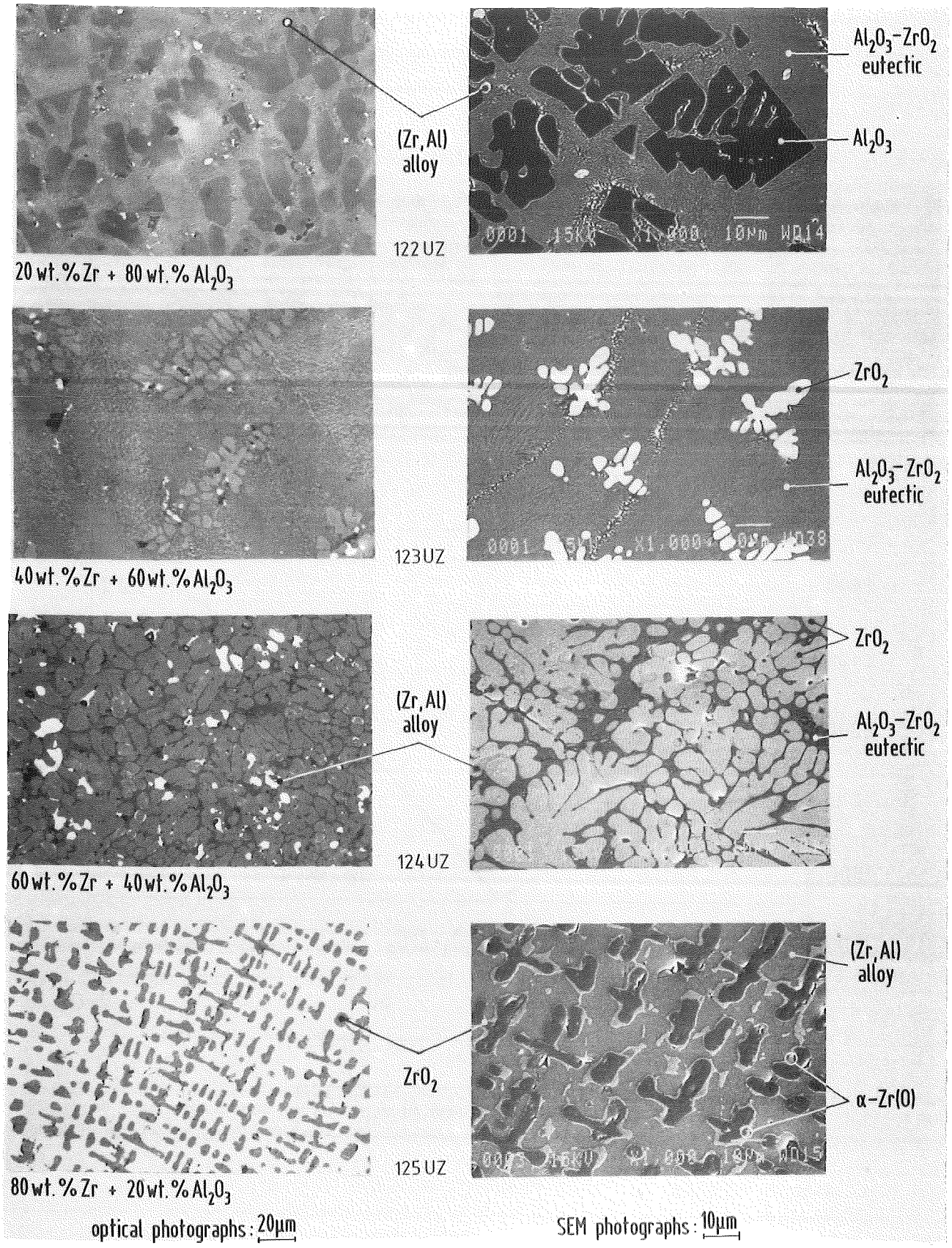


**Fig. 99. Microstructure of molten (Zr + $Al_2O_3$) specimens for various initial compositions**

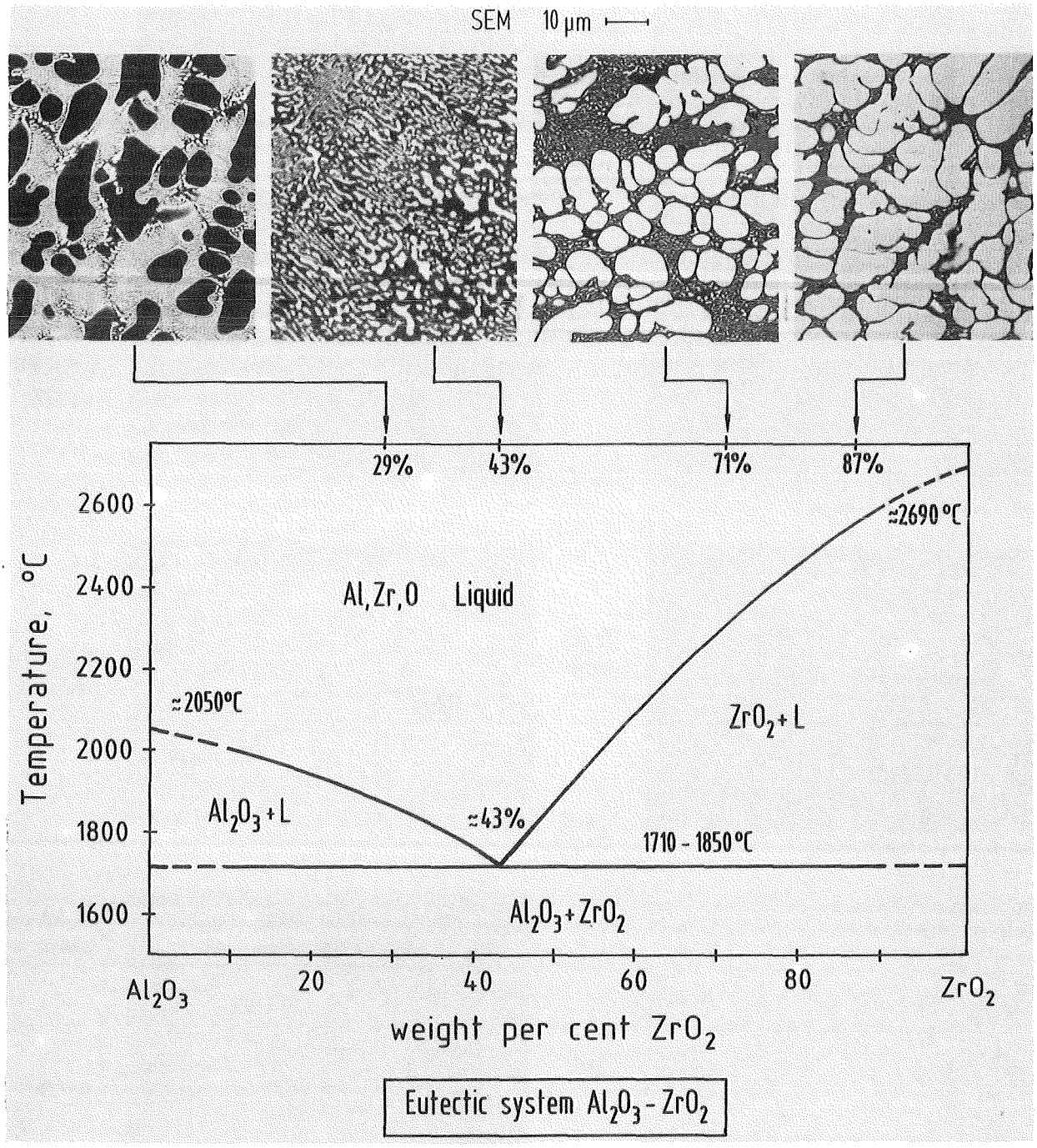


**Fig. 100. Microstructure of molten $Al_2O_3/ZrO_2$ specimens as function of composition**

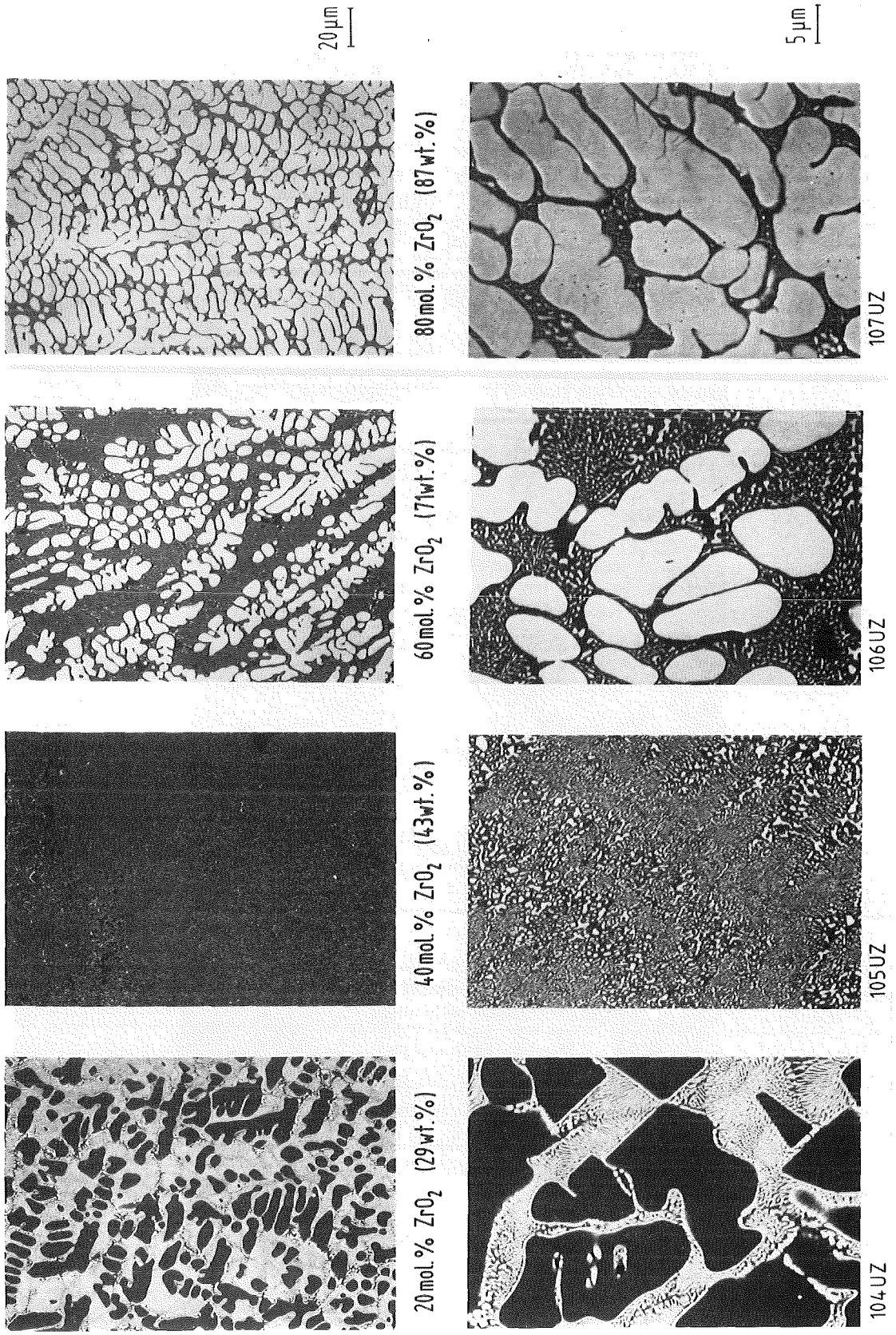


**Fig. 101. Microstructure of molten $ZrO_2 + Al_2O_3$ specimens as function of initial composition (SEM photographs)**

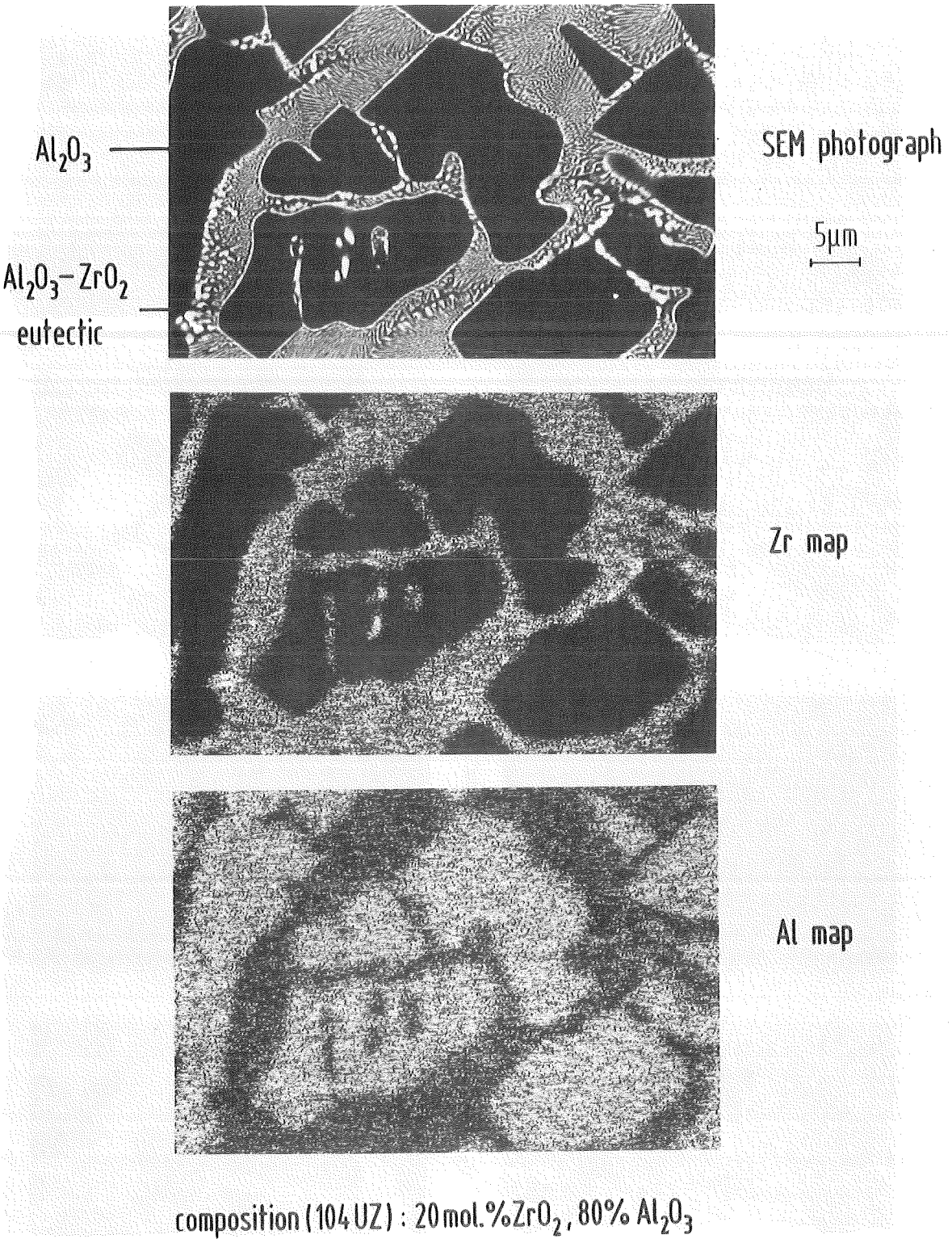


**Fig. 102. Zr and Al distribution in a molten $ZrO_2/Al_2O_3$ specimen**

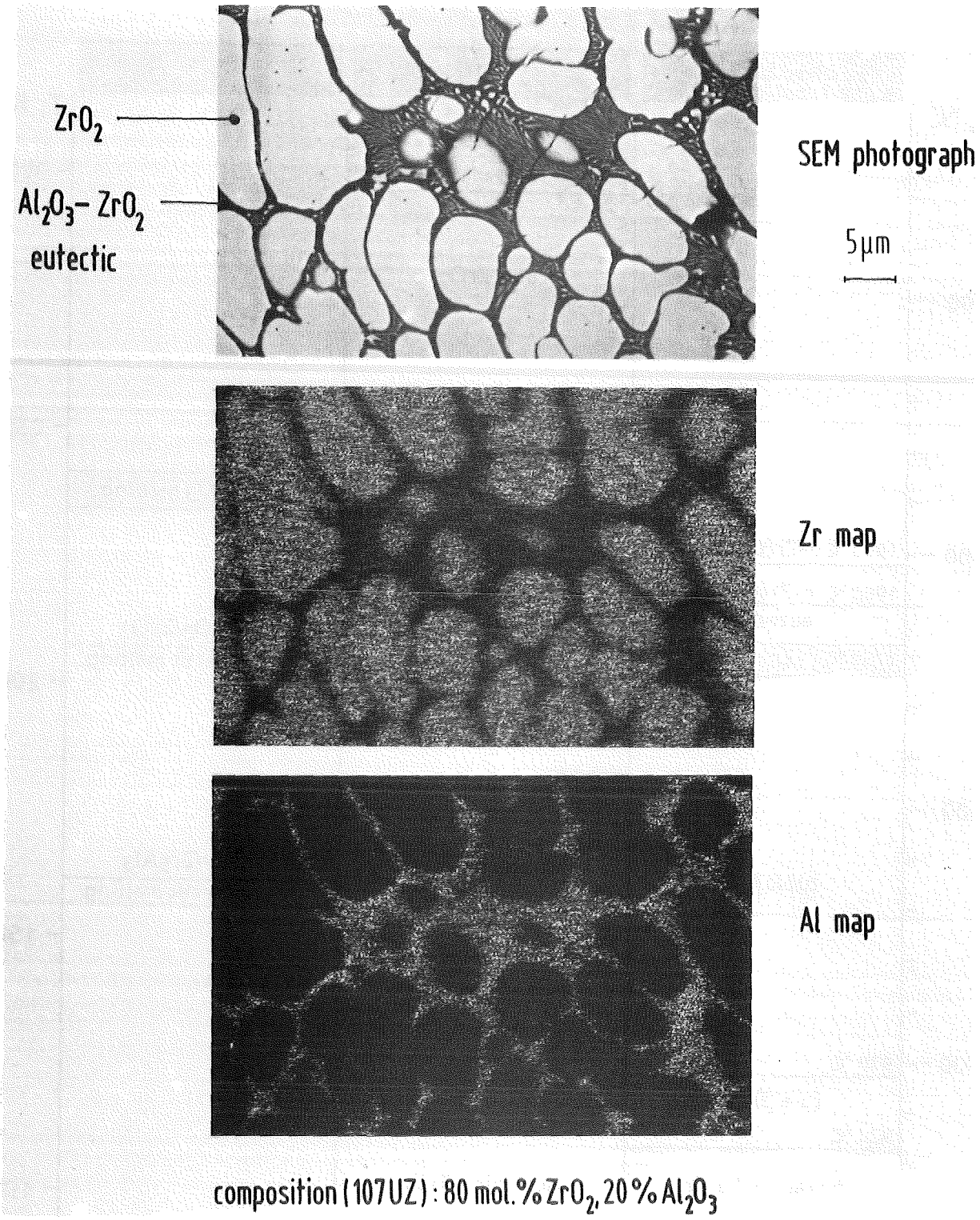


**Fig. 103. Zr and Al distribution in a molten $ZrO_2/Al_2O_3$ specimen**

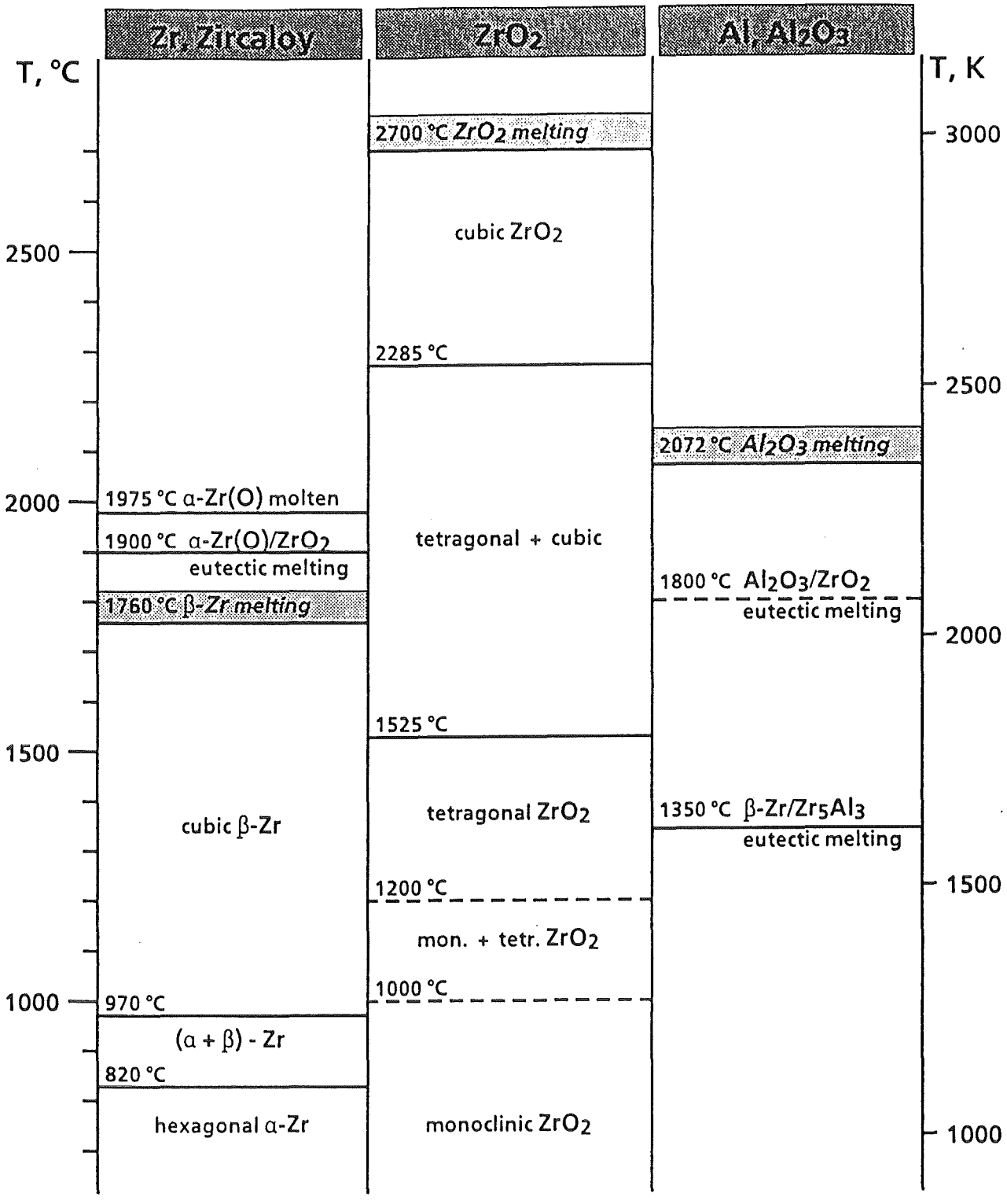


**Fig. 104. Phase transformation temperatures concerning Zircaloy cladding, its oxidation, and its interaction with $Al_2O_3$ (burnable poison rod material)**

# Appendix

## Appendix

### 1. Macrophotographs of Cross Sections of CORA Bundle B

The elevations of the cross-sectional cuts are given in Table A-1 and are illustrated in Fig. A-1 . The photographs of the individual cross sections of CORA bundle B are given in Figs. A-2 through A-7 .

### 2. Macrophotographs of Cross Sections of CORA Bundle C

The elevations of the cross-sectional cuts are given in Table A-2 and are illustrated in Fig. A-8 . The photographs of the individual cross sections of CORA bundle C are given in in Figs. A-9 through A-23 .

### 3. Preparation of the Metallographic Samples

The procedure for the preparation of the metallographic samples is provided with Table A-3 .

**Table A-1:** Cross Section Elevations of CORA Bundle B

| Cross Section No. | | Elevation*) |
|---|---|---|
| B04 | top | -55 mm |
| | bottom | -71 mm |
| B07 | top | 0 mm |
| | bottom | -16 mm |
| B08 | top | 91 mm |
| | bottom | 75 mm |
| B09 | top | 109 mm |
| | bottom | 93 mm |
| B10 | top | 251 mm |
| | bottom | 235 mm |
| B11 | top | 269 mm |
| | bottom | 253 mm |
| B13 | top | 507 mm |
| | bottom | 491 mm |
| B14 | top | 901 mm |
| | bottom | 885 mm |
| B15 | top | 919 mm |
| | bottom | 903 mm |
| B16 | top | 1141 mm |
| | bottom | 1125 mm |
| B17 | top | 1159 mm |
| | bottom | 1143 mm |

*) Referred to the bottom of heated zone (EL 5121).
Dimensions are based on a height of the sample of 16 mm; marks for cutting were 18 mm apart.

**Elevations of Remnants:**

| | |
|---|---|
| No. 3 top -73 mm | No. e bottom + 1 mm |
| No. 5 bottom -53 mm | No. e top + 73 mm |
| No. 6 top -18 mm | No. g bottom + 271 mm |

Fig. A-1. CORA test B, bundle sectioning

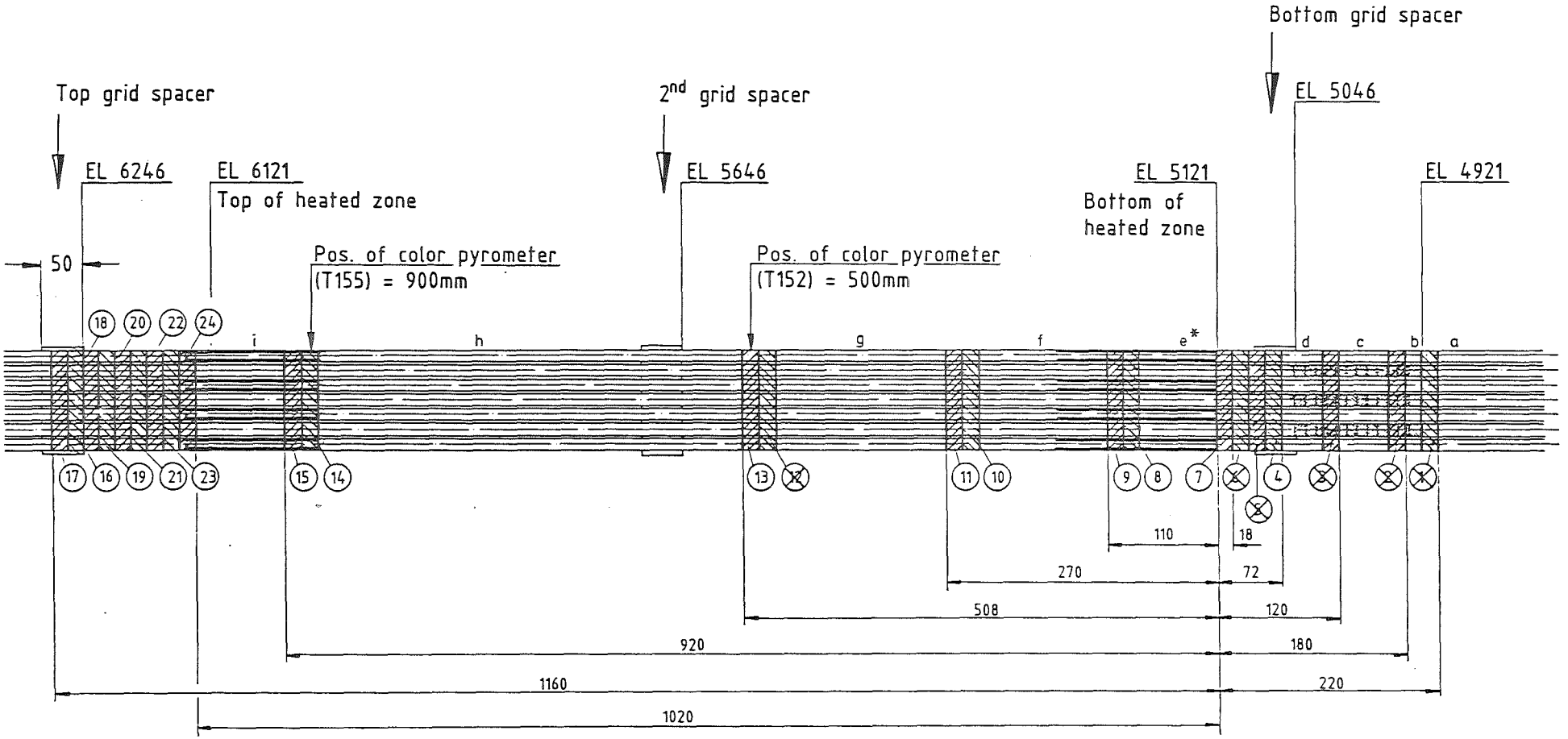


*) "e" is additionally cut into 6 vertical sections

Height of each sample : 16mm (Marking distance 18mm)

Bundle viewed from 30°, 120°, 210°, and 300°, respectively

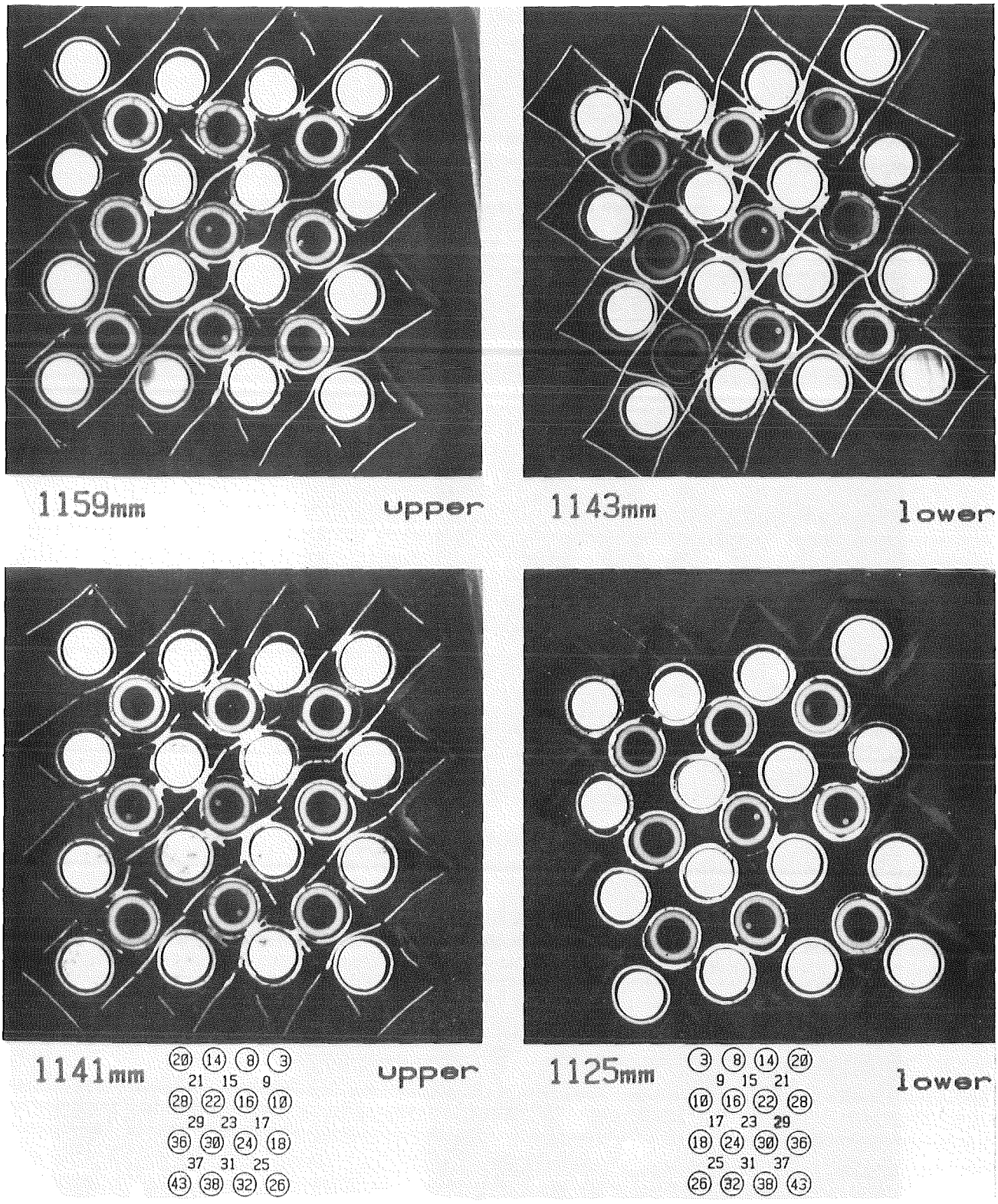


Fig. A-2. Cross sections of CORA bundle B

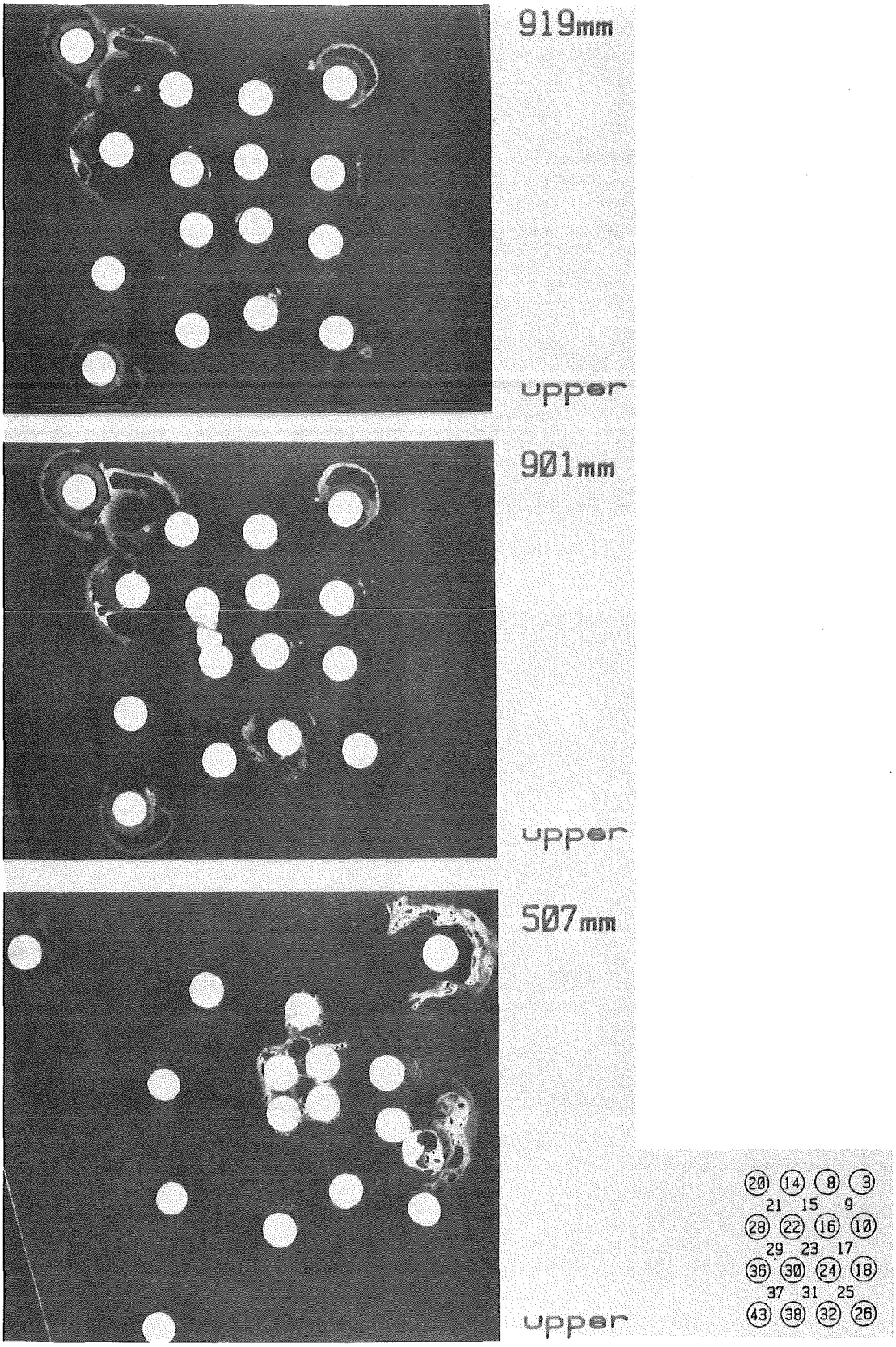


**Fig. A-3. Cross sections of CORA bundle B**

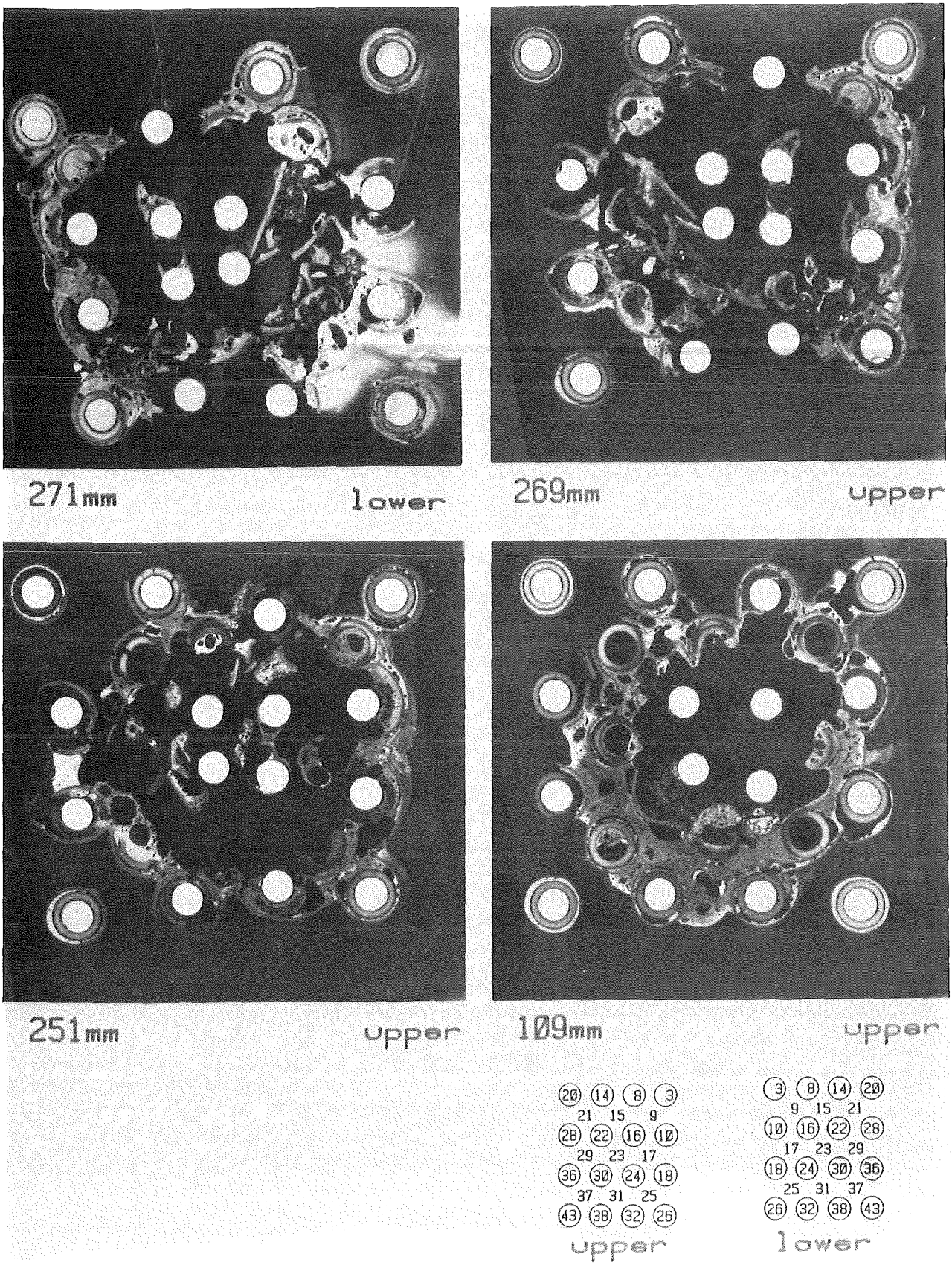


**Fig. A-4. Cross sections of CORA bundle B**

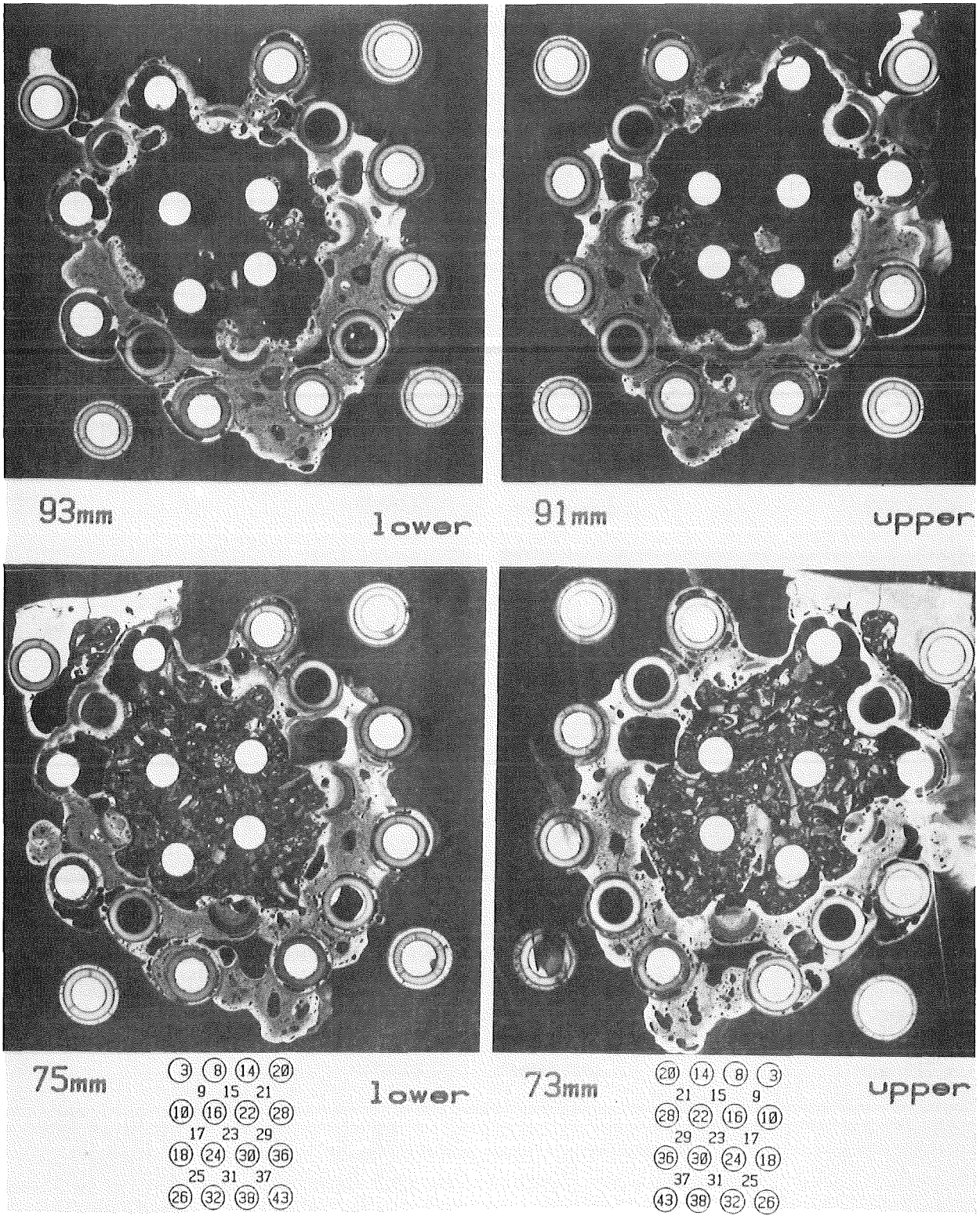


Fig. A-5. Cross sections of CORA bundle B

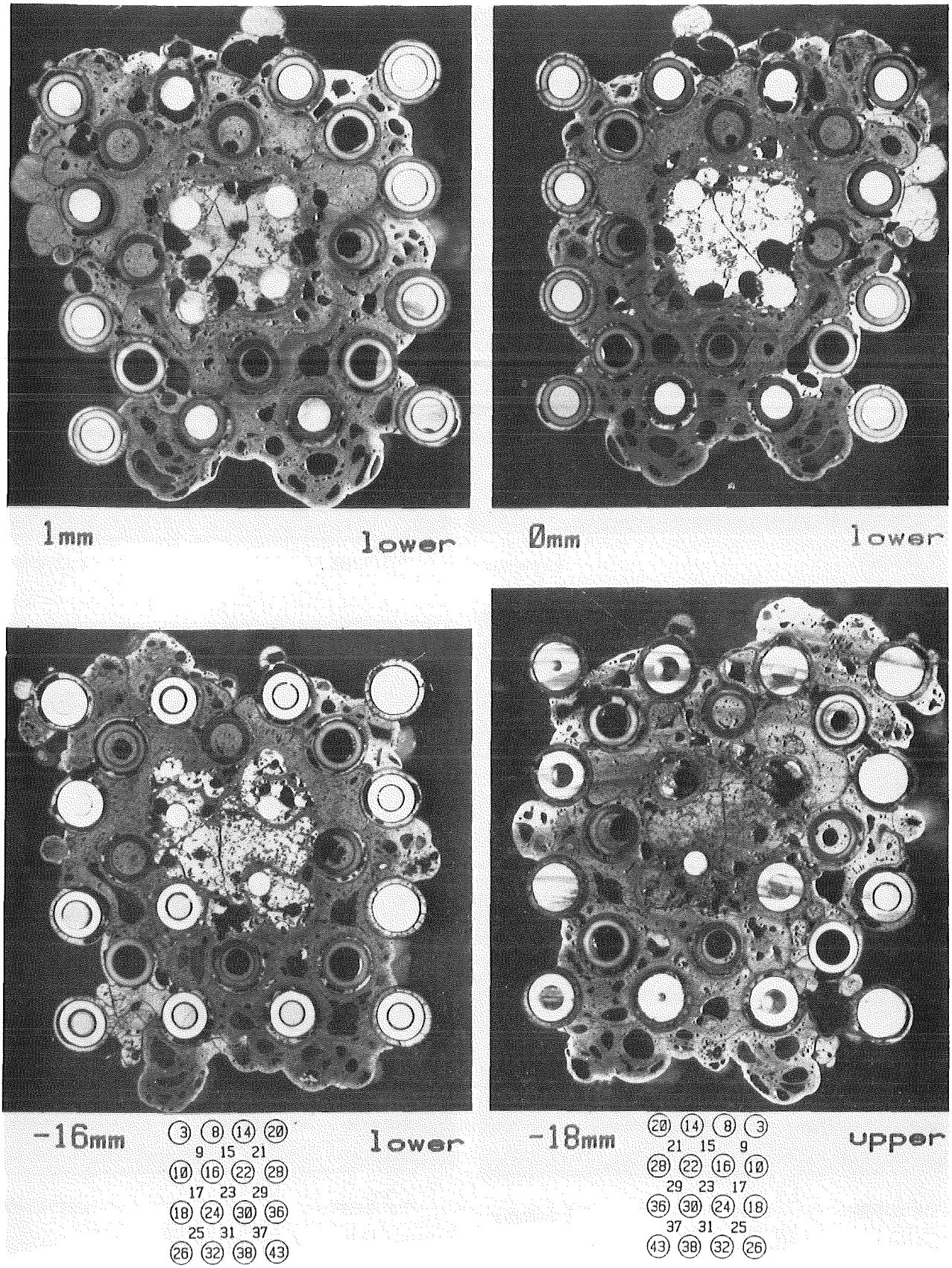


Fig. A-6. Cross sections of CORA bundle B

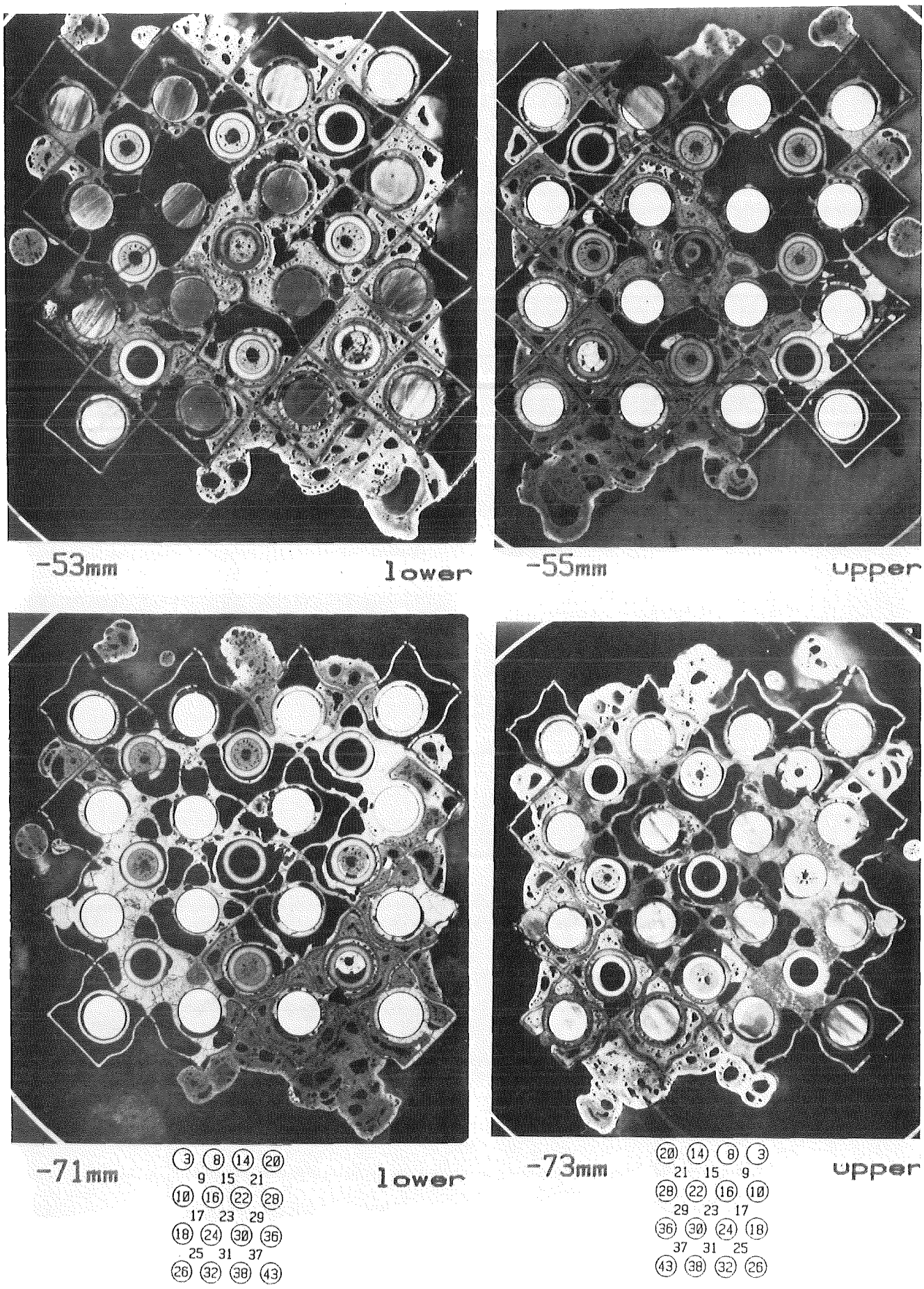


Fig. A-7. Cross sections of CORA bundle B

Table A-2: Cross Section Elevations of CORA Bundle C

| Cross Sect. No. | | Elevation*) | No. | | Elevation*) |
|---|---|---|---|---|---|
| C01 | top | -19 mm | C17 | top | 664 mm |
| | bottom | -32 mm | | bottom | 651 mm |
| C02 | top | - 4 mm | C18 | top | 679 mm |
| | bottom | -17 mm | | bottom | 666 mm |
| C03 | top | + 11 mm | C19 | top | 694 mm |
| | bottom | - 2 mm | | bottom | 681 mm |
| C04 | top | 26 mm | C20 | top | 709 mm |
| | bottom | 13 mm | | bottom | 696 mm |
| C5/6 | top | 56 mm | C21 | top | 724 mm |
| | bottom | 28 mm | | bottom | 711 mm |
| C07 | top | 71 mm | C22 | top | 809 mm |
| | bottom | 58 mm | | bottom | 796 mm |
| C08 | top | 86 mm | C23 | top | 824 mm |
| | bottom | 73 mm | | bottom | 811 mm |
| C09 | top | 224 mm | C24 | top | 899 mm |
| | bottom | 211 mm | | bottom | 886 mm |
| C10 | top | 239 mm | C25 | top | 914 mm |
| | bottom | 226 mm | | bottom | 901 mm |
| C11 | top„ | 314 mm | C26 | top | 984 mm |
| | bottom | 301 mm | | bottom | 971 mm |
| C12 | top | 329 mm | C27 | top | 999 mm |
| | bottom | 316 mm | | bottom | 986 mm |
| C13 | top | 484 mm | C28 | top | 1064 mm |
| | bottom | 471 mm | | bottom | 1051 mm |
| C14 | top | 499 mm | C29 | top | 1079 mm |
| | bottom | 486 mm | | bottom | 1066 mm |
| C15 | top | 634 mm | C30 | top | 1094 mm |
| | bottom | 621 mm | | bottom | 1081 mm |
| C16 | top | 649 mm | | | |
| | bottom | 636 mm | | | |

*) Referred to the bottom of the heated zone (EL 5121).
Sample height 13 mm, marking distance for cutting 15 mm.

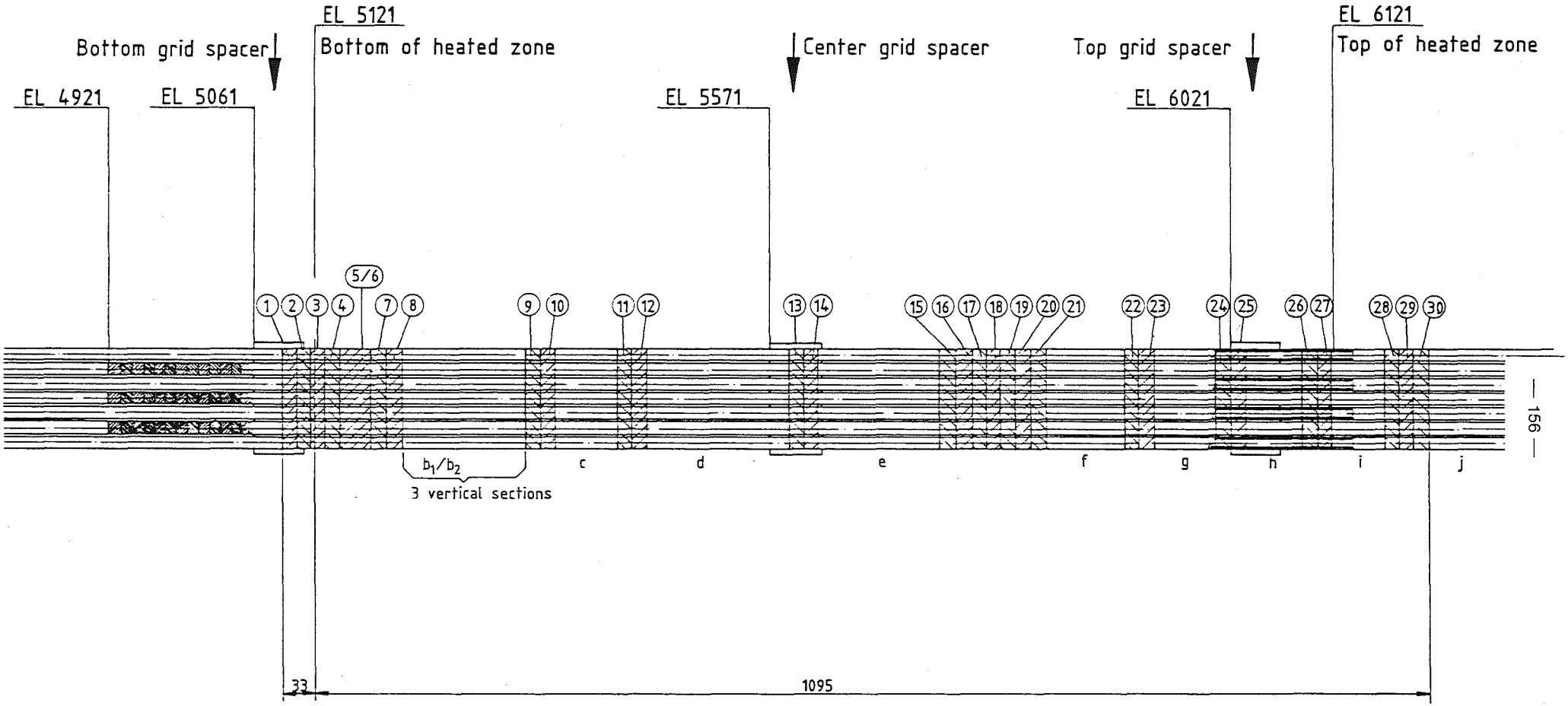


# Fig. A-8. CORA test C, bundle sectioning

Height of sample : 13mm (marking distance = 15mm)

Bundle viewed from 30°, 120°, 210° and 300° respectively

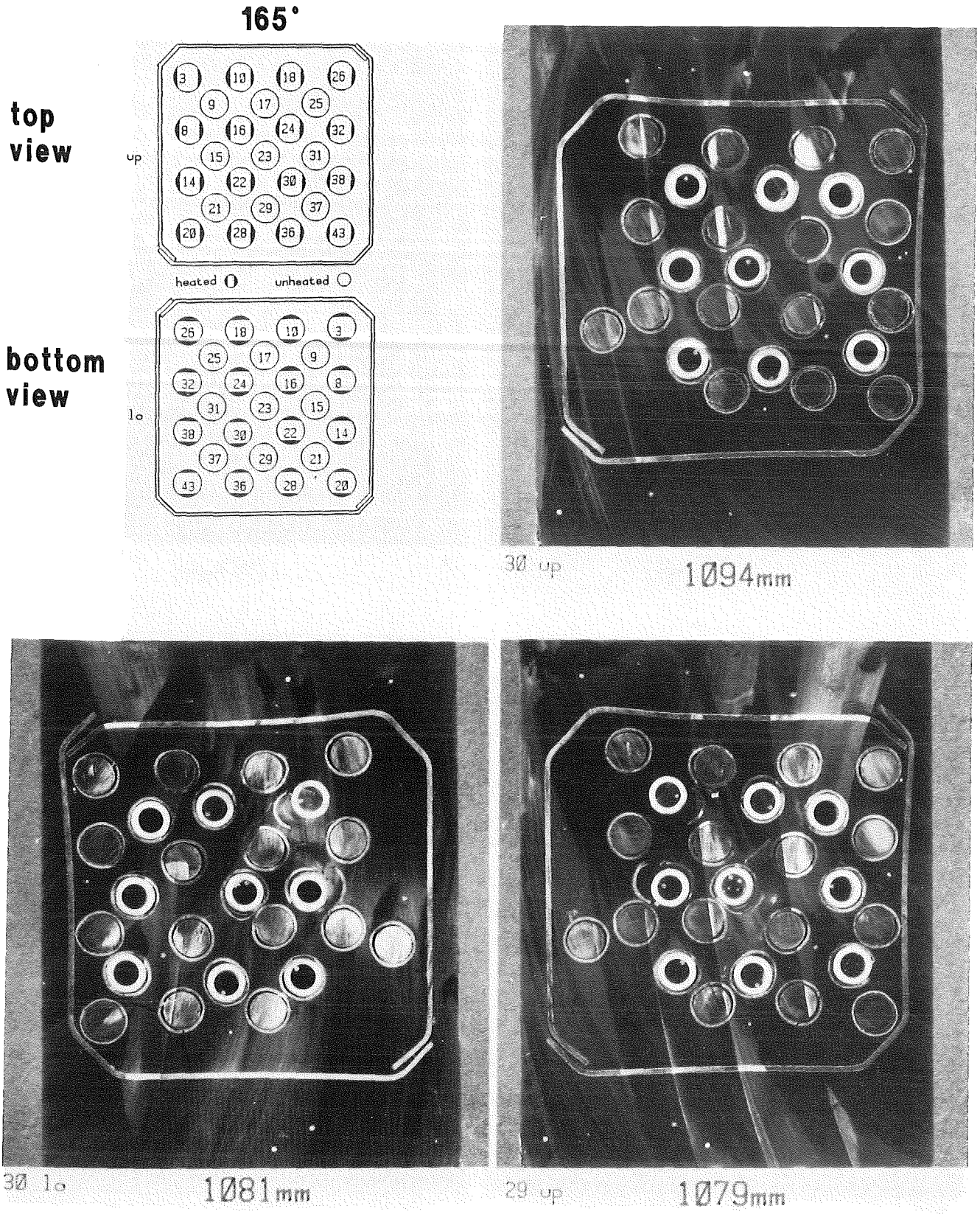


Fig. A-9. Cross sections of CORA bundle C

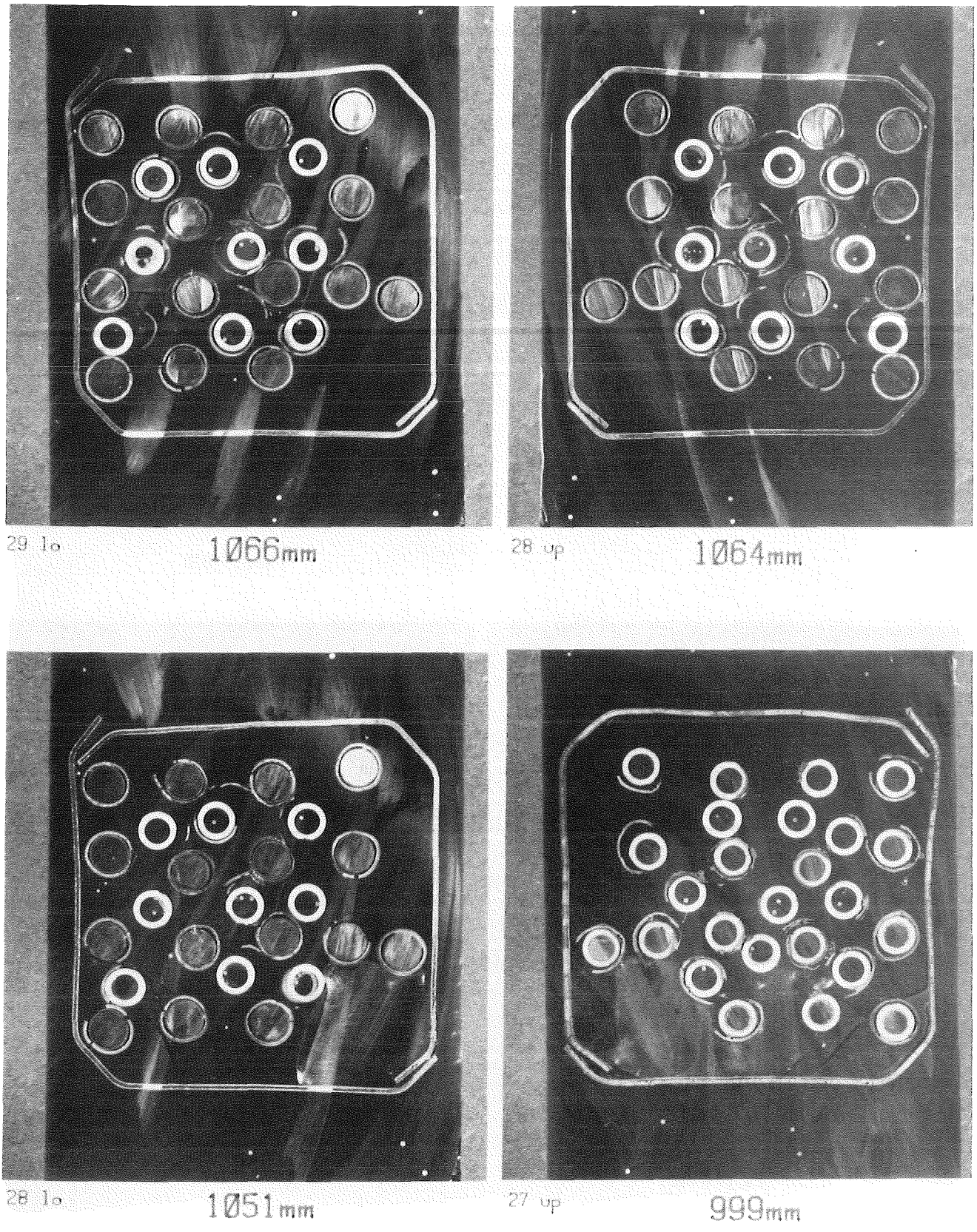


**Fig. A-10. Cross sections of CORA bundle C**

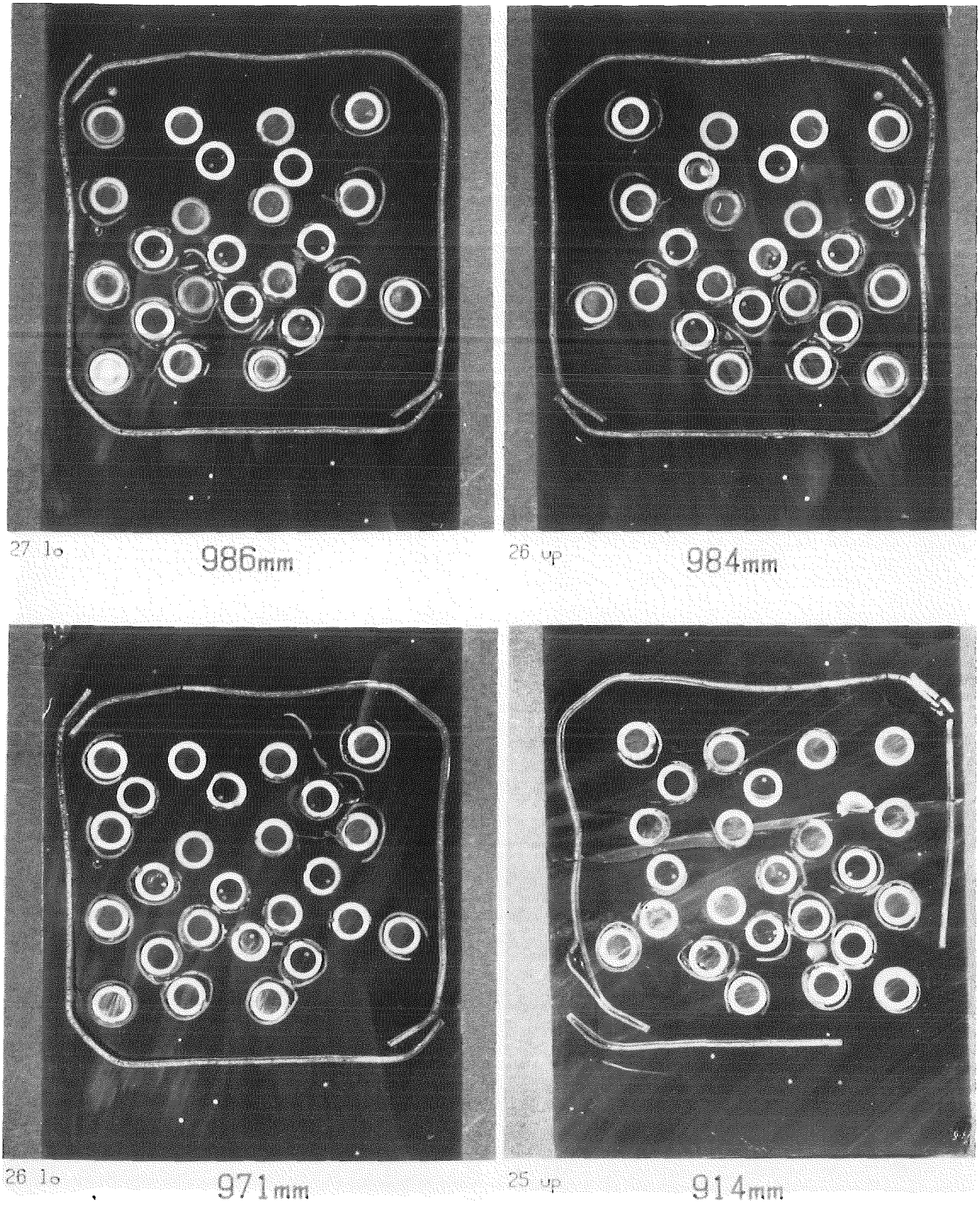


Fig. A-11. Cross sections of CORA bundle C

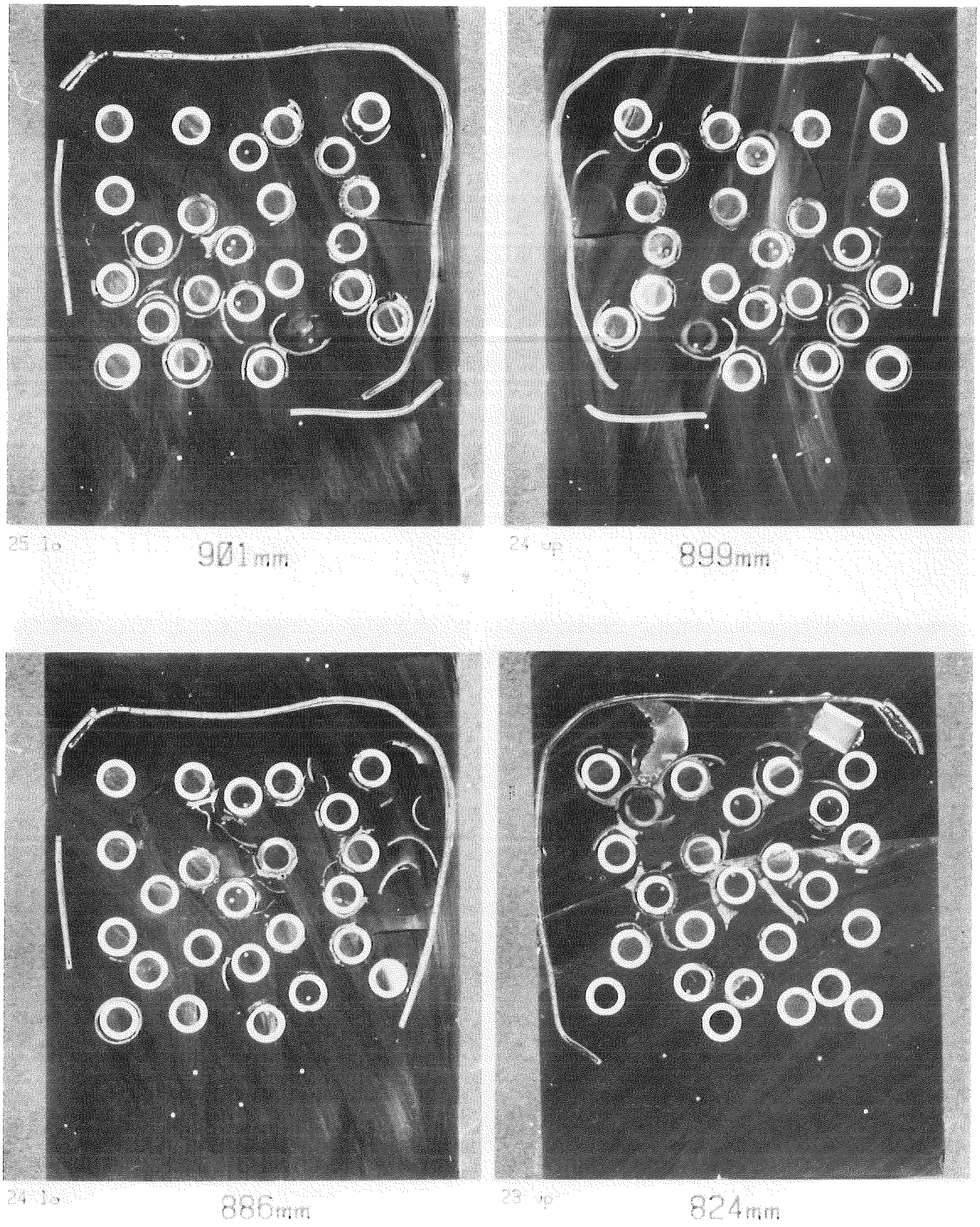


**Fig. A-12. Cross sections of CORA bundle C**

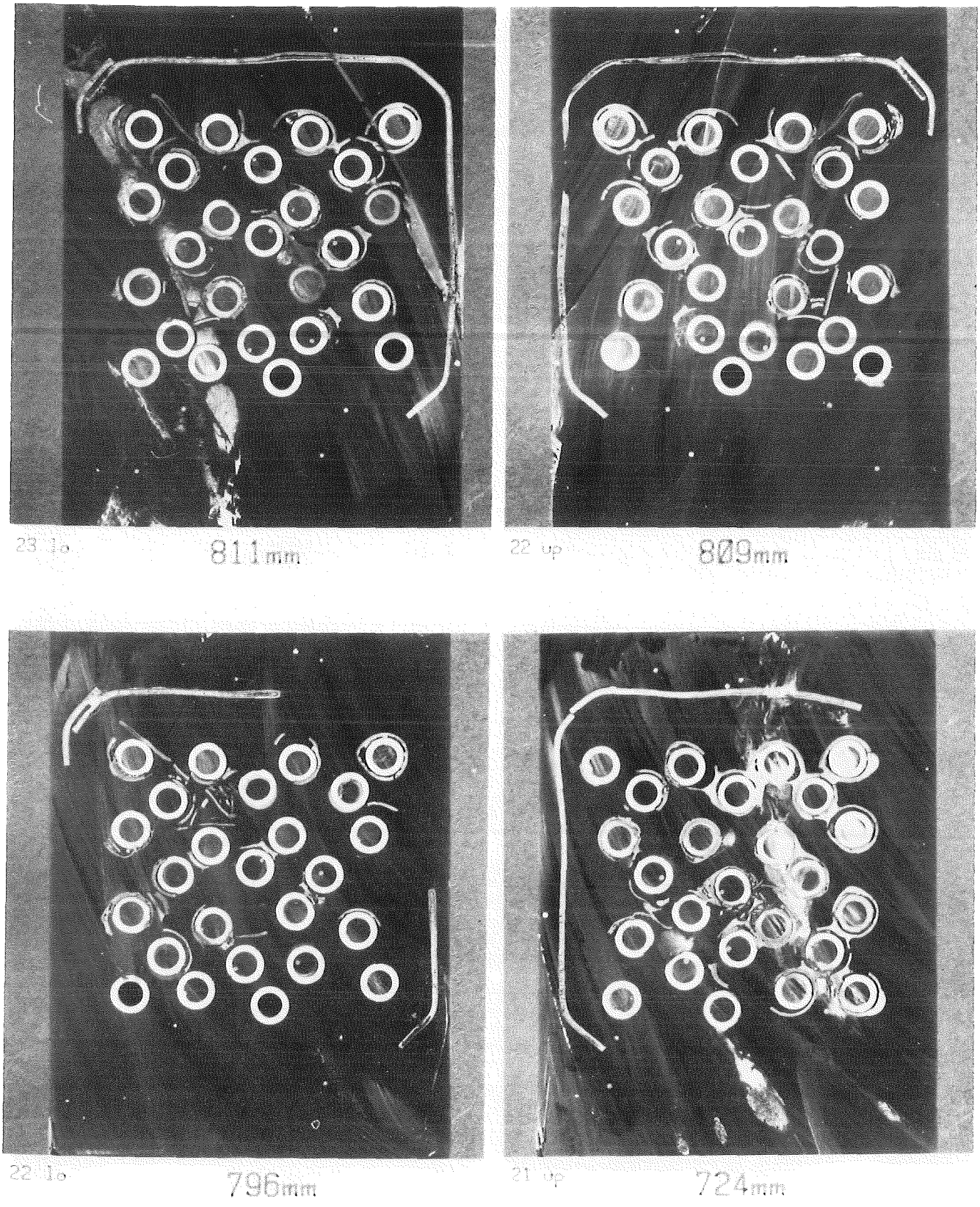


Fig. A-13. Cross sections of CORA bundle C

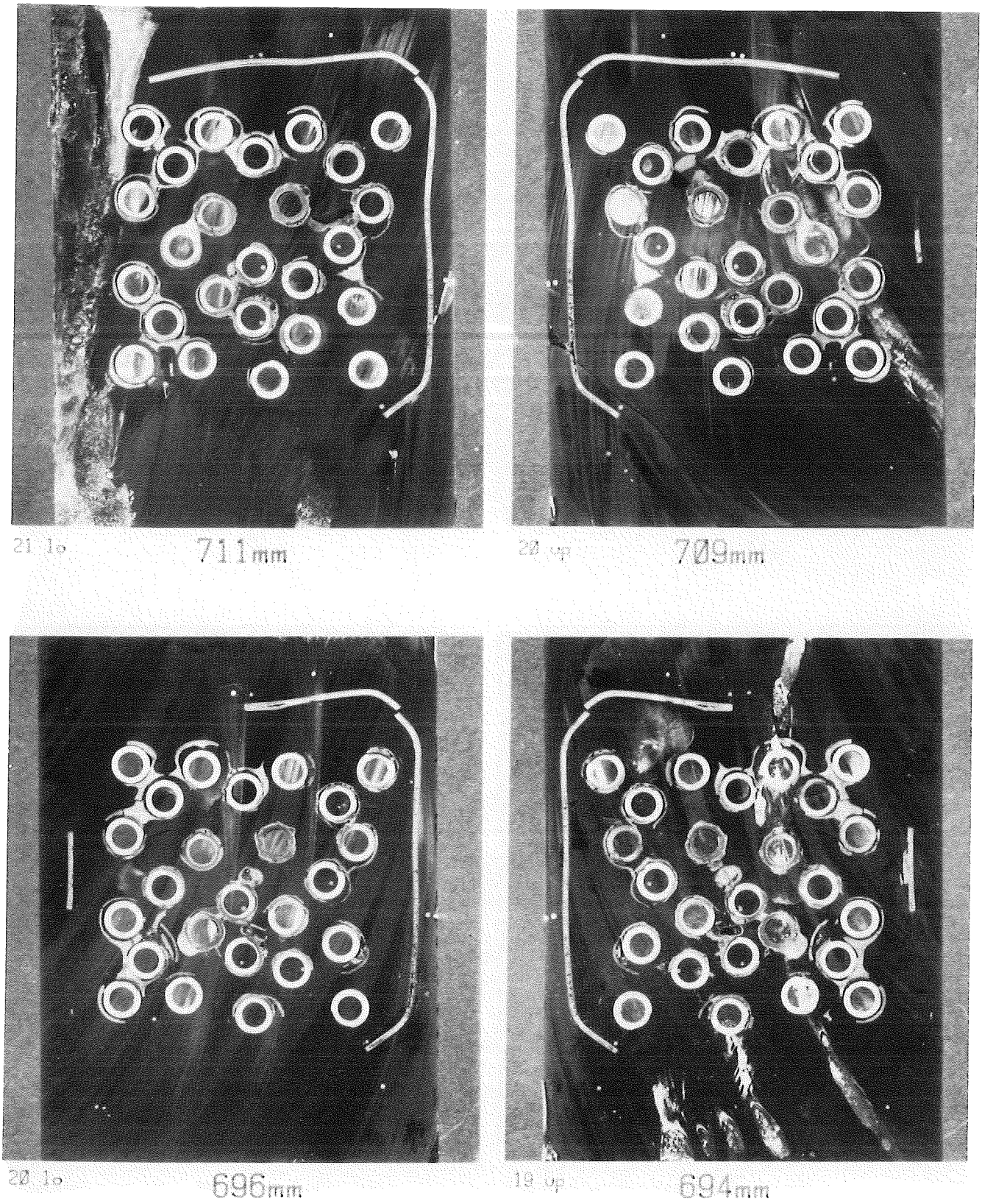


**Fig. A-14. Cross sections of CORA bundle C**

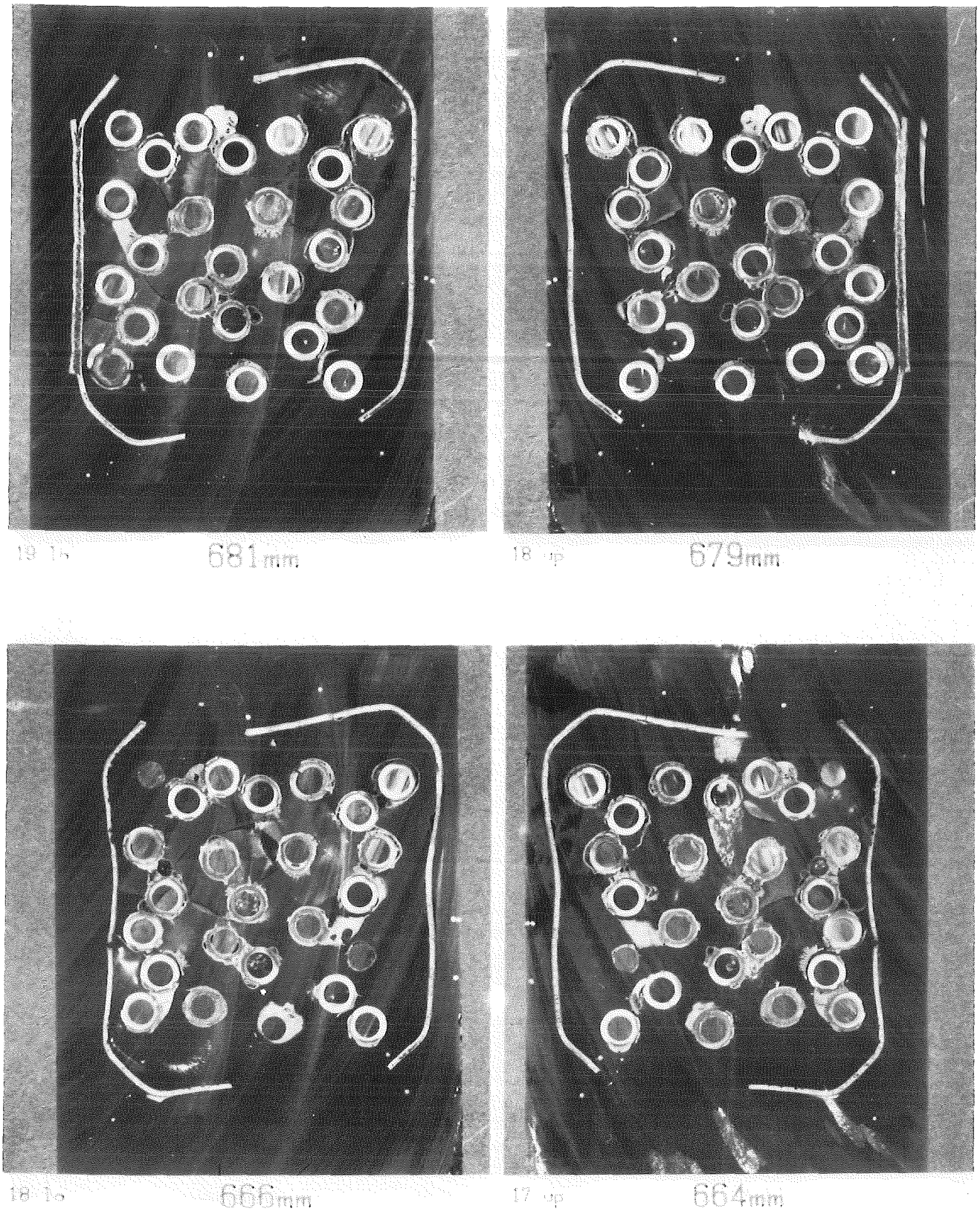


Fig. A-15. Cross sections of CORA bundle C

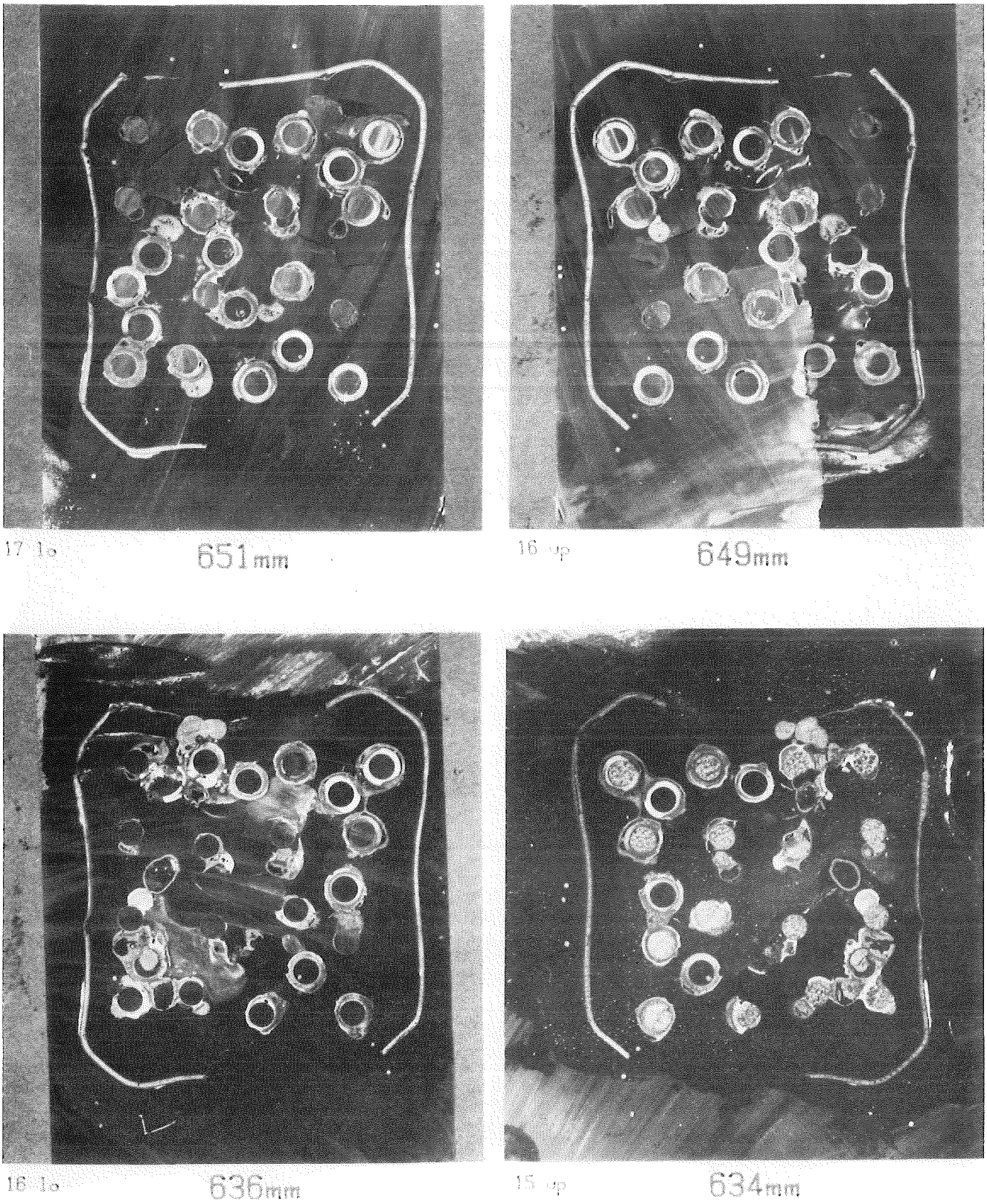


Fig. A-16. Cross sections of CORA bundle C

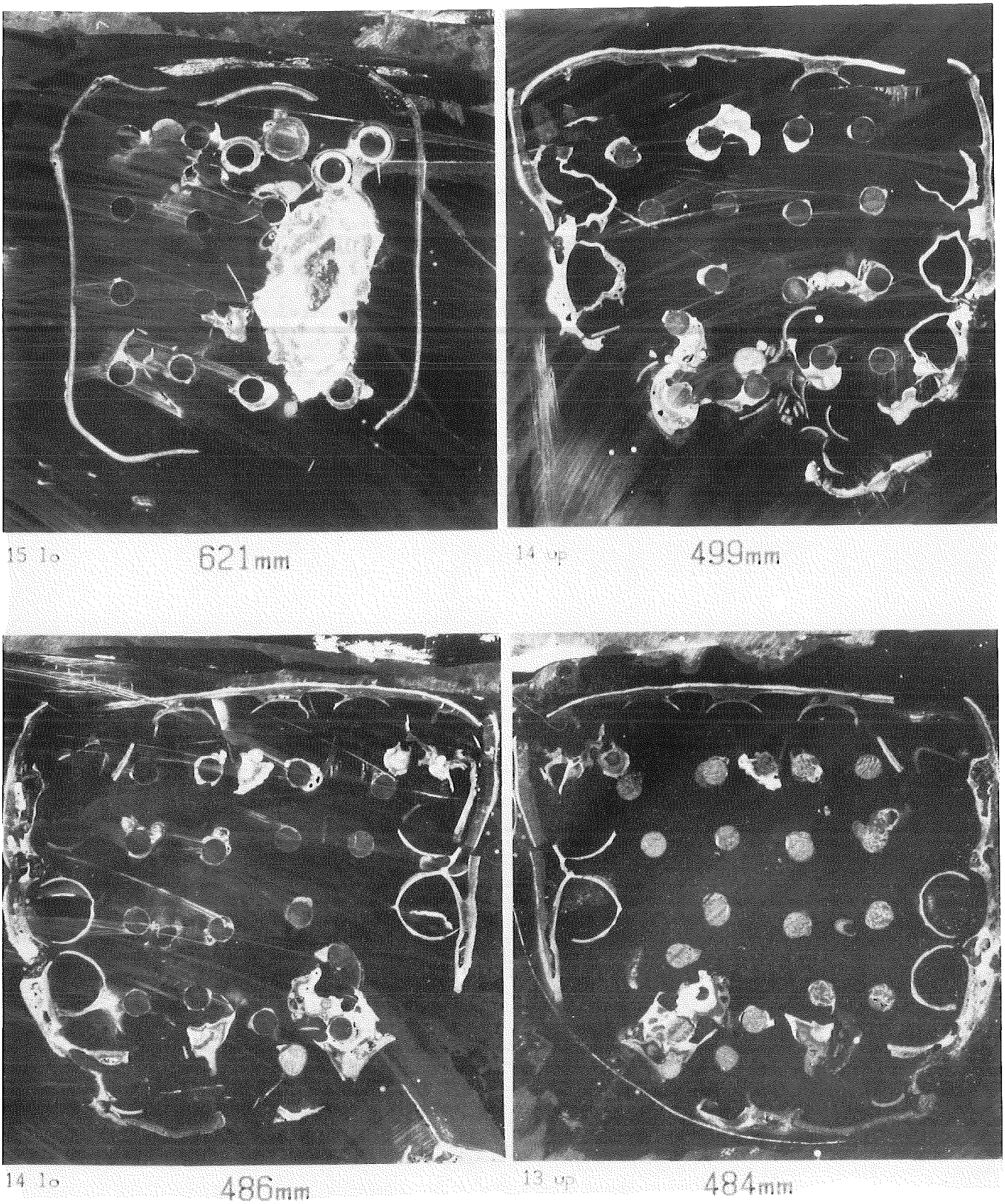


Fig. A-17. Cross sections of CORA bundle C

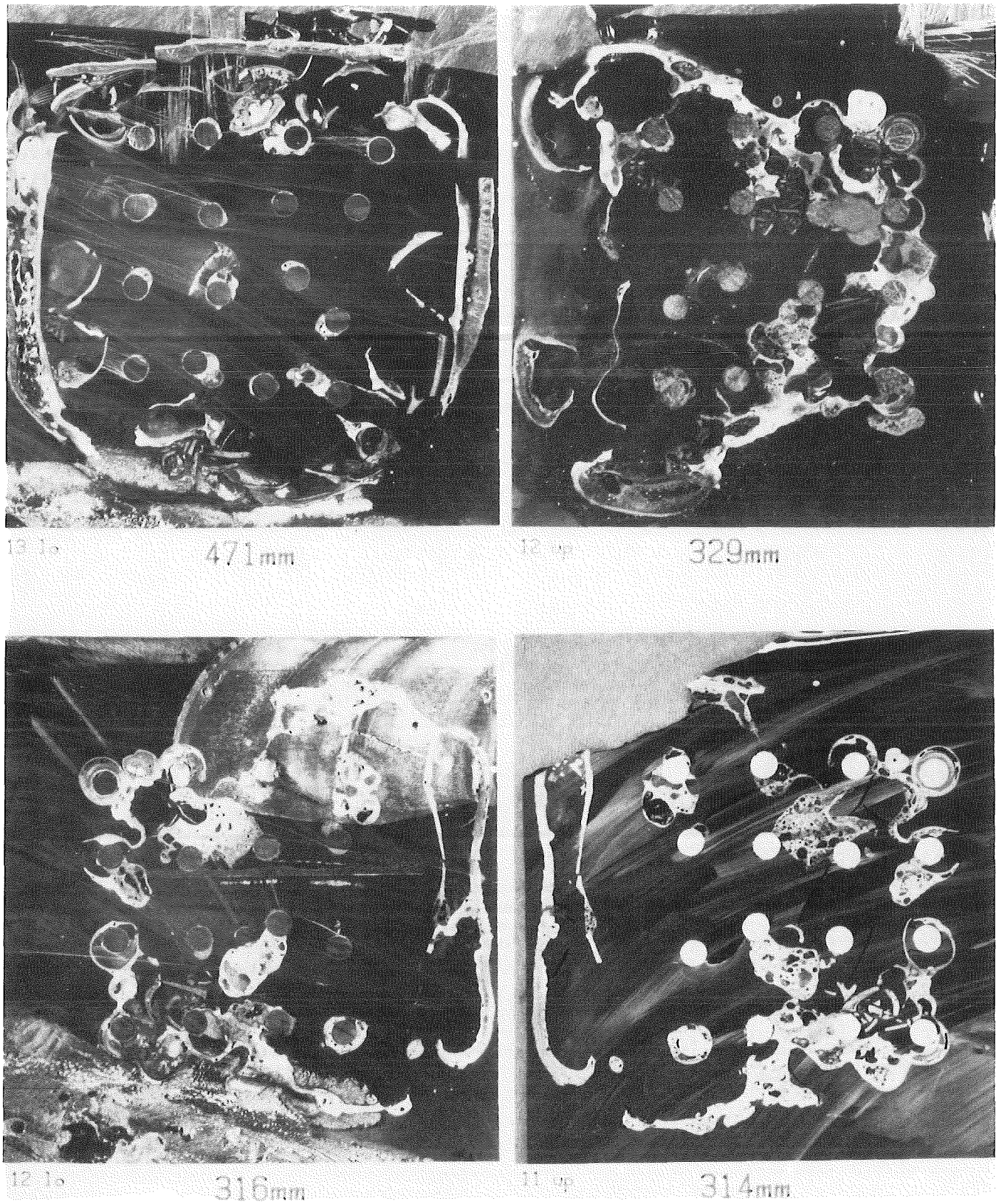


**Fig. A-18. Cross sections of CORA bundle C**

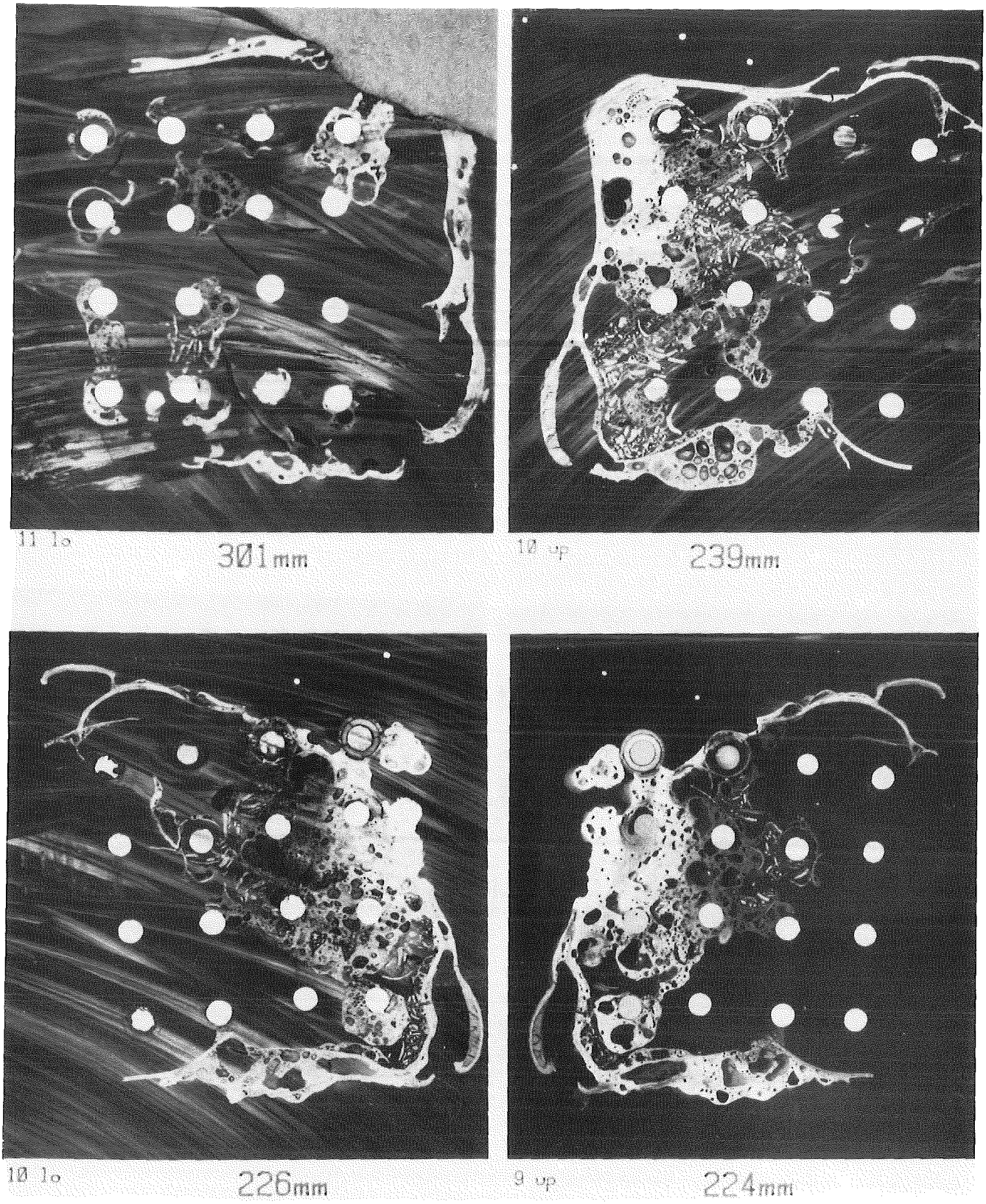


Fig. A-19. Cross sections of CORA bundle C

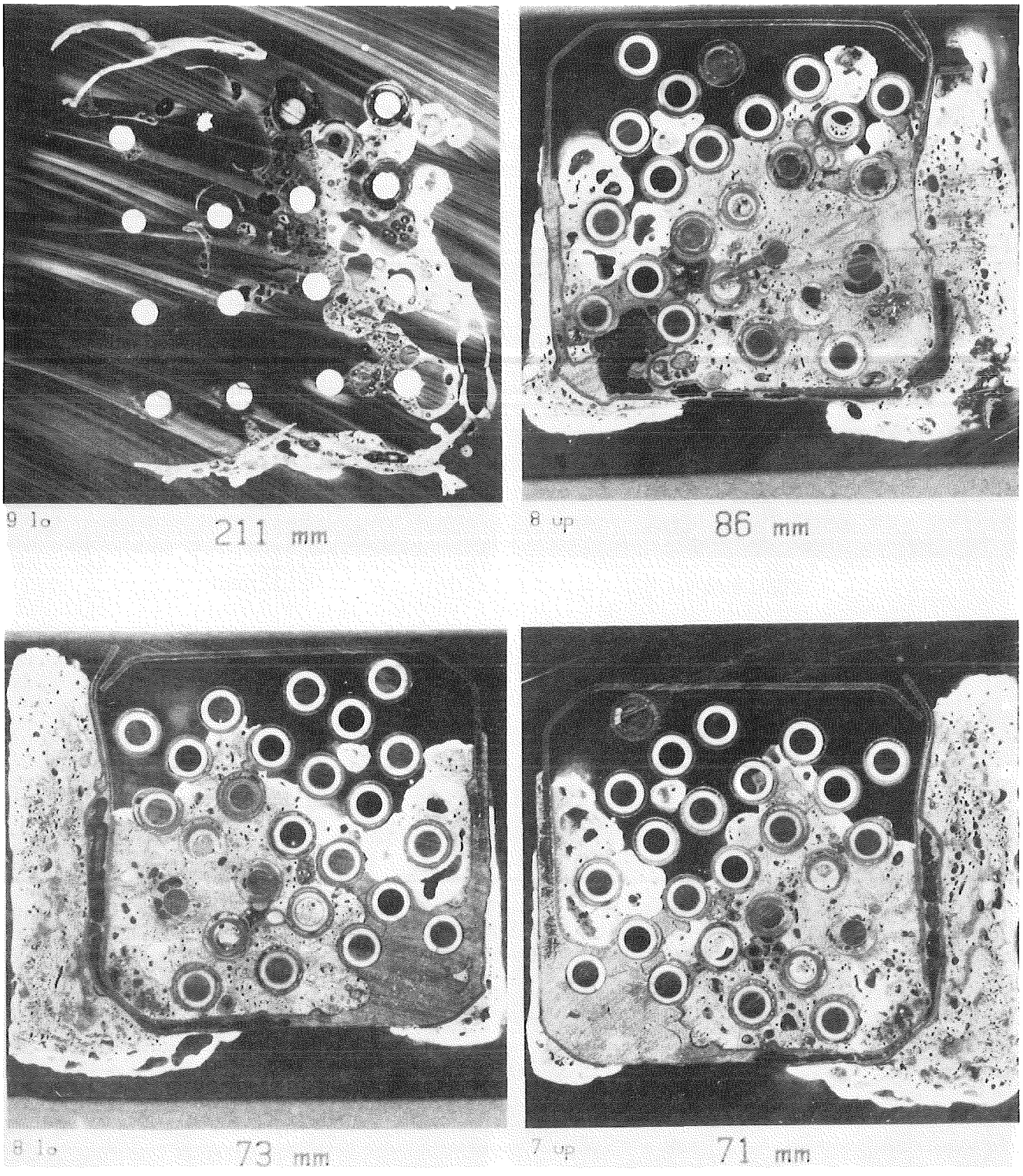


**Fig. A-20. Cross sections of CORA bundle C**

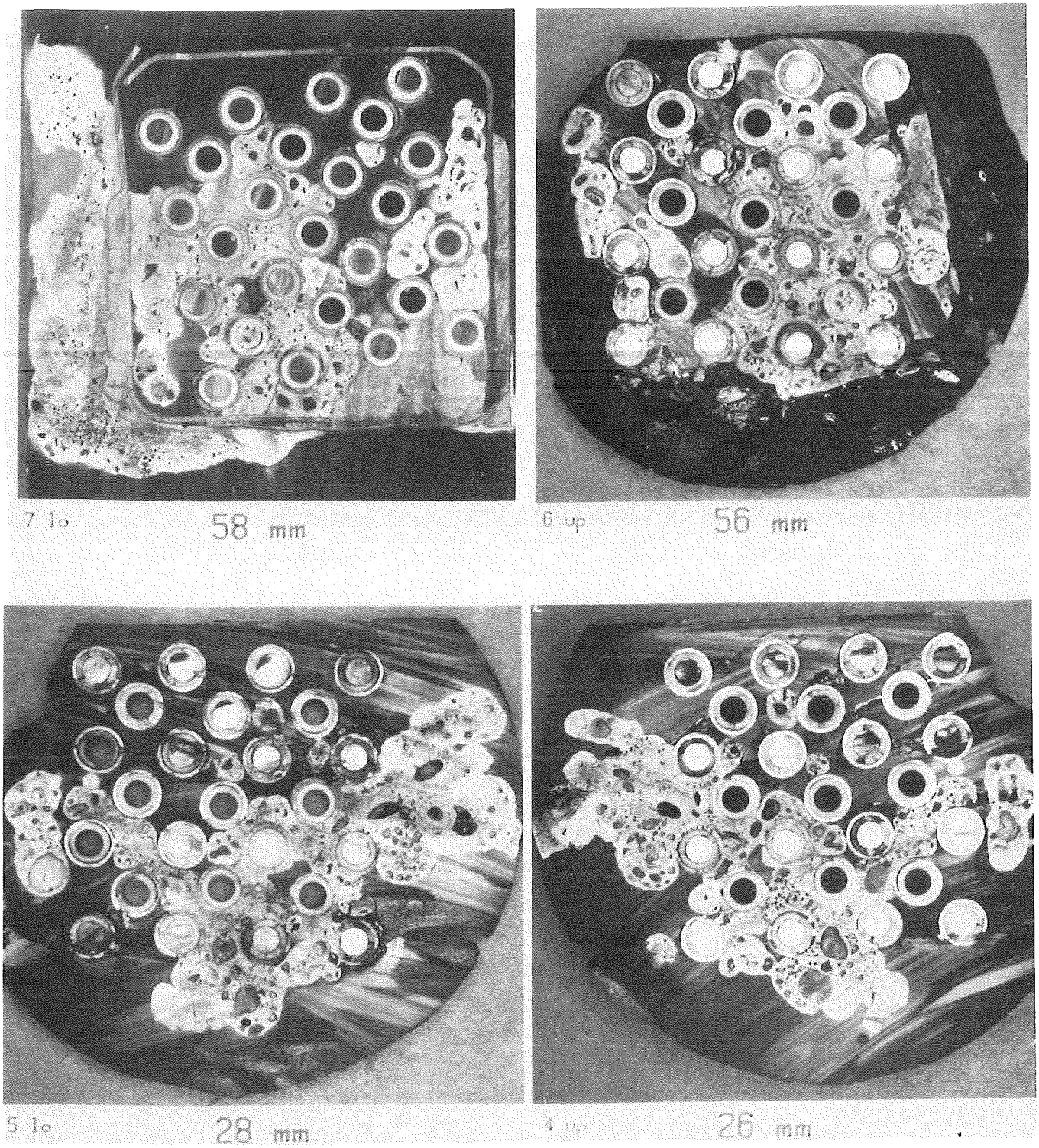


Fig. A-21. Cross sections of CORA bundle C

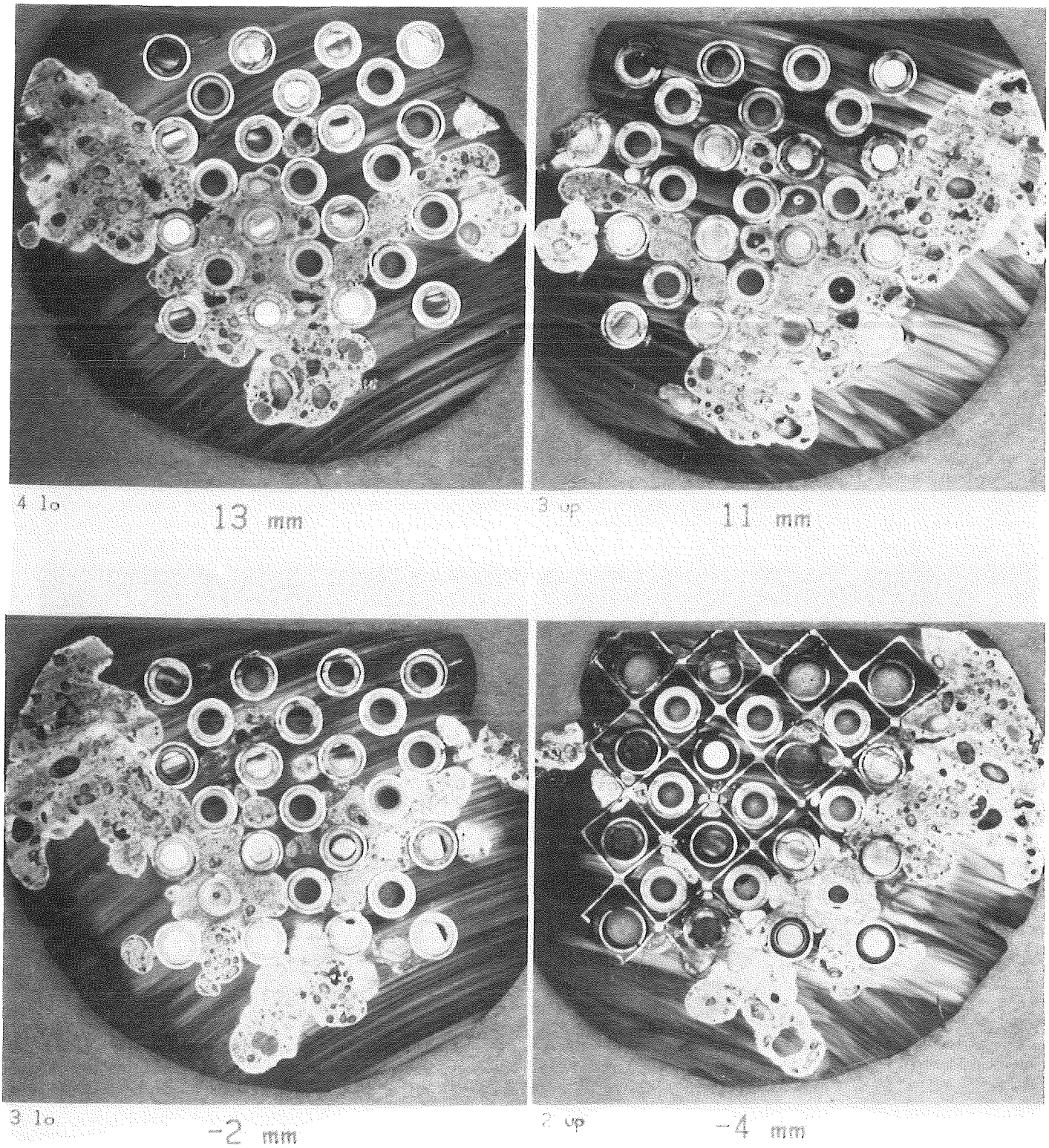


Fig. A-22. Cross sections of CORA bundle C

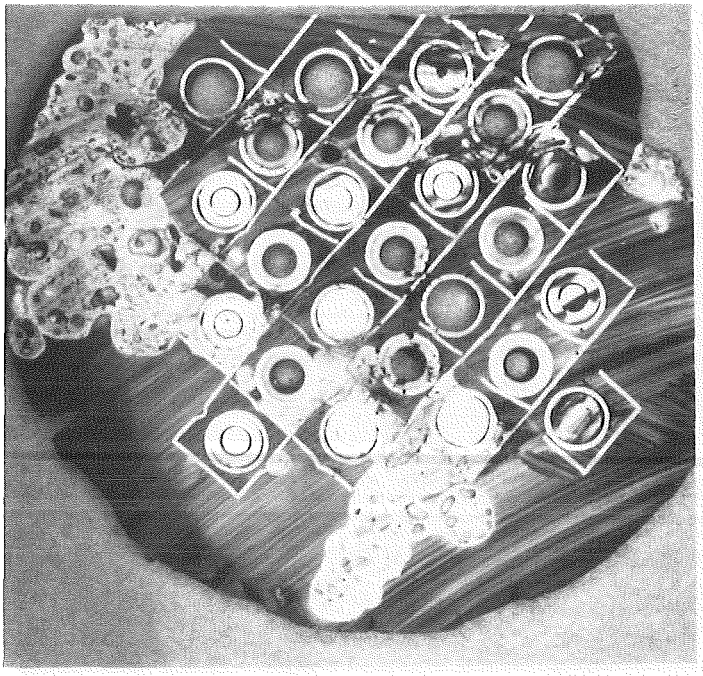

2 lo -17 mm

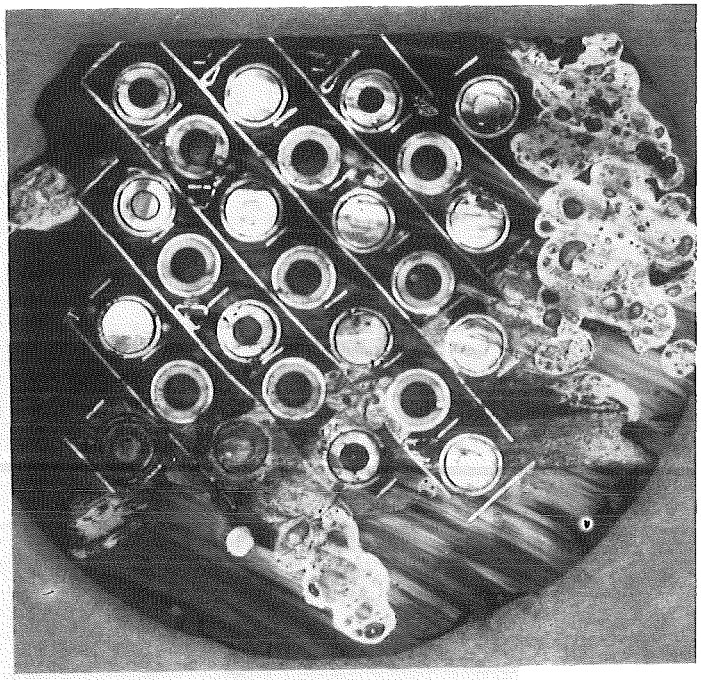

1 up -19 mm

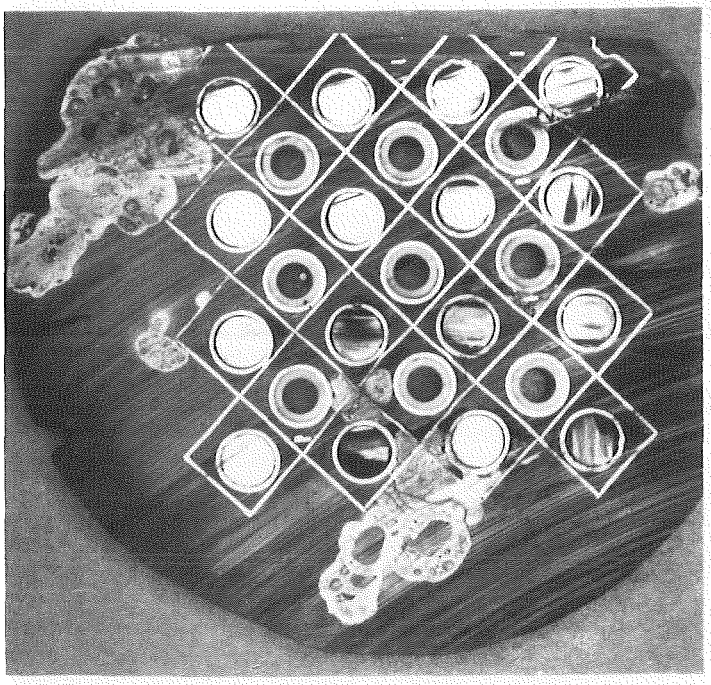

1 lo -32 mm

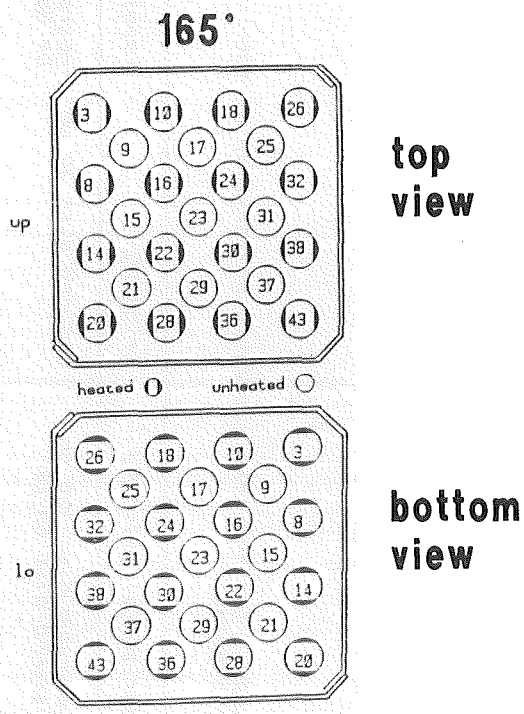


Fig. A-23. Cross sections of CORA bundle C

Table A-3: Procedure for the metallographic preparation of the CORA samples

| | Horizontal grinding | Grinding | Lapping | Polishing | | |
|---|---|---|---|---|---|---|
| Abrasive | Corundum disc 120 µm<br>Diamond disc 64 µm | Diamond disc 20 µm | Petrodisc-M or DP Net*) | PAW cloth | PAN-W | NAP cloth |
| Particle size | | | Diamond spray 6 µm | 6 µm | 3 µm | 1 µm |
| Lubricant | Water | Water | Blue l.**) | Blue l. | Blue l. | Blue l. |
| Revolutions of disc | 300 rpm | 300 rpm | 150 rpm (Net) or 300 rpm (Petrod.) | 150 U/min | 150 U/min | 150 U/min |
| Pressure | 200-400 N | 200-300 N | 100-150 N | 100 N | 100 N | 50 N |
| Time | To level | 5 min | 10 min | 10-20 min | 25 min | 25 min |

*) Petrodics-M and DP Net are registered trade marks of Struers company
**) Blue lubricant of Struers